Modelling the Binding of Organic Molecules to Metal-Organic Frameworks

Michelle Bound, MSci

Thesis submitted to the University of Nottingham for
the degree of Doctor of Philosophy

September 2017

Abstract

Modelling of the fundamental interactions between small organic molecule to metal-organic frameworks (MOFs) and MOF-like structures has been carried out using a variety of computational techniques to further understand and aid in the design of MOFs for gas storage and separation applications. MOFs are an emerging class of porous crystal materials made up of organic linkers and metal nodes that are being researched for many different applications including gas storage and separations. Understanding the adsorption process is vital for the future design of better adsorbents, tailored to application. There are many useful experimental techniques currently in use but the cost and complexity for many systems is great. In this thesis, the importance of computational investigations in this area is illustrated, in particular focussing on binding that occurs between MOF surfaces and gaseous molecules.

A number of computational techniques are employed in this work including *ab initio* electron correlation and DFT calculations, looking at binding between linker-like fragments and various organic molecules and classical GCMC simulation methods, used to study the uptake and binding of small gaseous molecules at, in particular, lower pressures. The different techniques used are evaluated and compared before being utilised on a variety of structures to illustrate the significance of functionalisation within organic linkers on adsorption within MOFs. Results show the importance of a combination of computational and experimental techniques to achieve the deepest understand of binding within MOFs and, to further develop and design MOFs for adsorption applications, optimum functionalisation of linkers within MOF structures is essential.

List of Publications

The work presented in this thesis has been published in part in the following peer reviewed papers (or in preparation for publication):

- The right isotherms for the right reasons? Validation of generic force fields for prediction of methane adsorption in metal-organic frameworks. M. J. Lennox, M. Bound, A. Henley and E. Besley, *Molecular Simulation,* 2017, **43**, 828-837.
- Effective binding of methane using a weak hydrogen bond. A. Henley, M. Bound and E. Besley. *The Journal of Physical Chemistry A*, 2016, **120**, 3701-3709.
- Methane adsorption in metal-organic frameworks containing nanographene linkers: a computational study. E. Bichoutskaia, M. Suyetin, M. Bound, Y. Yan and M. Schröder, *The Journal of Physical Chemistry C*, 2014, **118**, 15573-15580.
- Highly selective gas uptake and unique rotational dynamics in a (3,24)-connected Cu(II) MOF. W. J. F. Trenholme, D. I. Kolokolov, M. Bound, S. P. Argent, J. A. Gould, S. A. Barnett, A. J. Blake, A. G. Stepanov, E. Besley, T. L. Easun and M. Schröder, *In preparation*, 2017.

Acknowledgements

This is the most important part of all that you will read here as nothing would be written without the people who have held me up over the past few years. First and foremost, I would like to thank Elena Besley, my supervisor and mentor over the last 5 years. An inspiration and powerhouse, this woman never failed to pick me up through all my doubts. If I had had any other supervisor, I don’t think I would have made it to this point. Thank you for the determination and Russianisms; they will stay with me. Secondly, I need to thank Matt Lennox. One of the most intelligent humans I’ve met; I can’t thank you enough for your support and knowledge. I’d also like to thank Alice Henley for her essential contributions and the rest of the Elena Besley research group and extended members of the University of Nottingham computational groups for their support and computational input. In particular, thanks go to the ears who listened to my complaints and monologues about cats and dogs amongst many other things. Thank you to Martin Schröder and the Schröder group for all the experimental input. A special thanks to Tim Easun for the initial translation between groups and to Florian Moreau and Will Trenholme for their work, time and patience. Lastly, and most importantly, I need to thank my family and friends who held me together despite all the bumps in the road. I am not the same person I was when I started; thank you for sticking with me.

Let it Fly

I have drifted on this tide for too long
So these words are laced in swan song
Not a final farewell
But a setting free
The cage will still be there
But I’ve thrown away the key
The balloon inflated
I let it fly

I have touched upon greatness
But watched with tired eyes
It started with curiosity
I see her now
The small person on the stage
A word set in her gaze
An idea incepted
And on life went

It unfolded fast
A rug pulled from underfoot
While on a high-speed train
With bittersweet refrain
But we learn best from these times
And magic still resides
Running through the roots
Not to be buried in the past

So here we are
At the end of the beginning
It doesn’t feel like winning
But the heart is starting to glow
And that is where we’ll go
Spirit leading the way
The balloon inflated
We let it fly

List of Abbreviations

ADC	4,4’-azobenzenedicarboxylate
BE	binding energy
BET	Brunauer-Emmet-Teller
BPDC	biphenyl-4,4’-dicarboxylate
BSSE	basis set superposition error
CC	coupled cluster
DFT	density functional theory
FF	force-field
GCMC	grand canonical Monte Carlo
INS	inelastic neutron scattering
LJ	Lennard-Jones
MC	Monte Carlo
MFM	Manchester framework material
MOF	metal-organic framework
MP2	Moller-Plesset
NDC	2,6-napthalenedicarboxylate
NMR	nuclear magnetic resonance
NPD	neutron powder diffraction
OMS	open metal site
OPLS	optimized potentials for liquid simulations
UA	united atom
UFF	universal force field
vdW	van der Waals

Contents

Chapter 1

Introduction

And above all, watch with glittering eyes
the whole world around you because the greatest
secrets are always hidden in the most unlikely places.
Those who don't believe in magic will never find it.

\- *Roald Dhal, The Minpins*

1.1 Gas Storage

There is currently a huge demand for alternative energy sources as pressures of climate change, pollution and population numbers increase. Two major concerns have arisen which need to be addressed imminently including dwindling energy sources and global warming. To tackle both problems, the utilisation of cleaner fuels is essential but much research needs to be carried out before the alternatives can become commercially available.

Ideally, renewable energy sources will be utilised to meet global energy demands such as hydrogen (H_2). This is a promising candidate as it is carbon-neutral, is readily available from water for an infinite period and has a high mass energy density.[1] Although it has been known for many years that hydrogen is a promising alternative fuel for vehicular applications[2] and technologies have already been developed enough to allow hydrogen to be used as a fuel in some vehicles, these technologies are still in their infancy and are expensive. The biggest problem with using hydrogen as an energy source is the storage of hydrogen due to its low density and currently, the easiest storage method is to store hydrogen is in a highly compressed, gaseous form meaning that heavy vessels under extremely high pressures are required. This is very costly due to increase in vehicle weight when transporting the hydrogen and increase in energy required to compress the gas. Hydrogen can also be stored in a liquid state at very low temperatures and, although this has been applied to some vehicles already, adsorption/desorption can be very slow. Neither of these described methods has satisfied the hydrogen storage targets set for vehicular applications by the U.S. Department of Energy (DOE),[3] so much research is being carried out into finding alternative storage methods. One idea is for hydrogen to be stored as an adsorbed gas in porous solids which has a number of advantages. This method could lower the required pressure for gas storage, decrease time for adsorption/desorption kinetics at near ambient temperature and also offers the possibility of recycling.[4] The ultimate goal is to find light-weight materials that can store a high amount of hydrogen reversibly at near ambient conditions.

The use of renewable energy sources globally is some way off and focus has moved to natural gas (NG) which could potentially be used as a bridging fuel for both industrial and residential applications in addition to providing a feedstock for a variety of chemicals.[5] NG is a non-renewable fuel source composed primarily of methane (> 95%) with the remaining fraction comprised of C_2 hydrocarbons, C_2H_2, C_2H_4 and C_2H_6,[6] nitrogen, hydrogen sulphide and carbon dioxide.[7] Removing the hydrocarbons increases the purity of natural gas and provides a source of C_2 hydrocarbons for further chemical manipulation[8] and the lower contents of nitrogen and sulfur when compared with other fossil fuels means there are much lower NO_x and SO_x emissions making NG a much cleaner fuel.[9] Methane (CH_4) has the highest H to C ratio of any fossil fuel and therefore produces less CO and CO_2 per unit of energy when compared to other fossil fuels. In terms of carbon dioxide released, methane delivers twice the energy compared to coal and does so without dissipating mercury or producing uranium- and thorium-rich ash.[10] When initial tests were run on converting cars which ran on petroleum to run on NG the results showed an 86% reduction in CO released, 26% reduction in CO_2 and 77% reduction in NO_x released.[11]

Owing to the fact natural gas is already supplied to households across the world and to the price drop of natural gas due to the deployment of inexpensive technologies for its recovery from shale[10] it is an ideal alternative energy source before other renewable energy source technologies are developed. However, there are still challenges to overcome before NG can be used a bridging fuel. This includes a mass- and volume efficient, ambient temperature storage and delivery. Currently, there are two commercial methods of NG storage[12] including compression to 200-300 bar at room temperature and liquefaction at low temperature. Compressed natural gas (CNG) requires the use of heavy, thick-walled cylindrical storage tanks and multi-stage compressors to achieve a reasonable volumetric energy density (VED) although the amount of NG stored in a tank only reaches small driving ranges with added safety concerns. Expensive cryogenic vessels are required for storage as liquefied natural gas (LNG) which can suffer boil-off losses but achieves a slightly higher VED. Alternatives to these methods are obviously needed and current research is looking at porous adsorbents for this purpose. In particular, MOFs are of particular interest for the separation of C_2 hydrocarbons from methane[13–19] due to the potential of a cost-effective method for storing NG at ambient temperature and near-ambient pressures (~35 bar).

Research into reducing emissions by the utilisation of alternative energy sources may take years to become commercially viable and during this time, fossil fuels will still be used with the continued release of pollution into the atmosphere. However, research is also being carried out into controlling atmospheric carbon dioxide (CO_2) concentration by removing the gas from the air through carbon capture and storage (CCS) techniques. The largest contributor to CO_2 emission is from power plants and currently, the easiest method of reducing this emission without changing technologies is the post-combustion capture method.[20] This is where the process and technology of burning fossil fuels are kept the same but materials are added to the process post-combustion to capture CO_2 in low concentration before it is released into the atmosphere. There are many different technologies being researched for this purpose including aqueous ammonia-based adsorption, membranes, hydrate formation and physisorptive materials.[21] Physisorptive materials such as metal organic frameworks have been focused on in recent years for the capture of CO_2[22–29] due to their large surface areas, large pore volumes and the fact they can be easily adapted for purpose.

1.2 Physisorptive materials

There are many aspects to the research into gas storage but overall an efficient, reversible and high gas uptake is needed for the storage of all these gases and physisorptive materials are well suited to this application. Physisorptive materials considered for gas storage applications include carbon-based materials, zeolites, and metal organic frameworks.[30] These are highly porous, solid materials with which gaseous molecules undergo physisorption with the surface of the materials via weak intermolecular forces such as van der Waals' (vdW) interactions. This allows some interaction to occur between the sorbent and sorbate but a weak enough interaction that it can reversed by small changes in temperature or pressure. This is opposed to chemisorptive materials where chemical bonds are formed between the sorbent and sorbate which require activation energy and take a much greater amount of energy to break. MOFs are the focus in this work as they offer unique, desirable properties which can be enhanced for application through molecular design.

1.21 Metal-Organic Frameworks

MOFs are hybrid materials that bridge the gap between organic materials and inorganic materials. First introduced in the 1990s,[31] they consist of networks made up of inorganic nodes (metal ions or clusters) that are coordinated with organic linkers which, when repeated in three dimensions form crystalline networks with unique physical and chemical properties. They are highly porous due to high surface areas and low crystal density and can have high thermal and chemical stability.[21,32,33] The combination of these properties make MOFs ideal candidates for many applications including chemical catalysis,[34,35] sensing,[36] ion exchange[37] and drug delivery[38,39] but most importantly in this work, gas storage[40–47] and separation[48] applications. MOFs have shown great promise for H_2, CH_4 and CO_2 sorption and storage which has fuelled a wave of research interest in this area over the last decade.

A great number of studies have been carried out in recent years investigating MOFs and their properties and thousands of MOFs have been synthesised. MOFs have attracted particular attention in the area of gas sorption due to their tuneable pore geometry and designed chemical functionality as they are essentially made up of ‘building blocks’ which can be designed according to targeted properties by selection of different metal centres and functional linkers[49,50] to form millions of hypothetical MOFs. One of the most widely studied MOFs is MOF-5 or IRMOF-1 which is a well-known structure formed of Zn_4O clusters and benzene di-carboxylate linkers in the cubic *pcu* topology[51] with a reasonable carbon dioxide uptake[52,53] and high hydrogen uptake.[43,54] This MOF is part of a family of MOFs with the same network topology (an isoreticular series) whose linkers and metals can be interchanged to form similar structures with varying pore sizes and functionalities.[47] The structure of a MOF’s three-dimensional network can be identified by its topology using a method proposed by O'Keeffe *et al*.[55,56] which uses systematic terminology to classify the known structures using a three-letter symbol, e.g. *pcu*. Another well studied MOF is HKUST-1 which constructed of copper paddlewheel units and benzene tricarboxylate ligands with *tbo* topology.[57] This MOF, which is commercially available in gram scale shows promise for methane storage.[10] NOTT-112 also contains copper paddlewheel units coordinated to a hexacarboxylate ligand with a square planar geometry and a similar surface area to MOF-5.[58] With the presence of open metal sites and large pore volumes, NOTT-112 exhibits high hydrogen storage compared to MOF-5 illustrating the importance of the components of the structure for gas uptake.

The number of MOFs that have been synthesised is only a small fraction compared to the hypothetical possibilities. In conjunction with experimental techniques computational design is being increasingly used as a powerful tool to investigate new MOFs and calculate their properties. Screening of MOFs for methane-storage capacity has been carried out by Wilmer *et al.*[59] where a number of building blocks derived from existing crystallographic data of synthesised MOFs were recombined systematically in different ways to generate over 130,000 hypothetical MOF structures which were all screened for their methane uptake abilities. Given constraints of time, cost and available laboratory equipment and reagents they identified NOTT-107 within the top 2% of their database with an exceptional predicted uptake of methane and synthesis of this material proved that the experimental uptake agreed well with predicted values showing how computational design can guide experimental work. However, there are drawbacks to this technique as it is likely that structure-property relations were missed in the process and many MOFs may have been overlooked due to lack of geometrical optimisation of structures.

Work studying properties of MOFs and how this can be useful has been carried out by other researchers. Duren et al.[60] looks at calculating the geometric surface area as a characterisation tool for screening and comparing porous materials for adsorption applications. They show that the simple calculation of accessible surface area along with the probe diameter corresponding to the adsorbate of interest provides a relatively straightforward method to screen and compare adsorbents. They also demonstrate how this calculation can be used as a theoretical upper limit of adsorption of a perfect crystal to help gain insight into experimental surface areas which can be adversely affected by incomplete solvent removal during activation, crystal collapse or interpenetration.

More in-depth studies are also being carried out to investigate MOFs. Work studying the NU-100 MOF by Farha *et al*.[61] is an example of a more specific approach where promising topologies and linkers were considered before a full optimisation was carried out on the hypothetical MOF structures and various properties were calculated. NU-100 currently has one the highest CO_2 and H_2 uptakes seen in the literature to date showing how molecular simulations and computational design can guide experimental work and save cost in doing so. This in-depth process using a combination of density functional theory calculations, Monte Carlo simulations and grand canonical Monte Carlo simulations produced computational results in excellent agreement with experiment. Hence, these techniques are the basis of the research outlined in this thesis.

Gaining a deeper understanding and control of supramolecular host-guest interactions is crucial if practical materials are to be developed for targeted applications as these interactions play a significant role in the adsorption process, in particular at lower pressures where binding directly relates to uptake.[62] There have been many computational studies into selectivity within MOFs[63–65] and various strategies have been reported to enhance the host-guest interactions in MOFs including the incorporation of unsaturated metal centres or open metal sites (OMSs) and the functionalisation of the organic linkers to provide binding sites for guest species. The favourable role OMSs play in guest binding has been widely confirmed through *in situ* neutron diffraction experiments[41,66–70] clearly concluding that OMSs are the primary binding domains for guest molecules. Neutron spectroscopic experiments also give evidence to this observation and confirm the large translational and/or rotational hindrance of bound guest molecules at OMSs.[71] There have also been some investigations into the role of organic functionalisation in guest binding within MOFs[72–74] with computational research playing a key role in investigating suitable functional groups for gas storage purposes,[59,75] at both the atomic scale[27,76–78] and for large scale systems.[79–81] Therefore, herein this thesis attempts to investigate the role of the binding of various small organic molecules to MOFs and MOF-like structures through computational methods to further improve design of and gain insight into the adsorption process within MOFs for gas storage and separation applications.

1.23 Other Examples of Physisiorptive Materials

There are many more examples of physisorptive materials that are being researched for gas storage. Metal organic polyhedral are porous coordination nanocages formed between linkers such as carboxylic acid or metal clusters. They are ideal for gas sorption and separation applications due to containing nano-sized hydrophobic cavities with permanent porosity. MOFs, however, show a greater adsorption capability due to their larger surface areas.[82] Hyper-cross-linked polymers were introduced in the 1970s[83] and have been researched thoroughly since. Like MOFs, their pore sizes and surface areas can be predicted and controlled which led to development of other porous materials. Hyper-cross-linked polymers show potential for hydrogen storage and separation as they exhibit high thermal and chemical stabilities but their adsorption capabilities are limited by a smaller surface areas than MOFs.[30,84] Covalent organic frameworks have been researched in more recent years for gas adsorption applications and similar to MOFs, they are made up of building blocks which can be interchanged to form structures with wanted properties.[30] They are made up of strong covalent bonds without no heavy metal elements and therefore have lower densities than MOFs with comparable surface areas. However, to achieve comparable adsorption uptakes, enhancement with metal sites is necessary.[85] Porous aromatic frameworks, a subclass of porous organic frameworks have shown promise in sorption applications and have high stability with diamond as the starting point of their structure.[86] However, there is still more research needed into these materials for sorption applications. Covalent triazine frameworks are another porous organic polymer material which have only undergone research into gas sorption in recent years. These are nitrogen-rich materials showing potential for gas storage due to the accessible nitrogen sites within the framework but so far uptakes do not reach those achieved my MOFs.[87] Organic molecular porous materials have again, been studied in more recent years for gas sorption applications. Unlike the frameworks of other materials researched for gas adsorption, organic molecular materials are discrete molecules packed together by weak, non-covalent interactions. Although a number of these materials have been found to have solvent accessible voids with reasonable surface areas, in general they pack together to form dense, non-porous structures and are notoriously difficult to design and predict.[88] Overall, although there are many alternatives to MOF materials which show promise for gas sorption and separation applications, MOFs are well studied with great potential in this area and are therefore the focus of this work.

1.3 Thesis Outline

In Chapter 2 an overview of the computational theory used throughout the research undertaken in this work will be introduced including *ab initio* density-functional theory (DFT) and molecular grand canonical (GCMC) simulation methods. This leads on to Chapter 3 where the practicality of different force-fields (FF) used in GCMC simulations is investigated by comparison of three different FF to DFT calculations.[89] This chapter aims to provide a guide to the sort of FFs most useful for methane uptake within different MOF structures and validates the FFs used within this presented research.

Methane binding interactions are the focus of Chapter 4 which uses *ab initio* methods to investigate the binding between methane and various functionalised ligand-like structures.[90] The importance of weak H-bonding in these interactions is illustrated with suggestions on how to incorporate the functionalised molecules into MOF ligands for enhancement of methane surface interactions. Benchmarking of *ab initio* methods used throughout this work is also presented in this chapter. Chapter 5 continues the theoretical investigation looking at a hypothetical series of MOFs containing hexabenzocorene groups within the ligands.[91] The study looks at methane uptake within the MOFs and also CO_2 and H_2 uptake for the largest MOF of the series illustrating practicality of this particular functionalisation to help guide experimental investigations.

Finally, in Chapter 6, two novel copper MOFs designed for high CO_2 uptake and selective adsorption of C_2 hydrocarbons over methane, are studied. Both MOFs MFM-160[92] and MFM-180[93] contain functionalisation of ligands and the role that these functional groups play in adsorption is investigated using a combination of DFT, neutron powder diffraction (NPD), inelastic neutron scattering (INS) and ^{2}H NMR studies.

Overall, the work presented in this thesis demonstrates the significance of computational modelling of binding between small organic molecules and MOFs for gas adsorption and separation. Various fragments and whole MOF structures are considered to illustrate the important role of the organic ligands in the binding of gaseous molecules to MOF surfaces. Solely theoretical investigations, however, do not present a finished story and the combination of experimental and computational techniques to investigate adsorbate/absorbent interactions is essential for designing MOFs for targeted applications.

Chapter 2

Computational Methodology

The chemical interactions between metal-organic frameworks and guest gaseous molecules can be studied using a number of different computational approaches and levels of theory. In this section, standard computational methods used in the subsequent modelling chapters are briefly outlined. Starting with an introduction to traditional wavefunction-based methods of computational chemistry, a summary of electron correlation methods and density functional theory is given which introduces the *ab initio* methods used in this work to study interactions between various fragments of MOF-like structures and gaseous molecules. These electronic structure methods are focused on solving the Schrödinger equation for a single or few molecules corresponding to gas phase in a vacuum. To study more realistic conditions involved in metal-organic framework chemistry (i.e. complete MOF structures and their interactions with gaseous molecules), statistical simulation methods are used in the form of grand canonical Monte Carlo simulations which will be introduced later in the chapter.

2.1 Wavefunction-based quantum chemical approaches

2.11 The Schrödinger equation

The Schrödinger equation (Equation 2.1) can be solved to find the total energy of a system, E, of interacting electrons, N, and nuclei, M.

$$\hat{H}\Psi(N,M) = E\Psi(N,M) \tag{2.1}$$

The Hamiltonian operator, $\widehat{H}$, can be written as the kinetic (*T*) and potential energies (*V*) of the nuclei (*n*) and electrons (*e*)

$$\widehat{H}_{tot} = \widehat{T}_n + \widehat{T}_e + \widehat{V}_{ne} + \widehat{V}_{ee} + \widehat{V}_{nn} \tag{2.2}$$

$$\widehat{H} = \sum_i \frac{\hbar^2}{2m_e}\nabla_i^2 - \sum_A \frac{\hbar^2}{2m_A}\nabla_A^2 - \sum_i\sum_A \frac{e^2 Z_A}{r_{iA}} + \sum_{i>j}\frac{e^2}{r_{ij}} + \sum_{A>B}\frac{e^2 Z_A Z_B}{r_{AB}} \tag{2.3}$$

where *i* and *j* denote the electrons, *A* and *B* denote the nuclei, $\hbar$ is Planck's constant divided by 2π, m_e is the mass of an electron, m_A is the mass of the nucleus, ∇^2 is the Laplacian operator, *e* is the charge of an electron, Z is an atomic number and r_{ij} is the distance between particles *i* and *j*.

The variational theorem can used to find a better estimate of the ground state energy and systematically improve the wavefunction used. This states that the variational energy or the energy of any trial wavefuntion, E_{var}, is always an upper bound to the exact ground state energy, $E_{exact.}$ Therefore, any approximate Ψ will yield an energy that is higher than the ground state energy.

$$\frac{\int \Psi^* \widehat{H} \Psi \, d\tau}{\int \Psi^* \Psi \, d\tau} = E_{var} \geq E_{exact} \tag{2.4}$$

2.12 The Born-Oppenheimer approximation

The nuclei of atomic systems are much heavier than the electrons and move much more slowly in comparison and therefore the Born-Oppenheimer approximation can be used to simplify the wavefunction of the system. This assumes that the electrons move around fixed nuclei, *R* and separates the total wavefunction of the system into nuclear and electronic components

$$\Psi_{tot}(N,M) = \psi_M(N)\psi(M) \tag{2.5}$$

where $\psi_M(N)$ is the electronic wavefunction and depends on the nuclear coordinates. The problem is then reduced to solving the electronic Schrödinger equation for a set of nuclear geometries. The electronic Hamilton operator can be written as

$$\hat{H}_e = \hat{T}_e + \hat{V}_{ne} + \hat{V}_{ee} + \hat{V}_{nn} \tag{2.6}$$

2.13 The Hartree-Fock approximation

The simplest way to approximate electron-electron interactions is through the Hartree approximation, where, using the variational energy, the many-electron wavefunction is reduced into a product of N one-electron functions, spin orbitals $\chi_i(\boldsymbol{x}_i)$ consisting of a spatial orbital $\Phi_i(\boldsymbol{r})$ and one of the spin functions up-spin $\alpha(s)$ or down-spin $\beta(s)$.

$$\Psi(\boldsymbol{x}_1, \boldsymbol{x}_2, \boldsymbol{x}_3, \dots) = \chi_1(\boldsymbol{r}_1)\chi_2(\boldsymbol{x}_2)\chi_3(\boldsymbol{x}_3)\dots \tag{2.7}$$

$$\chi_i(\boldsymbol{x}_i) = \Phi_i(\boldsymbol{r}_i)\sigma(s_i) \tag{2.8}$$

Each electron therefore interacts with the average distribution of the other electrons but this does not account for exchange interactions. According to the Pauli principle, the total wavefunction for two electrons is antisymmetric with respect to exchange of electrons. By writing the wavefunction as an antisymmetrised product of orbitals this problem is solved and can be written as a Slater determinant:

$$\Psi = \frac{1}{\sqrt{N!}}\begin{vmatrix} \chi_1(\boldsymbol{x}_1) & \chi_2(\boldsymbol{x}_2) & \cdots & \chi_N(\boldsymbol{x}_N) \\ \chi_1(\boldsymbol{x}_1) & \chi_2(\boldsymbol{x}_2) & \cdots & \chi_N(\boldsymbol{x}_N) \\ \vdots & \vdots & \ddots & \vdots \\ \chi_N(\boldsymbol{x}_1) & \chi_N(\boldsymbol{x}_2) & \cdots & \chi_N(\boldsymbol{x}_N) \end{vmatrix} \tag{2.9}$$

The HF wavefunction can be put into the variational energy expression and the energy minimised with respect to changes in the orbitals to yield the Fock equation

$$\hat{f}\chi_i = \epsilon_i\chi_i \tag{2.10}$$

where ε_i is the orbital energy and $\hat{f}$ is the Fock operator, which is built from three operators; the core Hamiltonian operator, the Coulomb operator, $\hat{J}$ and the exchange operator, $\widehat{K}$ which can be written as

$$\hat{f} = -\frac{1}{2}\nabla_i^2 + \sum_A^M \frac{-Z_A}{r_{iA}} + \sum_j^N (2\hat{J}_j(\boldsymbol{x}_1) - \widehat{K}_j(\boldsymbol{x}_2)) \tag{2.11}$$

The Coulomb operator, $\hat{J}$ is the electrostatic repulsion of an electron at $\boldsymbol{x}_1$ from all other electrons in the system due to the charge of an electron in spin orbital χ_j and is represented by Equation 2.12.

$$\hat{J}_i(\boldsymbol{x}_1) = \int \left|\chi_j(\boldsymbol{x}_2)\right|^2 \frac{1}{r_{12}} d\boldsymbol{x}_2 \tag{2.12}$$

The exchange operator, $\widehat{K}$ is a purely quantum consequence of the antisymmetry of the electronic wavefunction and represented by Equation 2.13.

$$\widehat{K}_i(\boldsymbol{x}_1)\chi_i(\boldsymbol{x}_1) = \int \chi_j^*(\boldsymbol{x}_2)\frac{1}{r_{12}}\chi_i(\boldsymbol{x}_2)d\boldsymbol{x}_2\chi_j(\boldsymbol{x}_1) \tag{2.13}$$

The Coulomb operator in Equation 2.12 produces a false self-interaction energy which is cancelled out by the exchange term when *i* = j. This is not an issue for HF calculations but it is not accounted for when using DFT so this has to be considered.

2.14 Basis functions

Numerical solutions for the Hartree-Fock orbitals are only practical for atoms and diatomic molecules. Diatomic molecular orbitals (MOs) resemble linear combinations of atomic orbitals. For polyatomic molecules, the MO can be approximated by a linear combination of atomic orbitals with a set of L basis functions located on the nuclei η_μ

$$\phi_i = \sum_{\mu=1}^{L} c_{\mu i}\eta_\mu \tag{2.14}$$

in which $c_{\mu i}$ is the expansion coefficient and determines the weight of the contribution of the basis functions to the molecular orbital. This can be inserted into the Fock equation 2.10 for the orbitals. Multiplying from the left by an arbitrary basis function η_ν and integrating over space results in Equation 2.15 which can be rewritten as the Roothaan-Hall equation (Equation 2.16).

$$\sum_{\mu=1}^{L} c_{\mu i} \int \eta_\mu(\boldsymbol{r})\,\hat{f}(\boldsymbol{r})\eta_\nu(\boldsymbol{r})d\boldsymbol{r} = \epsilon_i \sum_{\mu=1}^{L} c_{\mu i} \int \eta_\mu(\boldsymbol{r})\,\eta_\nu(\boldsymbol{r})d\boldsymbol{r} \tag{2.15}$$

$$\mathbf{FC} = \epsilon\mathbf{SC} \tag{2.16}$$

This is the Fock equation in the atomic orbital basis, and all the L equations are collected in the matrix notation **C**. The **S** matrix contains the overlap elements between basis functions, the **F** matrix contains the Fock matrix elements and ϵ is a matrix containing the orbital energies in the diagonal terms.

Slater-type orbitals are physically correct basis functions which decay exponentially far away from the nucleus and are solutions to the Schrödinger equations of hydrogen-like atoms. These STOs can be approximated as linear combinations of Gaussian-type orbitals. Split-valence basis sets take the form X-YZg where X is the number of primitive Gaussians comprising each core atomic orbital basis function and the Y and Z represents the valence orbitals are composed of two primitive Gaussian functions each, inner and outer 2s and 2p orbitals respectively. Additional functions can be added such as polarisation functions which are denoted by * and diffuse functions, denoted by + and contain small orbital components. For example, 6-31+G* contains 6 Gaussian functions for 1s, 3 for the inner 2s and 2p orbitals, 1 Gaussian for the outer 2s and 2p orbitals, a set of diffuse s and p functions on heavy atoms and d functions on heavy atoms also. In this work, the basis sets used include these split-valence form sets and correlation-consistent basis sets which systematically converge post-Hartree-Fock calculations to the complete basis set limit using empirical extrapolation techniques. These are denoted by cc-pVNZ where cc-p stands for correlation-consistent polarised and the V represents valence-only basis sets with the N = D, T, Q… (D=double, T=triple…).

In Hartree-Fock theory, each electron sees the average density of all other electrons, giving a higher energy than the true energy of the system as it does not account for correlation effects. So, for any given basis set

$$E_{exact} - E_{HF} = \text{correlation energy} \tag{2.17}$$

where E_{exact} is the exact energy of the system, E_{HF} is the calculated HF energy and the correlation energy is approximately 20 kcal/mol per electron pair and therefore usually too large to be ignored.

2.15 Post-Hartree-Fock methods

Post-HF methods can be employed to account for the correlation effects. There are a variety of options available which can be systemically improved and work for larger systems including Møller-Plesset perturbation theory (MP2), coupled-cluster (CC) methods and alternatively density functional theory which will all be overviewed in this chapter.

2.16 Møller-Plesset perturbation theory

Of all the post-HF methods, MP2 theory is considered the most popular. This adds electron correlation effects by applying perturbation to the time-independent Schrödinger equation

$$(\hat{H}^{(0)} + \lambda\hat{V}) = E_n\Psi_n \tag{2.18}$$

where λ is an arbitrary real parameter, $\hat{V}$ is a perturbation to the unperturbed Hamiltonian $\hat{H}^{(0)}$, and the subscript *n* (= 1, 2, 3, ...) denotes different discrete states. Ψ_n and E_n can be expanded in Taylor series in powers of λ. The eigenvalue equation then becomes

$$\left(\hat{H}^{(0)} + \lambda\hat{V}\right)\left(\sum_{i=0}\lambda^i\Psi_n^{(i)}\right) = \left(\sum_{i=0}\lambda^i\mathrm{E}_n^{(i)}\right)\left(\sum_{i=0}\lambda^i\Psi_n^{(i)}\right) \tag{2.19}$$

Writing only the first terms gives

$$\left(\hat{H}^{(0)} + \lambda\hat{V}\right)\left(\Psi_n^{(0)} + \lambda\Psi_n^{(1)}\right) = \left(E_n^{(0)} + \lambda E_n^{(1)}\right)\left(\Psi_n^{(0)} + \lambda\Psi_n^{(1)}\right) \tag{2.20}$$

The zeroth-order system is simply the Schrödinger equation for an unperturbed system

$$\hat{H}^{(0)}\Psi_n^{(0)} = E_n^{(0)}\Psi_n^{(0)} \tag{2.21}$$

The first-order system contains terms that are multiplied by λ

$$\hat{H}^{(0)}\Psi_n^{(1)} + \hat{V}\Psi_n^{(0)} = E_n^{(0)}\Psi_n^{(1)} + E_n^{(1)}\Psi_n^{(0)} \tag{2.22}$$

Finally, for the second-order system, terms are multiplied by λ^2

$$\hat{H}^{(0)}\Psi_n^{(2)} + \hat{V}\Psi_n^{(1)} = E_n^{(0)}\Psi_n^{(2)} + E_n^{(1)}\Psi_n^{(1)} + E_n^{(2)}\Psi_n^{(0)} \tag{2.23}$$

When these expressions are multiplied through by $\Psi_n^{(0)*}$ and integrated, the following expectation values are found

$$E_n^{(0)} = \left\langle \Psi_n^{(0)} \middle| \hat{H} \middle| \Psi_n^{(0)} \right\rangle \tag{2.24}$$

$$E_n^{(1)} = \left\langle \Psi_n^{(0)} \middle| \hat{V} \middle| \Psi_n^{(0)} \right\rangle \tag{2.25}$$

$$E_n^{(2)} = \left\langle \Psi_n^{(0)} \middle| \hat{V} \middle| \Psi_n^{(1)} \right\rangle \tag{2.26}$$

The zeroth-order perturbation only describes the sum of the HF one-electron energies and apart from following the Pauli exclusion principle, ignores interelectronic repulsion. The first-order perturbation is the expectation value of the perturbated Hamiltonian while the system is in the unperturbed state and is therefore equal to standard HF energy. MP2, the second-order perturbation is therefore the first perturbation to improve upon HF theory and the result is the Møller-Plesset theorem: the correlation potential does not contribute in first-order to the exact electronic energy.

The MP2 energy term $E_0^{(2)}$ can be shown for the lowest quantum state (n=0) in Equation 2.23 where a and b denote virtual spin orbitals, r and s are occupied spin orbitals, and ε_a, ε_b, ε_r, and ε_s are the respective orbital energies.

$$E_0^{(2)} = \frac{1}{4}\sum_{ab}^{virt}\sum_{ij}^{occ}\frac{|\langle ab\|rs\rangle|^2}{\epsilon_a+\epsilon_b-\epsilon_r-\epsilon_s}\sum_{i,j,a,b}\frac{|\langle ab\|ij\rangle|^2}{\epsilon_a+\epsilon_b-\epsilon_r-\epsilon_s} \tag{2.27}$$

$$\langle ab\|rs\rangle = \langle ij|kl\rangle - \langle ij|lk\rangle \tag{2.28}$$

$$\langle ij|kl\rangle = \int\int \frac{\psi_i^*(\boldsymbol{r}_1)\psi_j(\boldsymbol{r}_1)\psi_k^*(\boldsymbol{r}_2)\psi_l(\boldsymbol{r}_2)}{r_{12}}d\boldsymbol{r}_1 d\boldsymbol{r}_2 \tag{2.29}$$

The total Hartree-Fock energy is simply the sum of zeroth- and first- order energies (Equation 2.26) and the total MP2 energy is given by the total HF energy plus the dynamic electron correlation effects (Equation 2.27).

$$E_0 = \langle \Psi_0 | H_0 + V | \Psi_0 \rangle = E^0 + E^1 = E_{HF} \tag{2.30}$$

$$E_{MP2} = E_{HF} + E_n^{(2)} \tag{2.31}$$

2.17 Coupled cluster methods

The accuracy of MP2 is satisfactory and the most popular post-HF method due to its low computational cost although it usually overestimates bond energies. MP3 and MP4 etc. methods are available but do not improve greatly on MP2 and have a much greater computational cost. However, there are more accurate methods available including coupled cluster (CC) methods. With CC methods, the computational cost is very high so practically can only be used on relatively small systems. Like MP2 theory, it is a post-HF method which adds a correction term taking into account electron correlation. CCSD(T) (coupled-cluster singles and doubles, with perturbative triples) has become the 'gold standard' of computational chemistry due to its high accuracy for a wide variety of small to medium systems.

CC theory aims to provide an exact solution to the time-independent Schrödinger equation. The essential idea behind CC theory is that the ground state wavefunction can be written as an exponential ansatz

$$|\Psi_{CC}\rangle = e^{\hat{T}} |\Phi_0\rangle \tag{2.32}$$

$$|\Psi_{CC}\rangle = \left(1 + \hat{T} + \frac{\hat{T}^2}{2!} + \frac{\hat{T}^3}{3!} + \cdots, \right) |\Phi_0\rangle \tag{2.33}$$

$$\hat{T} = \hat{T}^1 + \hat{T}^2 + \hat{T}^3 + \cdots, \tag{2.34}$$

where Ψ_{CC} is the coupled-cluster wavefunction, Φ_0 is the Slater determinant of the system and $e^{\hat{T}}$ is an exponential functional of the operator $\hat{T}$. This operator can be further split into a sequence of excitation operators (Equation 2.34).

$$\hat{T}_1|\Phi_0\rangle = \sum_{i,a} t_i^a \Phi_i^a \tag{2.35}$$

$$\hat{T}_2|\Phi_0\rangle = \sum_{i>j,a>b} t_{ij}^{ab} \Phi_{ij}^{ab} \tag{2.36}$$

where t refers to the one electron CC amplitude, i and j denote the occupied electrons and a and b denote the unoccupied electrons. All $\hat{T}_n$ contributions are connected and represent n-electron correlation effects. The CCSD method which involves the single and double excitations is the most common CC method used. For many systems, it produces qualitatively correct results but the double excitation does not account for all electron correlation effects, therefore triple excitations must be considered. These are notoriously difficult to calculate but coupled-cluster theory can be used with perturbative excitations such as in the CCSD(T) method where the triples are calculated with perturbation theory. This is the method that is used as the benchmark in Chapter 4 for calculations on methane binding.

2.2 Density functional theory

2.21 The Hohenberg-Kohn and Kohn-Sham equations

To gain accurate results for wavefunction based approaches, the computational cost increases greatly with system size. An alternative to a wavefunction based approach and currently the most popular method of quantum chemical calculation is DFT, which looks to compute the electron density $\rho(\boldsymbol{r})$. This greatly simplifies the three-dimensional wavefunction calculation approach down to one under the principle that the electron density can be used to find the total energy of a system regardless of size. This was proved by the Hohenberg-Kohn theorem in 1964[94] which stated that the ground state expectation value of any physical observable of a many-electron system is a unique functional of the electron density. The second Hohenberg-Kohn theorem illustrated that total energy functional as a minimum, the ground state energy E_0 in correspondence the ground state density, $\rho_0(\boldsymbol{r})$. DFT is therefore variational and the electron density that minimises the energy of the system is the most accurate electron density.

The Kohn-Sham (KS) approach[95] is the one electron Schrödinger equation where the real system of N interacting particles is replaced with a system of N non-interacting particles (typically electrons) that move in an effective potential $V_s(r)$ and generate the same electron density ρ as the real density of the interacting system. As with the HF approximation, the total electronic energy is made up of the electron-electron interactions, the nuclear-electron interactions and the electron kinetic energy T_e

$$E[\rho] = E_{ee}[\rho] + E_{ne}[\rho] + T_e[\rho] \qquad (2.37)$$

The electron-electron term can be separated into the classical Coulomb part, J, and the non-classical contributions of exchange and correlation, E_{ncl}. Here, the electron correlation is accounted for unlike HF theory where each electron interacts with the average potential of all other electrons and therefore the electrons can become too close to one another. The difference between the electron kinetic energy of the non-interacting system, which is given exactly by T_S, and the kinetic energy of the true interacting system is given by T_C. The total energy is

$$\begin{aligned} E[\rho] &= J[\rho] + E_{ne}[\rho] + T_S[\rho] + T_C[\rho] + E_{ncl}[\rho] \qquad (2.38) \\ &= J[\rho] + E_{ne}[\rho] + T_S[\rho] + E_{XC}[\rho] \end{aligned}$$

where E_{XC} is the approximated exchange-correlation functional containing all unknown terms.

2.22 Exchange-correlation functionals

The local density approximation (LDA) is the simplest model to approximate exchange-correlation functional and is derived from the homogeneous electron gas model and is written as

$$E_{XC}^{LDA}[\rho(\boldsymbol{r})] = \int \rho(\boldsymbol{r})\epsilon_{XC}\big(\rho(\boldsymbol{r})\big)d\boldsymbol{r} \tag{2.39}$$

where ρ is the electron density and ϵ_{XC} is the exchange-correlation energy of a particle in this uniform electron gas. The Slater exchange (Equation 2.40) is known analytically and represents the exchange part E_X.

$$E_X = \frac{3}{4}\sqrt[3]{\frac{3\rho(\boldsymbol{r})}{\pi}} \tag{2.40}$$

Monte Carlo calculations were used initially[96] to calculate the correlation energy E_C and from the results, several analytical methods were developed.[97,98] The LDA offers relatively poor approximations for the exchange-correlation functional and was improved by the generalized gradient approximation (GGA) which accounts for the non-uniformity of real systems by adding information about the gradient of electron density $\nabla\rho(\boldsymbol{r})$ along with the electron density $\rho(\boldsymbol{r})$ to form the exchange-correlation functional. There are many examples of GGA functionals including the popular BLYP (Becke-Lee-Yang-Parr). This separates the exchange and correlation parts of E_{XC}

$$E_{XC} = E_X + E_C \tag{2.41}$$

where for the BLYP functional, E_X is Becke's exchange functional[99] and E_C is the Lee-Yang-Parr correlation functional.[100]

Hybrid functionals are another type of exchange-correlation functional used widely for DFT calculations. These improve accuracy of the calculations by including a degree of exact HF exchange energy in E_{XC}. The HF orbitals are replaced with KS orbitals to find the energy of the HF exchange functional, E_X^{HF}, and then combined linearly with density functionals for the exchange and correlation. The most popular hybrid functional currently in use is the B3LYP functional[101] which uses the Becke 3-parameter (B3) exchange[102] with the LYP correlation functional

$$E_{XC}^{B3LYP} = (1 - a_0)E_X^{LDA} + a_0 E_X^{HF} + a_X E_X^{B88} + a_C E_C^{LYP} + (1 - a_C)E_C^{LDA} \tag{2.42}$$

where the parameters a_0, a_X and a_C are 0.20, 0.72 and 0.81, respectively. This functional is used for a great variety of systems for a wide range of applications in different fields providing good results with a relatively small computational cost.

2.23 Dispersion corrections

Dispersion corrections can also be added to improve upon these methods as standard exchange-correlation functionals fail to accurately model dispersion forces in a molecular system. This is due to the fact that only local effects influence the behaviour of the electrons in a system. Dispersion forces arise when an instantaneous dipole on one molecule or atom induces a dipole on another molecule in the system. This creates instantaneous dipoles between the two species, which results in a weak attraction force which is non-local. These dipoles do not form in standard DFT and therefore dispersion forces do not occur. In this work, an add-on term is used in the form of Grimme's D3 empirical correction[103–105] which provides good results on a variety of systems.

2.24 Basis set superposition error

Systems containing more than one molecule can show basis set superposition errors (BSSE) when looking at binding energies. This occurs when molecules approach one another and their basis functions overlap in the space between the molecules. The basis set of one molecule essentially ‘borrows’ the basis set of the other molecule, so the basis set for both molecules is relevant to calculating the energy of each individual molecule. When calculating binding energies, BSSE can arise if the molecules are modelled individually with only the orbitals of each individual species included for either molecule. The method used in this work to deal with BSSE is the counterpoise method.[106] This method involves comparing the energy of a molecule pair AB with the energy of A within the basis set of the whole system AB, and then repeating this procedure for molecule B. This method directly compensates for BSSE as the individual components of a system are explicitly modelled with the orbital space of the other components included.

2.3 Statistical mechanics approaches

Along with *ab initio* methods, statistical mechanics are also used in this work to study the interactions that can occur between guest gas molecules and MOF structures. Statistical mechanics is a branch of thermodynamics which attempts to calculate the macroscopic properties of the bulk system through the measurement of the macroscopic behaviour of a system found in equilibrium.[107] The microstate, macrostate and the statistical ensemble are essential to define when using these methods. A microstate is a unique snapshot of a system defined by microscopic properties; i.e. each atom has a particular position, velocity and energy associated with it. The macrostate is a system at equilibrium that passes through multiple microstates. An ensemble links micro and macrostate properties by describing a collection of different microstates belonging to the same macroscopic state. There are many examples of ensembles where three thermodynamic constraints are usually made to define the macroscopic property, M of the system which is determined by averaging the property over all microstates. Common examples of ensembles include the canonical (NVT) ensemble in which the number of molecules, N, the volume, V, and the temperature, T of the system are constant. Thus mimicking a closed system at thermal equilibrium with the surroundings. Another example of an ensemble of particular interest to this work is the grand canonical (μVT) ensemble in which the chemical potential, μ, volume and temperature of a system are kept fixed while N and the energy, E, are allowed to fluctuate. This represents systems seen in adsorption experiments where the system is in material and thermal equilibrium. These are particularly popular examples of ensembles but there are many more which are used extensively across computational science as they often represent systems seen in experimental conditions.

2.31 Stochastic Monte Carlo methods

Finite time periods and a large number of molecules are used to average properties determined by experiment. Calculating averages can be achieved using a number of methods such as Monte-Carlo (MC) based methods which will be the focus in this work. During MC simulations, a large number of randomly chosen microstates that belong to the same macrostate are simultaneously sampled. For a system in which the time-averaged and ensemble-average behaviours are identical, an ergodic system, the macroscopic property, M, may be linked to the property of the microstate using Equation 2.43.

$$M_{macroscopic} = \langle M \rangle = \sum_i M_i \eta_i \tag{2.43}$$

where $M_{macroscopic}$ is the macroscopic property measured at the macroscopic level, $\langle M \rangle$ is the ensemble average value of the property and M_i represents the value of M in microstate i and η_i is the probability of observing said microstate. If both the instantaneous values of M_i and the probability of observing each microstate are known, then the ensemble average value may be found.

In the grand canonical ensemble, the chemical potential, volume and temperature of all microstates are fixed, whilst the total number of molecules within the simulation volume, N_i, and the total energy of the system, E_i, are allowed to fluctuate between microstates through exchanges with an external reservoir. This mimics equilibrium adsorption experiments, in which an adsorbent is exposed to a bulk fluid. The partition function, Z, represents the sum of all possible accessible states of a thermodynamic system.[108] For a grand canonical ensemble the partition function, $Z_{\mu VT}$, is the sum of all possible combinations of the two variable E_i and N_i which follow a Boltzmann distribution:

$$Z_{\mu VT} = \sum_k \left(e^{-\beta E_i} e^{-\beta \mu N_i} \right) \tag{2.44}$$

$$\beta = \frac{1}{k_B T} \tag{2.45}$$

In which k_B is the Boltzmann constant. The number of particles is not fixed and the partition function describes all possible microstates. Therefore, the probability of observing a particular microstate in the ensemble which has energy E_i and number of molecules N is

$$\eta_i = \frac{e^{-\beta E_i} e^{\beta \mu N}}{Z_{\mu VT}} \tag{2.46}$$

This can then be substituted back into Equation 2.43 and the grand canonical ensemble can be used to calculate ensemble averages by:

$$\langle M \rangle_{\mu VT} = \sum_{i,N} M_i \eta_i = \frac{1}{Z_{\mu VT}} \sum_{i,N} M_i \left(e^{-\beta E_i} e^{\beta \mu N} \right) \tag{2.47}$$

M_i represents the average value of the property in microstate *i* over the total microstate volume. Classical behaviour of the system is assumed due to the extremely high number of microstates. This assumption involves considering a microstate where the positions and momenta of all particles are known as a single point in phase space. The macroscopic property, *M* can then be considered as a function of particle momentum, particle position and the probability of observing a particular configuration. Therefore, *M* is an integral over all momenta, υ, and positions *s* as shown in Equation 2.48.

$$M = \iint M(\boldsymbol{v}, \boldsymbol{s})\, \rho(\boldsymbol{v}, \boldsymbol{s})\, d\boldsymbol{v}\, d\boldsymbol{s} \tag{2.48}$$

where ρ is a probability distribution of the accessible configurations. The energy of the system can be de-coupled into kinetic and potential terms to simplify the integral. The kinetic terms depend on the momentum and the potential terms depend on the particle positions. The kinetic energy, E_k, for a single monoatomic particle is taken from the ideal gas theory and expressed as

$$E_k = \frac{V}{\Lambda^3} \qquad \Lambda = h\sqrt{\frac{\beta}{2\pi m}} \tag{2.49}$$

where m is the mass of the particle, Λ is the de Broglie wavelength and h is Planck's constant. The probability of observing a particular configuration, $\rho(\mathbf{s})$, may be defined as:

$$\rho(\boldsymbol{s}) = \frac{1}{Z_{\mu VT}} \cdot \frac{V^N}{N!\,\Lambda^{3N}} \cdot \left(e^{-\beta U(s)}\right) \cdot \left(e^{\beta\mu N}\right) \tag{2.50}$$

The energy can now be decoupled and the ensemble average value of M can be rewritten in classical form as equivalent to Equation 2.50:

$$\langle M\rangle_{\mu VT} = \frac{1}{Z_{\mu VT}} \sum_{N,i} \frac{V^{N_i}}{N!\,\Lambda^{3N_i}} \int M(\boldsymbol{s})\left(e^{-\beta U(s)} e^{\beta\mu N}\right) d\boldsymbol{s} \tag{2.51}$$

This equation can be calculated in a number of ways. In the simplest MC techniques, $\langle M\rangle$ is determined by conventional quadrature[107] in which a large number of random points are sampled in phase space and the integral for each point is evaluated. This approach is limited due to the extremely large number of configurations which must be sampled. Metropolis *et al.*[109] introduced a method to solve this problem through an importance sampling scheme. Many of the points in phase space have negligible Boltzmann factors as they are statistically unlikely to occur so their contribution to the ensemble average is minimal. Therefore, a sampling bias towards the configurations with a high Boltzmann factor and large contribution to the integral is employed. This means that a series of configurations with a large Boltzmann factor are chosen and evenly weighted, improving the convergence rate of the calculation by focusing of microstates with low energies and speeding up the calculation.

The simulation process of an MC algorithm follows a series of steps which attempts to introduce small, random perturbations to the system including particle translations, rotations (not monoatomic particles), insertions and deletions. A Markov chain[110] is generated as each configuration is only dependent on the immediately preceding configuration. The transition probability, $\pi(o \rightarrow n)$ is the probability of moving from the old configuration (o) to a new configuration (n) and the number of moves from (o) to (n) will be approximately equal to the number of moves from (n) to (o) for a system that has reached equilibrium. In MC simulations, the number of moves from old to new and new to old configurations must be identical so as the equilibrium distribution is not destroyed.[107]

$$\pi(o \rightarrow n) \cdot \rho(o) = \pi(n \rightarrow o) \cdot \rho(n) \tag{2.52}$$

where $\rho(o)$ and $\rho(n)$ represent the probabilities of observing the old and new configurations respectively which are defined by their Boltzmann factors. The transition probability is a product of the probability of attempting a move *att()* and accepting the move *acc()*. As the number of moves from old to new and new to old configurations must be identical, the probability of attempting a move must be symmetric also so Equation 2.52 can be rewritten as

$$acc(o \rightarrow n) \cdot \rho(o) = acc(n \rightarrow o) \cdot \rho(n) \tag{2.53}$$

To satisfy the detailed balance requirement, Metropolois *et al*[109] introduced alternative acceptance criteria due to the face that within an unbiased MC scheme $acc(o \rightarrow n)$ and $acc(n \rightarrow o)$ are equal to unity, resulting in the acceptance of every perturbation and therefore, the entirety of phase space is explored. In the Metropolis scheme, the probability of observing the old and new configurations is related to the acceptance probability. If $\rho(n)$ is greater than $\rho(o)$ then the move ($o \rightarrow n$) is accepted.

If the configuration (*o*) is much more likely than configuration (*n*), the move will not be accepted. The probability of accepting moves cannot exceed 1 so *acc(o→n)* and *acc(n→o)* are chosen as

$$acc(o \rightarrow n) = \min\left(1, \frac{\rho(o)}{\rho(n)}\right) \qquad acc(n \rightarrow o) = \min\left(1, \frac{\rho(n)}{\rho(o)}\right) \tag{2.54}$$

The potential energy of old and new configurations cannot be calculated directly (excluding extremely small systems) due to the complicated nature of the partition function. However, this can be eliminated by considering a ratio of the potential energies of configurations and depending upon the perturbation being attempted on the system.

For rotation and translation moves, acceptance depends on changes to the energy of the system so using Equation 2.54:

$$acc(o \rightarrow n) = \min\left(1, e^{-\beta\left(U(n)-U(o)\right)}\right) \tag{2.55}$$

For particle insertions and deletion moves, the potential energy of the system and the number of molecules in the system changes and therefore the acceptance probability depends upon both these factors. Again, using Equation 2.54:

$$acc(o \rightarrow n) = \min\left(1, \frac{V}{\Lambda^3(N+1)} e^{-\beta\left(\mu-U(N+1)+U(N)\right)}\right) \tag{2.56}$$

Expressing the chemical potential of the system in terms of the gas phase fugacity, *f*, is often more convenient

$$\mu = \frac{\ln(f\beta\Lambda^3)}{\beta} \tag{2.57}$$

This fugacity of a fluid can be related to pressure using an equation of state and in this work the Peng-Robinson equation of state[111] is used. Using Equation 2.57, the particle insertion acceptance probability becomes

$$acc(o \rightarrow n) = \min\left(1, \frac{\beta f V}{(N+1)} e^{-\beta\left(U(N+1)+U(N)\right)}\right) \tag{2.58}$$

And the particle deletion acceptance probability therefore becomes

$$acc(o \rightarrow n) = \min\left(1, \frac{N}{\beta f V} e^{-\beta\left(U(N)+U(N+1)\right)}\right) \tag{2.59}$$

Following this Metropolis GCMC method, the simulation of adsorption in a porous solid to generate an adsorption isotherm consists of a number of steps. Initially, the simulation is set up using a simulation cell which contains a porous, crystalline solid, free of adsorbent. The temperature is set, along with the total vapour pressure and the chemical potential is chosen by fixing the fugacity of the adsorbent species. The simulation can then begin, allowing the simulation cell to fill up with molecules by attempting to alter the system with various perturbation moves which are accepted or rejected based on the appropriate acceptance criteria described previously. Over time, the simulation progresses and the system will eventually reach equilibrium where the potential energy of the system decreases towards a steady minimum from where microstates fluctuate little. This equilibrium process may take from 10^6 to 10^8 MC steps and sampling of the properties of the system are then averaged over a further 10^7 to 10^8 MC steps. This process is then repeated over a range of external pressures to generate a full adsorption isotherm.

2.32 Pair potentials

Force-fields are typically used to find the potential energy term, *U(r)*. The potential energy of a system can be described using an analytical expression through the inclusion of bonded and non-bonded interaction terms. In this work bonded terms based on intramolecular interactions such as bond stretches are not included in the potential energy term as MOFs are treated as rigid structures with fixed bond lengths and angles to reduce simulation cost. Therefore, the force-field only includes the non-bonded terms which describe dispersion and electrostatic interactions between the MOF and adsorbate. The total potential energy of a system of N atoms interacting via pair potential is:

$$U(\overrightarrow{r_1}, \overrightarrow{r_2}, \ldots, \overrightarrow{r_N}) = \sum_{i} \sum_{j>i} U_2(r_{ij}) \tag{2.60}$$

where $r_{ij} = |\overrightarrow{r_j} - \overrightarrow{r_i}|$ is the separation distance between particles *i* and *j*. There are a number of commonly used examples of pair potentials. Arguably the simplest and most widely used pair potential is the Lennard-Jones (LJ) function combined with an electrostatic Coulomb term. The relatively short-range vdW interactions between non-bonded atoms are well described using the LJ potential in which the interaction between particles i and j, varies with separation distance, r_{ij}. The electrostatic interactions between charged atoms are taken into account by the Coulomb term which assigns a partial point charge (q) to each LJ interaction centre and calculating the interaction between partial charges *i* and *j* via a Coulomb potential.

$$U_{ij}(r) = \sum_{i} \sum_{j} 4\varepsilon_{ij} \left[\left(\frac{\sigma_{ij}}{r_{ij}} \right)^{12} - \left(\frac{\sigma_{ij}}{r_{ij}} \right)^{6} \right] + \frac{q_i q_j e^2}{4\pi\varepsilon_0 r_{ij}} \tag{2.61}$$

where q is the partial charge on particle *i* or *j*, e is the elementary charge, ε_0 is the vacuum permittivity, σ represents the LJ collision parameter between particles *i* and *j* and ε represents the LJ interaction well depth between particles *i* and *j*.

For interactions between atoms of difference types, the LJ cross-terms are calculated using the Lorentz-Berthelot mixing rules according to:

$$\epsilon_{ij} = \sqrt{\epsilon_i \epsilon_j} \tag{2.62}$$

$$\sigma_{ij} = \frac{\sigma_i + \sigma_j}{2} \tag{2.63}$$

The LJ potential is short range so the interaction energy tends to zero very quickly meaning atoms with a large separation contribute close to zero to the total system energy. Therefore, the LJ potential is usually truncated at a specified cut-off distance beyond which the interaction energy is negligible. In this work, a cut-off distance of 15 Å is used, unless stated otherwise. The combination of LJ and Coulomb pair potentials are commonly used in MOF simulations[112–115] with LJ parameters taken from various force fields described in Chapter 3.

Another simple and widely used pair potential, similar to the LJ is the Morse potential. This is the sum of two exponentials and is more suitable for attractive interaction that comes from the formation of a chemical bond.[116] This pair potential was used to study molecular vibrations and solids and inspired the development of bond-order potentials but is rarely used anymore. A more readily used pair potential is the Buckingham potential which provides a better description of strong repulsion due to the overlap of the closed shell electron clouds. However, the Buckingham potential becomes attractive when r becomes small which is problematic when dealing with short interatomic distances within a structure. This makes is unsuitable for MOF simulations and compared to the LJ potential, the Buckingham potential is more computationally expensive so this work utilises the LJ pair potential.

2.33 Summary of Lennard-Jones parameters

Framework LJ parameters (Table 2.1) for the metals were taken from the UFF.[117] Three different sources of LJ parameters for non-metals were investigated: UFF, OPLS-AA and DREIDING[118] in chapter 3, whilst chapter 5 uses just DREIDING LJ parameters, apart from for metal atoms. In the case of OPLS-AA methane, partial charges for CH_4 were taken from the OPLS-AA force field, while the CHELPG partial charges for the ligand fragments were calculated via DFT, following the methods described in Chapter 3 unless otherwise stated.

Table 2.1: MOF framework LJ parameters used in this work.

Atom Type	**UFF**		**DREIDING**		**OPLS-AA**	
	ε/k_B (K)	**σ (Å)**	**ε/k_B (K)**	**σ (Å)**	**ε/k_B (K)**	**σ (Å)**
Zinc	62.373	2.462	-	-	-	-
Copper	2.516	3.114	-	-	-	-
Carbon (aromatic)	52.838	3.431	47.856	3.470	35.225	3.550
Carbon (carboxylate)	52.838	3.431	47.856	3.470	52.838	3.750
Hydrogen (aromatic)	22.142	2.571	7.649	2.850	15.097	2.420
Hydrogen (amide)	22.142	2.571	7.649	2.850	0.000	0.000
Nitrogen	34.722	3.261	38.949	3.260	85.548	3.250
Oxygen (carboxylate)	30.193	3.118	48.158	3.030	105.676	2.960
Oxygen (ROR)	30.193	3.118	48.158	3.030	70.451	2.900
Oxygen (amide)	30.193	3.118	48.158	3.030	105.626	2.960
Sulphur	137.882	3.595	173.108	3.590	125.805	3.550

Methane Lennard-Jones parameters used in this work were taken from either the TraPPE-UA[119] or OPLS-AA[120] (Chapter 3) force fields (Table 2.2). In Chapter 5, the hydrogen model used for the H_2 molecules in uptake within MOF-L[7] used LJ parameters that came from experimental work and the model used was the same as used by Dakrim *et al.*[121] H_2 was modelled as a rigid structure with a set bond length of 0.74 Å and was represented by a single van der Waals sphere. This reproduced the quadrupole moment of a H_2 molecule by placing partial charges on the hydrogen atoms and at the centre of mass. The LJ parameters for the H_2 model are shown in Table 2.3. CO_2 molecules for uptake in this chapter were modelled using the TraPPE force field[119] and each CO_2 was modelled as a rigid structure free to move about the MOF with a fixed C-O bond length of 1.16 Å. CO_2 has a permanent quadrupole moment so was modelled as three van der Waals spheres by placing partial charges on the carbon and both oxygen atoms. The values of the LJ parameters are shown in Table 2.4.

Table 2.2: Methane LJ parameters used in this work.

Atom Type	**ε/k_B (K)**	**σ (Å)**
UA CH4	148.0	3.730
AA C_CH_4	33.213	3.500
AA H_CH_4	15.096	2.500

Table 2.3: Hydrogen LJ parameters used in this work.

Atom Type	**ε/k_B (K)**	**σ (Å)**
H	0.0	0.0
H_2 (centre of mass)	36.700	2.958

Table 2.4: Carbon dioxide LJ parameters used in this work.

Atom Type	**ε/k_B (K)**	**σ (Å)**
C	27.0	2.800
O	79.0	3.050

2.34 Simulation details

The GCMC simulations were carried out using the Multi-Purpose Simulation Code (MuSiC).[122] All perturbations were selected with equal probability. Force-field based calculations in this work (unless stated otherwise) were undertaken using the TraPPE parameters for CO_2 and CH_4, the latter of which was treated using a united atom (UA) description wherein the carbon and hydrogen atoms are combined into a single interaction site.[119] In the case of UA methane, only a LJ component was considered. Select systems (explicitly identified in Chapter 3) were further evaluated using the LJ parameters of the OPLS-AA CH_4 model,[64] which incorporates both LJ and electrostatic components. In the evaluation of gas-ligand binding using classical methods, unless stated otherwise the partial charges were extracted using the CHELPG technique,[123] originally developed by Breneman and Wiberg and these were derived from the complementary DFT calculations and used to describe the MOF fragment. As is typical in the MOF literature, metal atoms were described using UFF parameters, as these parameters are often not available in the DREIDING or OPLS force fields. All LJ parameters used in this work are listed above.

While the primary variables which are adjusted in this work is the choice of LJ parameters for framework atoms, in truth the ability of the *combined* MOF-guest LJ terms – following Lorentz-Berthelot mixing rules[124] explained earlier – to describe the MOF-gas interaction are evaluated. The TraPPE force field was developed to describe the bulk properties of the adsorbed gases, and has been shown to capture the adsorption isotherm well in the medium to high loading regimes in a wide range of MOFs.[125–127] Thus it is considered most sensible to assign the prediction of the low loading regime and guest-framework interactions to the choice of framework LJ parameters, and this is the approach that will be used in Chapter 3.

Simulation of bulk properties of a system requires careful choice of boundary conditions found at the edges of the simulation cell. For example, an isolated box containing 10^3 atoms has a significant percentage of atoms near the edge of the system therefore the simulation in not an accurate representative of the bulk phase.[107] Therefore, periodic boundary conditions are utilised in which a simulation cell is replicated an infinite number of times in each direction. This means that the movement of any particle i through the primary simulation cell is replicated in all the infinite other images of the cell and therefore particles re-enter the same box on the other side as soon as they attempt to exit the simulation cell. One constraint of interatomic interaction energies within the primary simulation cell is that particle i is only allowed to interact with the nearest periodic image of any particle. Therefore, the bulk properties of the system can be sampled effectively. An appropriately sized simulation cell is needed to prevent a particle interacting with the periodic image of itself thus the smallest dimension of the primary simulation cell must be at least twice the cut-off radius chosen for the truncation of LJ interactions.

2.35 Adsorption

To understand the process of physisorption, isotherms are used to measure gas adsorption under increasing pressure. There are multiple types of different isotherm and they can be used to identify a material and how adsorption is taking place within a material. During adsorption, at low pressure gaseous molecules interact with the surface of the material, gradually covering the surface and forming a monolayer. As gas pressure increases further, multi-layer coverage occurs and smaller pores in the material will fill first. As pressure increases further, complete coverage of the sample occurs and fills all the pores.

There are a number of adsorption models. In 1909, Freundich gave a purely empirical expression to represent the isothermal variation of adsorption of a quantity of gas adsorbed by unit mass of solid adsorbent with pressure. This equation is known as the Freundlich Adsorption Isotherm.

$$\frac{x}{m} = kP^{\frac{1}{n}} \tag{2.64}$$

where $\frac{x}{m}$ is the amount of adsorbate (x) divided by the weight of the adsorbent (m) to give the adsorption per gram of adsorbent, P is the pressure and k and n are constants which depend upon the adsorbent and gas at a particular temperature. This isotherm correctly established the relationship of adsorption with pressure at lower values but fails at higher pressures.

In 1916, Irving Langmuir published proposed a semi-empirical adsorption isotherm derived from a kinetic mechanism assuming that an equilibrium exists between adsorbed gaseous molecules and the free gaseous molecules.

$$\theta_A = \frac{V}{V_m} = \frac{K_{eq}^{A} p_A}{1 + K_{eq}^{A} p_A} \tag{2.65}$$

where θ_A is the fractional occupancy of the adsorption sites, V_m is the volume of the monolayer, K_{eq}^{A} is the equilibrium constant associated with the adsorbate and p_A is the adsorbate's partial pressure. This model assumes that only a monolayer is formed with the adsorbates immobile on the surface so there are no interactions between adsorbed molecules and the surface of the adsorbent is uniform with all adsorption occurring by the same mechanism. Again, this isotherm demonstrates the relationship of adsorption with pressure at low pressure values but fails to model physisorption at higher pressures.

BET theory was put forward in 1938 by Brunauer, Emmett and Teller as an extension to Langmuir theory, aiming to explain the physisorption of gases on surfaces through multilayer formation. It assumes that once adsorbed onto the surface, molecules can act as potential sites for other molecules to adsorb to form multiple layers infinitely and that the Langmuir theory can be applied to each layer.

$$\frac{p}{V(p^0 - p)} = \frac{1}{V_m C} + \left(\frac{C-1}{V_m C}\right)\frac{p}{p^0} \qquad (2.66)$$

where p^0 and p are the saturation and equilibrium pressures respectively, V is the amount of gas adsorbed (in volumetric untis) at equilibrium pressure, V_m is the monolayer capacity and C is a constant related to the heats of adsorption of the layers. This isotherm model demonstrates a relationship of adsorption with pressure that holds over higher and lower pressures.

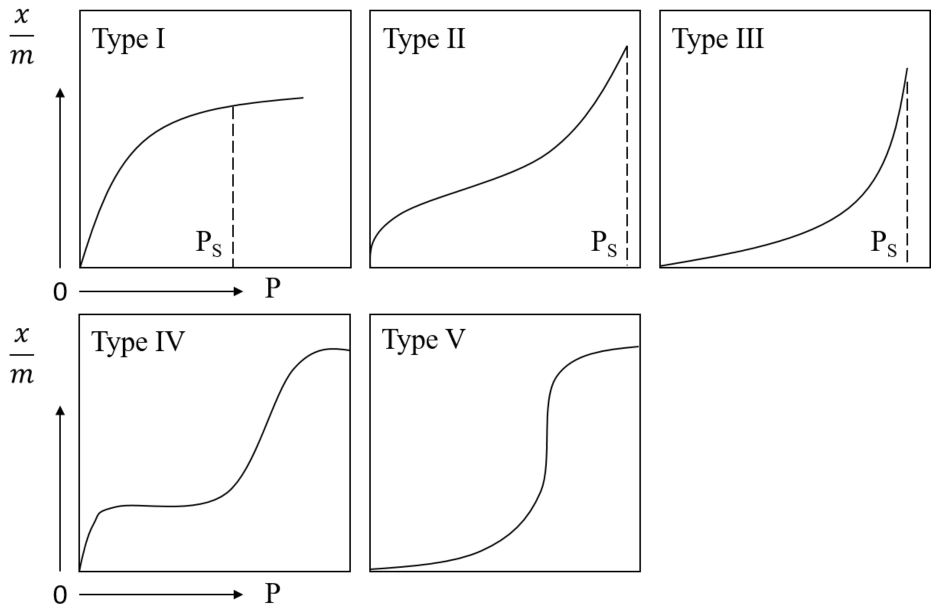

Figure 2.1: Different types of adsorption isotherms showing adsorption per gram of adsorbent against pressure, P. Type I, II and III isotherms show saturation pressure, Ps, when all the sites are occupied in the adsorbent and further increase in pressure do not cause any difference in adsorption.

Figure 2.1 shows different types of adsorption isotherms. The reversible Type I isotherm is concave to relative pressure and approaches a limiting value as $p/p_0 \sim 1$. This is a typical isotherm of microporous solids such as activated carbons, molecular sieve zeolites, COFs and MOFs which have relatively small external surfaces and the limiting uptake is governed by accessible micropore volume as opposed to internal surface area. This depicts monolayer adsorption which can be explained by the Langmuir adsorption isotherm.

The Type II reversible isotherm represents unrestricted monolayer-multilayer adsorption and is typical of a non-porous or microporous adsorbent. The Type III isotherm is also reversible and is convex over the entire range of the x-axis and also indicates unrestricted multilayer adsorption. This type of isotherm is seen when lateral interactions between adsorbed molecules is strong in comparison to interactions between the adsorbent surface and adsorbate.

Adsorption on mesoporous solids proceeds via multilayer adsorption followed by capillary condensation which results in Type IV and V isotherms. The initial part of the Type IV isotherm is attributed to monolayer-multilayer adsorption similar to the Type II isotherm. There is a plateau in adsorption as gases get condensed in tiny capillary pores of the material at a pressure below the saturation pressure of the gas. Type V isotherm can be directly compared to the Type III isotherm with initial formation of a multilayer and capillary condensation occurring as in the Type IV isotherm before saturation pressure is reached.

2.36 Henry's law and virial fitting

To gain insight into adsorption isotherms and calculate quantities of interest like isosteric heats of adsorption and selectivites it is useful assume a linear variation of the quantity of gas adsorbed versus pressure in the lowest part of the adsorption isotherm. This is known as the Henry's law region where Equation 2.67 can be applied.

$$n = K_H \cdot p \tag{2.67}$$

where p is the pressure, n is the quantity of gas adsorbed and K_H is the Henry's law constant. This initial Henry's law region is well documented but not all physisorption isotherms follow linearity at the lowest pressures. Surface heterogeneity or microporosity can cause convex curvature with respect to the adsorption axis at the lowest pressure region. A number of different empirical equations have been suggested to allow deviations from Henry's law in these physisorption isotherms.[128] Applying virial fitting analogous to the treatment of non-ideal solutions and imperfect gases provides a relatively simple was of obtaining K_H from experimental physisorption isotherms. A linear form of virial fitting is usually more reliable[129]

$$\ln\left(\frac{n}{P}\right) = A_0 + A_1 n + A_2 n^2 + A_3 n^3 \tag{2.68}$$

where P is pressure, n is the quantity adsorbed in mol/g and A_0-A_3 are virial coefficients. By extrapolation of the plot of ln(n/P) versus n it is possible to find K_H as

$$K_H = \lim_{P \to 0}\left(\frac{n}{P}\right) \tag{2.69}$$

Once the Henry's law constant is found, it can be used to calculate other properties of interest such a selectivity as is shown in Chapter 6. Using the K_H

constants determined from a range of isotherm data, the selectivity (S) of one gas, i, over the second gas, j, was determined from the equation:

$$S_{ij} = \frac{K_{Hi}}{K_{Hj}} \tag{2.70}$$

The selectivity is of great importance within chemical separation processes. In terms of MOFs and gas adsorbents the binding selectivity finds the ratios of binding of one gas compared to another. MOFs for separation processes are beyond the scope of this work but the selectivity gives insight into how ligands within MOFs can affect binding.

2.37 Isosteric heat of adsorption

If the adsorption isotherms are entirely reversible, that is that the desorption isotherm path coincides with the adsorption isotherm path, then one can assume that over the complete range of relative pressures thermodynamic equilibrium is achieved. Useful thermodynamic quantities can then be obtained from the adsorption isotherm as each point along the isotherm represents an adsorbed state defined by a value of n and a value of P.

The isosteric heat of adsorption represents the energy difference between the state of a system before and after the adsorption of a different amount of particles on the surface. It is often coverage-dependent due to lateral particle intermolecular interactions. To find this value adsorption isotherms are taken at different temperatures by Equation 2.71.

$$\frac{Q_{st}}{RT^2} = \left(\frac{d \ln P}{dT}\right)_n \tag{2.71}$$

where Q_{st} is the differential isosteric heat of adsorption, P is the pressure, T is the temperature, R is the gas constant and n is the amount of gas adsorbed.

2.38 Characterisation Tools

Evaluation of structure properties is important to fully understand porous structures and their interactions with adsorbate molecules. Porous solids are typically characterised by their surface area, available pore volume and the size of accessible void pores.[130] There are number of standard experimental techniques that are recommended for the evaluation of these structural properties[131] and by following these recommendations, new structures may be compared to existing frameworks fairly. Several computational strategies have also been developed in recent years which enable framework characteristics to be determined from the crystal structure of the material.

Experimentally, the surface area is generally determined by applying the Brunauer-Emmett-Teller (BET) formula[132] to a nitrogen adsorption isotherm at 77K. This extends Langmuir's monolayer theory[133] by explaining the physisorption of gases on surfaces through multilayer formation, as explained previously. The BET surface area can be calculated as the area of the monolayer which is know from the number of molecules and projected area of a single nitrogen atom, divided by the adsorbent sample mass, giving the nitrogen BET surface area, shown in Equation 2.67.[130]

$$A_{BET} = \sigma N_A V_m \tag{2.72}$$

where A_{BET} is the specific surface area, N_a is Avogadro's number and σ represents the adsorbate cross-sectional area, assuming that V_m is in units of mol/g. Once a BET plot has been constructed from the relevant N_2 isotherm, an appropriate linear pressure range to determine V_m must be chosen. The range is selected across the region of the isotherm that corresponds to monolayer formation, such that, the surface area is accurately predicted. For many MOFs with micropores less than 2 nm across, the pressure range determined by Braunauer *et al.*[132] ($0.05 \leq P/P_0 \leq 0.35$) is too large giving an overestimation of surface area. Rouquerol *et al.*[130] introduced a set of consistency criteria to determine the appropriate range over which V_m should be calculated. The criteria state that: only a range where $V(P_0\text{-}P)$ increases monotonically with P/P_0 should be selected; the value of C (Equation 2.66) resulting from linear regression should be positive; the monolayer loading V_m should correspond to a relative pressure that falls within the selected linear region; this pressure should be equal to the relative pressure corresponding to the monolayer loading calculated from BET theory $\left(\frac{1}{\sqrt{C}+1}\right)$ with a tolerance of 20%. An appropriate pressure range can then be chosen to determine the value of V_m to calculate the surface area.

In computational studies, the same method can be employed using a simulated nitrogen isotherm.[134] Differences between simulated and experimentally recorded surface areas can indicate defects within the synthesised crystal structure and/or structures that are not fully activated. Therefore, the GCMC BET surface area is considered the benchmark theoretical surface area of the ideal structure under model synthesis and activation conditions.[112]

The BET method remains a popular characterisation tool. However, the underlying theory relies of many assumptions which, for some adsorbents, over simplify or incorrectly describe the adsorption process.[60] For crystalline materials, the surface area can also be calculated geometrically directly from the crystal structure. The simplest geometric method is the van der Waals surface[135] which is generated by interlocking spheres located on each nucleus taking the atomic radius times a van der Waals radius. However, this method can produce small pockets where no solvent molecules can enter. One popular geometric method is the Connolly surface area which is widely use in protein science. This is determined from MC simulations in which a spherical probe is randomly inserted or ‘rolled’ over each of the framework atoms in a MOF structure. The surface area is then calculated from the percentage of insertions which do not result in an overlap with another probe or other framework atoms. A very similar method is the accessible surface area, or the solvent accessible surface area.[60] The difference between the two methods is that the Connolly surface area is calculated from the bottom of a probe molecule rolling across the surface, whereas the accessible surface area is calculated from the centre of a probe molecule. It has been shown that the accessible surface area rather than the Connolly surface area is more appropriate to characterise porous solids when assessing adsorption performance.[60] The accessible surface area method is generally less computationally expensive than simulating a nitrogen adsorption isotherm taking minutes rather than days and generally provides a surface area comparable to the simulated BET surface area when a nitrogen-sized probe is used.[60] Unless stated otherwise, in this work the surface area of MOFs was determined via the accessible surface area method, using a probe radius of 1.84 Å and a grid spacing of 0.25 Å.

The pore volume of a MOF can be determined using a similar MC scheme as used to calculate the accessible surface area. A spherical probe is inserted into the simulation cell and the total pore volume is evaluated based either on the fraction of the insertions which do not result in an overlap with a framework or on the total probe-framework interaction energy per unit mass of framework. Where the LJ parameters for the probe are chosen to match a helium atom, the second method has been shown to be analogous to the experimentally determined helium pore volume.[136] In this work, the helium pore volume at 298 K was determined using the Poreblazer tool kit of Sarkisov and Harrison[137] using a grid spacing of 0.25 Å.

The pore size distribution (PSD) of a structure is a probability density function giving the distribution of pore volume by characteristic pore diameters (d) present in a structure. The cavity diameter plays a key role in adsorption with packing and density of adsorbed molecules and the strength of the interaction with the framework walls dependent on pore size. Within MOFs, the pores are usually micropores (d < 20 Å) or mesopores (20 Å < d < 500 Å) as they are typically less than 30 Å in diameter. Experimentally, the PSD is calculated via the examination of the adsorption isotherms of nitrogen and other species or immersion microcalorimetry. Computationally, the PSD is calculated by MC simulations which are used to determine the largest sphere which can be inserted into a cavity without overlapping with any framework atoms.[138]

Chapter 3

Validation of Generic Force Fields for Prediction of Methane Adsorption in MOFs

3.1 Introduction

In recent years, the use of computational tools to aid in the evaluation, understanding and design of advanced porous materials for gas storage and separation processes has become ever-more widespread. High-performance computing facilities have become more powerful and more accessible and molecular simulation of gas adsorption has become routine, often involving the use of a number of default and commonly-used parameters. In this chapter, the primary focus is the application of molecular simulation, using a range of computational techniques, in the prediction of methane adsorption in metal-organic frameworks in the low-loading regime and the evaluation of the suitability of commonly chosen simulation parameters. In addition to confirming the power of relatively simple generic force fields to quickly and accurately predict methane adsorption isotherms in a range of MOFs, it is demonstrated that these FFs are capable of providing detailed molecular-level information which is in very good agreement with quantum chemical predictions. A number of chemical systems are highlighted in which molecular-level insight from generic force fields should be approached with a degree of caution and provide some general recommendations for best-practice in simulations of CH_4 adsorption in MOFs.

In 2004, the Snurr group,[139,140] employed molecular simulations to evaluate the adsorption of methane in a range of real and hypothetical MOF materials and demonstrated that, in the case of IRMOF-1 and IRMOF-6, grand canonical Monte

Carlo (GCMC) simulations were able to reproduce the experimental methane adsorption isotherms to within 5-10%. Since then, GCMC has been employed to predict CH_4 adsorption isotherms in a wide range of MOFs and related structures,[60,73-81] with reasonable agreement with experiment reported in many cases.

Molecular simulation can be invaluable in gaining additional information to experimental work. When a simulated isotherm is in reasonable agreement with experiment, it is possible to extract accurate and physically meaningful information from the simulations regarding the preferred adsorption sites and energetics of the adsorption process – information which is typically extremely challenging or impossible to obtain from experimental studies. This assumes that recovering the correct isotherm means that the underlying chemical and mathematical description is correct – that is, one can *only* correctly predict the isotherm if the descriptions of the atomic interactions and strengths are also correct. In this study, light is shed on this fundamental assumption in the case of CH_4 adsorption in a range of MOFs following a multi-level computational approach. The suitability of three common generic force fields (UFF,[117] DREIDING[118] and OPLS-AA[120,147]) for the prediction of macroscopic properties (adsorption isotherms) is evaluated against available experimental data, while the recovery of accurate atomistic-level information from force field calculations (small molecule interactions) is compared to density functional theory (DFT) calculations. While all three force fields perform reasonably well in both aspects of the study, we highlight a number of systems in which these generic force fields should be approached with caution before, finally, making some general recommendations for good practice in the choice of generic force field as applied to methane adsorption in MOFs.

3.2 Simulation details

The present work is not intended to provide a comprehensive review of simulations of adsorption in MOFs – several excellent review articles discuss this subject[64,148,149] and the reader is directed towards these for more detail. It is necessary, however, to briefly introduce some of the technical aspects of simulations of CH_4 adsorption in MOFs. In general, two broad classes of simulation are available: approaches in which the interactions between atoms are described using quantum chemical or *ab initio* derivations, and those using some combination of empirically derived force fields (so-called 'classical' approaches). Due to the relatively high computational cost – and thus small system sizes – associated with quantum chemical methods, adsorption properties are typically assessed using classical molecular simulations.

The adsorption of CH_4 in a range of MOF-based systems (Table 3.1) was evaluated in three different simulation environments. The interaction of single gas molecules with fragments of the MOF material was evaluated using DFT. The same single gas molecule – ligand interactions were also probed using analogous force-field based approaches, in which the dependence of gas-MOF interaction on location and guest orientation was studied. Finally, the adsorption isotherm was evaluated in the periodic MOF system using GCMC simulations and, where possible, compared to experimental adsorption data.

The chemical structure of each ligand fragment studied and the labelling scheme used in the present work is detailed in Table 3.1. Selected MOF sources for these ligands are listed, alongside the source of any reference experimental methane adsorption data used. Note that all ligands have been artificially passivated via the introduction of either hydrogen or a methyl group in place of the coordinating carboxylic acid group employed in MOF synthesis.

Table 3.1: Ligand fragments and associated MOFs studied in the present work. Colour scheme: Carbon – grey; Hydrogen – white; Nitrogen – blue; Oxygen – red; Sulphur – yellow.

Ligand Fragment	**Label**	**Example MOFs (w/ Metal)**	**Reference Adsorption Data**
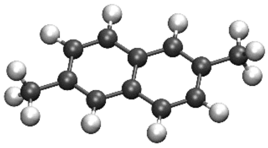	NDC	IRMOF-8 (Zn) MIL-140C (Zr)	Orefuwa *et al* [150]
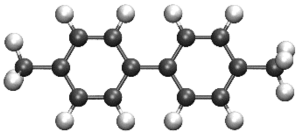	BPDC	UiO-67 (Zr) IRMOF-9 (Zn)	
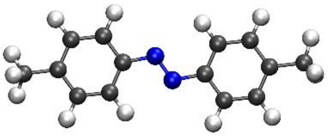	ADC	MIL-140D (Zr) PCN-250 (Fe)	
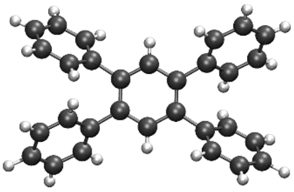	M181	MFM-181 (Cu) UTSA-33 (Zn)	Henley *et al* [151] He *et al* [152]
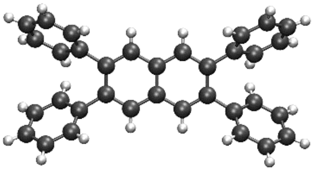	M182	MFM-18X (Cu)	
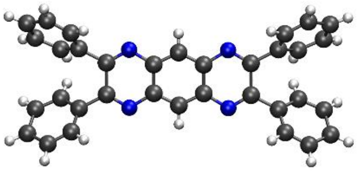	M183		
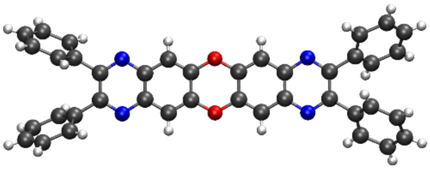	M185		

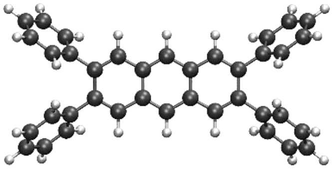	M183c		
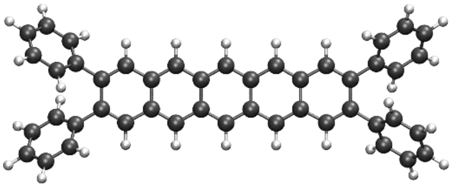	M185c		
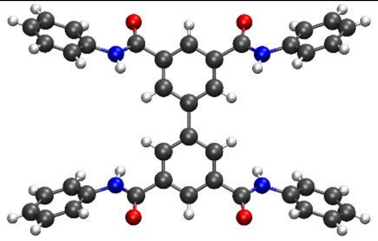	M188	MFM-188 (Cu)	Moreau *et al* [93]
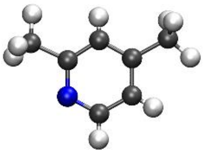	CUK1	CUK-1 (Co)	
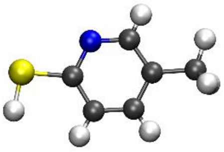	CUK2	CUK-2 (Co)	
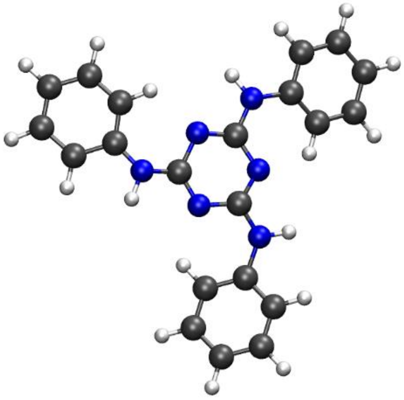	M160	MFM-160 (Cu)	Trenholme *et al* In Preparation[92]

3.21 Density functional theory calculations

The interaction of a single CH_4 molecule with fragments of the MOF was investigated using DFT with Grimme 3 dispersion correction[153] implemented in the Q-Chem software package.[154] In most cases, the fragment was the aromatic core of the ligand used in the MOF, with carboxylate groups replaced with either methyl groups or hydrogen. In order to fully investigate the interaction of guest molecules near the oxygen atoms of the carboxylate groups, several calculations were undertaken in which the fragment was the Zn-benzoate cluster typical of IRMOF-1. The interaction of the guest molecule with the fragment was evaluated in two steps, both using the B3LYP functional,[102] which has been shown to be suitable for the treatment of weakly bound light gas-aromatic systems[151,155] as well as the interaction between CH_4 and unsaturated metal centres in MOFs.[156,157] Geometry optimization of the guest-linker dimer was undertaken using the 6-31+G* basis set, followed by single-point energy calculations using the larger 6-311+G* basis set, from which the binding energy of the guest molecule was estimated following the counterpoise method for the correction of the basis set superposition error.[158] For each system, several initial geometries were evaluated and in all calculations the atoms of the linker fragment were kept fixed, while the guest molecule and its constituent atoms were allowed to adjust position upon optimisation. Thus, for each system, a range of binding locations were investigated and the strongest binding locations identified.

3.22 Force field-based calculations

At the core of any classical molecular simulation is the choice of mathematical functions used to describe atomic interactions. In the case of the relatively simple and non-polar methane molecule, the 12-6 Lennard-Jones form (Equation 2.50) is the most common choice. Although a number of groups have derived framework LJ parameters for specific MOF-guest systems,[114,159,160] the majority of studies make use of one of several generic force fields, of which the most common are UFF, DREIDING and OPLS-AA. Both UFF and DREIDING were developed and tested for their ability to predict crystal structures, bond lengths and bond angles for organic[118,161] and, in the case of UFF, organometallic molecular complexes,[162] while OPLS-AA was developed to correctly reproduce properties of bulk organic liquids, such as the heat of vaporisation and liquid density.[120,147] It should be noted that while all three force fields have been used to simulate gas adsorption in MOFs with some degree of success, none of them were designed to describe the interaction between a relatively isolated organic fragment or metal cluster with adsorbed species and, therefore, should not be assumed to be transferable to all MOF systems.

Unless stated otherwise, force-field based calculations in this work were undertaken using the TraPPE parameters for CH_4, which was treated using a united atom (UA) description.[119] Three primary sources of LJ parameters for the organic portion of the framework were explored: UFF, DREIDING and OPLS-AA. As stated previously, all LJ parameters used in this work are listed in the Appendix.

For each of the systems evaluated via DFT, complementary calculations were undertaken using classical, FF-based methods implemented in an in-house modified version of the Kh_d toolset.[163] In these simulations, the optimised MOF fragment from the DFT simulation was placed in a large simulation box. The box was then discretised on a 0.2 Å grid and, for each point on the grid, the interaction of the guest molecule with the fragment was evaluated using the chosen force field. In the case of single-atom molecules (i.e. united atom CH_4), only a single calculation was performed per point. For polyatomic species, 5000 randomly generated trial orientations were tested per point and both the orientational averaged interaction energy and the individual configurations resulting in the strongest interaction were recorded. Both the fragment and probe molecule were treated as rigid bodies.

3.23 Grand canonical Monte Carlo

For those MOFs for which experimental adsorption data was available, theoretical adsorption isotherms for CH_4 were generated via GCMC simulations carried out using the MuSiC software package.[122] Each simulation point was allowed at least 6×10^6 Monte Carlo steps to come to equilibrium and system properties were evaluated over a further 10×10^6 steps.

3.3 Results and discussion

3.31 Prediction of adsorption isotherms

Of the fourteen ligands included in the DFT/FF comparative study, several belong to MOF structures for which reliable low pressure CH_4 adsorption data at 273 K is available (IRMOF-8, MFM-188, MFM-181, MFM-182, MFM-183 and UTSA-33). Of these, a similar force field evaluation has been previously undertaken for IRMOF-8.[65] For each MOF, methane adsorption isotherms were simulated using UFF, OPLS-AA and DREIDING force fields (Figure 3.1). In subsequent analysis, we report adsorbed amounts as the absolute number of methane molecules per unit cell for both experimental and simulated data. In order to compare force field performance across different MOF systems, we report the deviation of simulation from a Langmuir isotherm fitted to experimental data. In all cases the R^2 value of the fitted isotherm was > 0.97. Fractional loading, θ, is defined with respect to the fitted saturation capacity of the experimental system.

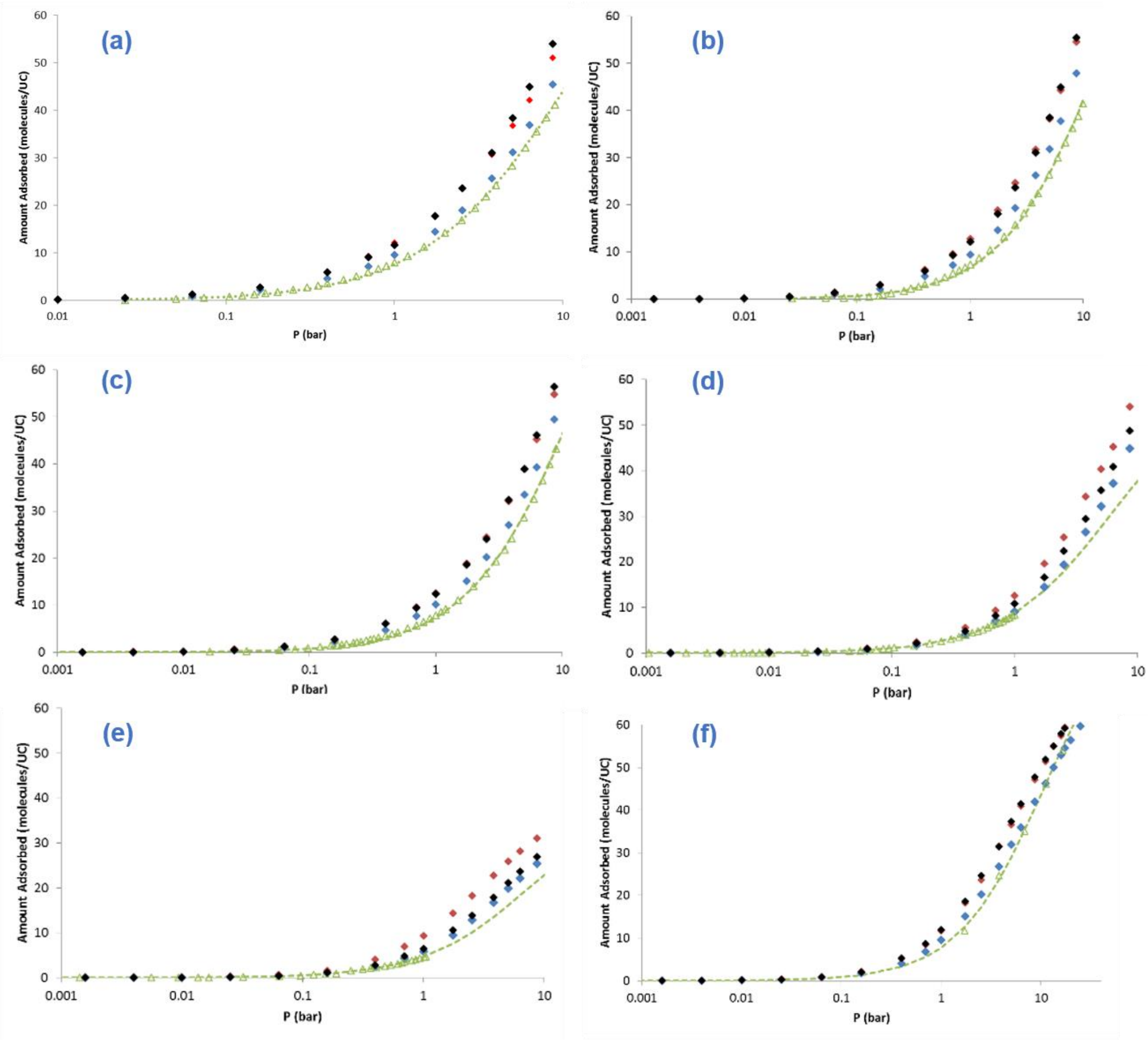

Figure 3.2: Experimental[93,150–152] (green triangles) and simulated (DREIDING – blue; OPLS – red; UFF – black) CH_4 adsorption isotherms at 273 K in (a) MFM-181, (b) MFM-182, (c) MFM-183, (d) MFM-188, (e) UTSA-33 and (f) IRMOF-8. The Langmuir fit of the experimental data is indicated by the green dashed line.

The isotherms recovered for MFM-181 (Figure 3.2) are representative of the trends observed in all seven systems. As has been noted previously in the case of covalent organic frameworks[143] and IRMOF-8,[65] UFF tends to significantly over-estimate adsorbed amounts compared to DREIDING, by between 15 and 50%. The OPLS-AA force field performs very similarly to UFF, over-estimating compared to DREIDING by between 8% and 40%. The largest discrepancy is evident at low fractional loadings ($\theta < 0.25$) and in all cases, the three force fields move towards convergence at higher pressures as the adsorption process begins to be dominated by methane-methane rather than methane-framework interactions.

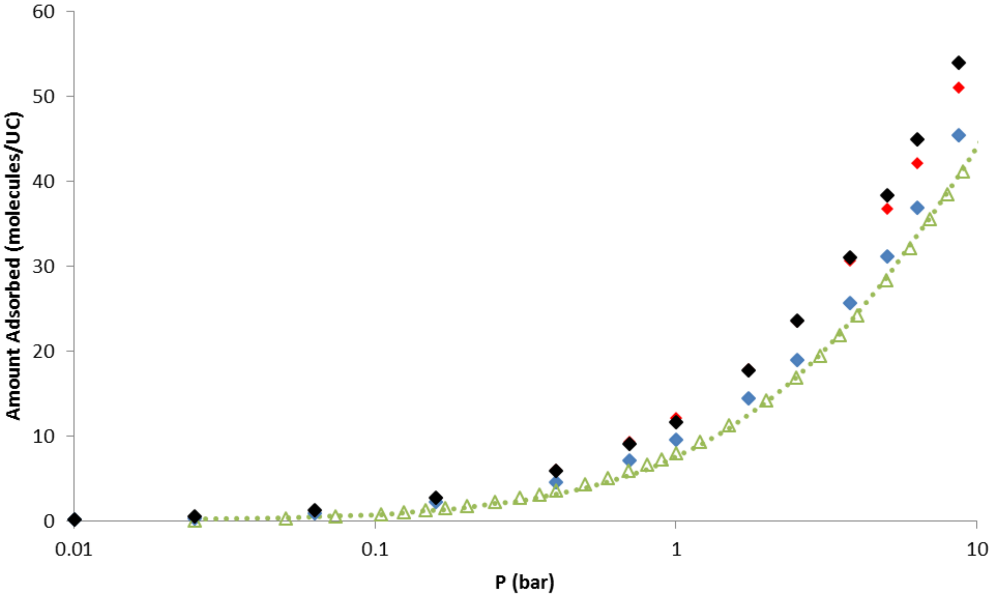

Figure 3.3: Experimental[151] (green triangles) and simulated (DREIDING – blue; OPLS – red; UFF – black) CH_4 adsorption isotherms at 273 K in MFM-181. The Langmuir fit of the experimental data is indicated by the green dashed line.

In all cases, the isotherms predicted from generic force fields were in qualitative agreement with experimental data in the low and medium loading regimes, here taken as fractional loadings $\theta < 0.5$. DREIDING was found to provide the closest quantitative agreement with experiment (Figure 3.2), though still over-estimates adsorbed amounts compared to experiment by 15-36% ($\theta < 0.25$) and 13-14% ($0.25 \leq \theta < 0.5$). It is worth restating that these percentages relate to the absolute number of molecules present in the unit cell. For the low loading levels and MOFs considered in this study, the difference between experiment and simulation is in the region of 5-10 molecules per unit cell (2-3 wt%, or 10-40 cm^3/g at standard pressure, although these values are, of course, strongly dependent on the density of the MOF system.

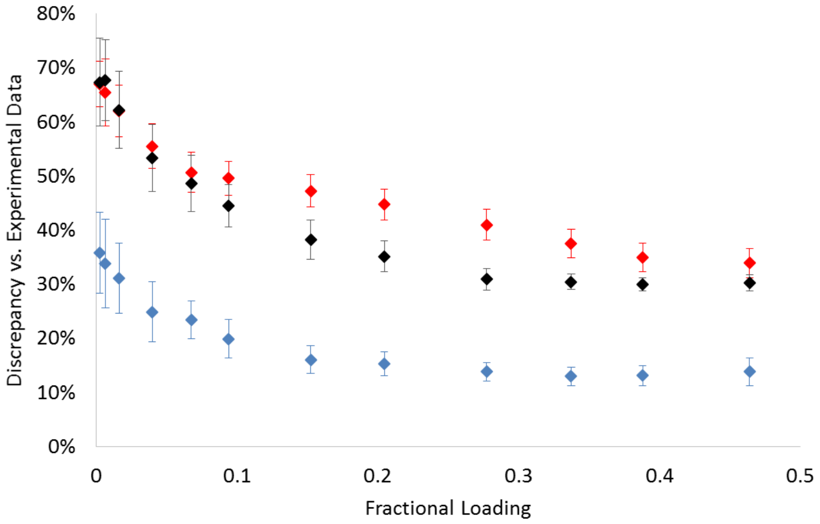

Figure 3.4: Average relative deviation between experimental and predicted adsorption isotherms as a function of fractional loading. Blue – DREIDING; red – OPLS; Black – UFF.

OPLS and UFF performed very similarly with respect to quantitative agreement with experiment (Figure 3.3), over-estimating by an average of 43% (OPLS) and 38% (UFF) for $\theta < 0.25$, and 27% (OPLS) and 24% (UFF) for $0.25 \leq \theta < 0.5$. Both force fields have been previously reported to over-predict the adsorption of methane and other gases with respect to experiment in a range of other systems. Yang and Zhong[164] reported an over-estimation in the cases of CH_4 on IRMOF-1 and Cu-BTC using OPLS-AA and suggested a re-parameterisation of the C and O atoms of the carboxylate groups, reducing ε_{ii} by as much as 30%. A similar reduction in ε_{ii} across all framework atoms was suggested for UFF by Fairen-Jimenez *et al*[165] and Pérez-Peritello *et al*[146] (who scaled ε_{UFF} by 0.59 and 0.69 respectively) based on simulations of methane adsorption in ZIF-8 and ZIF-69, while a similarly large over-estimation (~50%) has been reported in UiO-66(Zr) using UFF.[145] This suggests that while UFF and OPLS-AA are suitable for qualitative prediction of adsorption isotherms in MOFs, both are likely to over-estimate the amount adsorbed, as well as low-coverage properties such as heats of adsorption or Henry's constants, by a significant amount.

Although DREIDING has been shown to significantly over-estimate methane adsorption when compared to experiment in ZIF-8,[146] very good agreement was observed in the case of UiO-66(Zr)[145] (~9-20% over-estimation for $\theta < 0.5$) and in the present work, while simulations in IRMOF-1 and IRMOF-6[139] and in IRMOF-8[65] found excellent quantitative agreement with experiment (5-10% difference when averaged over the full isotherm). While there are too many variables to fully rationalise these apparent differences in quantitative agreement (e.g. the quality of the experimental data and experimental sample, the physical characteristics and composition of the MOF and the choice of simulation software), we are able to investigate the influence of one particular simulation parameter on the computed isotherms, namely the choice of cut-off radius, i.e. the atomic separation beyond which LJ interactions are assumed to be negligible.

The cut-off radius (r_c) is typically expressed in terms of multiples of the largest LJ σ parameter used in the simulation – σ for methane in this work. Suggested values of r_c range from 2.5σ for typical LJ fluids, which can be expected to introduce an error in the total energy of the system in the region of 10%,[110] to 5.5σ in Monte Carlo simulations of vapour-liquid coexistence.[166,167] In the present work, $r_c = 15$ Å (4σ) was implemented, while in the systems described above, the cut-off radius ranged from 12.8 to 18 Å (3.4σ to 4.8σ). Following the work of Düren *et al*,[139] 12.8 Å has proven a popular choice of cut-off radius in simulations of gas adsorption in MOFs and is used for the series of MOFs in Chapter 5. It is worth noting that this radius corresponds to just under half the width of the unit cell of IRMOF-1 and thus represented a compromise between computational accuracy and efficiency. Further increase in the cut-off radius would have required a significantly larger simulation box (eight unit cells instead of one) and increased CPU time as a result. In order to better understand the influence of cut-off radius on adsorbed amounts, methane adsorption isotherms were simulated in the systems previously introduced, as well as IRMOF-1, using the DREIDING force field and a cut-off radius ranging from 10 to 25 Å (2.6σ to 6.7σ).

For all systems studied, increasing the cut-off radius was found to increase the amount adsorbed across the full pressure range considered. The recovered isotherms begin to converge, both in terms of the number of adsorbed molecules and total system energy, for a cut-off radius of 15 Å and are statistically indistinguishable for cut-off radii of 20 Å and above (Figure 3.4). For a cut-off radius of 15 Å, the simulated isotherms were quantitatively accurate to within 5% of those recovered using a 25 Å cut-off. This accuracy improves to within 3.5% for a cut-off of 17 Å.

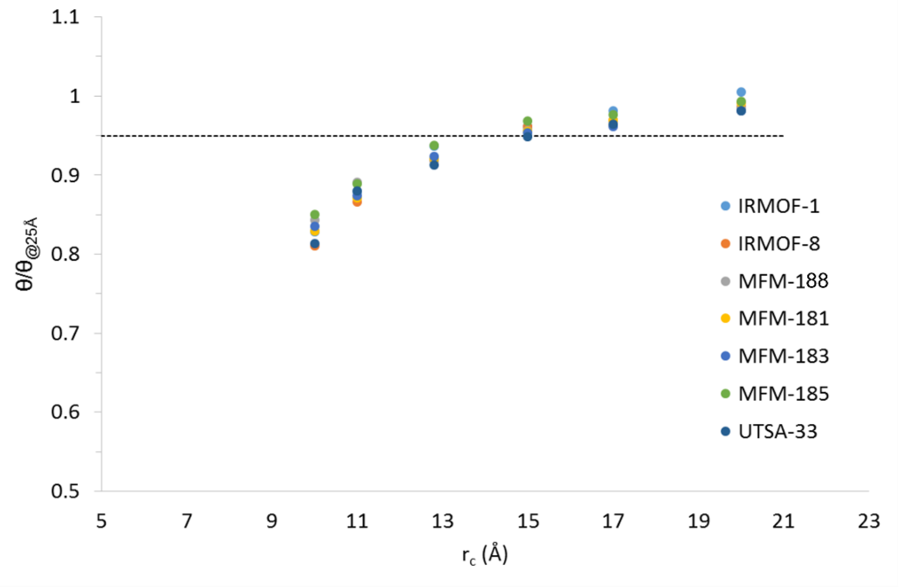

Figure 3.5: Dependence of amount adsorbed on cut-off radius, averaged for each system over the entire pressure range (0 – 70 bar). The ratio of the fractional loading predicted at a given cut-off, r_c, to that predicted in the same system using a cut-off of 25 Å, is shown on the y-axis. The dashed line indicates a ratio of 0.95.

As illustrated for IRMOF-1 (Figure 3.5), the recovered isotherms in each MOF are all qualitatively similar and qualitatively correct in comparison to the experimental isotherm, even for the smallest cut-off implemented (r_c = 10 Å). For the smallest cut-off used, the excess amount adsorbed is 10-30 cm^3/g lower at standard pressure than that predicted in simulations using larger cut-off radii (r_c > 15 Å). Furthermore, the adsorption mechanism and predicted adsorption sites are identical in all cases.

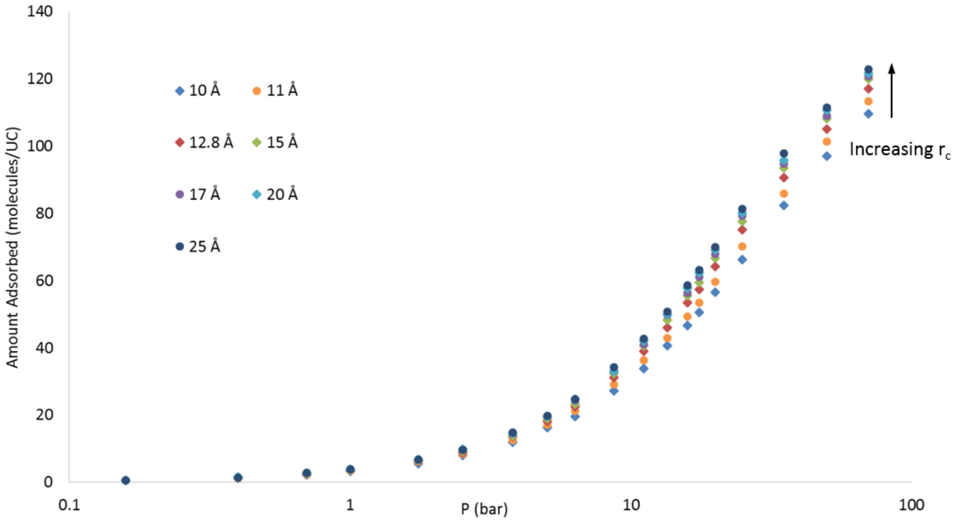

Figure 3.6: Simulated CH_4 isotherms in IRMOF-1 at 273 K for r_c ranging from 10 to 25 Å.

We suggest that while a 12.8 Å cut-off is likely to introduce a statistically significant under-estimation of the amount adsorbed, the isotherm is likely to fall within 10% of the converged adsorption isotherm and in no way invalidates predictions of capacity or suitability for methane adsorption applications. We would recommend, however, that a cut-off of at least 15 Å (4σ), and preferably greater than 17 Å (4.5σ) be implemented in future work. The influence of cut-off radius does exhibit some system-dependence, however, and care should be taken to ensure these values are appropriate for the system of study.

Although all three force fields thus appear to over-estimate the strength of interaction between methane and the framework, they typically predict isotherms which are in reasonable agreement with experiment. We now consider whether having an isotherm which *looks* correct means that the associated atomistic detail of the prediction is physically insightful and chemically accurate for these systems at low loading (i.e. relatively isolated methane molecules interacting with the MOF). When evaluating the accuracy of these atomistic-level predictions, it is helpful to consider two classes of system – those whose ligand cores are based purely on carbon and hydrogen, and those whose cores incorporate other elements (oxygen, sulphur and nitrogen in this study). Note that the ligand fragments evaluated here have been methyl-, rather than COOH-terminated. The influence of the omitted carboxylate group – which is of particular relevance to the OPLS-AA force field – is evaluated subsequently in the case of the Zn-benzoate cluster typical of IRMOF-1.

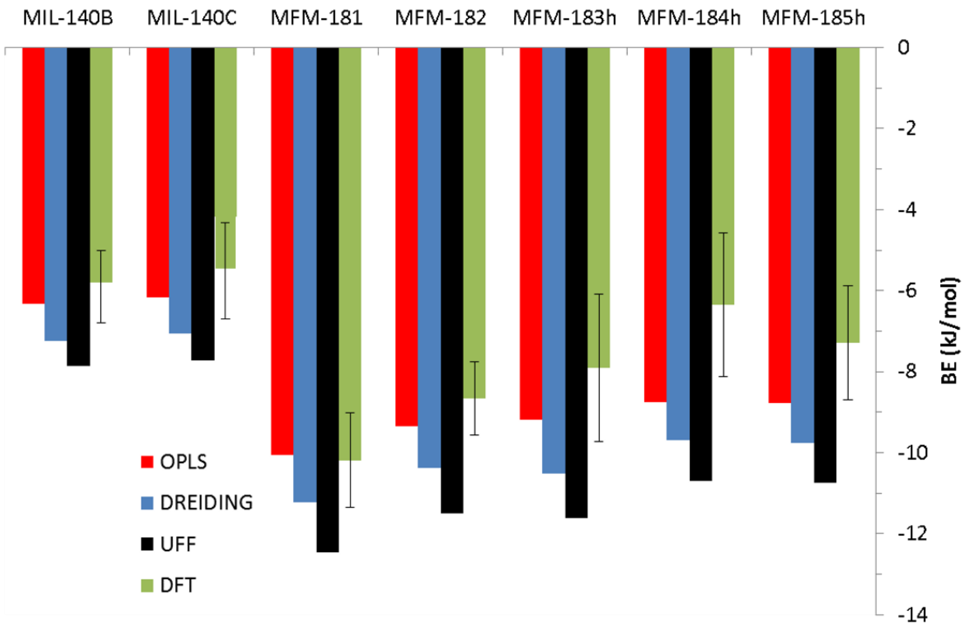

Figure 3.7: CH4-Ligand binding energies for carbon-rich ligands as predicted via DFT (green), DREIDING (blue), OPLS (red) and UFF (black). Bars indicate the upper and lower limits of observed DFT binding sites.

In the case of carbon-rich ligands (Figure 3.6), it is clear that while all three generic force fields are in the right ball-park, they tend to return a slightly stronger binding energy (BE) than that predicted by DFT. The smallest discrepancy is observed for OPLS, over-predicting by 1.2 kJ/mol (~20%) on average compared to the average DFT BE. It should be noted, however, that with the exception of the NDC ligand, OPLS predictions all fall within the range of BEs returned from DFT. Similarly, while DREIDING over-predicts the binding energy by an average of 2.2 kJ/mol (~35%) compared to the DFT average, it is less than 1 kJ/mol out when compared to the strongest binding sites predicted from DFT. It is clear, however, that the interaction strengths predicted from UFF are large, even when compared to the strongest sites observed in DFT (an over-prediction of ~25 % compared to the strongest DFT sites and ~48 % when compared to the DFT average).

In addition to evaluating the binding energy predicted by the three force fields, the predicted binding locations and spatial dependence of interaction energy were compared to those determined from DFT calculations. It should be noted that as all three force fields share a common mathematical form (the 12-6 Lennard-Jones potential), their predicted potential energy surfaces are very similar in shape. In fact, the variation in predicted binding location for each FF is less than the 0.2 Å accuracy of the calculations employed in this study. As illustrated for the NDC ligand (Figure 3.7) and BPDC ligand (Figure 3.8) excellent agreement was observed between DFT and FF in terms of position with respect to the aromatic core of the ligand, although all three FFs generally predicted a shorter CH_4-ligand separation distance than in DFT (a discrepancy of 0.4 to 0.6 Å on average). This was found to be the case for all of the carbon-rich ligands included in this study and suggests that, in principal, most generic 12-6 LJ potentials should be capable of predicting binding location for these types of systems. While UFF, DREIDING and OPLS are thus equally capable of predicting chemically meaningful binding locations for methane near organic ligands which are primarily carbocyclic in nature, OPLS and DREIDING would appear to offer the most accurate description of the interaction strength.

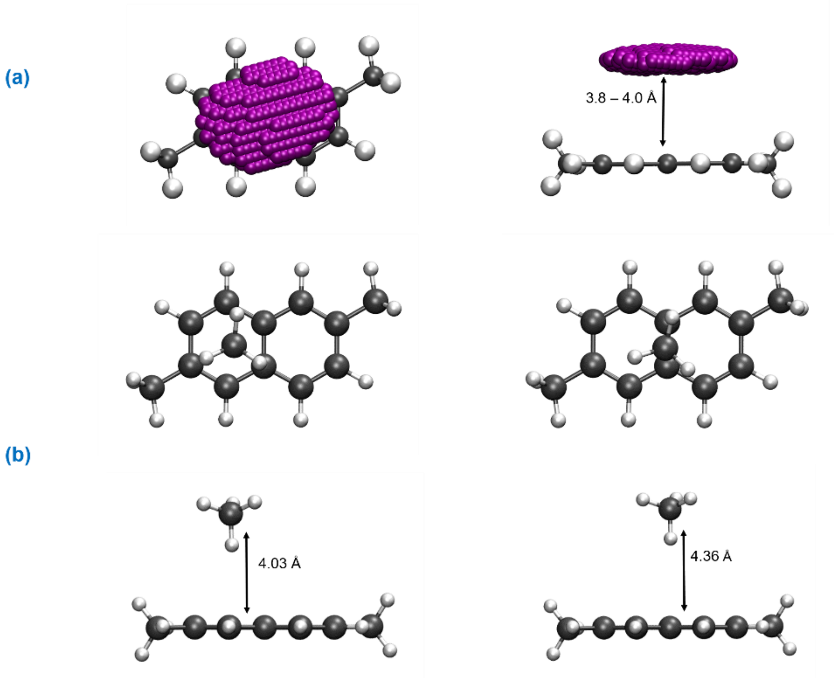

Figure 3.8: Strongest CH_4-NDC interaction sites as predicted by (a) LJ force fields and (b) DFT.

The two carbon-rich ligands NDC and BPDC show the closest agreement in location between DFT and FF produced sites. For both ligands, the strongest FF sites occur on an average plane over the whole structure. A number of DFT sites were found for all ligands and the strongest interactions for NDC and BPDC (Figure 3.7 and 3.8) were found to be in the centre of the ligand and in the centre of the aromatic rings, echoing the FF calculations with a difference of < 0.4Å away from the ligands. The strongest DFT binding interactions are very similar for both the NDC and BPDC ligands and are shown the left of Figure 3.7b and Figure 3.8b respectively. They occur at the centre of the aromatic rings with a binding energy of 6.80 and 6.75 kJ/mol^{-1}

respectively which is in excellent agreement with both the OPLS and DREIDING estimates (Figure 3.6).

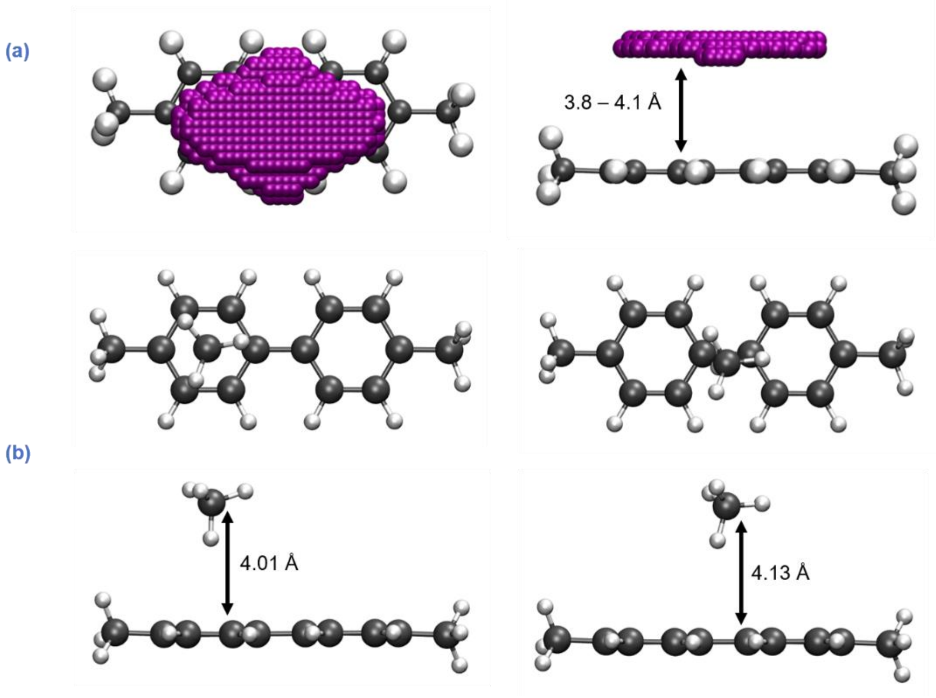

Figure 3.9: Strongest CH_4-BPDC interaction sites as predicted by (a) LJ force fields and (b) DFT.

In the case of ligands with significant heterogeneity in their composition, such as those which incorporate S-, N- or O-heteroatoms or functional groups (such as the azo-, amide and amine moieties in this study), the combination of the standard MOF force fields with TraPPE-UA CH_4 generally performs well in predicting the interaction strength and location of the strongest binding sites observed in DFT (Figure 3.9). As observed for the carbon-rich fragments, using UFF leads to a significant over-prediction of binding strength (by 5-45 %, and 17 % on average). In contrast to the carbon-rich fragments, however, DREIDING and OPLS are seen to perform almost identically in cases where nitrogen or oxygen atoms are present in the fragment. Both force fields over-predict by 7 to 8 % on average when compared to DFT, but, with the exception of the heterocyclic ligands of MFM-183 and MFM-185, fall within 1.2 kJ/mol of the DFT predictions.

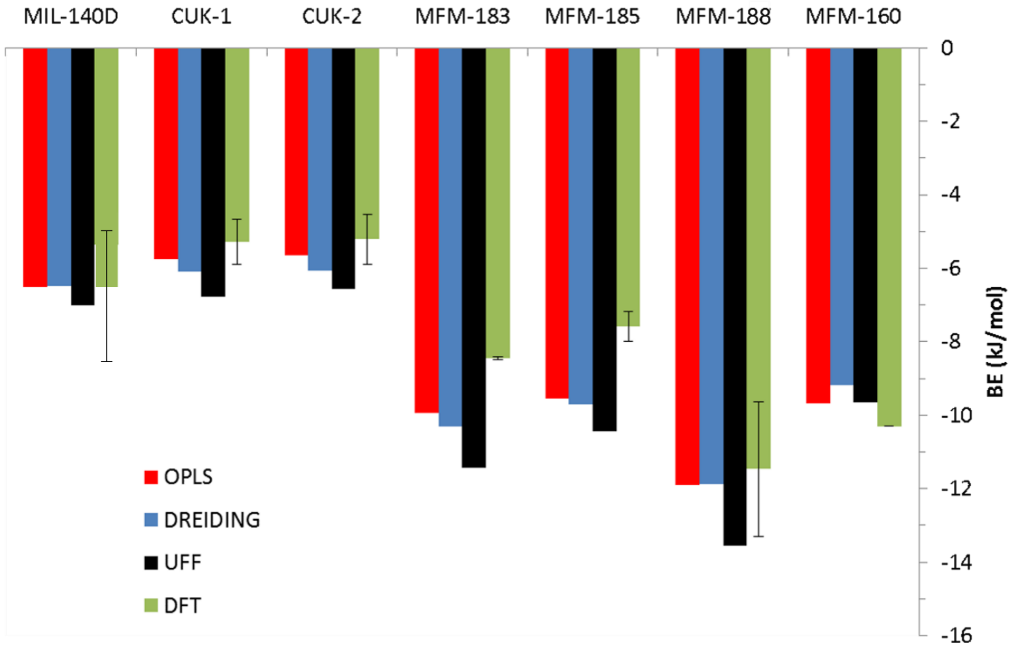

Figure 3.10: CH_4-Ligand binding energies for N-, O and S-containing ligands as predicted by DFT (green), DREIDING (blue), OPLS (red) and UFF (black). Bars indicate the upper and lower limits of observed DFT binding sites.

In the case of the BPDC ligand the average binding energy for OPLS and DREIDING calculations are in excellent agreement with the DFT results. As with most of the other ligands one of the strongest sites is above the ring and the location is consistent across DFT and FF-based calculations (Figure 3.10). However, it is the only linker for which the highest DFT binding energy exceeds that of the FF-based calculations. The strongest binding site with a binding energy of 8.69 kJmol^{-1}, shown on the right of Figure 3.10 is over the nitrogen atoms within the molecule. The location of the CH_4 molecule is also much closer to the molecule within the DFT calculations when compared to the FF predicted positions shown at the top of the figure with a ~ 0.4 Å difference.

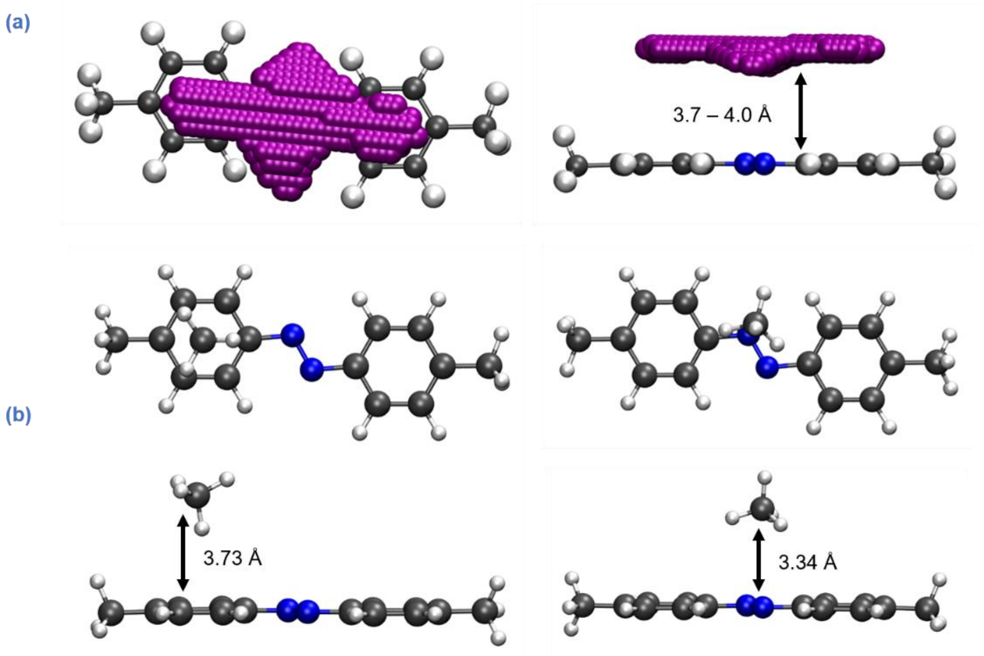

Figure 3.11: Strongest CH_4-ADC interaction sites as predicted by (a) LJ force fields and (b) DFT.

The cases of CUK-1/2, MFM-183/5 and MFM-160 are particularly interesting. These fragments contain heterocycles with one (pyridine; CUK1/2), two (pyrazine; MFM-183/5) or three (triazine; MFM-160) N-heteroatoms per ring. In each case, the strongest binding location for CH_4 was found to be directly above the heterocycle in both DFT and FF-based calculations. The magnitude of over-prediction in interaction strength from FF-based calculations varies significantly, however. For the low nitrogen content CUK1/2 fragments, both DREIDING and OPLS predict the interaction strength extremely well, both falling within the range of BEs observed in DFT. The location of the CH_4 molecule above the rings in both cases are very consistent between the two methods (Figure 3.11). In the case of pyrazine-containing fragments, however, both force fields over-predict the interaction strength considerably (by 17-28%). Further increase of the nitrogen content, surprisingly, does not lead to further over-prediction – in the case of the triazine-based MFM-160, both

OPLS and DREIDING *under*-predict the binding energy by 5-10%. The strength of interaction between methane and N- or O-containing heterocyclic ligands is thus heavily influenced by the electronic structure of the heterocycle and care should be taken when relying on classical simulations to extract quantitative energetic information in MOFs with complex heterocyclic ligands.

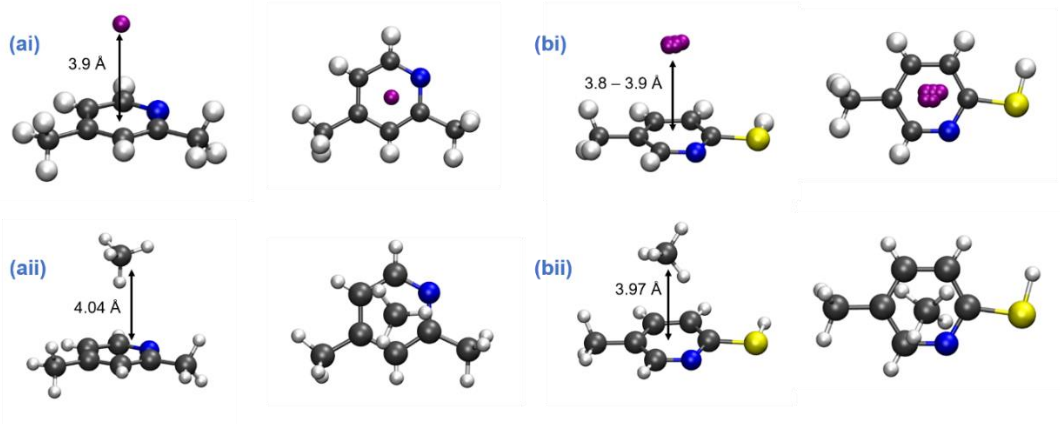

Figure 3.12: Strongest CH_4-CUK1 (a) and CH_4-CUK2 (b) interaction sites as predicted by (ai, bi) LJ force fields and (aii, bii) DFT.

In previous work, methane binding around the heterocyclic ligands of the MFM-18X series was shown to be heavily influenced by weak hydrogen bonding between methane and the N- or O-heteroatoms.[151] It should be remembered that a simple LJ potential should not be expected to be able to predict these types of interactions. In the case of the ligands of MFM-183 and MFM-185, all three force fields were actually found to capture the strength of interaction and CH_4-ligand separation surprisingly well in the regions where weak N--H hydrogen bonding was observed in DFT (Figure 3.12) but over-predicted the strength of interaction near the O-heteroatom by ~1.5 kJ/mol (34%). Employing a more complex model to describe methane (OPLS-AA, which includes both LJ and Coulombic potential terms) did not result in an improvement. All binding sites – both above the aromatic core and in regions in which weak hydrogen bonding is to be expected – are now over-predicted by 25-50% (an increase from the 17 to 35% over-prediction observed for FF/TraPPE-UA).

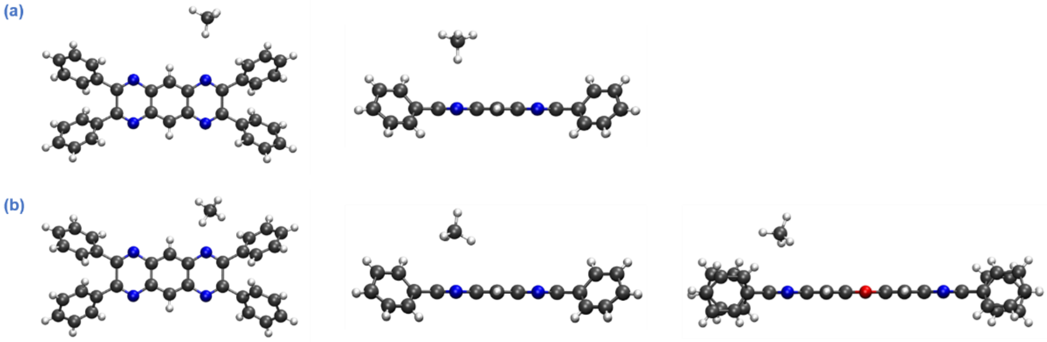

Figure 3.13: Binding of CH_4 with the MFM-183 and MFM-185 fragments predicted via DFT (a) and FF/OPLS-AA (b) top view (left) and side view (right). Note that binding above the pyrazine ring of MFM-185 (bottom-right image) could not be reproduced in DFT calculations.

Interestingly, the preferred CH_4 orientations predicted by FF/OPLS-AA simulations do not match those observed in DFT (Figure 3.12). The interaction between the partial positive charge on the hydrogen of CH_4 and either the π-electrons of the aromatic or partial negative charge of the heteroatom leads to CH_4 aligning itself such that a single H atom is directed towards the ligand. In the case of OPLS-AA CH_4, methane tended to align itself with 2-3 hydrogen atoms pointed towards the ligand in order to maximise the LJ component of the force field – i.e. the opposite of that predicted by DFT. Not only does the inclusion of point charges on methane fail to lead to an improvement in accuracy in the description of ligand-guest interaction energy, it also predicts methane orientations which are inconsistent with DFT-based predictions. Furthermore, both UA and OPLS-AA treatments of CH_4 predict strong binding of methane directly above the pyrazine ring of the MFM-185 fragment – a site which could not be replicated in DFT calculations.[151] Therefore, for systems in which complex, non-LJ type interactions may be present, quantum chemical calculations represent an excellent, complementary tool for investigation and validation of classical predictions.

Although OPLS was seen to consistently over-predict CH_4 adsorption isotherms at low loading compared to both DREIDING and to experimental data (Figures 3.2 and 3.3), it was found to be the best-performing FF in terms of predicting the interaction of methane with the organic core of the MOF. The major difference between the two cases is the presence of metal oxide clusters in the GCMC simulations – the fragments investigated via DFT excluded the carboxylate groups. Further BE calculations were thus undertaken for the CH_4--Zn-benzoate cluster, representative of the metal-ligand combination of IRMOF-1 (Figure 3.13). As was the case for the organic fragments, all three force fields are able to correctly reproduce the binding locations observed in DFT – sites which have been previously explored by Dubbeldam *et al*.[168] Furthermore, all three force fields performed reasonably well in reproducing the binding energies predicted by DFT, with DREIDING correctly predicting the DFT binding energies to within 1 kJ/mol across the system. Both UFF and OPLS over-predicted by 1-2 kJ/mol in regions in which the primary interaction is with the benzene rings (Figure 3.13a and 3.13c). Near the carboxylate groups (Figure 1.13b), however, OPLS significantly over-predicted (2-3 kJ/mol; ~20-30%) in comparison to DFT and the other two force fields, primarily a result of the much higher ε_{ij}/k_B parameter for the carboxylate oxygen in OPLS (105.7 K) compared to the other two force fields (30.2 K in UFF; 48.2 K in DREIDING).

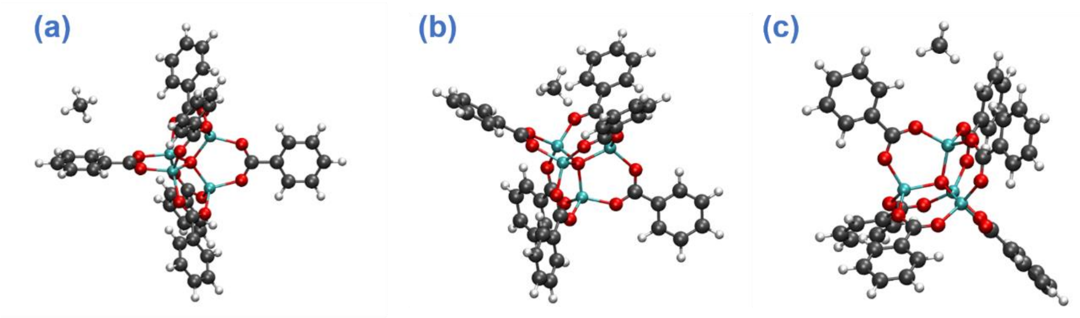

Figure 3.14: Methane binding near the Zn-benzoate cluster, identified via DFT: (a) above a benzene ring; (b) sited in the 'corner' formed where three benzoate moieties intersect; (c) between two benzene rings, interacting primarily with the edges of the rings and oxygen atoms.

These preliminary results suggest that while the OPLS force field will produce an isotherm which will often look qualitatively correct, a significant over-estimation of the adsorption isotherm at low pressure is likely in any MOF using carboxylic acid as a coordinating group. Any subsequent analysis of preferred adsorption sites will be artificially skewed towards these regions of the MOF. This can be seen clearly in the work of Yang and Zhong,[164] in which their re-parameterisations of the OPLS force field for CuBTC and IRMOF-1 primarily affected the ε_{ii} parameter for the carboxylate oxygen.

Although UFF and OPLS perform very similarly in the prediction of isotherms – both over-estimate adsorption at low loading by ~30-50% in the cases studied – they do not appear to over-estimate for the same reasons. While OPLS appears to capture interactions near the ligand well, it significantly over-estimates the interaction near carboxylate groups. Comparison of FF and DFT binding energies suggests that UFF over-estimates the interaction of CH_4 with all regions of the framework by a similar magnitude. UFF may, therefore, be expected to still give qualitatively accurate predictions of the relative importance of different adsorption locations within the structure for most systems. It has been shown, however, that the reliability of classical force fields in predictions of methane binding near the metal cluster of a MOF is strongly dependent on the metal and its coordination state,[115,141,169,170] particularly for systems in which open-metal sites are present, and care should be taken in the interpretation of simulation data in these cases.

3.4 Conclusions

In this multi-level computational study, the suitability of generic force fields for use in the prediction of methane adsorption isotherms and adsorption mechanisms in MOFs at low coverage has been evaluated through a combination of classical and quantum chemical simulations. It has been demonstrated that while all three commonly used generic force fields tested in this work (DREIDING, UFF and OPLS-AA) are suitable for the qualitative prediction of adsorption isotherms, DREIDING provides superior quantitative agreement with experimental data, confirming the general literature consensus. It’s also shown, however, that DREIDING over-estimates the adsorbed amount by up to 25% on average for fractional loadings less than 0.5. Furthermore, it’s demonstrated that selecting a cut-off radius of less than 17 Å (4.5σ) is likely to introduce a systematic and statistically significant underestimation in the amount adsorbed when compared to the converged result. This underestimation is relatively minor (5-10%) and will further depend upon the implementation of the cut-off. In the present work, the LJ term was simply truncated at r_c. Alternatively, one may shift the potential to produce a smooth decay to zero at r_c and/or choose to include a further tail correction to the LJ energy.

Comparison of DFT and FF-based simulations of gas-ligand binding has shown that DREIDING and, in particular, OPLS-AA are capable of predicting the binding location and binding energy to a high degree of accuracy (to within 0.5 Å and 1-2 kJ/mol). The level of accuracy attained by FF predictions decreases significantly in the case of ligands containing high concentrations of nitrogen or oxygen, however, and we recommend treating quantitative FF predictions of gas binding in these types of MOF systems with a certain degree of scepticism.

Based both on the results presented and the literature data summarised herein, there are several suggestions that can be made as to best practice in choice of generic force field for predictions of methane adsorption in MOFs. UFF is likely to over-estimate both the adsorption isotherm and the interaction of methane with organic ligands by a significant amount and it is shown to be best not to rely on this force field for quantitative predictions of low-coverage adsorption properties. It is possible that the scaling factors suggested by Fairen-Jimenez[165] and Pérez-Peritello[146] may satisfactorily address this shortcoming, although this was not explored in the present work. While OPLS-AA performed well in predictions of gas-ligand binding, it is likely to over-estimate gas adsorption in MOFs which use carboxylic acid as a coordinating group and did not offer a significant improvement over UFF or DREIDING in the prediction of adsorption isotherms. DREIDING offered the best performance of the three tested force fields in the prediction of adsorption isotherms in all the systems considered in this study, and in literature studies in which more than one force field was evaluated.[65,115,146] It also performed very well in the prediction of gas-ligand interactions and, as it considers each element to have only one set of LJ parameters, has the advantage of being easily implemented in simulations.

Given the huge number of potential MOF structures, this chapter is not a comprehensive study of methane adsorption in MOFs but intended as a guide in the selection of appropriate force fields for adsorption simulations and highlight some of the limitations and potential pit-falls of these approaches. Computational tools are – rightly – becoming more commonplace in the search for high-performance MOF adsorbents but, as with all tools, need to be used appropriately. From here onwards in this work, the DREIDING force field will be used in the study of adsorption within MOFs of interest, unless stated otherwise.

Chapter 4

Methane Capture Using Weak Hydrogen Bonding

4.1 Introduction

There are many strategies being explored to enhance the performance of porous materials for gas storage applications including increasing surface area, reducing solubility in water and developing pore structure. One strategy involves the investigation of selected functional groups to identify targets that will improve surface interactions. This can be achieved through the analysis of binding interactions that occur at molecular level between various functional groups and gas molecules of interest for gas storage, such as methane. There are multiple different binding interactions involved but in this chapter weak hydrogen bonds are the focus. The weak hydrogen bond is an important type of noncovalent interaction, which has been shown to contribute to stability and conformation of proteins and large biochemical membranes, stereoselectivity, crystal packing and effective gas storage in porous materials.[171–173]

The binding of a series of functionalised organic molecules specifically selected to exhibit weak hydrogen bonds with methane molecules is systematically investigated here using second order Møller-Plesset perturbation theory. The methods used throughout the text are also explored and benchmarked. To increase the strength of hydrogen bond interactions, the functional groups include electron-enriched sites to allow sufficient polarisation of the C−H bond of methane.

Weak hydrogen bonds comprise a class of hydrogen bonds (HB) with typical values of the binding energy less than 17 kJ mol^{-1} (or 4 kcal mol^{-1}) but greater than the van der Waals limit of 1 kJ mol^{-1} (or 0.25 kcal mol^{-1}). This type of weak interaction allows the enhancement of affinity for methane without creating sites which are difficult and expensive to regenerate.[174] Examples of the weak hydrogen bond include C—H···O interactions, where the hydrogen atom forms a bond between two moieties of which one or even both are of moderate to low negativity, and C—H···π interactions in π electron rich molecules.[171] IUPAC has previously discussed extending the definition of the hydrogen bond to include any attractive interaction X—H···Y—Z, where some evidence of bond character exists between H and Y moieties, and X is more electronegative than H, even if only moderately (in the case of X as carbon).[175] Within this definition, X—H is the donor and Y is the acceptor. The H···Y distance is generally 2-3 Å, and 30-80% of weak hydrogen bonds have an H···Y distance of less than the sum of the van der Waal radii of H and Y species. This often makes weak hydrogen bond interactions difficult to distinguish. The X—H···Y angle is optimised at 180° but typically ranges from 90° to180°, and the H···Y—Z angle is optimised where the Y lone pair is directed at the hydrogen atom, or where maximum charge transfer occurs. The hydrogen bond character has been also shown in C—H/π interactions, which play an important role in many fields that include crystals,[173] conformational analysis,[176,177] organic reactions[178,179] and molecular recognition.[180–182] C—H/π interactions govern the stability of biological structures where they affect both binding affinity and conformation. In these studies, it is also customary to use methane as the simplest model of an aliphatic compound.

As discussed in the introduction an alternative natural gas storage method involves packing fuel tanks with porous material, such as MOFs, to adsorb the gas.

This exploits weak van der Waals interactions between methane and the pore walls to achieve a density comparable to compressed natural gas but allowing ambient temperatures and moderate pressures (typically 35 bar) in less bulky fuel tanks. Attachment of carefully selected functional groups to the porous materials can, in principle, enhance the interactions between methane and the pore walls to increase the packing density of methane at low pressures. Computational studies of the binding of guest molecules with functionalised ligands at the atomic scale[76–78,183] have shown that finding favourable adsorption sites in the organic ligands holds a key to enhancing the ability of porous materials to capture gases. Torrisi *et al.*[77], for example, showed that aromatic rings functionalised by certain groups can enhance the intermolecular interaction in different ways: methyl groups increase the inductive effect, lone-pair donating groups promote acid-base type interactions, and hydrogen bonding occurs in acidic proton containing groups.

The primary aim of this chapter is to enhance the targeted design of MOFs and other porous materials and their ability to coordinate with one of more methane molecules via weak hydrogen bond interactions through the selection of functionalised organic molecules. The considered molecular complexes use an oxygen atom as the binding site 2for the methane molecule, and X—H exists as a C—H bond in methane and so is classed as a weak donor. To maximise the strength of the hydrogen bond interaction the organic linkers were selected to ensure that the Y—Z moiety is a strong acceptor, e.g. O=C.

4.2 Computational methods

Optimised geometries and binding energies for the functional groups supported by an aromatic or cyclohexane ring with methane were calculated for nine methane-ligand complexes using Q-Chem quantum chemistry package.[184] The carbon and hydrogen atoms within the ring of the linker were fixed upon geometry optimisation leaving the atoms of the functional group and the methane molecule free to find the minimum energy configurations. In the dimer, trimer and tetramer configurations, geometry optimisation was obtained using the resolution of identity MP2 level of theory (RI-MP2) with the cc-pVDZ basis set, and the binding energies were calculated at the MP2 level using cc-pVQZ basis set and the Boys and Bernardi counterpoise correction.[158] Partial charges on each atom were obtained using the CHELPG scheme developed by Breneman and Wiberg.[123]

Benchmarks for the equilibrium structure and binding energy of a small formaldehyde–methane dimer are presented in Table 4.1 to show that the adopted computational approach is comparable in accuracy with the CCSD(T) method for the binding energies. Unlike the computationally expensive CCSD(T) method, the adopted computational approach can be used to study larger (tetramer) systems without compromising the accuracy of predictions. Table 4.1 shows that the MP2/cc-pVQZ binding energies calculated for the structures optimized at the RI-MP2/cc-pVDZ and MP2/cc-pVDZ levels of theory are in good agreement with those predicted directly from the MP2/ cc-pVQZ equilibrium structure. The CCSD(T)/cc-pVQZ binding energy obtained for the dimer optimized at the CCSD(T)/cc-pVDZ level of theory also has a very close value. The table also explores the binding of the formaldehyde-methane dimer using density functional theory (DFT) and various basis sets. Results show reasonable agreement with the most computationally expensive CCSD(T) method. All DFT methods slightly overestimate the binding interaction with omegaB97X-D showing the closest agreement to the

CCSD(T) method. Calculations using DFT methods will be carried out in later chapters.

Table 4.1: Benchmarking RI-MP2, MP2, CCSD(T) and DFT calculations for a model formaldehyde-methane dimer

Geometry optimisation, level of theory/basis set	**Distance between H(CH$_4$) and O(CH$_2$O), in Å**	**Binding energy, level of theory/basis set**	**Binding energy, in kJ mol^{-1}**
RiMP2/cc-pVDZ	2.54	RiMP2/cc-pVDZ	-0.91
		MP2/cc-pVQZ	-2.20
MP2/cc-pVDZ	2.54	MP2/cc-pVDZ	-0.91
		MP2/cc-pVQZ	-2.20
MP2/cc-pVQZ	2.61	MP2/cc-pVQZ	-2.21
CCSD(T) /cc-pVDZ	2.99	CCSD(T)/cc-pVDZ	-0.95
		CCSD(T)/cc-pVQZ	-2.24
B3LYP/6-31+G*	2.60	B3LYP/6-311+G*	-3.08
B3LYP/6-31G**	2.57	B3LYP/6-311++G**	-2.87

The linker candidates presented in Table 4.2, all containing oxygen to create a strong hydrogen bond acceptor, were tested for their ability to bind methane. Functional groups with more than one accepting site were tested on their ability to form trimer and tetramer structures by including additional methane molecules.

Table 4.2: Selection of functionalised organic molecules screened for methane binding using a weak hydrogen bond

Label	Functional group	Structure	Label	Functional group	Structure
A	C_6H_5-OH phenol	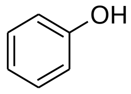	**F**	C_6H_5-OOH phenyl hydroperoxide	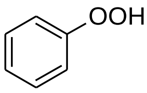
B	C_6H_5-C(=O)-H benzaldehyde	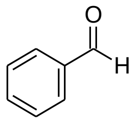	**G**	$C_{10}H_6O_2$ 1,4-napthoquinone	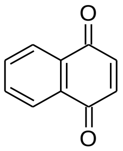
C	C_6H_{11}=O cyclohexanone	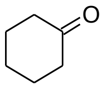	**H**	C_6H_5-SO_3H benzenesulfonic acid	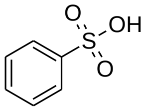
D	C_6H_5-COOH benzoic acid	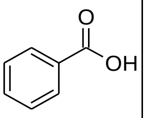	**I**	C_6H_5-PO_3H_2 phenylphosphonic acid	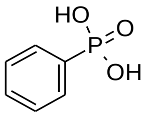
E	C_6H_5-NO_2 nitrobenzene	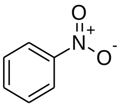			

4.3 Results and discussion

Figure 4.1 shows the lowest energy dimer configurations between methane and either phenol, benzaldehyde, or cyclohexanone molecule. For the phenol-methane dimer (Figure 4.1a), the lowest energy conformation corresponds to the interaction between the hydroxyl group on phenol and methane where the C—H bond of methane is pointing directly to the lone pair of the oxygen atom with the C—O···H being in the plane of the ring. The binding energy has a moderate value of -3.17 kJ mol^{-1}, the C—H···O angle is found to be 180° and the intermolecular $H_{(CH_4)}$···O distance is 2.58 Å. In this dimer, the interacting hydrogen of methane carries a small positive charge of +0.16 m*e* and both the oxygen and the $C_{(CH_4)}$ become more negatively charged upon binding. The above description indicates a typical HB-like, cohesive interaction. In the benzaldehyde-methane dimer (Figure 4.1b), the strongest interaction was found to be between the formyl substituent functional group attached to a phenyl ring and methane molecule where the C—H···O=C atoms are located along a straight line with the $H_{(CH_4)}\cdots O_{(O=C)}$ distance of 2.57 Å being shorter than the sum of the van der Waal radii of hydrogen and oxygen. A binding energy of -3.32 kJ mol^{-1} is comparable to that for the phenol-methane dimer shown in Figure 4.1a. A ketone functional group represents a binding site similar in strength and nature to the formyl group. This has been demonstrated in Figure 4.1c showing the cohesive interaction between cyclohexanone and methane. This dimer has the H—C bond of the methane pointing at the carbonyl oxygen such that the C—H···O=C atoms are aligned along a straight line. In this configuration, there is very little steric repulsion due to the way the carbonyl fixes the shape of the aliphatic ring. The moderate binding energy is expected of the carbonyl species due to the electron donating effect of the ring.

(a) A: C_6H_5OH (Phenol) Dimer

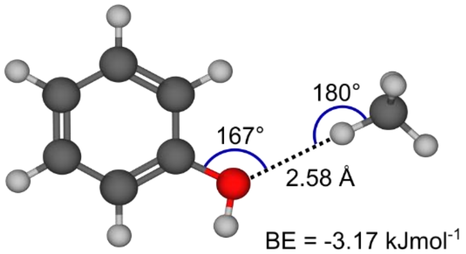

(b) B: C_6H_5CHO (Benzaldehyde) Dimer

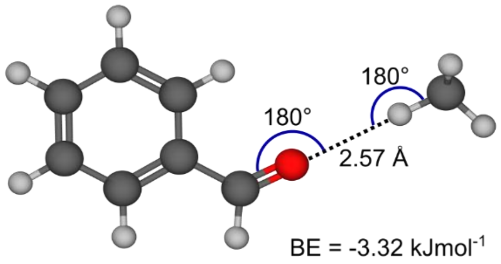

(c) C: $C_6H_{11}O$ (Cyclohexanone) Dimer

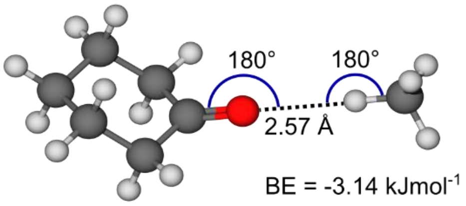

Figure 4.1: The dimer configurations optimised at the MP2/cc-pVQZ level for C_6H_5OH (phenol) – CH_4 dimer (a), C_6H_5CHO (benzaldehyde) – CH_4 dimer (b), and $C_6H_{11}O$ (cyclohexanone) – CH_4 dimer (c). The sites showing the strongest binding energies (BE) with methane are found to be hydroxyl (a), aldehyde (b) and ketone (c) groups. The atoms shown in grey, white and red represent carbon, hydrogen and oxygen, respectively.

For the benzoic acid molecule, two dimer complexes have been identified, as shown in Figure 4.2. In dimer I the methane molecule interacts with the carbonyl-type oxygen atom via a weak HB-like interaction. Similar to the benzaldehyde – methane dimer (Figure 4.1b), the C—H···O=C interaction occurs linearly along the same axis, in the plane of the phenyl ring. The short intermolecular distance of 2.55 Å agrees with the moderate binding energy of -3.75 kJ mol^{-1}. However, in the benzoic acid – methane dimer I the carbonyl oxygen atom is involved in two weak HB interactions making it a bifurcated HB acceptor and limiting the flexibility of rotation about the C—OH bond. Dimer II of this complex involves the methane molecule interacting directly with the OH oxygen site. In this case, the $O_{(OH)}\cdots H—C$ atoms are located on the same axis and the $C—O\cdots H$ angle of 149° suggests that the lone pair of the oxygen atom is somewhat unavailable to the methane in this configuration. The interatomic distance is short, at 2.58 Å, but the binding energy remains weak having the value of -2.89 kJ mol^{-1} despite the $O_{(OH)}$ having a more negative charge than the $O_{(C=O)}$ in the functionalized benzene. Although the binding is weaker in dimer II than in dimer I, both interactions are accompanied by an increase in positive charge at the hydrogen atom and an increase in negative charge at both the $C_{(CH_4)}$ and O atoms. In the nitrobenzene – methane complex, only one dimer was tested due to the symmetry of the functional group, which gave a conformation in which the C—H bond of the methane directs to the N—O bond giving a $H_{(CH_4)}\cdots O_{(NO)}$ distance of 2.57 Å (Figure 4.2c). The binding energy of -3.65 kJ mol^{-1} is comparable to that of the benzoic acid dimer I shown and is moderate as expected of a highly polarizing group such as $–NO_2$.

D: C_6H_5COOH (Benzoic Acid)
(a) Dimer I

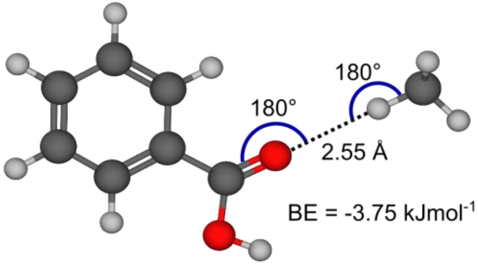

(b) Dimer II

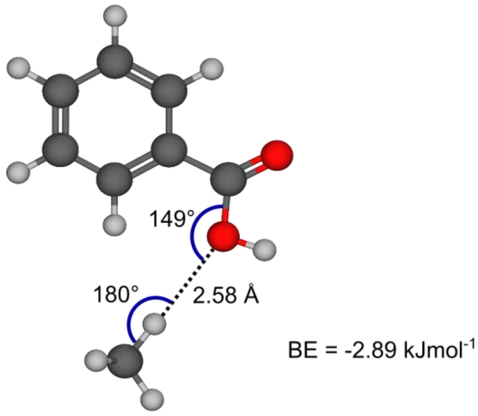

E: $C_6H_5NO_2$ (Nitrobenzene)
(c) Dimer

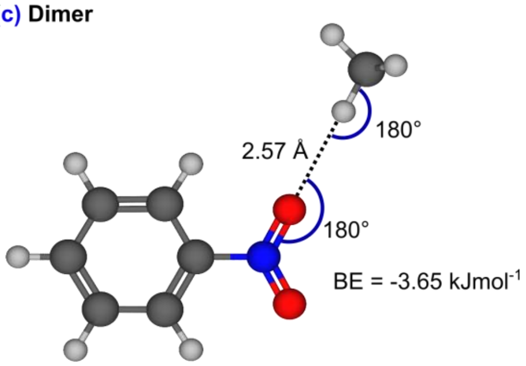

Figure 4.2: The MP2/cc-pVQZ optimised configurations of C_6H_5COOH (benzoic acid) – CH_4 dimer complexes: configurations I (a) and II (b), where methane binds at one of the two oxygen sites, and $C_6H_5NO_2$ (nitrobenzene) – CH_4 dimer complex (c). The atoms shown in grey, white, red and blue represent carbon, hydrogen, oxygen and nitrogen, respectively.

F: C_6H_5OOH (Phenyl Hydroperoxide)

(a) Dimer I

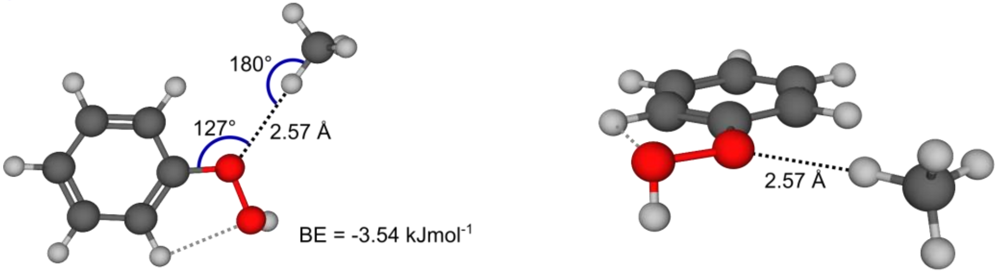

(b) Dimer II

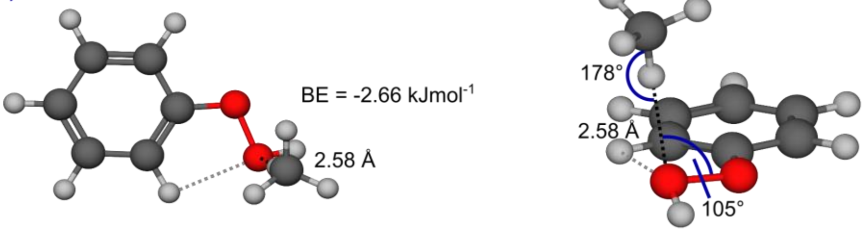

Figure 4.3: The MP2/cc-pVQZ optimised configurations of C_6H_5OOH (phenyl hydroperoxide) – CH_4 complexes: dimer I (a) and dimer II (b). The atoms shown in grey, white and red represent carbon, hydrogen and oxygen, respectively.

The interaction of methane with the peroxide functionalized benzene (phenyl hydroperoxide) results in two dimer. In dimer I presented in Figure 4.3a the methane interacts with the oxygen atom closest to the phenyl ring. The C—H bond of the methane points to the lone pair of the oxygen nearest the ring such that the $O_{(C—O)}\cdots H—C$ atoms are in the plane of the ring with an intermolecular distance of 2.57 Å. The peroxide bond, however weak, serves as a good accepting site due to the electron rich nature of the adjacent oxygen atoms. The binding resulted in a significant increase of charge to -15.2 m*e* on the methane molecule. Dimer II shown in Figure 4.3b has the methane interacting with the oxygen atom furthest from the phenyl ring. In this weaker dimer the methane molecule is located above the plane of the phenyl ring with the methane C—H bond positioned towards the lone pair of the accepting oxygen thus acting as a bifurcated HB acceptor with an $O_{(OH)}\cdots H_{(CH_4)}$ distance of 2.58 Å. The $H_{(O—H)}$ atom rests just under the plane of the ring. Despite the $O_{(OH)}$ being more negatively charged than the $O_{(C—O)}$ atom, methane binds more weakly at the

$O_{(OH)}$ atom (the binding energy of -2.66 kJmol^{-1}) than at the $O_{(C—O)}$ atom (the binding energy of -3.54 kJmol^{-1}). This is thought to be due to the $O_{(OH)}$ atom acting as a bifurcated HB acceptor.

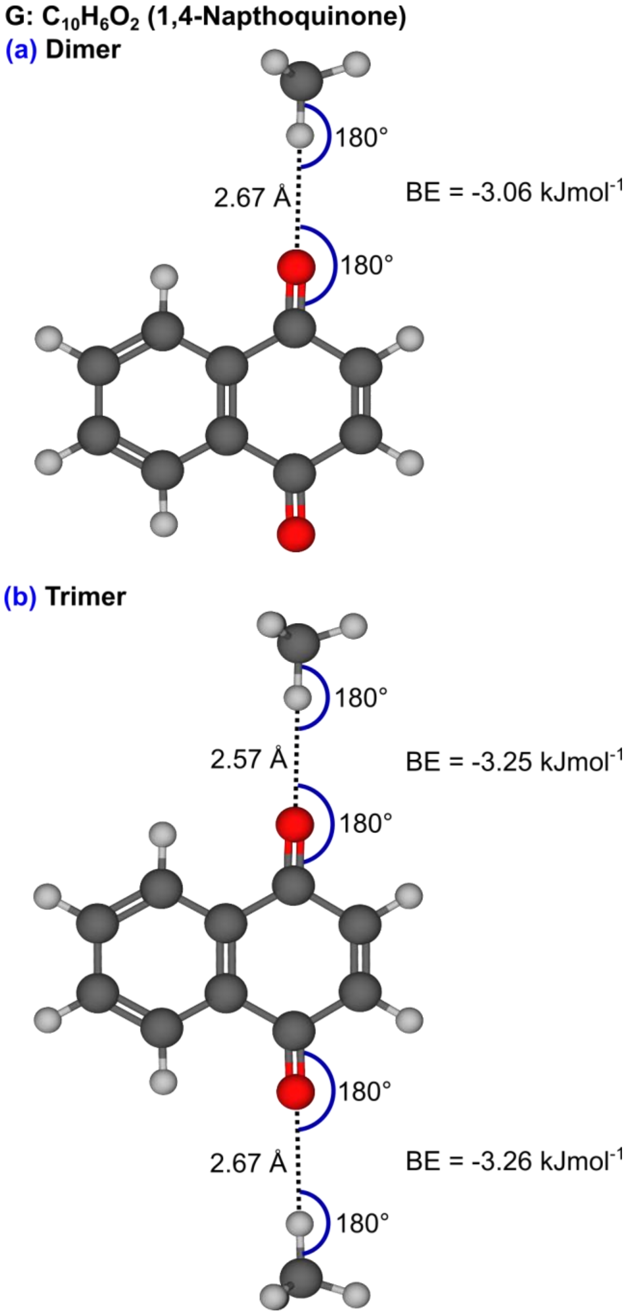

Figure 4.4: The MP2/cc-pVQZ optimised configurations of $C_{10}H_6O_2$ (1,4-napthoquinone) – CH_4 complexes: dimer (a) and trimer (b).

1,4-Napthoquinone is the largest and one of only two non-fully aromatic species tested. The dimer form shows only one oxygen atom accepting a weak HB but the trimer exhibits both available oxygen atoms involved with methane molecules. These complexes can be viewed in Figure 4.4. In the dimer, a moderately strong interaction with a relatively long intermolecular distance of 2.67 Å between the carbonyl oxygen and the methane hydrogen was found giving a binding energy of -3.06 kJ mol^{-1}. A marginal charge gain of -2.69 m*e* on the methane molecule occurred upon dimer formation. Due to the symmetry of the structure it was unnecessary to test dimer formation at the other oxygen site. As expected, upon forming the trimer the binding energies of each interaction are predicted to be similar having the values of -3.25 kJ mol^{-1} and -3.26 kJ mol^{-1}. The $H_{(CH_4)}\cdots O_{(C=O)}$ distances vary by 0.1 Å but this results in little effect on the binding.

H: $C_6H_5SO_3H$ (Benzenesulfonic Acid)

(a) Dimer I

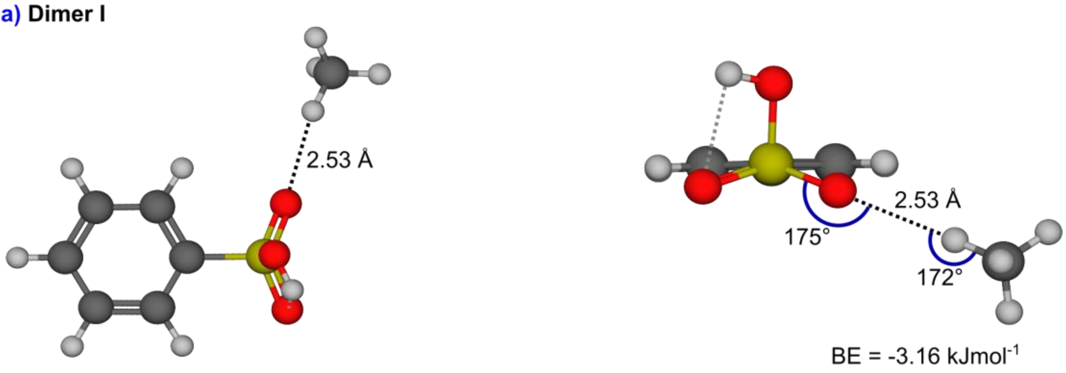

(b) Dimer II

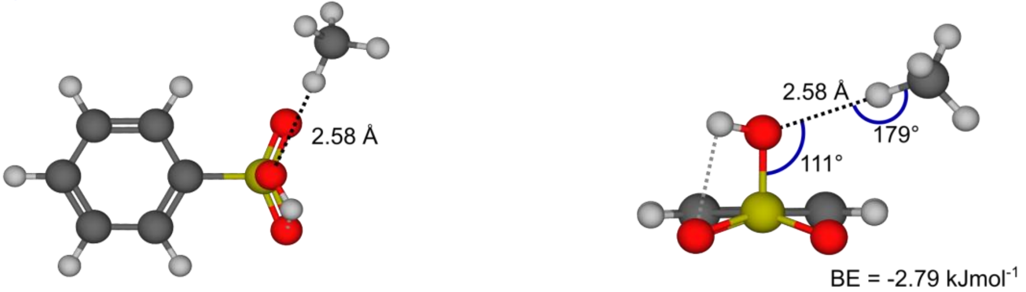

(c) Dimer III

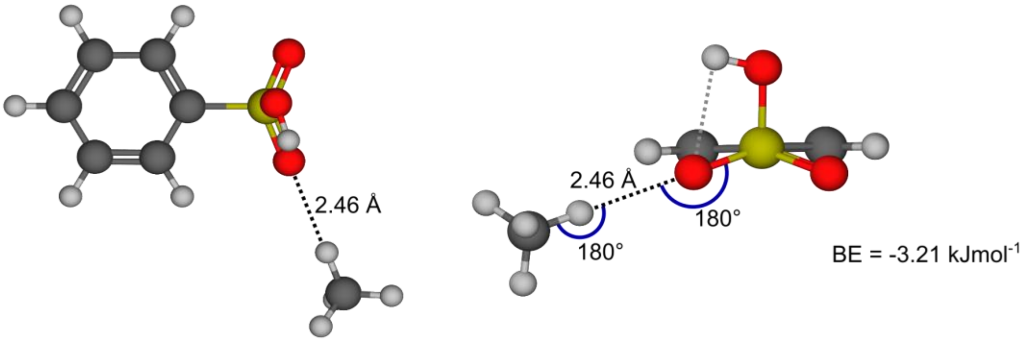

Figure 4.5: The MP2/cc-pVQZ optimised configurations of $C_6H_5SO_3H$ (benzenesulfonic acid) – CH_4 dimer complexes with methane molecules interacting directly with available oxygen sites. The atoms shown in grey, white, yellow and red represent carbon, hydrogen, sulphur and oxygen, respectively.

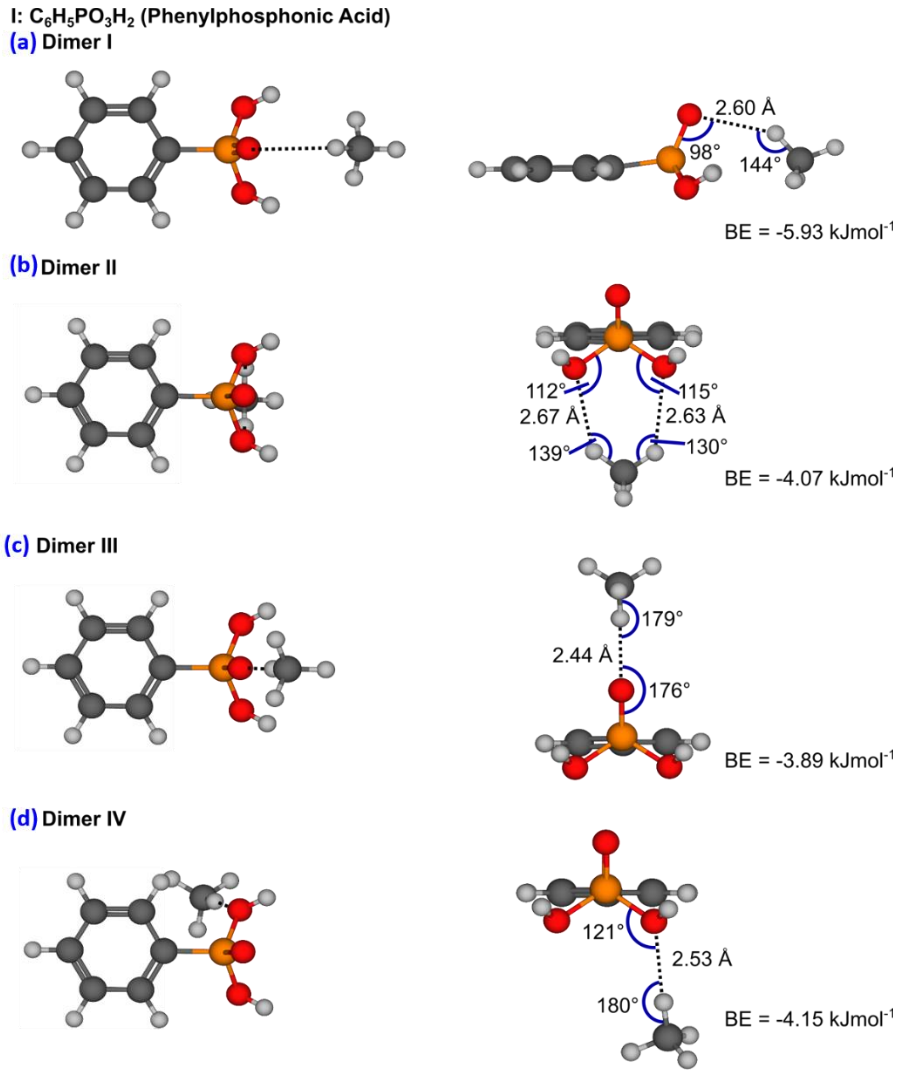

Figure 4.6: The MP2/cc-pVQZ optimised configurations of $C_6H_5PO_3H_2$ (phenylphosphonic acid) – CH_4 dimer complexes (a-d) with methane molecules interacting directly with available oxygen sites. The atoms shown in grey, white, orange and red represent carbon, hydrogen, phosphorous and oxygen, respectively.

The sulfonic acid group has three oxygen atoms available to accept a HB interaction from a methane molecule and the functional group is flexible across many of its bonds. There is a weak hydrogen bond within the linker itself, it exists as O—H···O=S and so one S=O bond is involved in this interaction whereas the other is not. The dimer complexes tested encompassing the benzenesulfonic acid molecule are shown in Figure 4.5. Dimer I shown in Figure 4.5a involves the methane interacting with the oxygen not inherently exhibiting a weak HB within the functional group. It shows a moderately strong interaction with the binding energy of -3.16 kJ mol^{-1} and an intermolecular distance of 2.53 Å. In dimer II (Figure 4.5b) the methane interacts with the S-OH type oxygen atom. This weaker dimer with the binding energy of -2.79 kJ mol^{-1} shows a strongly directional interaction towards the lone pair of the $O_{(OH)}$ atom at a $O_{(OH)} \cdots H_{(CH_4)}$ distance of 2.58 Å. Dimer III shown in Figure 4.5c is comparable with dimer I in structure and binding strength as expected by the similar nature of the accepting oxygen. However, this oxygen atom is a bifurcated HB acceptor making it more negatively charged (-0.58e) compared to that of the accepting oxygen in dimer I (-0.50e) which gives rise to the slightly stronger binding in dimer III.

Figure 4.6 shows the methane complexes formed with phenylphosphonic acid (a-d). As with the sulfonic acid group, there are three available oxygen atoms for binding methane and so there are many dimer arrangements that can be formed. Both dimers I and II (Figures 4.6a and 4.6b) only show weakly directional interactions but the binding energies are strong compared to all other functional groups investigated. Neither dimer gets stabilised via a weak hydrogen bonding interaction judging by the optimised geometries of the dimers. The dimer I configuration of phenylphosphonic acid and methane displays the methane in close proximity with the functional group and the binding energy is the largest found for any dimer tested at -5.93 kJ mol^{-1}. Dimer II, although binding methane strongly (the binding energy of this complex is -4.07 kJ mol^{-1}), is particularly inefficient in the way it binds to two $O_{(OH)}$ binding sites which in principle, could be occupied by several methane molecules to form a trimer (as in the case of trimer I shown in Figure 4.8a) or even a tetramer. The binding energies at these $O_{(OH)}$ sites are greater when absorbing two or three methane molecules per organic linker. Dimer III (Figure 4.6c) shows a strong, directional interaction between the methane and the $O_{(P=O)}$ atom that is stabilised by a weak HB with a short intermolecular distance of 2.44 Å. The binding was accompanied by a charge increase at the methane of +22.0 m*e*. Dimer IV shows a strong binding site where the C—H bond of methane points to the lone pair of the accepting $O_{(OH)}$ atom with an intermolecular distance of 2.53 Å (Figure 4.6d). Due to the symmetry of the functionalized benzene molecule, there exists an identical $O_{(OH)}$ atom accepting site.

Superimposing the two dimer structures of the benzoic acid group gives a trimer configuration (Figure 4.7a) similar to that of the separate dimers but with both interactions weakened, as indicated by a significant lengthening of the $O_{(C=O)} \cdots H_{(CH_4)}$ distance to 2.94 Å and a decrease in both values for the binding energy. Despite the interaction at the carbonyl group occurring at a larger distance than the sum of the van der Waals radii of oxygen and hydrogen, the optimised geometry suggests a very directional interaction towards the oxygen lone pair symptomatic of an HB. For nitrobenzene, introducing another methane molecule to the system at another available oxygen site gives the trimer structure shown in Figure 4.7b. Similar to the benzoic acid group, upon forming the trimer, both methane molecules distance slightly from the accepting oxygen atoms and the binding becomes weaker. The binding energies are smaller than expected of a formally negatively charged oxygen. The trimer structure of phenyl hydroperoxide (Figure 4.7c) is formed from superimposing dimers I and II which produces moderately strong interactions at each accepting site. Both methane molecules come closer to the functional group, each giving intermolecular distances of 2.52 Å - 2.53 Å. The binding energy at the $O_{(OH)}$ site increased but the binding energy at the $O_{(C—O)}$ site decreased slightly.

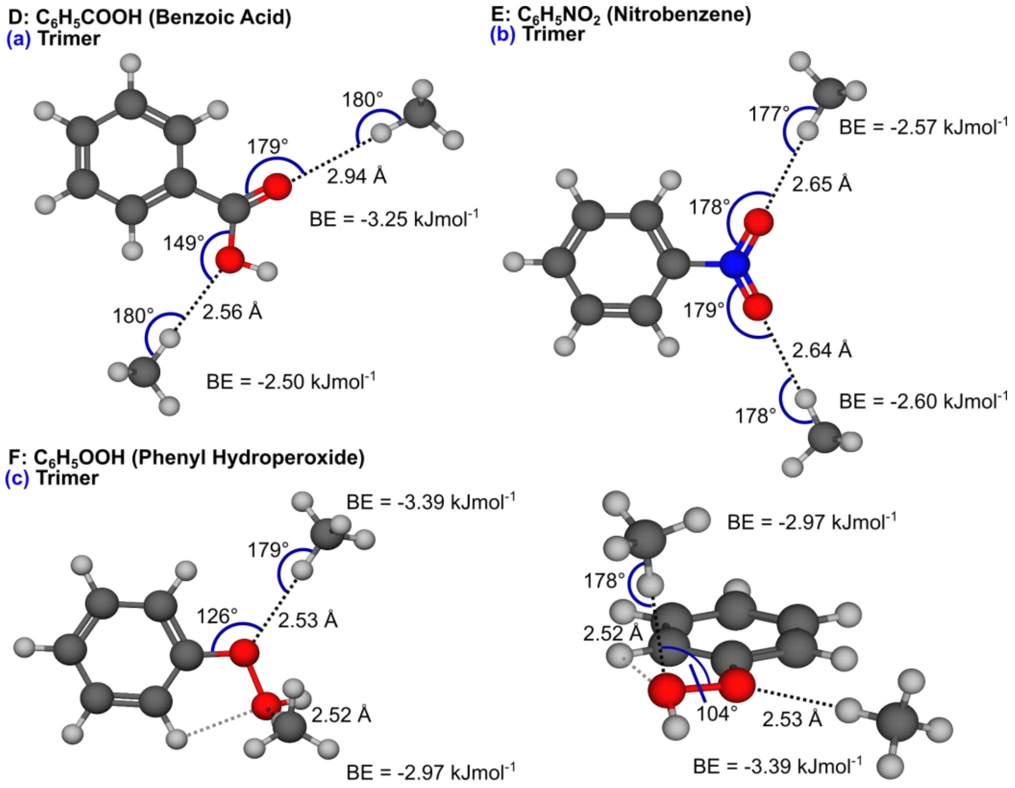

Figure 4.7: The MP2/cc-pVQZ optimised trimer configurations of C_6H_5COOH (benzoic acid) – CH_4 (a), $C_6H_5NO_2$ (nitrobenzene) – CH_4 (b) and C_6H_5OOH (phenyl hydroperoxide) – CH_4 (c). The atoms shown in grey, white, red and blue represent carbon, hydrogen, oxygen and nitrogen, respectively.

H: $C_6H_5SO_3H$ (Benzenesulfonic Acid)

(a) Trimer I

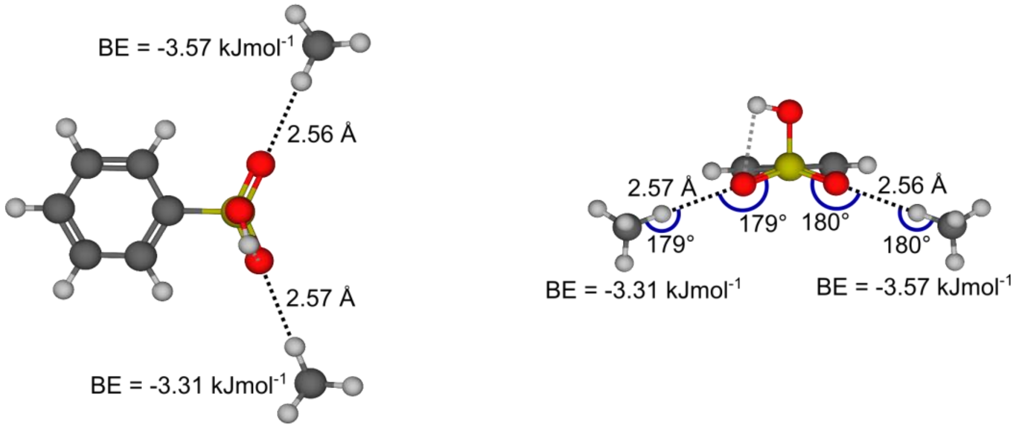

(b) Trimer II

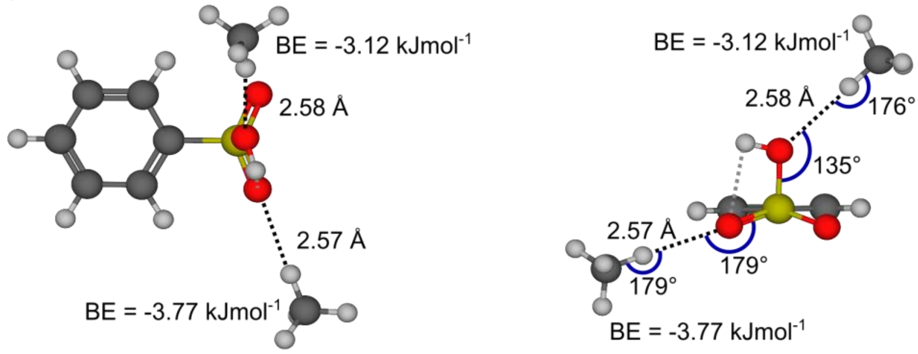

(c) Trimer III

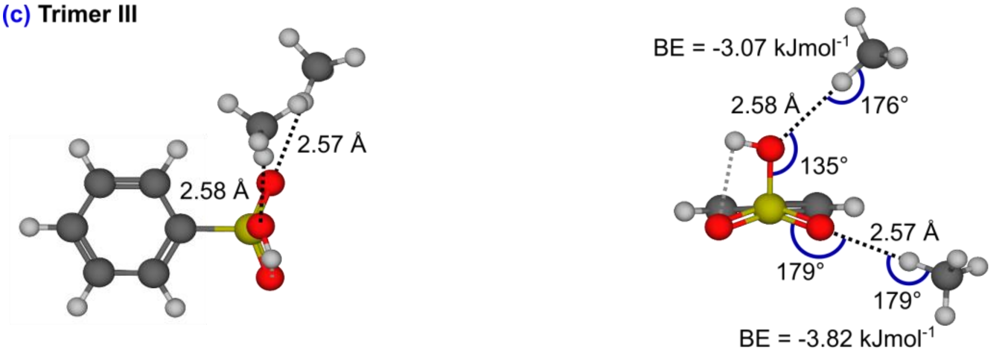

Figure 4.8: The MP2/cc-pVQZ optimised configurations of $C_6H_5SO_3H$ (benzenesulfonic acid) – CH_4 complexes. Benzenesulfonic acid trimers showing a combined structure of (a) dimers I and III, (b) dimers II and III and (c) dimers I and II. In these complexes (a-c), the binding energies are stronger at both HB sites with respect to the corresponding dimer structures.

I: $C_6H_5PO_3H_2$ (Phenylphosphonic Acid)

(a) Trimer I

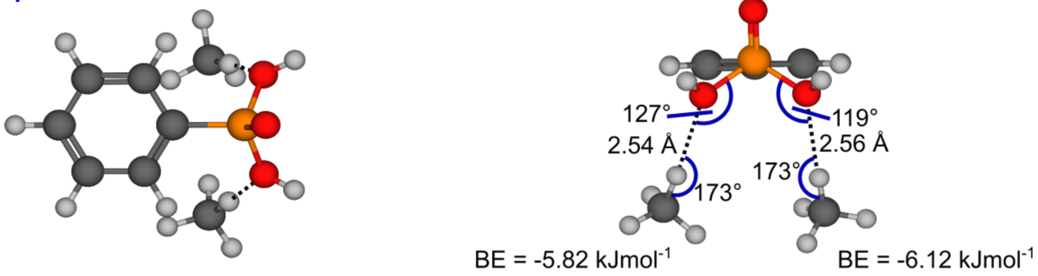

(b) Trimer II

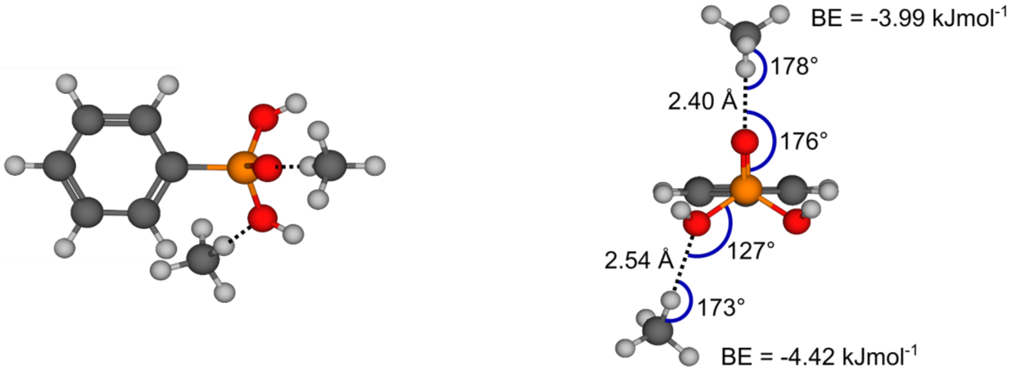

(c) Trimer III

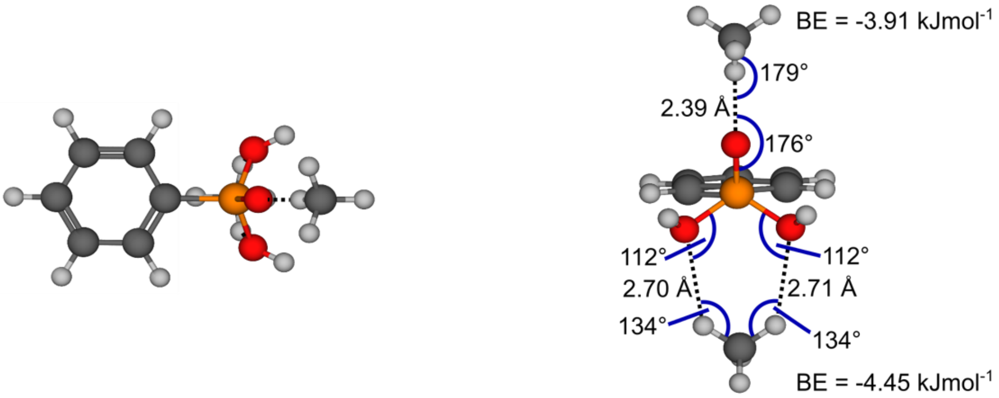

Figure 4.9: The MP2/cc-pVQZ optimised configurations of $C_6H_5PO_3H_2$ (phenylphosphonic acid) – CH_4 complexes. $C_6H_5PO_3H_2$ (phenylphosphonic acid) – CH_4 complexes: (a) trimer I with methane molecules binding to each $O_{(OH)}$ atom similar to dimer IV but with stronger interactions; trimers showing a combined structure of (b) dimers III and IV and (c) dimers II and III.

With many binding sites available in the sulfonic acid group, several trimer conformations have been constructed thus allowing investigation of binding methane in higher ratios of methane to ligand. Trimer I, combining the structure of dimers I and III, has been used to investigate the effect of binding methane in a 2:1 ratio (Figure 4.8a). It is shown that both individual dimer interactions have been strengthened upon forming the trimer. The interaction at the bifurcated HB acceptor oxygen (left) involves a charge increase at methane upon binding in the complex of +12.8 m*e* and that at the other methane (right) of +5.50 me. Other examples of methane binding in a 2:1 ratio are shown in trimer II, formed by superimposing dimers II and III (Figure 4.8b) and trimer III, which involves a combination of dimers I and II (Figure 4.8c). In these complexes, the binding energies have also been found to strengthen at both HB sites with respect to the corresponding dimer structures. The interactions are directional and typical of weak HB interactions. The sum of the binding energies found in each of the trimers is very similar.

As with the benzenesulfonic acid, several trimers for phenylphosphonic acid were tested to investigate the effectiveness of binding more methane molecules upon each linker. The trimer I involves methane molecules binding to each $O_{(OH)}$ atom similar to dimer IV but with stronger interactions. There is a slight asymmetry to the configuration as displayed by the angles, distances and the resulting binding energies shown in Figure 4.9a. Trimer II (Figure 4.9b) is a combination of dimers III and IV in which the binding energy is strengthened slightly giving moderately strong interactions of -3.99 kJ mol^{-1} and -4.42 kJ mol^{-1} at the $O_{(P=O)}$ site and $O_{(P\text{-}OH)}$ site, respectively. Both interactions are highly directional and so are typical of weak hydrogen bonds. The final trimer tested is a combination of dimers II and III with a directional, weak HB-like interaction at the $O_{(P=O)}$ site. The second methane molecule binds to both $O_{(P\text{-}OH)}$ sites below the functional group as shown in Figure 4.9c. Both interactions are of significant strength yet methane binds more strongly within trimer I where methane binds both more strongly and more efficiently.

For benzenesulfonic acid, combining the three dimers further gave a promising tetramer complex with three strong, directional HB interactions and short intermolecular distances (Figure 4.10a). The $O_{(OH)}\cdots H_{(CH_4)}$ and $O_{(S=O)}\cdots H_{(CH_4)}$

interactions strengthened relative to the corresponding dimers allow us to conclude that introduction of more methane molecules to the dimer complex is favourable. This could be a very powerful route to efficient capture of methane at increased pressures. The strongest interactions were found in the $C_6H_5PO_3H\cdots(CH_4)_3$ tetramer shown in Figure 4.10b with very large binding energies and short intermolecular distances. Each of the $C—H\cdots O_{(OH)}$ angles is slightly distorted from the optimised angle of 180° found in the corresponding dimers. This is expected to be due to the steric repulsion between the methane molecules. Charge increases at the methane molecules of +1.46 m*e*, +2.26 m*e*, and +2.72 m*e* were calculated corresponding to the binding energies of -6.21 kJ mol^{-1}, -4.05 kJ mol^{-1}, and -6.17 kJ mol^{-1}, respectively. Combining strong binding sites with a high methane to functional group ratio, the tetramer complexes of benzenesulfonic acid and phenylphosphonic acid demonstrate that these functional groups exhibit significant potential for enhanced CH_4 capture.

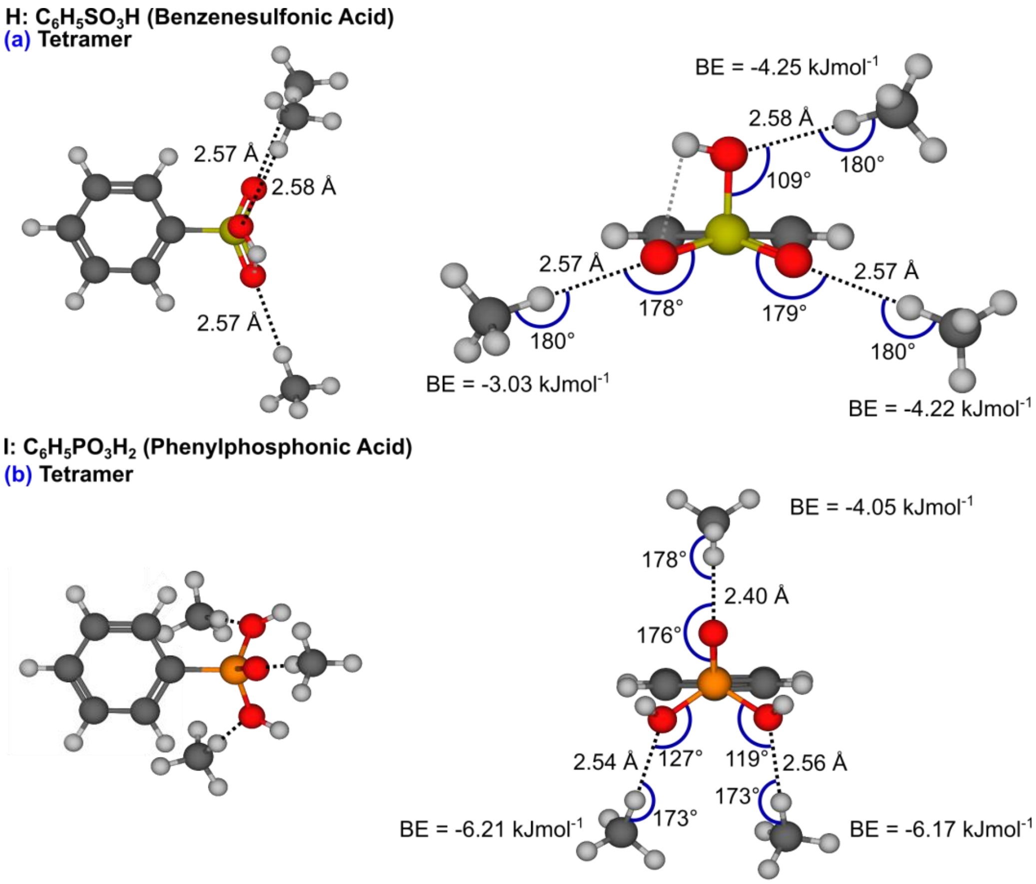

Figure 4.10: The MP2/cc-pVQZ optimised tetramer configurations of $C_6H_5SO_3H$ (benzenesulfonic acid) – CH_4 (a) and $C_6H_5PO_3H_2$ (phenylphosphonic acid) – CH_4 (b) complexes. The atoms shown in grey, white, orange red and yellow represent carbon, hydrogen, phosphor, oxygen and sulfur, respectively.

The interactions of the dimer complexes compare well with results of similar studies. Research by Yu and co-workers focuses on the separation of CO_2 from CH_4 in membrane materials with studies of functional groups bonded to hexane and their interactions with methane compared to carbon dioxide at the same level of theory.[185] Three of the functional groups R-COOH, R-SO_3H and R-PO_3H show similar dimer interactions with methane compared to our work illustrating a consistency in result and how this work can be applied to other porous materials. However, the use of the aromatic groups seems to have an effect, particularly with the R-OOH group in which the results differ most significantly indicating the base structure has an impact on the overall interaction and needs to be taken into consideration.

Overall, the dimer complexes show significant HB character towards the oxygen atom lone pair from intermolecular distances and directional geometries. There is no general trend for carbonyl containing linkers being superior in their methane sorption ability than hydroxyl containing linkers. There is no clear trend between the binding energy and charge increase at the methane suggesting that the interaction cannot be explained simply on a basis of charge on the methane as the dipole-dipole interaction within a HB is more complex. As seen in Table 4.3, the charge at the hydrogen atom of the methane is always more positive than that of the adjacent carbon atom, fitting well with the requirements for a hydrogen bond.

Table 4.3: The dimer complexes listed in order of increasing binding strength with the corresponding atomic charges of carbon, Q_C and hydrogen Q_H as determined by CHELPG charge analysis. Dimers I and II of the phenylphosphonic acid (**I**) linker have been excluded as they do not show clear hydrogen bonding character.

Label	**Dimer**	**Binding energy, in kJ mol^{-1}**	**Q_c, me**	**Q_H, me**
F	C_6H_5-OOH dimer II: H—O···H—CH_3	-2.66	-0.48	0.15
H	C_6H_5-SO_3H dimer II: H—O···H—CH_3	-2.79	-0.50	0.15
D	C_6H_5-COOH dimer II: H—O···H—CH_3	-2.89	-0.48	0.14
G	$C_{10}H_6O_2$	-3.06	-0.49	0.15
C	C_6H_{11}=O	-3.14	-0.50	0.17
H	C_6H_5-SO_3H dimer I: S=O···H—CH_3	-3.16	-0.50	0.16
A	C_6H_5OH	-3.17	-0.50	0.16
H	C_6H_5-SO_3H dimer III: S=O(···H) ···H—CH_3	-3.21	-0.53	0.19
B	C_6H_5-C(=O)-H	-3.32	-0.46	0.14
F	C_6H_5-OOH dimer I: C—O···H—CH_3	-3.54	-0.45	0.11
E	C_6H_5-NO_2	-3.65	-0.52	0.17
D	C_6H_5-COOH dimer II: H—O···H—CH_3	-3.75	-0.49	0.16
I	C_6H_5-PO_3H_2 dimer III: P=O···H—CH_3	-3.89	-0.57	0.23
I	C_6H_5-PO_3H_2 dimer IV: H—O···H—CH_3	-4.15	-0.50	0.16

4.4 Conclusions

The lowest energy configurations and the associated binding energies were calculated for ligand-methane complexes involving nine different functional organic groups. It has been demonstrated that some organic molecules contain several binding sites available for various dimer, trimer and tetramer conformations with methane molecules. Although the dipole across the C—H bond in methane is relatively weak, the methane can bind *via* hydrogen bonding accepting species such as carbonyl oxygen atoms. Each of the calculated energies gained from forming the dimers was enough to surpass RT (at room temperature). The Ph-PO_3H_2 ligand was the most encouraging candidate tested for binding methane *via* hydrogen bonding; the strongest binding energy calculated resulted from the $O_{(OH)}\cdots H_{CH4}$ interaction of the [Ph-$PO_3H_2\cdots CH_4$] dimer. The phosphonic acid group also gave promising results upon introducing more methane molecules with the [Ph-$PO_3H_2\cdots(CH_4)_3$] tetramer exhibiting the greatest binding energies calculated overall, suggesting binding in methane to ligand ratios of greater than 1:1 is feasible and can even be preferable. This could aid with sorption of methane at higher pressures.

The geometries found gave intermolecular ($O\cdots H_{CH4}$) distances similar to, or shorter than, the sum of the van der Waals radii reinforcing the claim of weak hydrogen bonding interactions. It was also found that the C—H bond of methane generally directs towards the lone pair of the accepting oxygen, symptomatic of hydrogen bonding character. The investigations of trimers and tetramers were particularly promising with binding energies among the highest calculated through the study and the increase in methane to linker ratio causing methane to bind more efficiently.

The functional organic molecules selected in this work can be potentially incorporated into porous structures for enhanced methane capture. There are many examples of metal-organic frameworks containing phenol groups on their backbones[30] as well as $–NO_2$[31] and –COOH[32] groups incorporated in the pore. Carboxylate group has been widely used for the construction of stable porous structures due to its strong coordination ability to metal ions.[186] Although sulfonic and phosphoric acid groups can bind strongly to metal ions, the free forms of these functional groups can still be inserted in metal-organic frameworks by using carboxylate linkers with highly charged metal ions such as Zr(IV) or Hf(IV).[34]

A weak interaction between an aliphatic C—H group and an aromatic π system plays a vital role in molecular recognition for numerous ligand-binding proteins. The interaction has been also used in drug design to increase the inhibitory activity and selectivity. Furthering the understanding of these interactions and quantifying their energetics will have an important influence on the above applications. However, this investigation can only identify functionalised organic molecules that have potential to increase interaction between a porous material and methane molecules. To further develop the understanding of these interactions and the potential of these functionalised groups to enhance intramolecular bonding, studies of MOFs containing the targeted functionalised groups should be carried out, as illustrated in the next section where a series of theoretical MOFs containing the targeted functional group hexabenzocoronene is investigated.[91]

Chapter 5

Methane Adsorption in a Series of MOFs Containing Nanographene Linkers

5.1 Introduction

The ability to tailor and control the density, internal pore volume and the internal surface area of MOFs[61,187] is crucial for utilising these materials in high-capacity gas uptake applications. In this chapter, a new series of MOFs was computationally designed in an effort to increase the surface area and pore volume and therefore improve capacity for methane uptake. The series are (3,24)-connected-{$Cu_2(COO)_4$} paddlewheel-based MOF networks of *rht* topology containing hexabenzacoronene as a central part of the linker. Results confirm that the use of the hexabenzocoronene unit leads to a significant enhancement uptake of CH_4 and other gases for the entire family of MOFs. This suggests that hexabenzocoronene is an excellent candidate for replacing the phenyl ring, a conventional central element of the linkers used in the (3,24)-connected {Cu_2} paddlewheel-based MOFs.[187] An exhaustive computational analysis explores the effects of the dimensions of the proposed hexabenzocoronene-based linkers on the gas storage capacity and other properties of this model family of MOFs, focusing first on the surface area, pore volume, framework density and then moving onto structure-property relationships. Particular attention was focused on the thermodynamic conditions at which the maximum gravimetric and volumetric uptake of CH_4 can occur. A similar computational strategy has been adopted previously by Fairen-Jimenez *et al.*[188] in the study of hydrogen adsorption in hypothetical MOFs with the *rht* topology.

5.2 Structural properties

The structural models are based on the (3,24)-connected network with *rht* topology previously used by Yan *et al.*,[189,190] Nouar *et al.*,[184] Yuan *et al.*,[106,191] and Farha *et al.*[61,187] The *rht* topology has been selected to avoid the interpenetration and/or interweaving that greatly affects the gas sorption properties. The new structures contain vacant sites at each of the Cu(II) ions within the binuclear paddlewheel nodes, which promote binding between the metal and the adsorbate gas molecules. The asymmetric unit of NOTT-112[190] (Figure 5.1a) is used in this work to form the Cu(II) paddlewheel cluster within the *rht* network topology with *Fm3m* group symmetry, and replace the central phenyl core with hexabenzocoronene moiety (Figure 5.1b) to promote the linker elongation and efficient occupation of the void space by guest molecules. As shown in Figure 5.1a and 5.1b, the replacement of the central part in the linker of NOTT-112 with hexabenzacoronene leads to an increase of its dimensions by almost 60%. Seven different linker fragments, labelled L^1-L^7 (Figure 5.1c), have been used with the hexabenzocoronene central element to construct a family of frameworks with *rht* network topology.

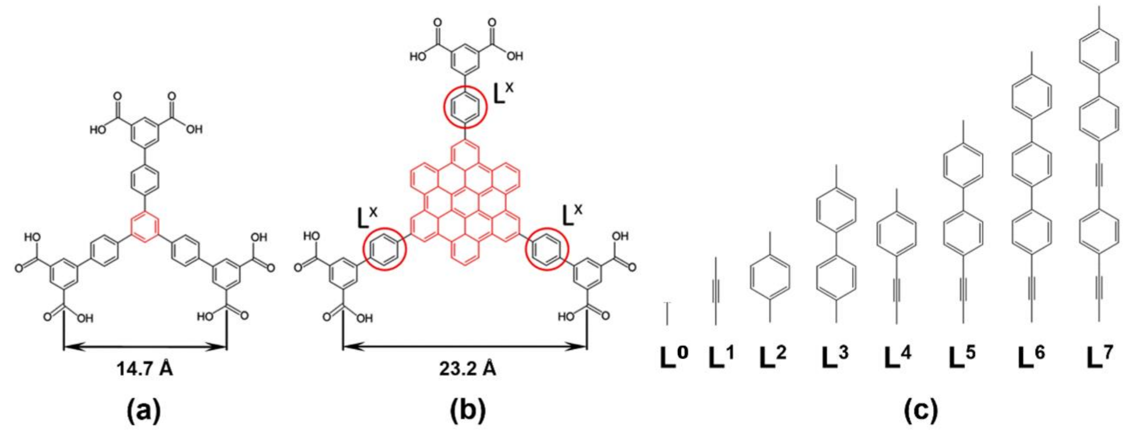

Figure 5.1: Views of (a) organic linker of NOTT-112;[190] (b) organic linker containing hexabenzocoronene and the L^2 fragment; (c) the L^0-L^7 linker fragments.

An additional framework, labelled MOF-L^0, has been built from a hexacarboxylate linker where three isophthalate units are directly connected to the central hexabenzocoronene part. The structures of the designed frameworks have been optimized using molecular mechanics, and their dimensions have been compared to unmodified MOFs containing a phenyl ring as the central core of the linker. The new series exhibit increased surface area and pore volume when compared to experimentally obtained MOF linkers. The structure of a member of the model MOF family, MOF-L^1, containing hexabenzocoronene and the shortest organic linker L^1 with organic branched arms, is shown in Figure 5.2.

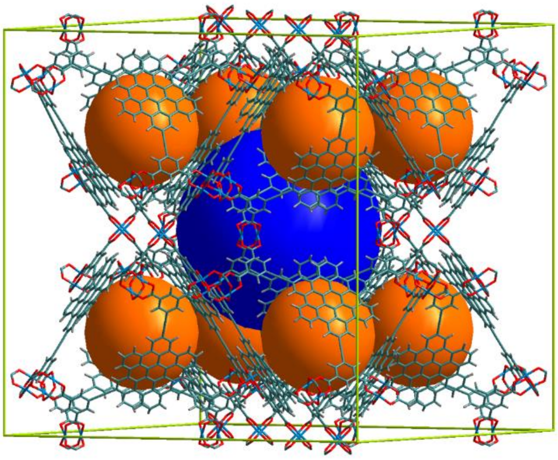

Figure 5.2: View of the structure of model MOF-L[1] containing hexabenzocoronene and the shortest organic linker L[1].

NOTT-112 was chosen a starting point for structure preparation of the series of MOFs studied in this work. The *rht*-network topology, copper paddlewheel cluster and group symmetry of Fm3m were maintained. The series of MOFs were built, and geometry optimization of the structures undertaken using molecular mechanics simulations. These calculations were performed with the Forcite module of Materials Studio.[192] Universal Force Field (UFF) parameters[117] were used for the bonded and non-bonded interactions, with the exception of electrostatic interactions for which the Ewald sum technique was employed.[193] Partial atomic charges were calculated using charge equilibration approach[194] developed by Goddard for use in molecular dynamics simulations. During geometry optimisation the convergence criteria for the maximum change in the length of the unit cell is 0.01 Å. A slightly different approach was used for the largest structure MOF-L^7. Density functional theory calculations were performed to derive the charges, as in Chapter 3, which were then used in the geometry optimization calculation to predict the final structure of MOF-L^7. These were performed on clusters derived from the unit cells and atomic coordinates of MOF-L^7, which included metal ion nodes and the organic linker representative of the respective unit cells (Figure 5.1b). All DFT calculations were performed with the Q-Chem quantum chemistry package[184] at B3LYP level of theory and the 6-31G* basis set. Partial atomic charges were extracted using the CHELPG technique.[123] The final charge values were used for simulation of H_2 and CO_2 sorption. It was noted that through each cycle of optimisations, the differences between partial atomic charges on the atoms within the MOF decreased. This illustrated the structural convergence of the MOF through repeated optimisations. It was also noted that the partial charges on the central hexabenzocoronene part of the linker and also the nodes containing the open Cu(II) sites varied by a very small amount during optimisations. The biggest differences in partial charges were in the areas linking the nodes and central parts of the linker illustrating the structural change that the linker underwent through the optimisations from slightly curved to primarily straight linkers.

Replacement of the central part of the hexacarboxylate with hexabenzocoronene in the (3,24)-connected MOF networks leads to a significant change not only in the dimensions but also in other structural properties of the proposed family of model MOFs. A summary of the structural properties of the MOFs family containing hexabenzocoronene central part, which include the geometric surface area, pore volume, framework density, and unit cell length, is given in Table 5.1.

Table 5.1: The structural properties of the model MOFs family containing hexabenzocoronene molecule as a central linker fragment.

Framework	**Geometric surface area, (m^2/g)**	**Pore volume, (cm^3/g)**	**Framework density, (g/cm^3)**	**Unit cell length, (Å)**
MOF-L^0	2589	1.33	0.61	47.01
MOF-L^1	4172	1.88	0.46	52.93
MOF-L^2	5048	2.40	0.36	59.44
MOF-L^3	5784	3.19	0.28	65.98
MOF-L^4	5784	3.50	0.26	70.06
MOF-L^5	6497	4.52	0.20	76.93
MOF-L^6	7014	6.09	0.15	87.93
MOF-L^7	7514	7.42	0.12	94.68

The Brunauer-Emmett-Teller (BET) surface area of NOTT-112 is reported to be 3800 m^2/g,[190] whereas the surface area of MOF-L^2 is 5048 m^2/g, approximately 33% increase upon modification of the central element of the linker. The model MOF-L^3 framework, which has been obtained by replacing the central element of the NOTT-119[189]/PCN-69[191] linker with hexabenzocoronene, also exhibits an enhanced geometric surface area of 5784 m^2/g, which compares favourably with the surface area of unmodified NOTT-119 (BET surface area of 4118 m^2/g)[189] and PCN-69 (BET surface area of 3989 m^2/g).[191] Similar increase in the surface area has been achieved in MOF-L^4 (5784 m^2/g), whose structure can be compared to that of the unmodified NOTT-116 (BET surface area of 4664 m^2/g)[189] and PCN-68 (BET surface area of 5109 m^2/g)[106] MOFs, and in MOF-L^1 (4172 m^2/g), which can be compared to the unmodified PCN-61 (3500 m^2/g)[195] MOF.

An alternative way to compare the proposed model family of MOFs with existing unmodified structures (right panel of Figure 5.3) are presented against the modified model MOFs with the identical central part (highlighted in blue, left panel), which was decorated by an additional nine benzene rings. The optimised length of the cubic unit cell of MOF-L^2 is calculated to be 59.44 Å, which is comparable to the unit cells of the isoreticular MOF structure designed by Fairen-Jimenez *et al*. using the L^3 fragment[188] (58.32 Å), NOTT-119[189] (56.30 Å) and PCN-69[191] (59.15 Å simulation; 56.61 Å experiment). A discrepancy between the model and experimental values of the length of unit cell might be due to the fact that organic linkers in the computationally designed MOFs remain predominantly straight, while the linkers of PCN-69[191] and NOTT-119[189] bend to a certain extent.[191] The geometric surface areas of the model MOFs are also similar: 5049 m^2/g for MOF-L^2 and 5194 m^2/g for the model MOF designed by Fairen-Jimenez et al. using the L^3 fragment;[196] however, the BET surface area for the synthesised MOFs is somewhat smaller, e.g., 4118 m^2/g for NOTT-119,[186] and 3989 m^2/g for PCN-69.[197]

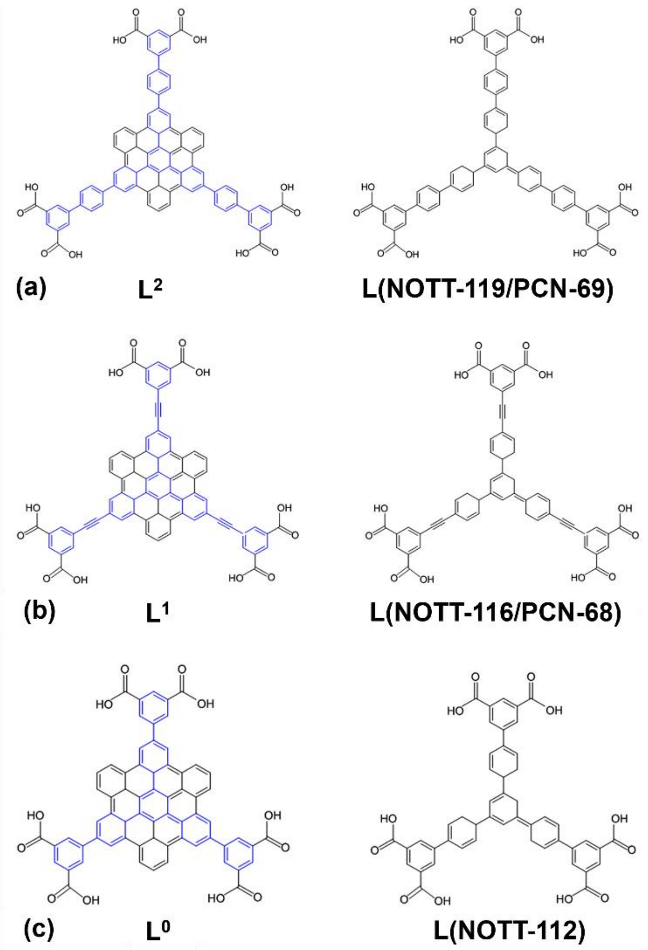

Figure 5.3: Comparison of linker geometries of three members of the proposed model MOFs family, based on hexabenzocoronene molecule, with existing experimental MOFs: a) model MOF-L^2 and NOTT-119[189]; b) model MOF-L^1 and NOTT-116[189]; c) model MOF-L^0 and NOTT-112.[190]

The model MOF-L^1 framework shown in Figure 3 has a basic structure similar of the existing unmodified existing frameworks NOTT-116[189] and PCN-68[106] and the model MOF designed by Fairen-Jimenez *et al*. using NOTT-112 and the L^4 fragment.[188] The optimised length of the unit cell of MOF-L^1 is predicted to be 52.93 Å, in good agreement with the available experimental (52.74 Å in PCN-68[106]) and computational data (53.73 Å in the model MOF[188] based on NOTT-112 and L^4 fragment). Such good agreement between the experimental data is observed because the organic linkers in these MOFs are entirely straight.

However, the predicted geometric surface area for MOF-L^1 (4171.97 m^2/g) is smaller than the BET surface area for NOTT-116[189] (4664 m^2/g), BET surface area for PCN-68[106] (5109 m^2/g) and the geometric surface area for the model MOF designed by Fairen-Jimenez *et al.* using NOTT-112 and the L^4 fragment[188] (5033 m^2/g). Finally, the smallest MOF-L^0 framework can be directly compared to NOTT-112. The unit cell length of 47.01 Å in MOF-L^0 is exactly the same as the one experimentally obtained for NOTT-112,[190] although the geometric surface area of MOF-L^0 (2589 m^2/g) is lower than the BET surface area of NOTT-112 (3800 m^2/g).[190] The comparison method used in Figure 5.3 shows MOF structures of very similar dimensions, but the estimation of their accessible surface area depends very strongly on the method and type of a probe used.

The largest MOF of the proposed family, MOF-L^7, exhibits a surface area of 7514 m^2/g, which exceeds the largest BET surface area reported in experiment to date in this series, that of NU-109 (7000 m^2/g).[187] The MOF-L^7 framework density of 0.12 g/cm^3 is also at the limit close to the lowest calculated density for porous crystals reported for the MOF-399 compound (0.126 g/cm^3).[198] The remaining members of the proposed family exhibit structural properties comparable with typical values achieved in the synthesis of ultrahigh porosity MOFs.[188] A longer organic linker typically provides larger void space and a greater number of adsorption sites within a framework. However, linkers with a very large number of phenyl repeat units make a MOF liable to structure interpenetration, poor solubility, low synthetic yields, and cumbersome purification protocols. The use of MOFs with the *rht* topology, based on a singular net for the combination of 3- and 24-connected nodes, removes any concern for catenation (interpenetration or interweaving of multiple frameworks) and makes them an ideal target in design of ultrahigh porosity. The desolvation and associated activation using supercritical CO_2 and solvent exchange and processing[187,189] is a particularly promising method that allows generation of MOFs with ultrahigh surface areas.

5.3 Gas uptake performance

Grand Canonical Monte Carlo simulations have been used to predict CH_4 uptake in the model MOF structures at T = 273 K and T = 298 K and for pressures up to 70 bar. The gravimetric and volumetric sorption isotherms of the model MOFs for CH_4 uptake are presented in Figure 5.4, and the summary of sorption data at 35 and 70 bar is given in Table 2. At 273K and 70 bar, the model MOF structures with the L^3-L^7 linker fragments show a significant gravimetric uptake exceeding 50 wt%. The model MOF-L^7 with the longest linker exhibits the highest absolute gravimetric uptake of 78 wt%. Whereas MOF-L^7 has extremely large pore openings, the dimensions of MOF-L^4 are comparable to those of NOTT-119[189]/PCN-69[191], which have been synthesized successfully. As the computational isotherms correspond to a perfect structure with no impurities or pore collapse, the uptake values for CH_4 shown in Figure 5.4 can only be considered as the upper limit. Various structural defects or collapsed regions that may occur naturally in experimental samples will lower these theoretical estimates. On a volumetric basis at high pressures the structures exhibit the opposite trend so that the lowest volumetric uptake of CH_4 (138.24 cc cc^{-1} at T = 273 K and 70 bar) corresponds to the structure with the longest linker, MOF-L^7.

Figure 5.4: Calculated adsorption isotherms for CH_4 in model MOFs with the L^0-L^7 organic linkers: gravimetric (top) and volumetric (bottom) results at T=273 K (left) and T=298 K (right).

On the other hand, the framework with no linker fragment, L^0, exhibits an impressive volumetric uptake of CH_4 of 273 cc cc^{-1} at 273K and 70 bar, although the gravimetric uptake of this MOF is only 32 wt% at these conditions. At 298 K, the overall trend remains the same confirming that the model MOFs with short linkers achieve high volumetric but low gravimetric sorption, but the MOFs with long linkers exhibit a low volumetric and high gravimetric uptake for CH_4. In general, low volumetric uptake is a consequence of the low density of MOFs.

MOFs with the linkers L^1 and L^2 underperform systematically in both volumetric and gravimetric metrics. An increase in temperature at constant pressure makes the overall CH_4 uptake performance worse so that only three structures exceed the gravimetric uptake of 50 wt%, namely MOF-L^7 with 63.5 wt%, MOF-L^6 with 59 wt% and MOF-L^5 with 50 wt% gravimetric uptakes (see Table 5.2 for further details). The volumetric uptake also decreases with increase of temperature in all considered model MOF structures. It can be generally observed at 298 K and 70 bar that the model MOFs L^2-L^7 show higher gravimetric uptake than NU-111 (36 wt%)[199], PCN-68 (35 wt%)[106] and NOTT-119 (30 wt%)[189] reported in the literature. The observed strong temperature dependence on CH_4 uptake may potentially provide an efficient tool for gas uptake and subsequent release.

Table 5.2: Summary of CH_4 sorption characteristics in MOF-L^0 - MOF-L^7 calculated at T = 273 K and T = 298 K and the pressures of 35 bar and 70 bar.

	70 bar				**35 bar**			
	T=273 K		**T=298 K**		**T=273 K**		**T=298 K**	
	wt%	**V/V, cm^3/cm^3**	**wt%**	**V/V, cm^3/cm^3**	**wt%**	**V/V cm^3/cm^3**	**wt%**	**V/V cm^3/cm^3**
MOF-L^0	32.0	273	28.5	243	28.0	239	23.8	203
MOF-L^1	39.4	254	33.7	2167	31.5	203	25.1	162
MOF-L^2	44.7	241	39.5	199	34.7	175	26.6	134
MOF-L^3	53.7	208	43.2	167	34.3	133	26.2	102
MOF-L^4	57.2	204	46.0	164	36.3	129	27.9	99
MOF-L^5	62.7	177	50.0	141	36.8	104	28.7	81
MOF-L^6	71.8	153	57.9	124	40.6	87	32.2	69
MOF-L^7	78.0	138	63.5	113	43.1	76	34.9	62

As Table 5.2 and Figure 5.4 confirm, for a constant temperature the CH_4 uptake is lower at 35 bar than that at 70 bar. At 35 bar and 273 K the model MOF-L^7 framework shows the highest gravimetric uptake of 43.1 wt%, whereas the highest volumetric uptake of 239 cc cc^{-1} is shown by MOF-L^0.

GCMC simulations have also been performed to predict CO_2 and H_2 sorption in the largest framework of the considered model MOF family, MOF-L^7.

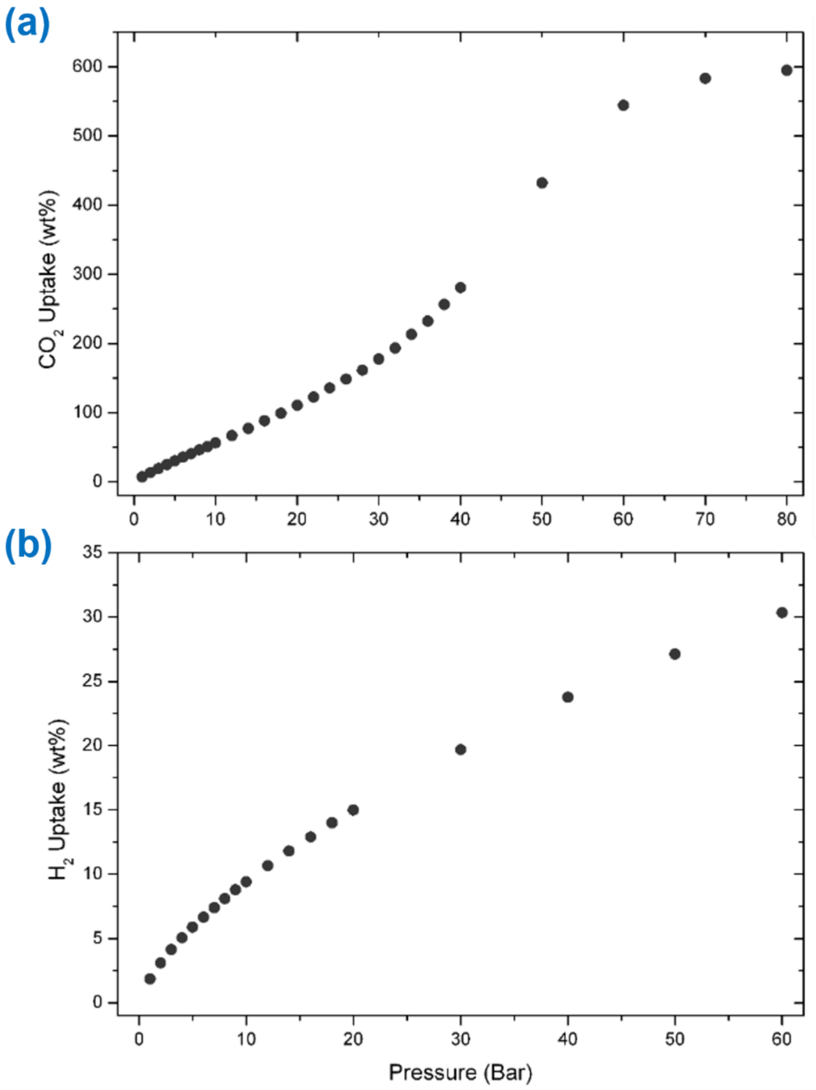

Figure 5.5: Adsorption isotherms in the model MOF with the **L**^{7} organic linker calculated for (a) CO_2 at T = 298 K and (b) H_2 at T = 77 K.

Simulation of CO_2 sorption (Figure 5.5) reveals a high CO_2 storage capacity for MOF-L^7 at 298 K, 80 bar of 595 wt%. Due to its very large pore size MOF-L^7 is not suitable for the CO_2 sorption at low pressures, but at high pressures a stepwise behaviour in the adsorption isotherm is observed, and a significant amount of CO_2 is adsorbed in the structure. Therefore, pressures suitable for CO_2 storage in these structures must be higher than 70 bar. The highest experimental values for total CO_2 uptake achieved so far have been reported for NU-100 (232 wt%)[61] at 40 bar and 298 K and MOF-210 (248 wt%)[200] at 50 bar and 298 K. The uptake of 30.4 wt% for

H_2 gas in MOF-L^7 has been obtained at 60 bar and 77 K, and is a value that is twice greater than the known experimental values for the best performing MOFs with NU-100 and MOF-210 showing total H_2 uptakes of 16.4 wt%[61] and 16.7 wt%,[200] respectively.

5.4 Conclusions

A family of model MOFs based on the (3,24)-connected MOF networks with the *rht* topology has been proposed in which the central part of the organic linker has been replaced with hexabenzocoronene molecule. An exhaustive multiscale computational analysis allows not only prediction of the physical and chemical properties of the proposed MOFs family, but also a direct comparison of the model structures with existing MOFs of similar structure. It has been shown that a replacement of the central linker fragment with hexabenzocoronene molecule significantly increases the size and gas uptake capability of the entire MOFs family with *rht*-network topology. The presence of the central hexabenzocoronene increases the geometric surface area not only through the provision of additional benzene rings but also by providing extra rigidity to the linker skeleton. The structure optimization of the model MOF-L^0 and MOF-L^1 frameworks shows a good agreement with the available experimental data for the MOFs with similar structure and straight linkers, such as NOTT-112[190] and NOTT-116[189]/PCN-68.[106] However, the calculated surface area of MOF-L^4 is predicted to be somewhat larger than the surface area of NOTT-119[189] and PCN-69[191], despite the fact that the linkers in these MOFs have similar length and structure. This is because in the calculations the linker fragments remain straight in model MOFs with hexabenzocoronene molecule whereas the linkers of NOTT-119[189]/PCN-69 are bent.

The GCMC simulations of CH_4 uptake have been performed on the optimised MOF structures at pressures up to 70 bar and at two temperature values, T = 273 K and T = 298 K. This study confirms that a number of the designed MOFs formally reach the DOE targets[201] for CH_4 storage, but none of the proposed MOFs achieves both gravimetric and volumetric uptake targets. In addition to CH_4 storage capability, the GCMC simulations of CO_2 and H_2 have been performed for the largest family member, MOF-L^7, which exhibits outstanding sorption properties at high pressures. Following the positive conclusions of this work, experimental efforts are being made to synthesise MOFs containing hexabenzocoronene within the core of the linker. Although no successful synthesis has yet been carried out, this illustrates how the computational study of theoretical MOFs can guide experimental studies. Overall, it has been demonstrated that a replacement of the central fragment with hexabenzocoronene molecule is a viable linker modification method, which might have the potential in enhancement of gas uptake for CH_4 and other gaseous molecules.

Chapter 6

Gas-Sorbent Interactions within Copper MOFs MFM-160 and MFM-188

6.1 Introduction

Understanding the mechanism of gas-sorbent interactions is of fundamental importance for the design of improved gas storage materials. In this chapter, two new copper MOFs, MFM-160[92] and MFM-188[93] and their interactions with CO_2, CH_4 and various hydrocarbons are investigated. The studies aim to and reveal the importance of the combination of functional groups, open metal sites and appropriate pore geometry in improving MOF-substrate interactions for gas uptake and storage.

The use of MOFs containing polar functional groups such as amines and amides has proved effective for uptake of CO_2 at low pressure, whilst MOFs with very large surface areas have shown exceptional storage capacity for CO_2 at higher pressures.[24,195,202–204] The amide group (-OCNH-) is of particular interest because it offers dual-functionality from both CO- and NH- sites. Notably, the introduction of amide groups in MOFs has been reported to strengthen the host-guest interactions in MOFs.[27,202,205] However, experimental observation of the precise role of amides in guest binding in MOFs is still largely lacking. Triazine also offers interest and has been used as a core to great effect in MOFs with high CO_2 uptake[206,207] as well as in MOFs capable of selectively adsorbing C_2 hydrocarbons over CH_4.[6,8]

Here the crystal structure and gas uptake properties are reported for the (3,24)-connected Cu^{II} MOF, MFM-160 and the tetra-amide tetra-isophthalate Cu^{II} complex MFM-188, designed for both high CO_2 uptake and selective sorption of C_2

hydrocarbons over methane. Gas binding is investigated by a combination of DFT studies and ^{2}H NMR studies carried out by the Manchester Schröder group in MFM-160, and DFT studies with neutron powder diffraction (NPD) and inelastic neutron scattering (INS) carried out by the Schröder group in MFM-188. These crystallographic and dynamic experiments successfully establish a detailed molecular mechanism for guest binding within these MOF structures.

6.2 Results and discussion: MFM-160

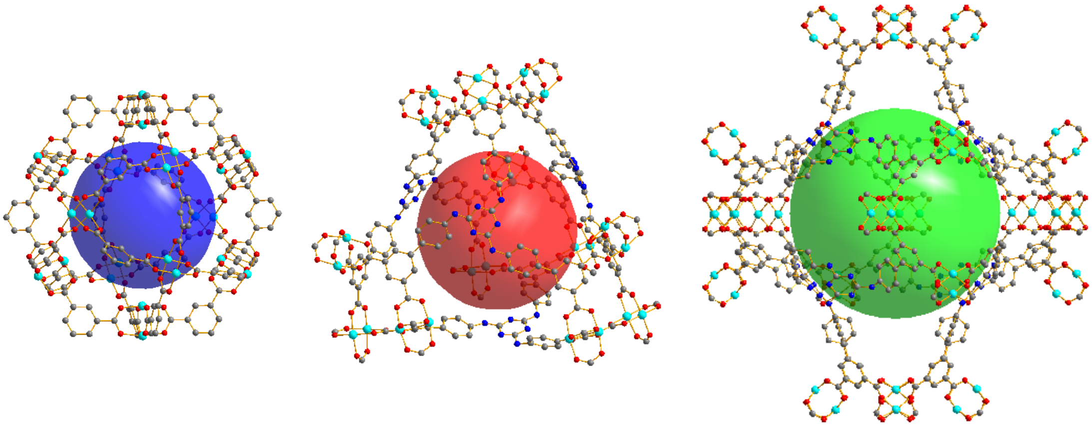

Figure 6.1: Cages A, B and C in MFM-160.

As synthesised MFM-160 is a (3,24)-connected framework of *rht* topology containing three distinct cages, A, B and C (Figure 6.1). Cage A is a truncated cuboctahedron formed from 12 $\{Cu_2(O_2CR)_4\}$ paddlewheel units and the isophthalate terminus of 24 different hexacarboxylate H_6L linkers (Figure 6.2). The spacing between cuboctahedra is determined by the distance between isophthalate moieties on neighbouring arms of the linker. This results in the formation of the larger cages B (truncated tetrahedron) and C (truncated cube).

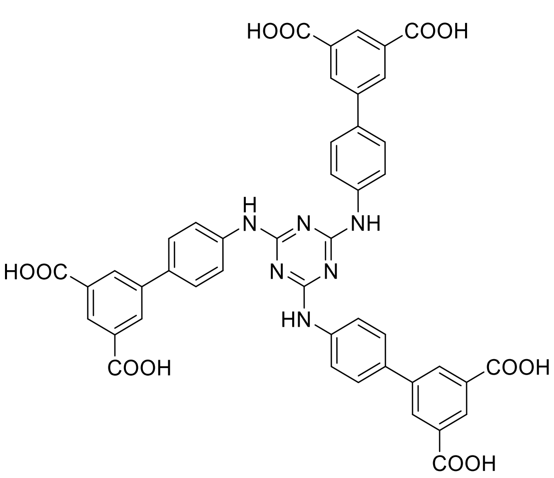

Figure 6.2: Structure of H_6L hexacarboxylate linkers in MFM-160.

The potential accessible volume of desolvated MFM-160 is 77%, as calculated by the VOID algorithm within the software PLATON[208] (after removal of all guest solvates and coordinated water molecules) with a calculated crystal density of 0.540 g cm^{-3}. The permanent porosity of the framework was confirmed *via* an N_2 sorption isotherm measured volumetrically at 77 K which indicated reversible type-I behaviour and an uptake of 983 cc g^{-1} (123 wt%) at 1 bar (Figure 6.3). The slight changes in gradient in the range 30 – 120 mbar are assigned to the sequential filling of the microporous and mesoporous cages. The estimated Braun-Emmett-Teller (BET) surface area of MFM-160a as calculated from this isotherm was 3847 m^2 g^{-1}, with a total pore volume of 1.52 cm^3 g^{-1}.

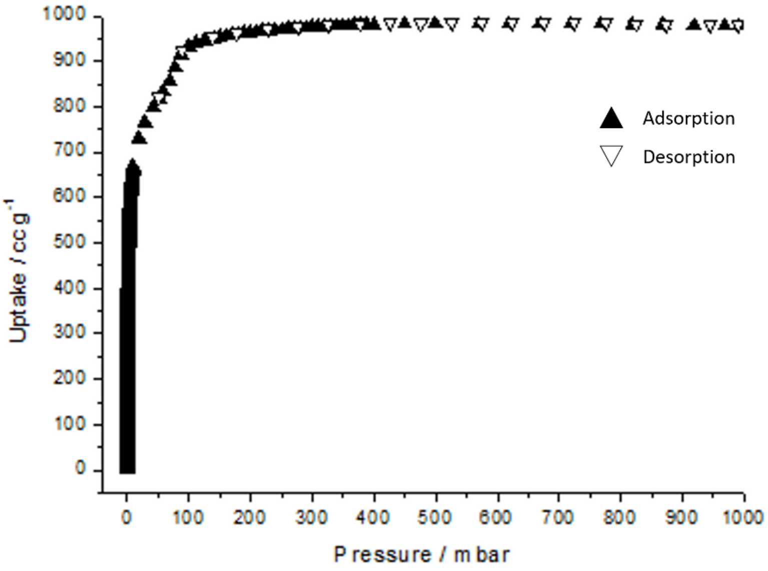

Figure 6.3: N_2 isotherm for MFM-160 at 77 K from 0-1 bar.

6.21 0-20 Bar gas sorption isotherms

High pressure (0-20 bar) gravimetric isotherms were performed using CO_2 and CH_4 at 298 K and 273 K (Figure 6.4) and at 77 K and 87 K for H_2. MFM-160 shows exceptional capacity for CO_2 storage at 20 bar with 558 cc g^{-1} (110 wt%) and 719 cc g^{-1} (141 wt%) uptake at 298 K and 273 K respectively. This unsaturation uptake of CO_2 at 298 K is one of the highest reported to date: to the best of our knowledge the current record uptake under these conditions is 627 mmol g^{-1} (123 wt%) in MOF-177.[203] At 195 K and 1 bar MFM-160 nears saturation at 881 cc g^{-1} (173 wt%). CH_4 uptake at 20 bar was 199 cc g^{-1} (14.2 wt%) at 298 K and 274 cc g^{-1} (19.6 wt%) at 273 K.

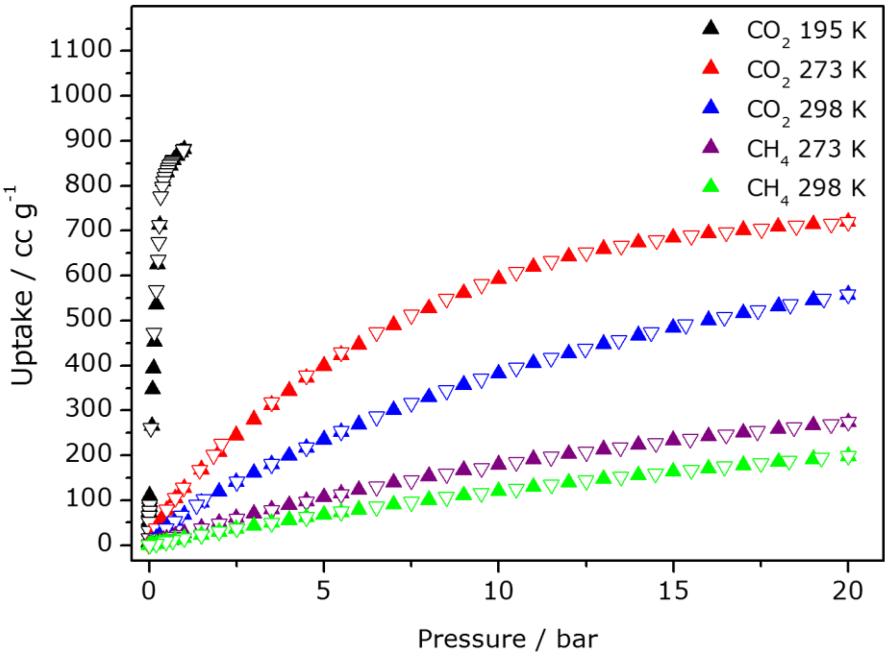

Figure 6.4: CO_2 and CH_4 isotherms for MFM-160 from 0-20 bar (filled triangles: adsorption; open triangles: desorption).

6.22 Low pressure hydrocarbon sorption isotherms

Low pressure (0-1 bar) isotherms of C_2 hydrocarbons were run at 273 K and 298 K for comparison with the data obtained for CH_4. As shown in Figure 6.5, the uptakes of C_2H_2, C_2H_4 and C_2H_6 at 273 K are 212.3 cc g^{-1} (24.68 wt%), 175.2 cc g^{-1} (21.94 wt%) and 201.3 cc g^{-1} (27.02 wt%) respectively. At 298 K these values become 127.8 cc g^{-1} (14.85 wt%), 115.0 cc g^{-1} (14.40 wt%) and 110.0 cc g^{-1} (14.76 wt%). Whilst these capacities are slightly lower than those reported with similar materials,[6,8] the extremely low uptake of CH_4 at 1 bar (15.3 cc g^{-1} at 298K, 27.1 cc g^{-1} at 273 K) in MFM-160 makes the material of great interest for selective separation of C_2 hydrocarbons over CH_4.

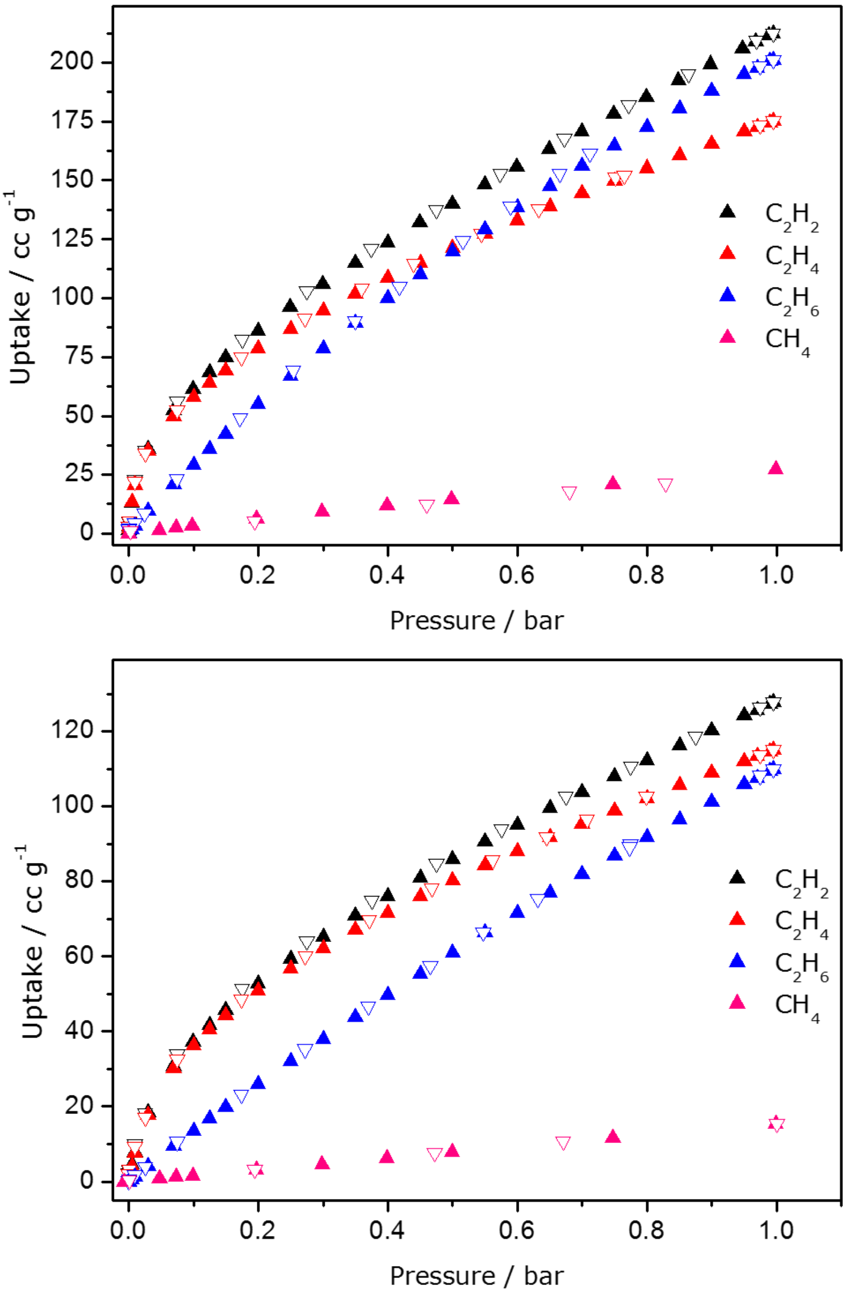

Figure 6.5: Hydrocarbon isotherms for MFM-160 from 0-1 bar at 273 K (top) and 298 K (bottom).

To estimate the selectivity of each hydrocarbon over CH_4 Henry's law was employed, in which constants (K_H) were determined using a virial fit of the measured isotherm data (See Appendix Figures A.1 to A.10). Using these constants, the selectivity (S) of one gas, *i*, over the second gas, *j*, was determined from Equation 2.70 as discussed in Chapter 2.

The selectivities for C_2H_2:CH_4, C_2H_4:CH_4 and C_2H_6:CH_4 at 273 K were calculated to be 104:1, 130:1 and 10:1 respectively. At 298 K this becomes 79:1, 70:1 and 9:1 respectively. To the best of our knowledge the C_2H_2:CH_4 separation of 79:1 at 298 K is the third highest reported for a MOF (for Cu-TDPAT[6] it is 127:1 and for Cu-TDPAH[8] 81:1). Notably this is significantly higher than the selectivities reported for smaller-pore Cu MOFs such as UTSA-50a[16] and UTSA-15a[18] (68:1 and 56:1 respectively). The C_2H_4:CH_4 separation in MFM-160a at 298 K is second-highest only to that for Cu-TDPAT (85:1).[6]

The selectivity for C_2H_2 over CO_2 (15:1 at 298 K; 16:1 at 273 K) demonstrates the potential of MFM-160 for the purification of acetylene, in which CO_2 is a common impurity. A study by Li *et al.*[209] strongly suggested that the presence of N atoms within MOF channels does not improve selectivity for C_2H_2 over CO_2. Thus, in the case of MFM-160, we attribute this selectivity to the greater vdW interactions between the framework and the slightly larger C_2H_2 molecules, as described by Samsonenko and co-workers for selective uptake of C_2H_2 over CO_2 in porous formates.[210] The separation of CO_2 from C_2H_2 is notoriously difficult as a result of their similar size and sublimation points:[211] accordingly the high selectivity for C_2H_2 over CO_2 is a very promising finding. This work represents the second highest selectivity for a metal-organic framework for this separation, exceeded only by $Cu_2(pzdc)_2(pyz)$, reported by Matsuda *et al.* in 2005 (C_2H_2:CO_2 = 26:1 at 11 mbar and 270 K).[212] However, the saturation uptake of C_2H_2 in $Cu_2(pzdc)_2(pyz)$ is just 42 cc g^{-1} in comparison to 212 cc g^{-1} in MFM-160 at 1 bar and 273 K. It should be noted that re-running of these isotherms gives identical results, showing the stability of MFM-160 to repeated activation and re-use.

6.23 Heats of adsorption

Isosteric heats of adsorption (Q_{st}) for each gas were calculated using a virial method to fit the sorption isotherms at 273 K and 298 K. The zero-loading heats of adsorption for CO_2, C_2H_2, C_2H_4 and C_2H_6 are 30.04, 36.65, 35.69 and 23.76 kJ mol^{-1}, respectively. Each has a higher zero-loading Q_{st} than CH_4 (23.11 kJ mol^{-1}) which, in common with the work reported by Liu *et al.*[8] on Cu-TDPAH, we tentatively assign to be a result of increased vdW and electrostatic interactions between the larger gas molecules and the framework, contributing to the observed selectivity for C_2 hydrocarbons over CH_4. The Q_{st} values follow the same pattern as the selectivities at 298 K ($C_2H_2 > C_2H_4 >> C_2H_6$), although at 273 K the C_2H_4:CH_4 selectivity is greater than the C_2H_2:CH_4 selectivity (130:1 *versus* 104:1).

6.24 Solid state ^{2}H NMR studies of activated and gas-loaded MFM-160

In order to gain a greater understanding of the C_2H_2:CO_2 separation and of the behavior of both gases within the MOF, ^{2}H-NMR studies were carried out on a partially deuterated analogue of MFM-160, denoted MFM-160-d_{12} (Figure 6.6). Phenyl ring dynamics can affect the adsorption properties in two ways: firstly, the phenyl rings themselves provide an accessible adsorption site as a result of the aromatic π-system; secondly the phenyl rotation directly affects the effective MOF pore size and geometry. Probing the framework dynamics is also of interest for comparison with other known MOFs, thus improving the knowledge of carboxylate-based MOF structure-property relationships.

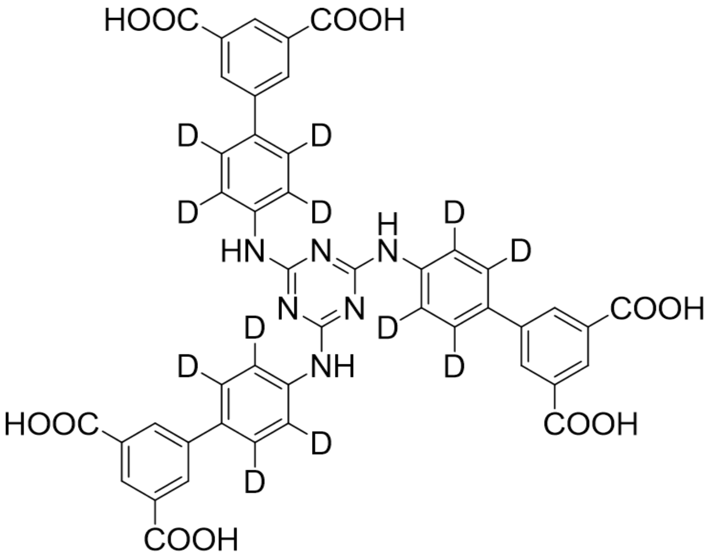

Figure 6.6: Partially deuterated analogue of MFM-160, MFM-160-d_{12} used for ^{2}H-NMR studies

The investigation of structural dynamics in MFM-160-d_{12} was probed in the activated material, in the presence of CO_2 (1 bar and 5 bar loadings) and in the presence of C_2H_2 at 0.32 bar and 1 bar. As the low pressure uptake of C_2H_2 is significantly higher than that of CO_2, respective pressures of 0.32 and 1 bar were chosen for an equimolar comparison between the two gases. The loading of 0.32 bar C_2H_2 and 1 bar of CO_2 each correspond to ~3.1 gas molecules per linker, where the empirical formula of MFM-160-d_{12} = 1043.43 g mol^{-1} (the mass of Cu_3L-d_{12}). The higher loadings of 1 bar C_2H_2 and 5 bar CO_2 correspond to 5.9 and 10.8 molecules per linker respectively. The solid state ^{2}H NMR results (experimental and simulated) for the activated material is shown is Figure 6.7 while the results for CO_2/C_2H_2 loaded materials are shown in the Appendix figures A.11 - A.15.

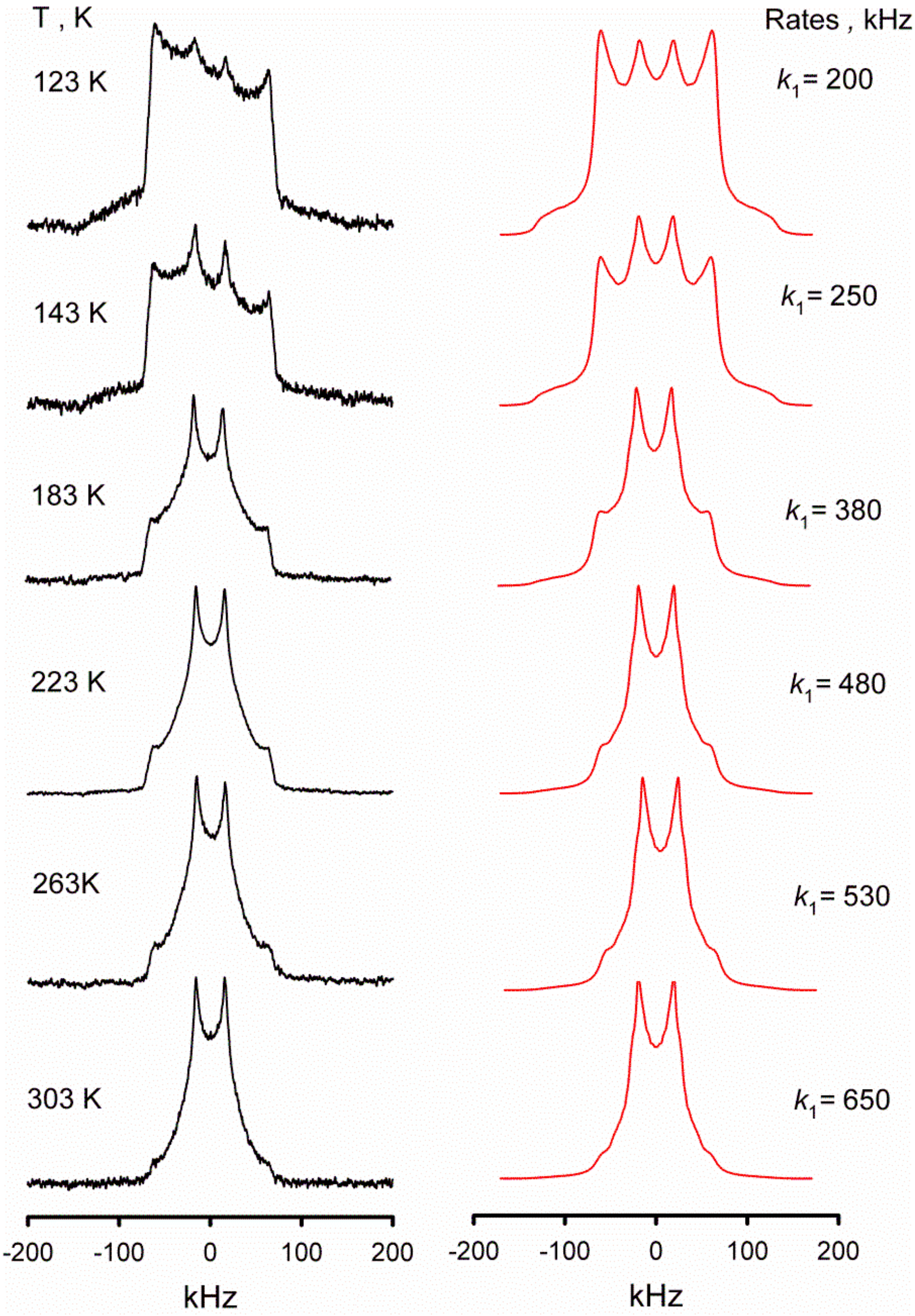

Figure 6.7: Temperature dependence of ^{2}H NMR line shape for the phenyl fragments in guest-free MFM-160-d_{12} (experimental - left, simulation - right).

In activated MFM-160-d_{12}, the temperature-dependent behaviour of the ^{2}H NMR spectra line shapes shows that the deuterated phenyl rings are mobile due to a similar phenomenon that has been reported for UiO-66.[213] Results indicate that the phenyl motion at each given temperature is characterised by a distribution of rotation rates, which suggests that the rotational potential fluctuates to a certain degree across the framework.

Considering the C_2 symmetry of the phenyl fragment, the uniaxial rotation around the C_2 axis can be modeled either by a 4-site, or a 6-site jump rotation model (Figure 6.8). It should be noted that the larger number of possible jump sites in most cases of an axial rotation can be effectively modelled by the 6-site jump model.[214] The comparison between the two models and the experimentally observed ^{2}H NMR patterns show that only the 6-site jump rotation gives a proper agreement with our data.

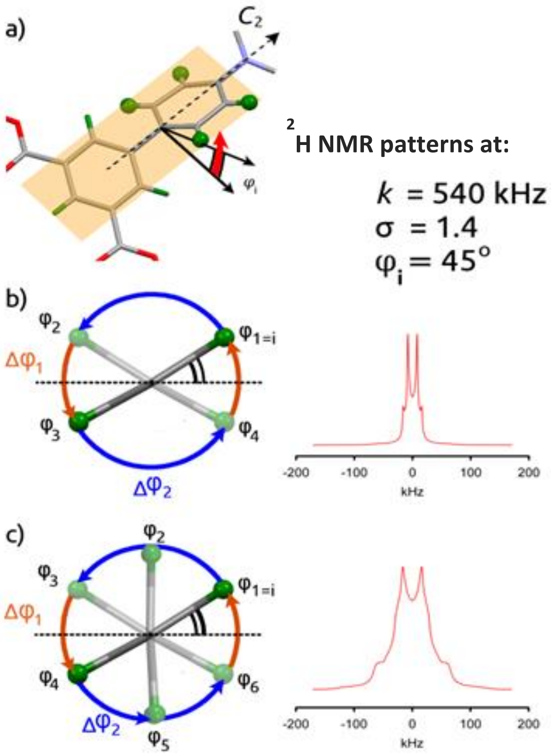

Figure 6.8: The scheme of stable phenyl ring orientation sites depending on the jump rotation model: (a) The staring position of the mobile phenyl ring plan is tilted by and axial angle φ_i. The axial jump-rotation about the phenyl group's C_2 symmetry axis is then realised by either (b), an n = 4 site exchange motion, or by (c), an n= 6 site exchange. The distribution of the orientation sites is governed only by the value of the first position $\varphi_1 = \varphi_i$. All elementary jumps are assumed to be governed by the same rate constant $k = k_1/n$. Even in the case of the same value of φ_i in the intermediate jump rate the two models give qualitatively distinct patterns.

Although the distribution of the jump sites has to obey the C_2 symmetry, the initial position of the phenyl orientation might be distorted from a fully homogeneous case (Figure A.16). This distortion is easily introduced into the reorientation model as an angular parameter φ_i. For a 6-site jump rotation mechanism the jump positions are thus given as follows: $\varphi_1 = \varphi_i$, $\varphi_2 = \pi/2$, $\varphi_3 = \pi - \varphi_1$, $\varphi_4 = \pi + \varphi_1$, $\varphi_5 = \pi/2$, $\varphi_6 = \pi + \varphi_2$. Within such a model we assume that all positions have equal probability. In our model, the angle $\varphi_i = 45^\circ$, where φ_i is the angle between the plane of the mobile phenyl ring and the plane of the aromatic ring fixed to the Cu(II) node. Thus it follows that the value $\Delta\varphi_1 = 2\varphi_i$ can be directly compared with the crystal structure observations. The kinetic component of the model is generally complex, with multiple rate constants defining each elementary jump exchange. However, in this case we have found that a simple kinetic matrix defined by one rate constant is sufficient to provide good agreement with the experimental observations.

This 6-site jump rotation model accurately simulates the experimental temperature dependence of the ^{2}H NMR spectra line shape. The $\Delta\varphi_1 = 2\varphi_i \sim 90^\circ$ is consistent with the crystallographic data and underlines that the orientation of the phenyl rings is not homogeneously distributed. The log-normal distribution width is almost constant over the temperature and is $\boldsymbol{\sigma} \sim 1.3$-$1.4$. Thus the present inhomogeneity is considerably lower than that observed in UiO-66 and may be attributed to the flexible nature of MFM-160.

The most striking features of the ^{2}H NMR spectra for MFM-160-d_{12} are the kinetic parameters of the deuterated phenyl motion; the Arrhenius plot (Figure 6.9) is linear and shows an activation barrier, $E_0 = 2.1$ kJ mol^{-1} and the collision factor, $k_{00} = 1.4\text{x}10^6$ Hz. Such small values are in great contrast to those reported previously for any other solid state material previously reported and have been confirmed for many different samples of MFM-160-d_{12}. In fact, the activation barrier is comparable with the torsional barrier for methyl groups in xylenes or 2-methylimidazole, *i.e.* aromatic systems where the internal steric interactions are minimised. The torsional barrier for methyl groups in these compounds was measured experimentally by using neutron scattering techniques and ^{2}H NMR spectroscopy which have shown that in both cases E_0 does not exceed 1.5 kJ mol^{-1}.[215,216]

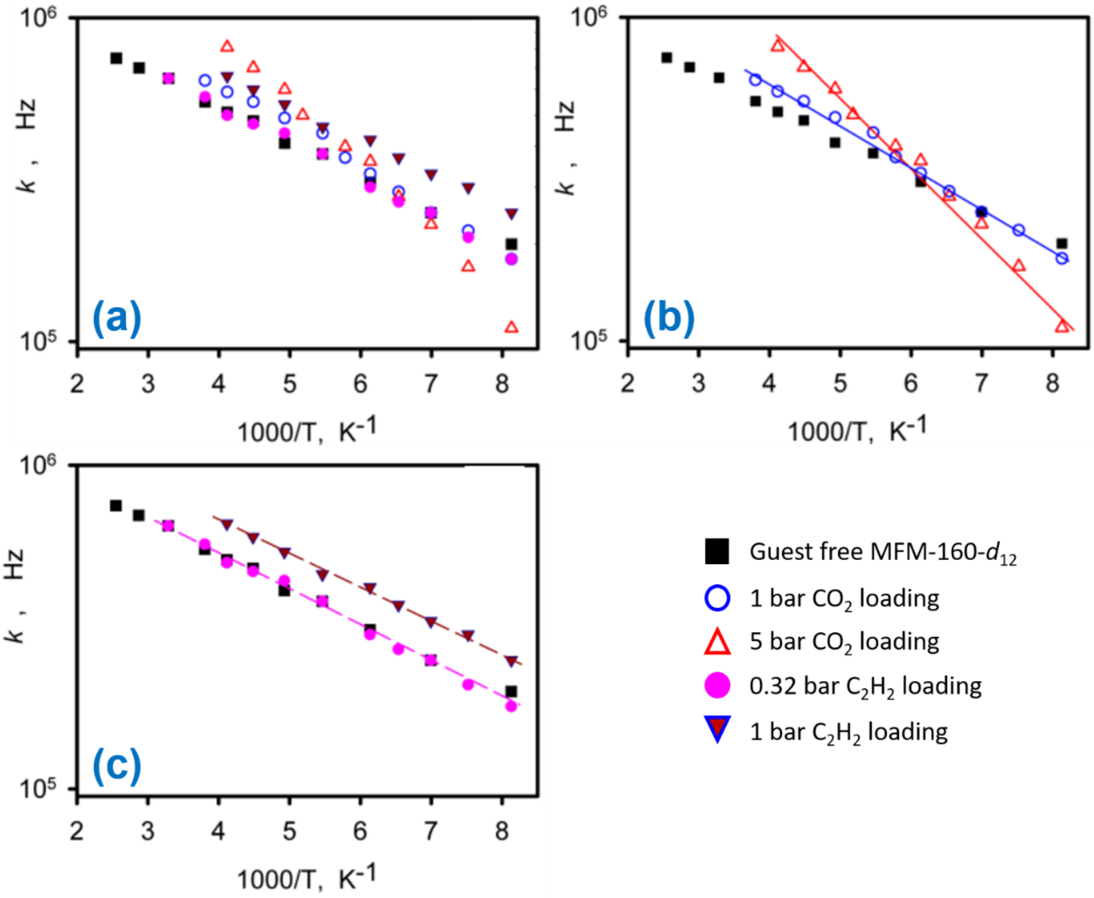

Figure 6.9: Arrhenius plots of the rotation rate constants k_1: a) Arrhenius plot of all gas-loaded samples, b) Arrhenius plot of CO_2-loaded MFM-160 and c) Arrhenius plot of C_2H_2-loaded MFM-160. All gas loadings were performed at 298 K.

In this regard it is interesting to consider the possible sources of steric interaction hindering phenyl rotation in MFM-160 (Figure 6.10 a). The electrostatic interactions are maximized when all aromatic rings are in one plane, in which case the closest interatomic distances are: d_1 ~ 2.2 Å, d_2 ~ 3.1 Å and d_3 ~ 2.0 Å. Therefore, the main interaction is likely governed by sites III and I. These distances do not offer an obvious explanation for the ultra-low value of k_{00} (usually ~ $10^{11\text{-}13}$ Hz in MOF materials). However, this may be attributable to a short intramolecular hydrogen bond (1.91 Å) between the phenyl protons and the triazine N atoms observed in the crystal structure (Figure 6.10 b) restricting the rotation of the ring.

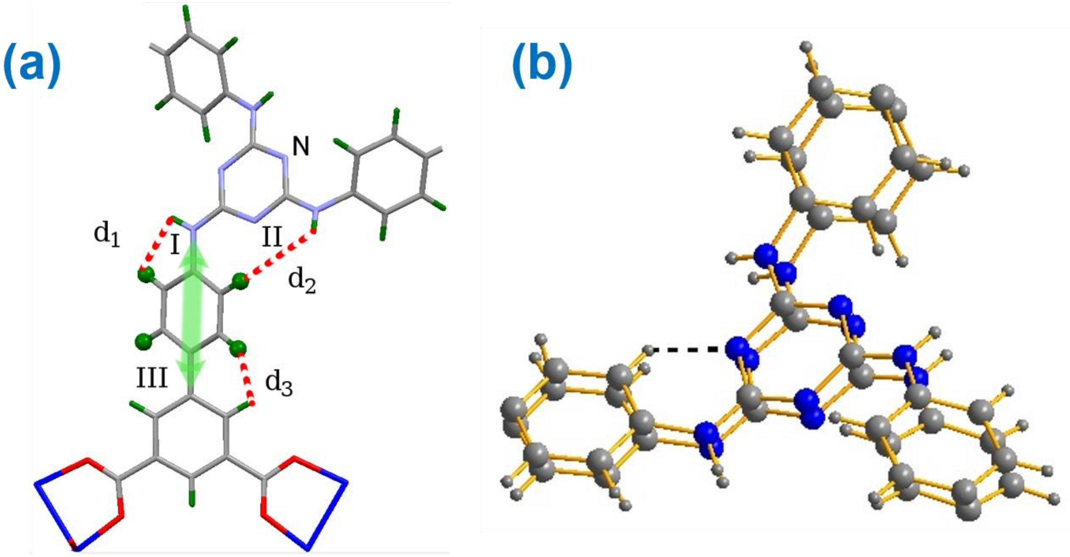

Figure 6.10: Interactions within MFM-160 (a) view of the deuterated (green) mobile phenyl ring for an MFM-160-d_{12} ligand. The scheme shows the possible interaction sites (I, II and III) that might influence the rotational potential for phenyls and (b) view of the disordered phenyl rings and intramolecular hydrogen bonding observed in the single crystal structure of MFM-160.

The gas-loaded materials (See Figures A.11 – A.15 in Appendix), show the same mechanism of phenyl molecular rotation. Although the effect of the guests is not very strong in absolute values, it is unexpected (Figure 6.11). With CO_2 as the guest species, the concentration dependence at 123 K is as expected with a higher gas loading resulting in a slower rate of phenyl rotation. For the higher loading of ~5 bar (at 298 K), the decrease in rotation rate is more pronounced and evident even without detailed numerical analysis of the observed line shape. However, at 223 K this effect is inverted: with increased loading of CO_2, the speed of phenyl rotation *increases*, a phenomenon never before observed in a MOF or any other solid state material. On a quantitative level the effect is clearly seen on the Arrhenius plot (Figure 6.8 b) for the corresponding rotation rate constants; the slope for the CO_2-loaded material is notably steeper in comparison to that of the guest-free material. While not very pronounced for the intermediate loading (1 bar) with E_1 = 2.6 kJ mol^{-1}, k_{10} = 2.3 x 10^6 Hz, the effect becomes more evident at higher concentration (5 bar) with E_2 = 4.2 kJ mol^{-1}, k_{20} = 7.6 x 10^6 Hz. In the latter case the barrier is approximately doubled and the collision factor increases six-fold, well beyond any possible error.

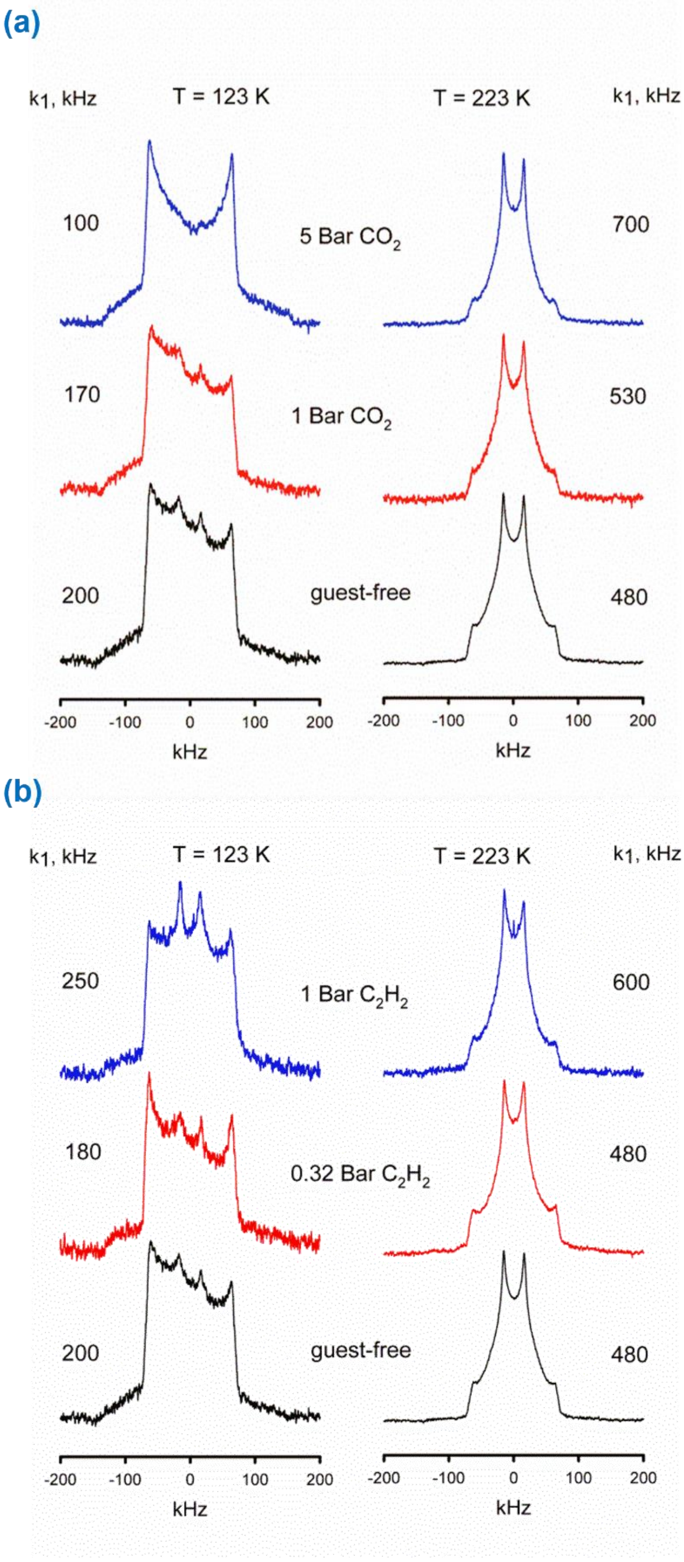

Figure 6.11: Comparison of the experimental line shapes and rotation rates for guest-loaded MFM-160-d_{12} at 123 K and 223 K.

For the C_2H_2-loaded material, the situation is different: at the intermediate concentration (~0.32 bar at RT), conditions in which the C_2H_2 concentration is equimolar to that of CO_2 at 1 bar, no effect on the phenyl dynamics is observed and the rotation is characterised by the same parameters as for the activated MOF; E_3 = 1.9 kJ mol^{-1} and k_{30} =1.2 x 10^6 Hz. Upon increasing C_2H_2 concentration to 1 bar, the speed of phenyl ring rotation clearly increases, however the activation barrier remains the same E_4 = 1.9 kJ mol^{-1} but the collision factor rises to k_{40} = 1.8 x 10^6 Hz. This is shown on the corresponding Arrhenius plots (Figure 6.9 c). This behaviour can be interpreted in terms of guest-host interactions. The two different loadings of CO_2 clearly affect both the rotation potential and the collision factor and the more gas adsorbed, the stronger the effect. The rise of the torsional barrier indicates that CO_2 molecules bind in close proximity to the phenyl linkers and increase the molecular density around them. The increase in collision factor is also explained as a result of the increased number of phenyl-guest collisions. It is possible to easily observe the collision factor behaviour because of the extremely low starting value for the guest-free material, i.e. k_{00} =1.4 x 10^6 Hz while normal pre-exponential factors for an elementary rotation are typically in the range of 10^{11-13} Hz.

A different dynamical response upon introduction of C_2H_2 indicates a distinct interaction pattern: at lower loading the phenyl rings do not interact with C_2H_2 at all and only at higher loadings is there a subtle increase of the collision factor. This shows that occupancy of C_2H_2 sites around the mobile phenyl rings is low, even at higher concentrations. Thus, C_2H_2 coordinates predominantly to the Cu(II) paddlewheel sites and interacts with the phenyl rings only through random collisions, most likely when most of the metal sites are occupied. At 0.32 bar C_2H_2 (3.1 gas molecules per formula unit) the Cu(II) sites are very likely to be saturated with C_2H_2 bound strongly and not able to influence phenyl rotation, as shown by ^2H NMR spectroscopy. However, with an equimolar loading of CO_2, where the Cu(II) sites were also expected to be saturated, the phenyl ring rotation is much more affected by the guest CO_2 molecules than for C_2H_2, strongly suggesting that CO_2 occupies binding sites on the linker while open Cu(II) sites are still available. These ^{2}H NMR observations therefore provide a good insight into the selectivity for C_2H_2 over CO_2, as the stronger binding of C_2H_2 at the open Cu(II) sites is very likely to account for the greater uptake of C_2H_2 at low pressures. In comparison, the C_2H_2:CO_2 selectivity in $Cu_2(pzdc)_2(pyz)$, a MOF without open Cu(II) sites, was assigned to the binding of C_2H_2 with free carboxylate oxygen atoms lining the pores.[41]

6.25 Computational modelling of gas binding sites in MFM-160

To further understand these observations from ^{2}H NMR and to help explain the hydrocarbon selectivity demonstrated by MFM-160, density functional theory calculations, as implemented in the Q-Chem quantum chemistry package,[154] were utilised. The strength of adsorption sites was analysed using a fragment of the linker formed by the central triazine ring and three phenyl rings (Figure 6.12). The binding energies between the guest molecule and the linker were calculated in addition to their relative positions corresponding to the strongest binding. These calculations were performed in two stages. The geometry optimisation was carried out using dispersion-corrected DFT calculations at the B3LYP/6-31+G** level of theory and the binding energies were subsequently calculated at the higher B3LYP/6-311+G** level. Binding energies were corrected for basis set superposition error as outlined in Chapter 2.

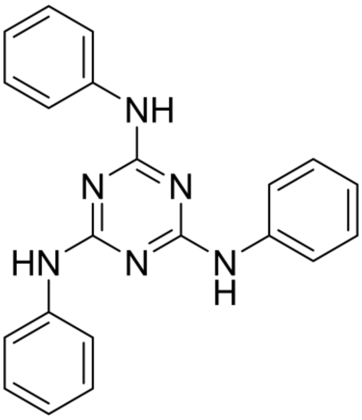

Figure 6.12: Fragment of the MFM-160 linker used for binding energy calculations.

An extensive search for binding sites between all guest molecules and the linker fragment was performed including CO_2, C_2H_2, C_2H_4, C_2H_6 and CH_4. A range of binding sites was found for all molecules and two binding sites of CO_2 and the linker fragment are shown in Figure 6.13. The first binding site shows interaction over the triazine core (top of Figure 6.13). This interaction is comprised of electrostatic interaction between the oxygen atoms in the CO_2 molecule and the nitrogen atoms in the central ring to give a binding energy of –9.41 kJ mol^{-1}. The strongest binding of CO_2 to the linker fragment was found to be above the arm of the linker (bottom of Figure 6.12), in which the CO_2 molecule interacts with a binding energy of -19.54 kJ mol^{-1}. The interaction is dominated by a strong electrostatic interaction between the carbon of CO_2 and the nitrogen of the central ring. This interaction is enhanced by two weak hydrogen bonds between the other oxygen of CO_2 and nearby protons of the neighbouring phenyl ring and the bridging –NH group. These interactions have a significant cooperative effect on the binding of CO_2 to the linker fragment. As stated earlier, the slow rotation of the phenyl ring observed by ^{2}H NMR spectroscopy was attributed to a hydrogen bond between a phenyl proton and an N atom of triazine core. Therefore, the increased rotation upon CO_2 loading may be explained by the weakening or removal of this hydrogen bond upon CO_2 binding at this site. Increased occupancy of gas at this site at higher CO_2 loading would also explain the increased rate of rotation from the 1 bar to the 5 bar-loaded sample. Overall, CO_2 interacts more strongly with the linker fragment than the hydrocarbons, giving a range of binding energies from –9.41 to –19.54 kJ mol^{-1}.

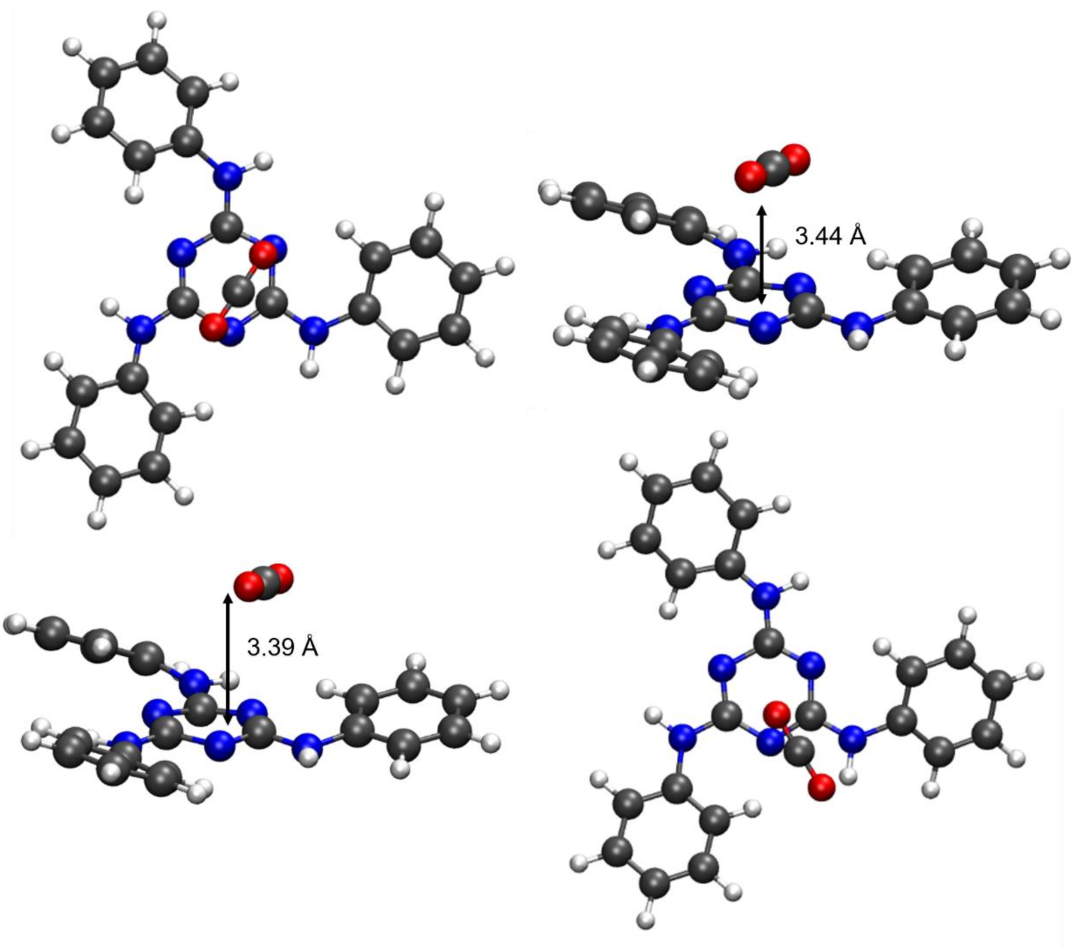

Figure 6.13: CO_2 binding with MFM-160 above the central triazine core of the linker (top) and above the nitrogen containing arm of the linker (bottom).

Two similar binding sites have been found for C_2H_2 and are shown in Figure 6.14. The binding over the central triazine core (top of Figure 6.14) is governed by an interaction between the π-bonds of C_2H_2 and the delocalised π system of the central ring to give a binding of -13.32 kJ mol^{-1}. The strongest binding site for C_2H_2 is over the bridging amine nitrogen between the triazine ring and the outer phenyl rings with a binding energy of -18.2 kJ mol^{-1}. There is a cooperative binding effect with the hydrogens of the C_2H_2 interacting with the triazine ring and the neighbouring phenyl ring but the binding is dominated by an interaction between the π-bonds of the C_2H_2 and the bridging nitrogen. As with CO_2, this interaction is likely to affect the hydrogen bond between the phenyl proton and the triazine core, leading to the increased phenyl rotation rate observed by ^2H NMR spectroscopy upon addition of 1 bar C_2H_2. At lower pressures (0 to 0.32 bar), this site is unoccupied, as confirmed by the E_0 and k_{00} values at 0.32 bar remaining equal to those observed in the guest-free material. Between 0.32 and 1 bar, where the Cu(II) paddlewheel sites are expected to be saturated, the increased occupancy of this site disrupts the intramolecular hydrogen bond of the linker and the phenyl rotation increases. It would have been interesting to observe the effect of a higher loading of C_2H_2 on the rotational dynamics, but there are well-known safety concerns with the use of this gas above 1 bar.

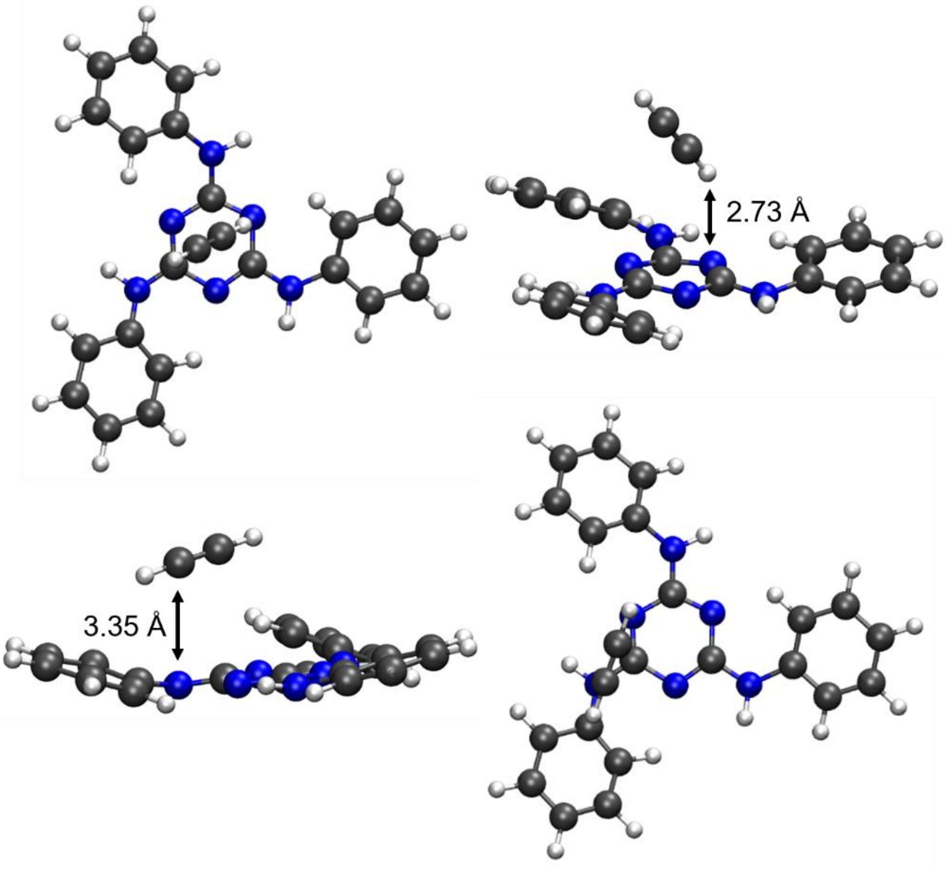

Figure 6.14: C_2H_2 binding with MFM-160 above triazine core of linker (top) and over the arm of the linker (bottom).

The π-bond interaction of C_2H_2 with the linker leads to stronger interactions overall compared to the other hydrocarbons and as a result the C_2H_2 molecule interacts with a similar range of binding energies as CO_2 (–13.32 to –18.16 kJ mol^{-1}). These comparable binding energies strongly suggest that the triazine functionality is not responsible for the selectivity for C_2H_2 over CO_2. As stated earlier, it is likely that increased vdW interactions between C_2H_2 and the framework in comparison to those with CO_2, as well as the former's higher affinity for the open Cu(II) sites, are responsible for the selective uptake.

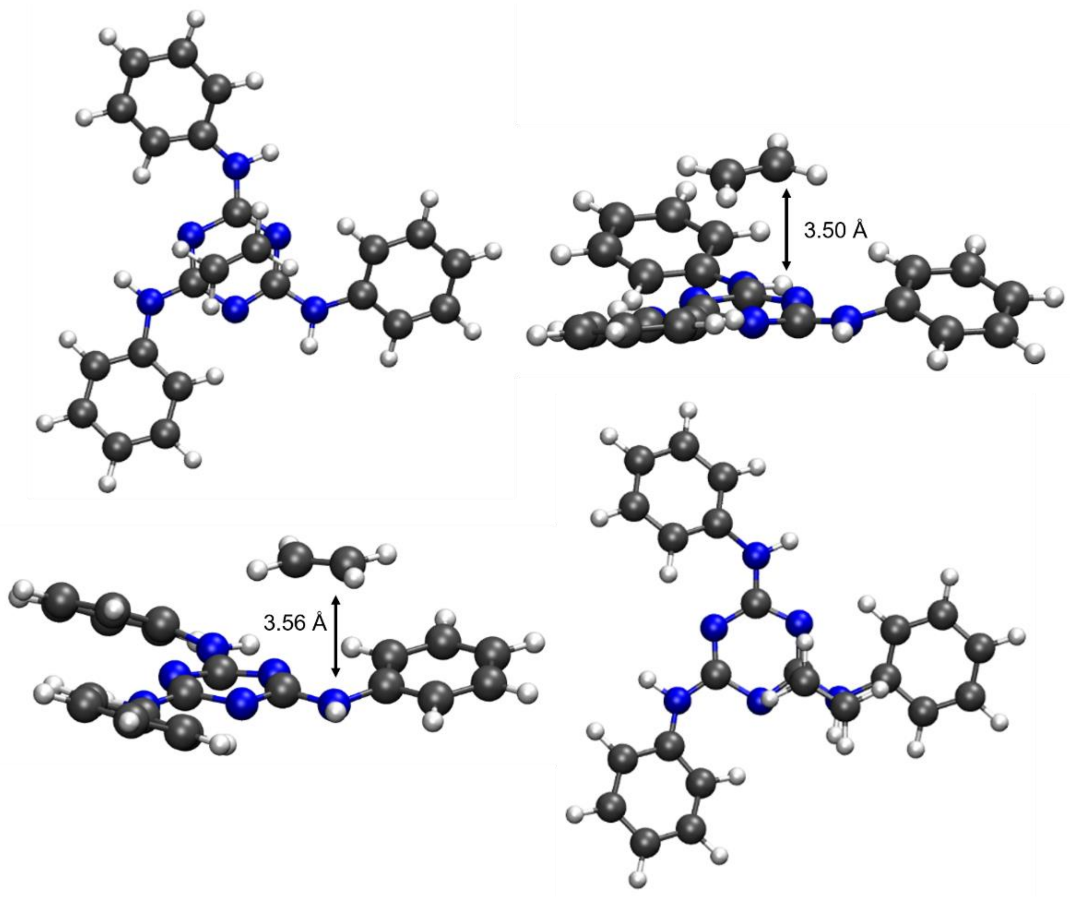

Figure 6.15: C_2H_4 binding with MFM-160 over the triazine core of linker (top) and with the nitrogen-containing arm of the linker (bottom).

The range of interactions between the hydrocarbons C_2H_4 and C_2H_6 and the linker were also investigated and found to be very similar; –11.7 to –16.2 kJ mol^{-1} and

–10.2 to –16.3 kJ mol^{-1} respectively. The strongest interaction between C_2H_4 and the linker (top of Figure 6.15) and also C_2H_6 and the linker (top of Figure 6.16) occurs over the central triazine ring. This is an interaction between the central carbon-carbon bond of the two hydrocarbons, C_2H_4 and C_2H_6 and the delocalised π system of the central ring. Weaker interactions are also seen between the central carbon-carbon bond of the hydrocarbons, C_2H_4 (bottom of Figure 6.15) and C_2H_6 (bottom of Figure 6.16) and the bridging –NH group. On average, the binding of C_2H_4 is stronger than C_2H_6 due to the strength of the interaction between the alkene double bond and the linker.

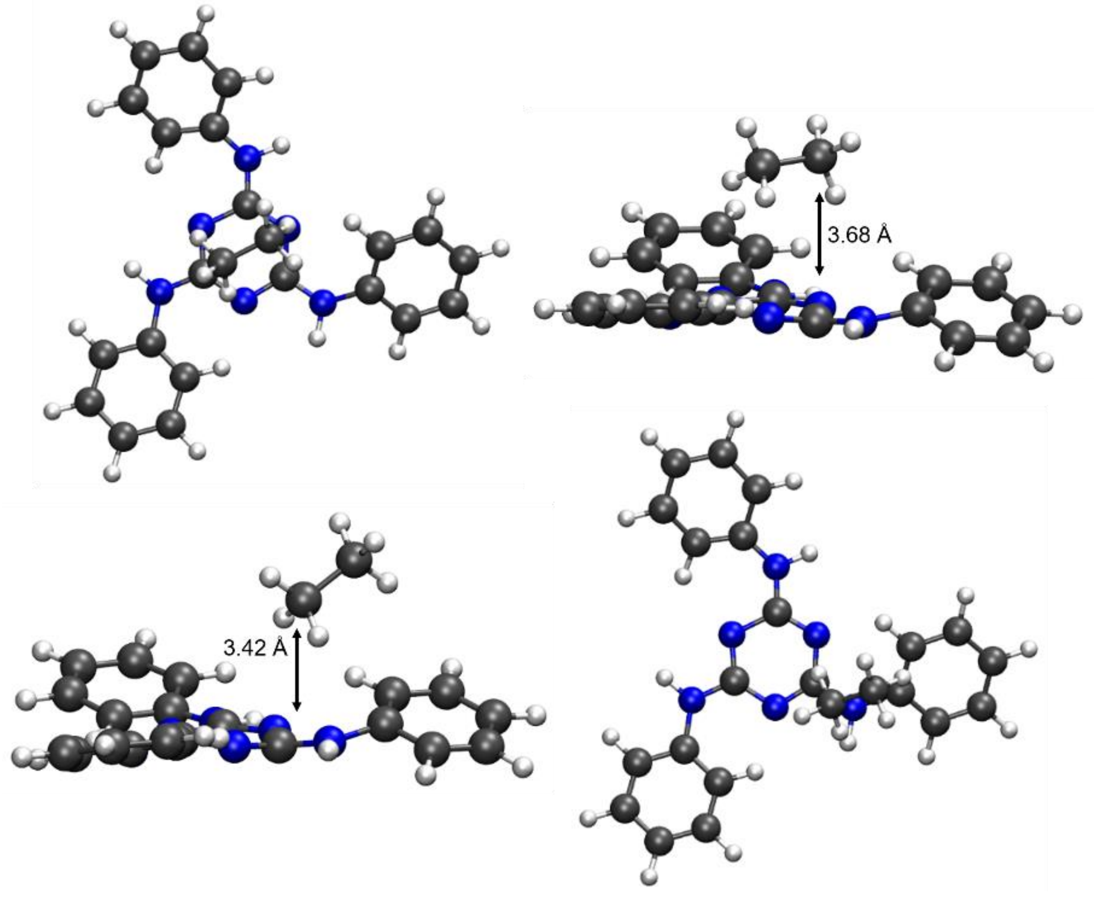

Figure 6.16: C_2H_2 binding with MFM-160 over arm of linker (top) and above triazine core of linker (bottom).

To complete the computational investigation of MFM-160, we found that the strongest binding of CH_4 to the linker was found to be where the CH_4 molecule interacts above the central triazine ring to give a binding energy of –10.33 kJ mol^{-1}

(top of Figure 6.17). There is a weak hydrogen bond between a CH_4 hydrogen atom and a nitrogen atom of the triazine ring. There are also additional weak electrostatic interactions between other CH_4 hydrogen atoms and the central ring. Another site was found above the arm of the linker (bottom of Figure 6.17) with weak vdW interations between a hydrogen of CH_4 and the bridging –NH group to give a BE of -4.52 kJ mol^{-1}. The binding energy interactions between CH_4 and the linker are the weakest of all those studied, consistent with the experimental isotherm data.

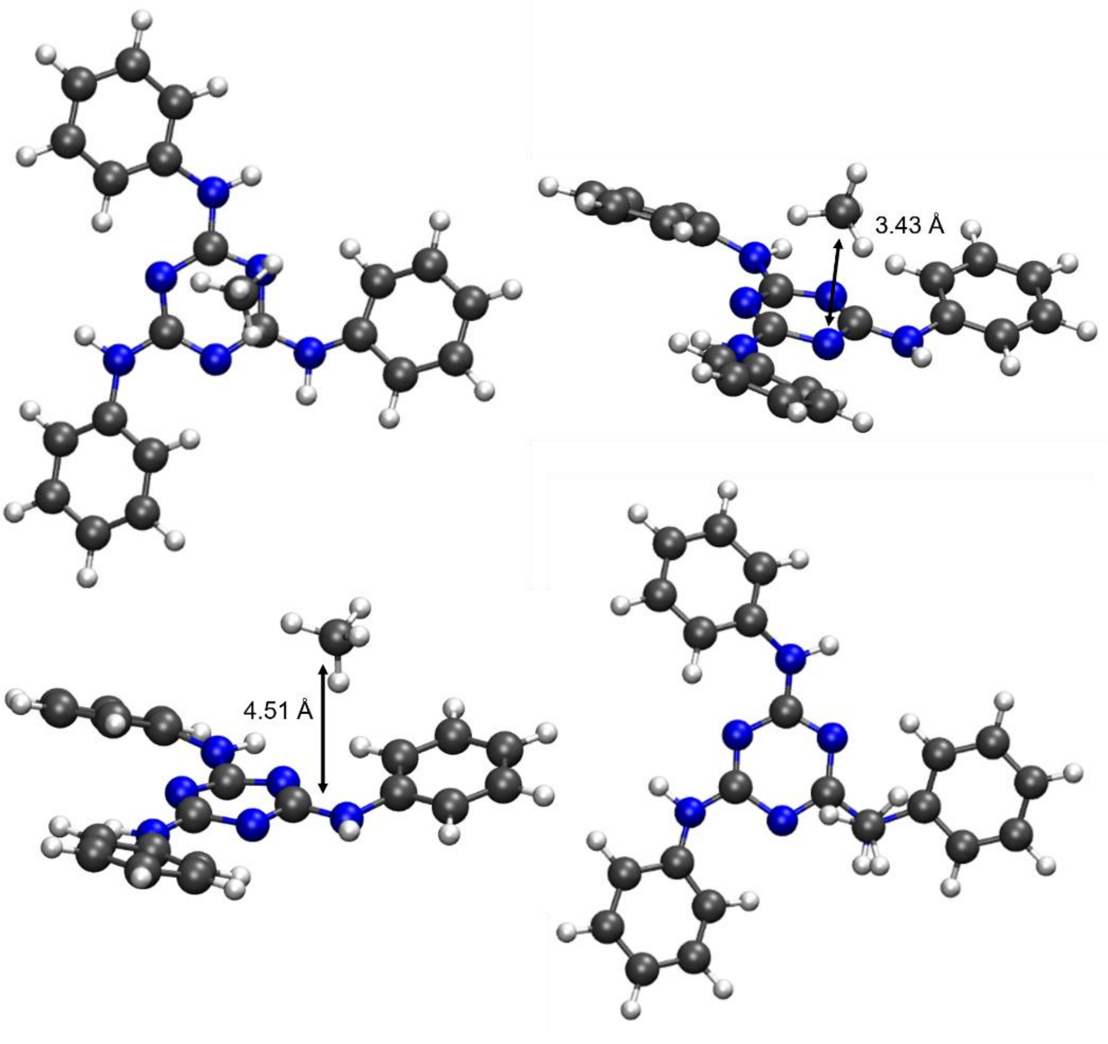

Figure 6.17: CH_4 binding with MFM-160 above the triazine core of the linker (top) and above the nitrogen containing arm of the linker (bottom).

6.26 Summary

Overall, the synthesis and studies of this new, highly porous (3,24)-connected Cu(II) MOF have shown that its activated form, MFM-160 exhibits an exceptional capacity for uptake of CO_2 at 20 bar and 298K (110 wt%). It is also shown that the relatively poor uptake of CO_2 and CH_4 at lower pressures ($\leq$ 1 bar) makes MFM-160 a material of great interest for the purification of natural gas and of acetylene, as confirmed by Henry's Law. A ^{2}H NMR spectroscopic study of phenyl rotation dynamics showed an ultra-low rotation barrier and very slow phenyl rotation. The rotation was shown to increase upon gas loading, a unique phenomenon not previously observed in a solid state material and is attributed to an intramolecular hydrogen bond, which is weakened by gas binding, leading to an increased rate of rotation. The results of DFT calculations are consistent with this theory, as both gases show clear binding interactions near this hydrogen bond.

6.3 Results and discussion: MFM-188

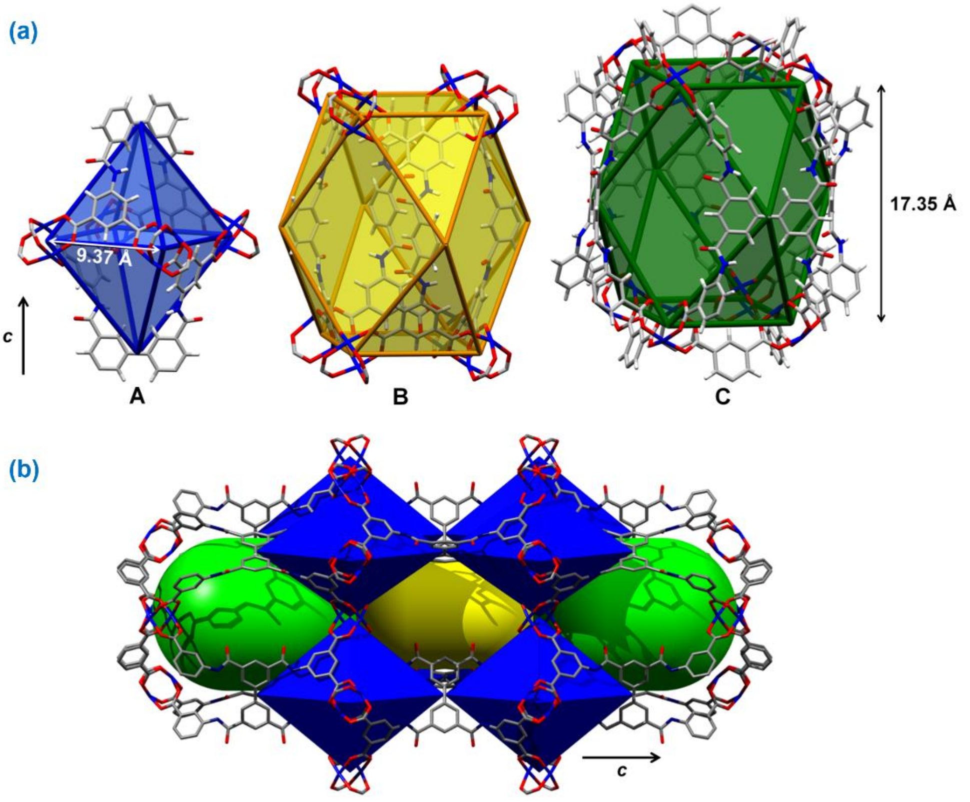

Figure 6.18: View of the crystal structure of MFM-188. (a) Polyhedral representation of the three types of cages: A (octahedral), B and C (cubahedral). (b) The assembly of these cages in 3D space forming the MFM-188 framework. Cages A, B and C are highlighted in blue, yellow and green, respectively.

As synthesised, the structure of MFM-188 can be viewed as 3D alternate packing of three types of metal-ligand cages (denoted as A, B and C in Figure 6.18 a) with ***lwg*** topology. The smallest cage A is comprised of four {Cu_2} paddlewheels and two H_8L ligands (Figure 6.19), and has an elongated, distorted octahedral geometry (internal size of ~ 9.4 x 9.4 x 13.4 Å). The {Cu_2} paddlewheels occupy the four equatorial vertices with two biphenyl cores from the ligands occupying the apical vertices. Corner-sharing of cages A with biphenyl groups running along the *c* axis and with paddlewheels along the *a/b* axis extend the structure (Figure 6.18 b). Two further distorted cuboctahedral cages (B and C) result from this assembly, each comprising of eight {Cu_2} paddlewheels and four ligands. The length of cage C, defined by the separation between the centroids of the two closest {Cu_2} paddlewheels along the *c* direction, is 17.4 Å. Each Cu^{II} site has a coordinated water molecule at the axial position and point to the center of Cage C. Cages B and C are connected through shared lozenge-shaped windows on the *ab* plane and through their apical square-shaped windows along the *c* direction. Taking the van der Waals radii into account, cages B and C have internal pore size of ~ 11 x 11 x 17 Å and ~ 17 x 17 x 17 Å, respectively. Each cage B and C is surrounded by eight cages A, while each cage A is surrounded by four cages B and four cages C, with cages A, B and C present in a 2:1:1 ratio. The total accessible volume of MFM-188 upon removal of guest solvents is 73 % using the PLATON/VOID routine.[208] Within the void space of MFM-188, there is a high concentration of pendent amide (-OCNH-) groups pointing into cage B (O-centres) and into the cage C (N-H centres), thus endowing these cages with a combination of open metal sites and multiple functional groups. In contrast, none of the amide groups protrude into cage A, which is functionalized solely with phenyl rings.

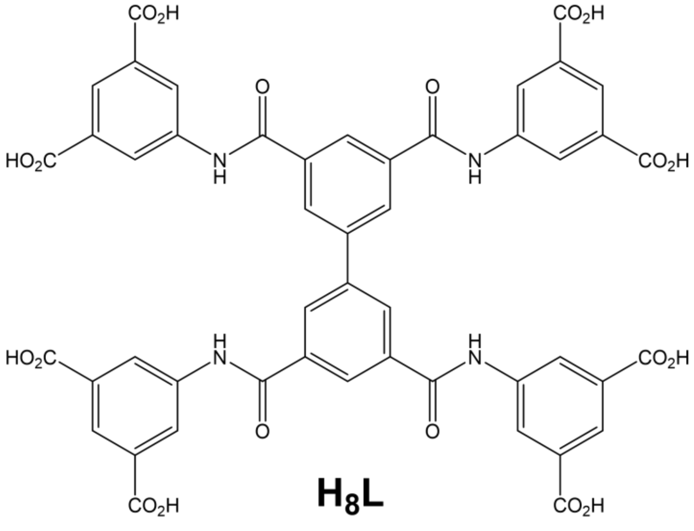

Figure 6.19: Chemical structure of the tetra-amide octacarboxylate linker H_8L used in the synthesis of MFM-188.

N_2 adsorption at 77 K shows a reversible type I isotherm for MFM-188 with a Brunauer Emett Teller surface area of 2568 m^2 g^{-1} (Figure 6.20). The pore size distribution, calculated using a non-local density functional theory (NLDFT) model,[217] revealed two broad peaks centred at 12.5 and 14.7 Å, in good agreement with the pore size measured for cages A, B and C. Importantly, the total pore volume measured from the N_2 isotherm (1.12 cm^3 g^{-1}) compares favourably with that (1.07 cm^3 g^{-1}) calculated from X-ray crystal structure (calculated by powder X-ray diffraction), confirming complete activation of the material. The overall porosity of MFM-188 is moderate in comparison to the most porous MOFs reported to date.[187]

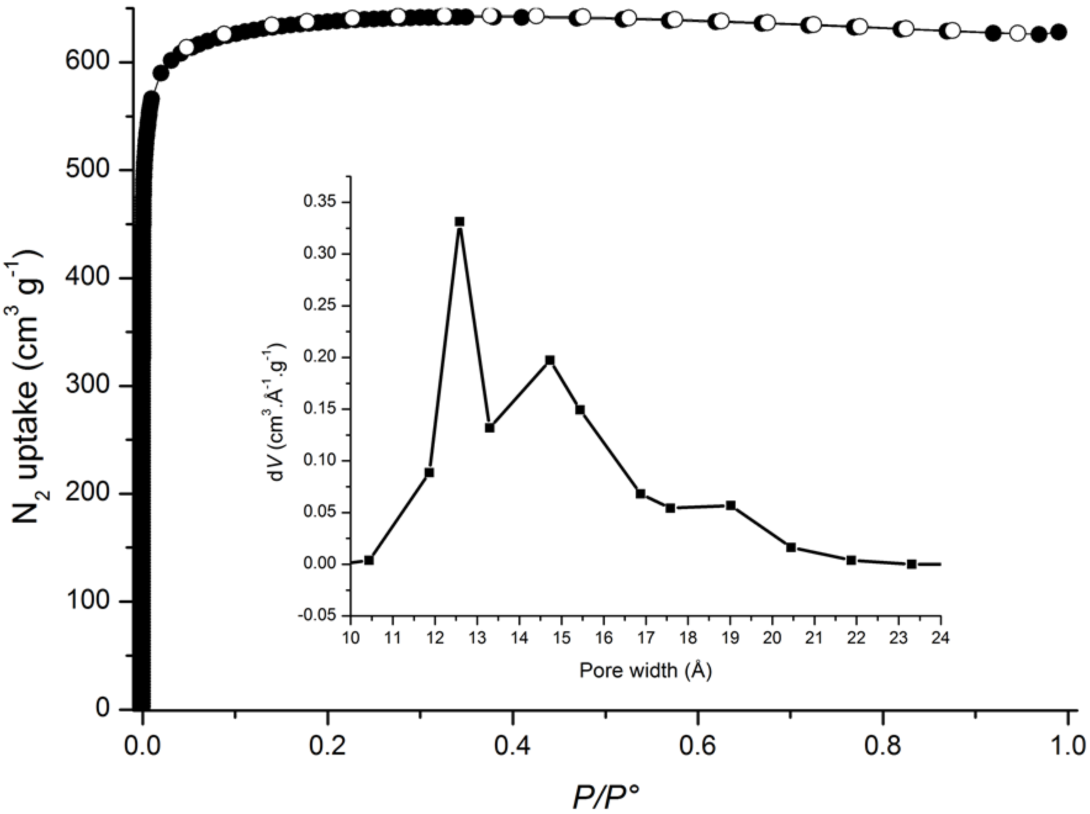

Figure 6.20: N_2 sorption isotherm for MFM-188 at 77 K. Insert plot shows the pore size distribution.

6.31 CO_2 and C_2H_2 adsorption analysis

The uptake of CO_2 and C_2H_2 by activated MFM-188 was investigated up to 1 bar, and in both cases the isotherms show fully reversible adsorption with a CO_2 uptake of 120 cm^3 g^{-1} (23.7 wt% or 86.7 v/v) recorded at 298 K and a C_2H_2 uptake of 232 cm^3 g^{-1} (27.0 wt% or 166.7 v/v) at 295 K (Figure 6.21 a). Importantly, these gravimetric uptakes are amongst the highest reported, and are only outperformed in the case of CO_2 adsorption by MOF-74Co (30.6 wt%) and MOF-74Mg (35.2 wt%),[218] both of which present a narrower pore channel and a much higher density of OMSs (MOF-74Co: 6.4 mmol g^{-1}; MOF-74Mg: 8.2 mmol g^{-1}; MFM-188: 3.3 mmol g^{-1}). Interestingly, MFM-188 shows the highest CO_2 uptake of other amide-functionalized MOFs such as the ***rht***-[Cu$_3$(TPBTM)][202] (23.3 wt%) and ***fof***-NOTT-125[27] (18.2 wt%). The CO_2 uptake of MFM-188 at 0.15 bar is 3.9 wt%. To the best of our knowledge, the gravimetric capacity of C_2H_2 (27.0 wt%) in MFM-188 represents the highest value observed to date for porous solids, exceeding FJI-H8[68] (26.0 wt%), NJU-Bai-17[205] (25.8 wt%), HKUST-1[219] (23.3 wt%) and SIFSIX-1-Cu[220] (22.1wt %). The CO_2 and C_2H_2 uptake capacity in MFM-188 increase considerably at 273 K to 217 cm^3 g^{-1} (42.9 wt%) and 297 cm^3 g^{-1} (34.5 wt%), respectively.

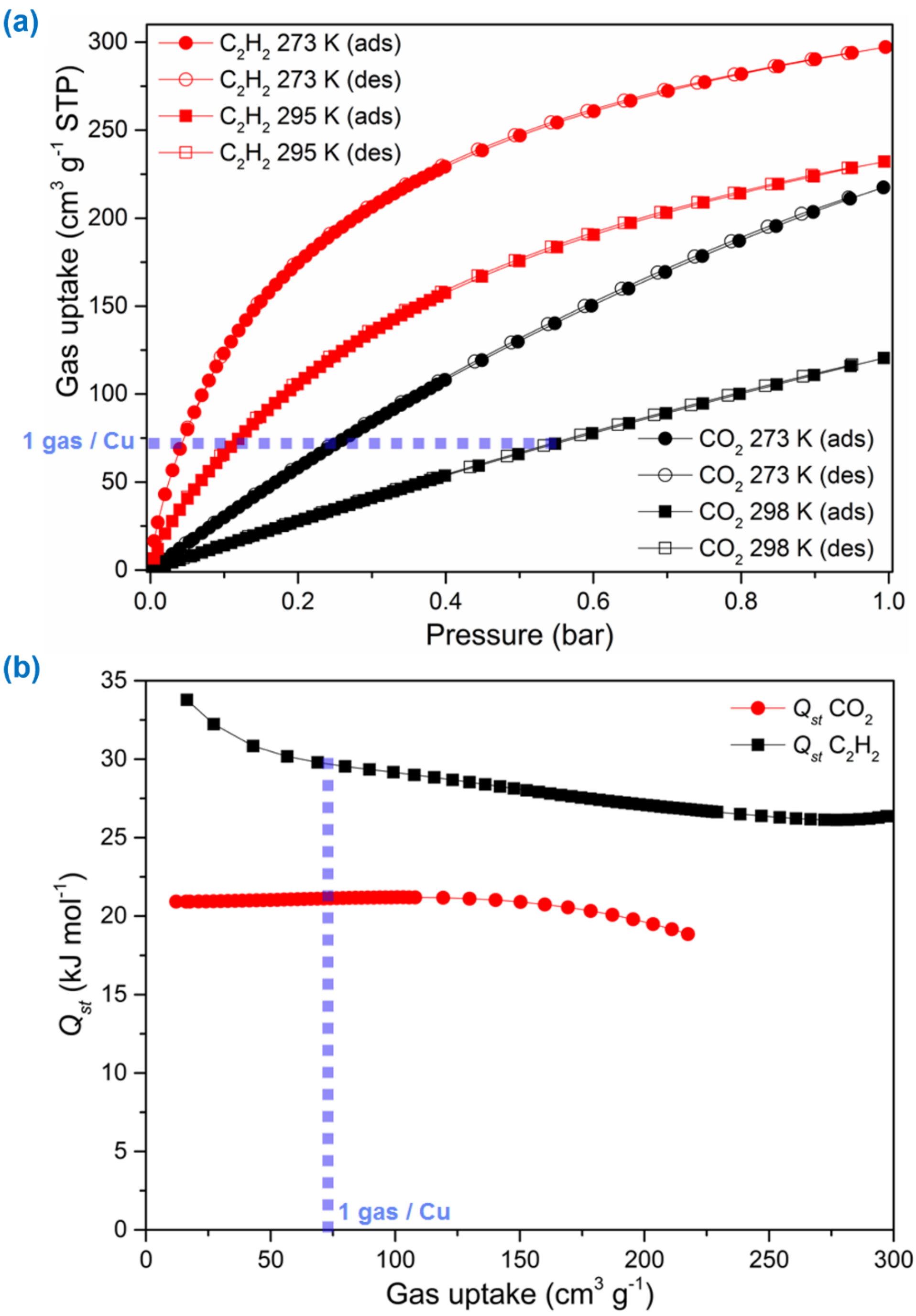

Figure 6.21: Gas adsorption isotherms for MFM-188. (a) Comparison of the CO_2 and C_2H_2 adsorption isotherms for MFM-188 at 273-298 K and 1.0 bar. (b) Variation of the isosteric heats of adsorption for CO_2 and C_2H_2 adsorption in MFM-188.

The Q_{st} values at zero coverage determined by virial analysis of adsorption isotherms are moderate but comparable to typical Cu^{II} MOFs where adsorption of gas molecules occurs primarily on OMSs,[202,205,206,219,221] with Q_{st} (CO_2) = 21.0 kJ mol^{-1}

and Q_{st} (C_2H_2) = 32.5 kJ mol^{-1}. Interestingly, the Q_{st} plots do not display any major decrease across the whole adsorption range (Figure 6.21 b), suggesting the presence of other favourable binding sites in addition to OMSs. We were thus motivated to investigate further the role of pendent amides and OMSs in CO_2 and CH_2 adsorption in MFM-188.

The CO_2 adsorption isotherms at 273 and 298 K as well the C_2H_2 isotherms at 273 and 295 K were fitted to the virial equation in the form of Equation 6.1. P is the pressure expressed in bars, N is the amount expressed in mol g^{-1}, T is the temperature in K, a_i and b_j are virial coefficients, and m, n represent the number of coefficients. The values of the virial coefficients a_0 to a_m were then used to calculate the isosteric heat of adsorption using Equation 6.2. Q_{st} is the coverage dependent isosteric heat of adsorption and R is the universal gas constant.

$$\ln(P) = \ln(N) + \frac{1}{T}\sum_{i=0}^{m} a_i N^i + \sum_{j=0}^{n} b_j N^j \tag{6.1}$$

$$Q_{st} = -R\sum_{i=0}^{m} a_i N^i \tag{6.2}$$

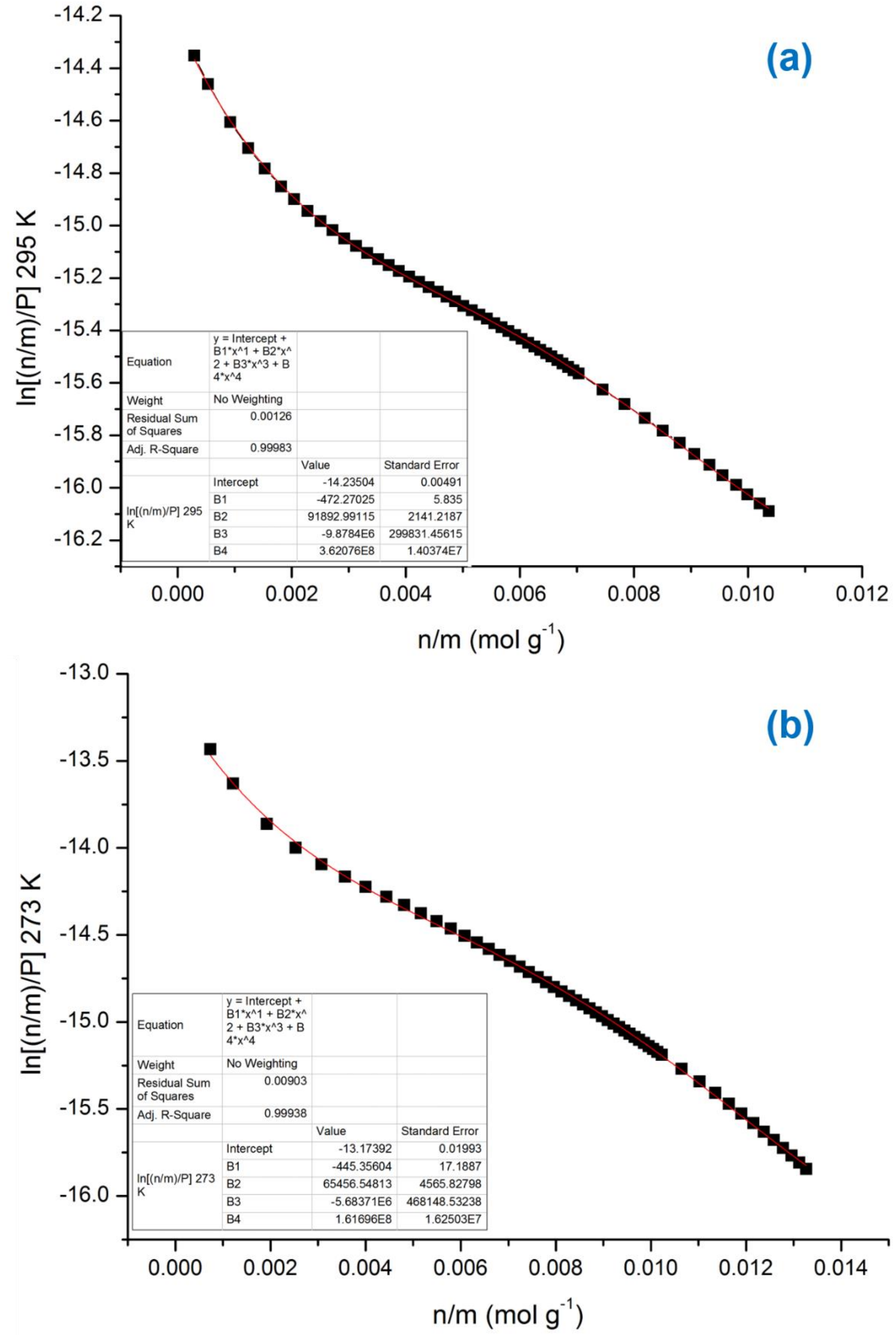

Figure 6.22: Virial fitting of C_2H_2 adsorption isotherm at 295 K (a) and 273 K (b).

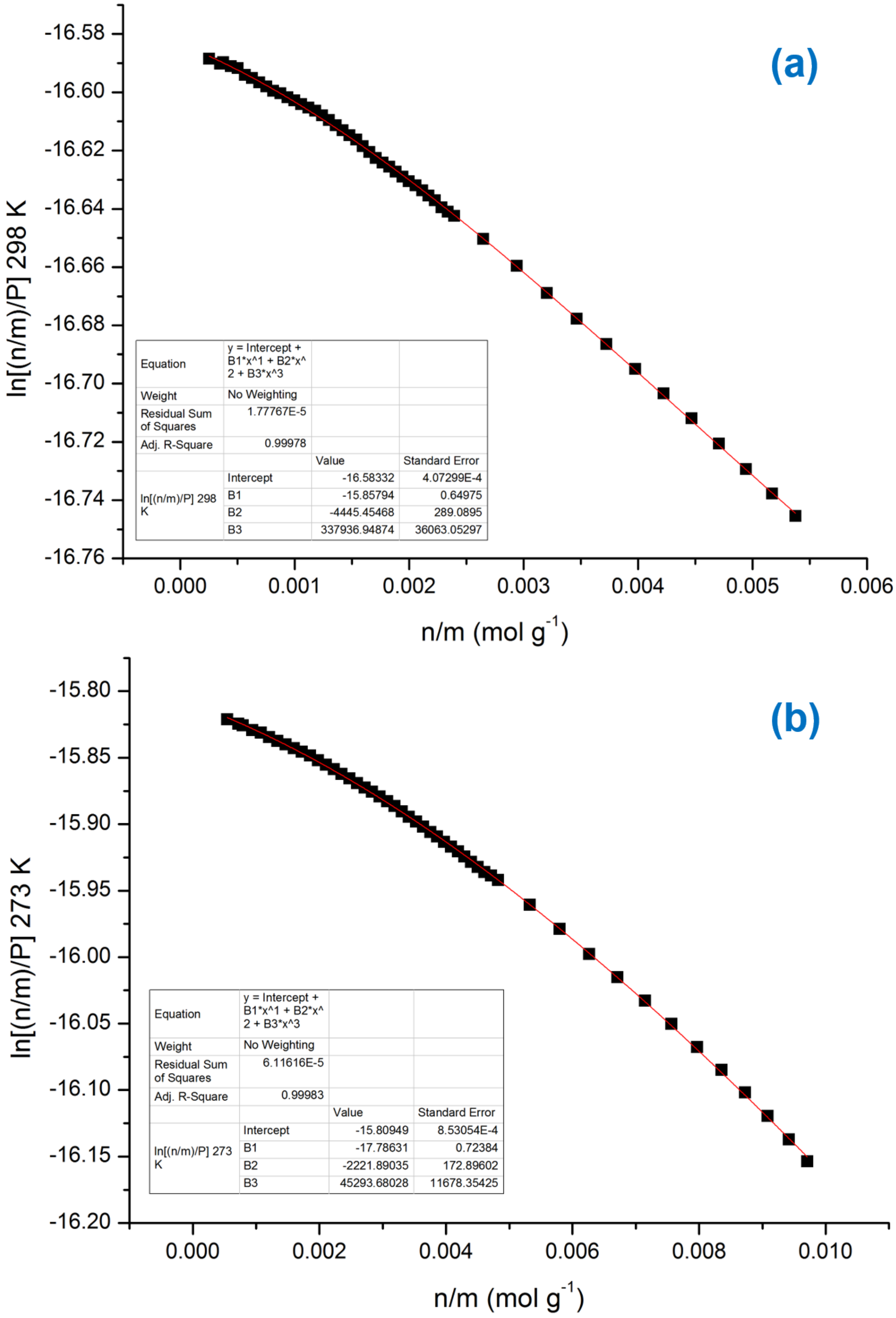

Equation	y = Intercept + B1*x^1 + B2*x^2 + B3*x^3		
Weight	No Weighting		
Residual Sum of Squares	1.77767E-5		
Adj. R-Square	0.99978		
		Value	Standard Error
ln[(n/m)/P] 298 K	Intercept	-16.58332	4.07299E-4
	B1	-15.85794	0.64975
	B2	-4445.45468	289.0895
	B3	337936.94874	36063.05297

Equation	y = Intercept + B1*x^1 + B2*x^2 + B3*x^3		
Weight	No Weighting		
Residual Sum of Squares	6.11616E-5		
Adj. R-Square	0.99983		
		Value	Standard Error
ln[(n/m)/P] 273 K	Intercept	-15.80949	8.53054E-4
	B1	-17.78631	0.72384
	B2	-2221.89035	172.89602
	B3	45293.68028	11678.35425

Figure 6.23: Virial fitting of CO_2 adsorption isotherm at 298 K (a) and 273 K (b).

The locations of adsorbed CO_2 and C_2D_2 molecules within desolvated MFM-188 were determined by *in situ* neutron powder diffraction (NPD) as a function of gas loading. NPD patterns were recorded at 7 K for the desolvated material and at loadings of 1.75 CO_2/Cu (127 $cm^3 g^{-1}$) and 3.2 C_2D_2/Cu (234 $cm^3 g^{-1}$), which correspond to the adsorption uptakes at 1 bar and room temperature for the respective gas species. Successive Fourier difference map analysis of NPD data followed by Rietveld refinement allowed identification of the position, occupancy and orientation for adsorbed gas molecules within the framework cages. Six different sites (1, 2, 3, 4, 5 and 6 in the order of decreasing occupancy) were observed for adsorbed guest molecules: one in cage A, one in cage B and four in cage C, all of them having the same crystallographic multiplicity (Figure 6.24). Notably, 83% of loaded CO_2 and 72% of loaded C_2D_2 molecules were found in cage C, which contains open Cu^{II} sites and the N-H sites of amides pointing to the centre of the cage. The smallest cage A plays a different role in CO_2 and C_2D_2 uptakes with a minimum contribution to the CO_2 adsorption, but considerable effect to the C_2D_2 binding.

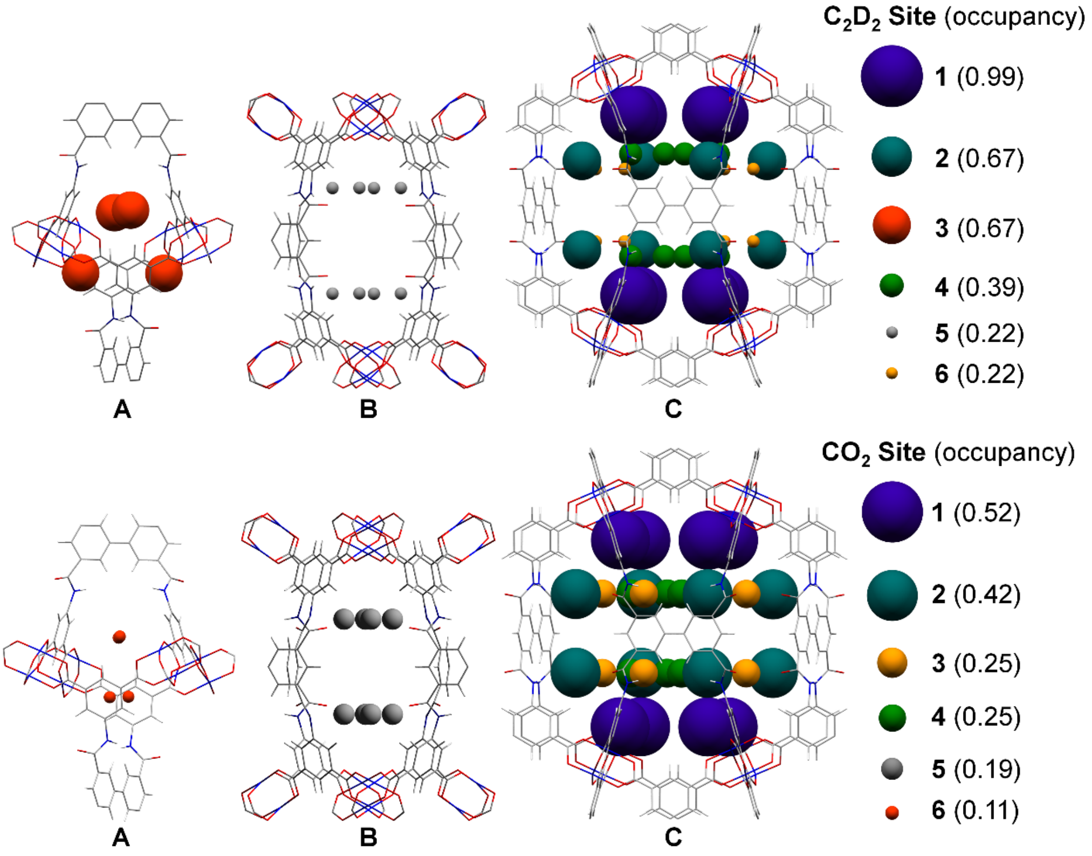

Figure 6.24: View of the distribution of adsorbed gas molecules within three different types of cages in MFM-188 as determined from NPD data. Representation of C_2D_2 (top) and CO_2 (bottom) positions in the cages A, B and C of MFM-188 at a loading of 1.75 CO_2/Cu and 3.2 C_2D_2/Cu respectively. The radii of the coloured balls figuring the various sites are proportional to corresponding crystallographic occupancies.

In the structure of MFM-188·7CO_2, the CO_2 molecules at site 1 bind at OMSs in cage C (occupancy = 0.52). The linear body of CO_2(1) is perpendicular to the Cu-Cu axis with $C_{CO2}\cdots Cu = 2.35(3)$, $O_{CO2}\cdots Cu = 2.34(3)$ Å (Figure 6.25 a). The second most populated site 2 (occupancy = 0.42) is also located in cage C where adsorbed CO_2 molecules form H-bonds with both the free amide groups (-NH) and the adjacent isophthalate -CH groups [$N\cdots O_{CO2} = 2.66(6)$ Å, <N-H···O = 109°; $C\cdots O_{CO2}= 2.75(4)$ Å, <C-H···O = 141°] (Figure 6.25 b). CO_2(3) and CO_2(4) are also found in cage C (occupancy = 0.25 for both) at the centre of the cage and forming weak supramolecular interaction to isophthalate -CH groups [$C\cdots O_{CO2}=3.66(6)$ Å, <C-H···O = 156°] (Figure 6.25 c-d). The remaining CO_2(5) and CO_2(6) sites are found in cage B and A

(occupancy = 0.19 and 0.11, respectively). Given the long distances between $CO_2(5)$/$CO_2(6)$ and the framework surface (above 5 Å), no specific binding interaction could be identified, thus excluding the presence of dipole interactions between the amide –C=O and adsorbed CO_2 molecules in cage B.

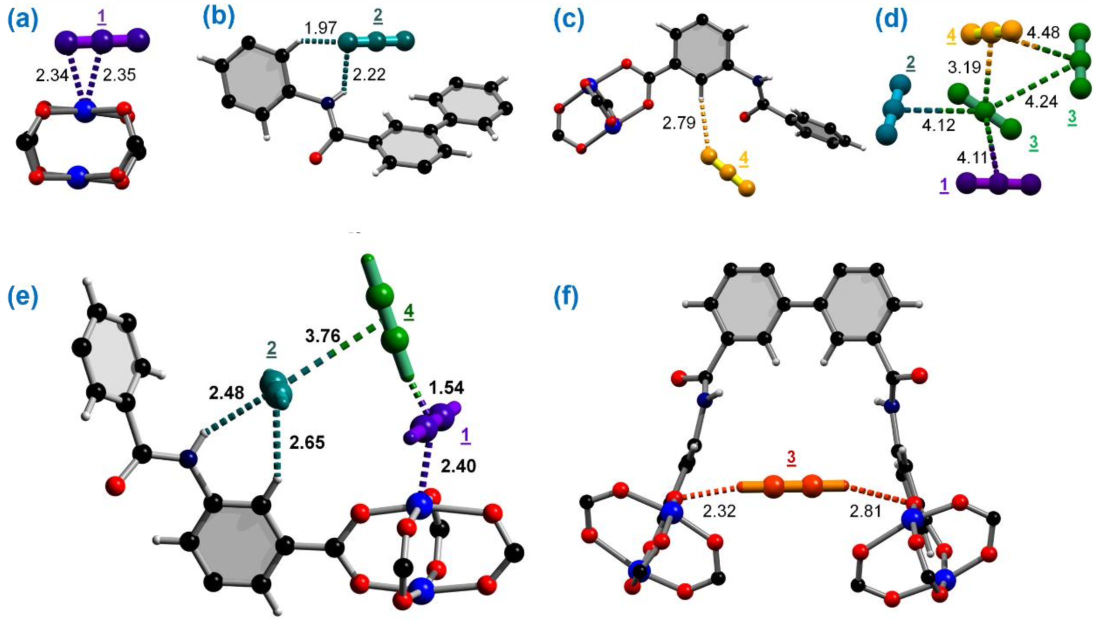

Figure 6.25: Crystallographic resolution of CO_2 and C_2H_2 binding in MFM-188. Framework atoms: C, black; O, red; H, white; N, blue; Cu, blue. Extra framework gas molecules are slightly magnified and coloured according with the binding site they occupy. Distances are shown in Å. View of the binding of adsorbed CO_2 molecules at site 1 (a), 2 (b) and 4 (c). (d) View of the packing of adsorbed CO_2 molecules within cage C. View of the cooperative binding of adsorbed C_2H_2 molecules at site 1, 2, 4 (e) and at site 3 (f).

MFM-188·12.8C_2D_2 exhibits a different distribution of adsorbed C_2D_2 molecules within the cages, indicating the presence of different gas-sorbent binding mechanisms. The OMSs are fully occupied by $C_2D_2(1)$ molecules with a side-on interaction between the C≡C bond and the Cu^{II} center, Cu···C = 2.60(3), 2.37(3) Å (Figure 6.25 e), similar to those determined for C_2D_2-loaded HKUST-1.[219] $C_2D_2(2)$ and $C_2D_2(3)$ are found in cage C and A, respectively, (same site occupancy of 0.67). $C_2D_2(2)$ forms H-bonds *via* its C≡C(δ-) π electrons to the N-H groups pointing into the pore [N···C_{C2H2} = 3.24(5) Å, <N-H···C = 147°] and electrostatic supramolecular interaction with the C-H groups from the adjacent isophthalate group [C···C_{C2H2} = 3.47(1) Å, <C-H···C = 149 °]. Significantly, this represents the first example of formation of H-bonding between the C_2H_2 and an amide group in solid state. C_2D_2(3) is located at the triangular window of the smallest octahedral cage A where C_2D_2 molecules are H- bonded to carboxylate oxygen atoms [C_{C2H2}···O = 3.72(4), 3.37(4) Å, <C-D···O = 143°, 169°] (Figure 6.23 f). In addition, the combination of C_2D_2(1) and C_2D_2(2) generates another adsorption site (4) with an occupancy of 0.49 in cage C, stabilised via the intermolecular C_2D_2···C_2D_2 dipole interactions (Figure 6.25 e). Specifically, C_2D_2(4) is perpendicular to C_2D_2(1) and strong intermolecular H-bonding is observed between these two sites [C^4···C^1 = 2.58(5) Å, <C-D^4···C^1 = 164°]. C_2D_2(4) is reinforced by C_2D_2(2) through π···π interactions of 3.76(1) Å and a dihedral angle of 84°. C_2D_2(5) and C_2D_2(6) are found in cage B and C, respectively, (occupancy of 0.22 for both) and without specific binding interaction to the MOF host. Thus, C_2D_2 displays a dual-side role behaving as an H-acceptor from amides N-H and aromatic C-H groups, but a H-donor to the carboxylate oxygen, thus enhancing the C_2D_2-MOF binding strength. In contrast, CO_2 participates in H bond formation as an acceptor only. The highly cooperative binding of acetylene at both the open Cu^{II} sites and free amides, coupled with the well-defined micropore windows, leads to the record high C_2H_2 adsorption capacity in MFM-188.

6.32 Inelastic neutron scattering (INS) of gas-sorbent dynamics

Static crystallographic experiments are unable to gain dynamic insight into the gas-sorbent systems. To directly visualise the binding dynamics of adsorbed CO_2 and C_2H_2 molecules with accessible functional groups, inelastic neutron scattering (INS) was measured for MFM-188 as a function of CO_2 and C_2H_2 loading at 11 K

(Figure 6.26). The INS spectra for bare MOF show multiple features, fully modelled *via* DFT calculations (Figure 6.26 c). The peak at 65 meV corresponds to the out-of-plane wagging modes of the N-H group, and peaks at 84 meV and 112-156 meV originate from various deformational motion of the phenyl rings and wagging modes of aromatic C-H groups. Comparison of the INS spectra for bare and CO_2-loaded MFM-188 shows an overall stiffening effect as evidenced by a global shift of peaks to slightly higher energy (Figure 6.26 a). In addition, a noticeable change in the peak at 65 meV and several small changes to the peaks between 84 and 156 meV were observed, indicating the reduction of the motion of both amide N-H and aromatic C-H groups (Figure 6.26 d). This suggests the formation of H-bonds between CO_2 molecules and these functional groups, particularly with amide N-H sites.

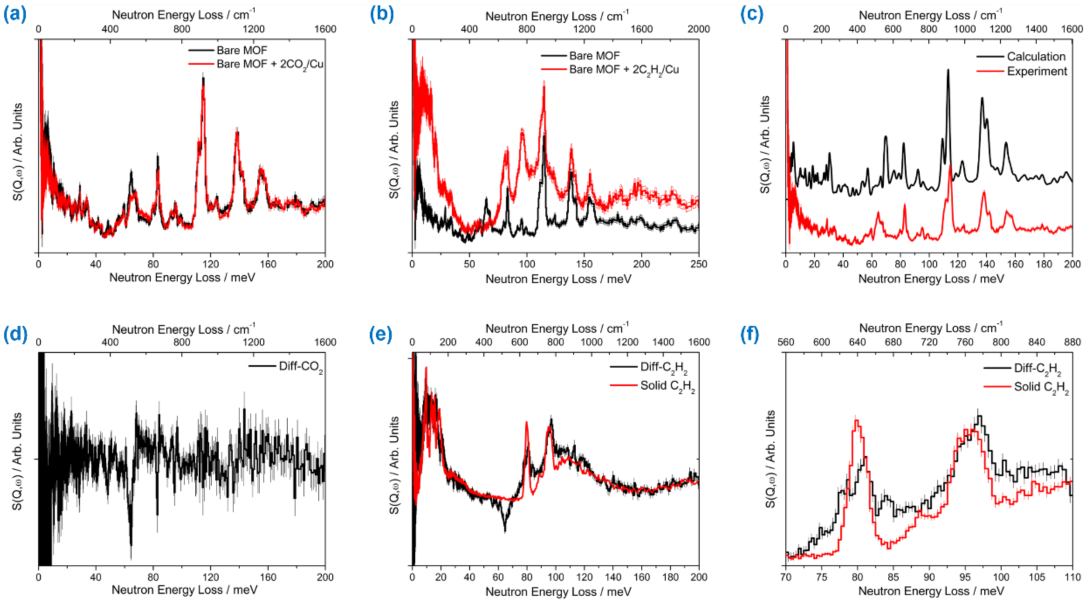

Figure 6.26: INS spectra for MFM-188 as a function of guest loading. Comparison for bare MFM-188 and for (a) CO_2 and (b) C_2H_2-loaded MFM-188. (c) Comparison of the experimental and DFT calculated INS spectra for MFM-188. Comparison of the difference plots for INS spectra of bare MFM-188 and the (d) CO_2 and (e) C_2H_2-loaded MFM-188, and the experimental INS spectra of condensed (e) C_2H_2 in the solid state. (f) Enlarged details for the INS spectra showing the C_2H_2 internal vibrational modes.

In comparison, the INS spectra of C_2H_2-loaded MFM-188 shows significant increase in intensity due to the recoil motion from the H atoms on adsorbed C_2H_2

(Figure 6.26 b). Comparison of the difference INS spectra (*i.e.,* signals from adsorbed C_2H_2 and changes of the local MOF modes) and that of the solid C_2H_2 shows a number of interesting observations. Firstly, the low-energy INS peaks (below 25 meV, assigned as the translational modes of C_2H_2 molecules) of the difference spectra shift slightly to the lower energy region but maintain the resolved three-fold peak profiles as observed in free solid C_2H_2. This indicates that the C_2H_2 molecules are ordered with restricted translational motions within MFM-188. Secondly, the INS peaks at 80 and 95 meV (assigned as the acetylene asymmetric and symmetric C–H bending mode, respectively) split from a single-peak profile to a double-peak profile upon adsorption, indicating the presence of adsorbed species resulting from slightly different binding energies to the MOF host (Figure 6.26 f). This is in excellent agreement with the presence of the strongly bound C_2H_2 molecules to the OMSs and free amides, and weakly bound C_2H_2 molecules to the phenyl rings and in the centre of the cages, as observed by NPD. Thirdly and most importantly, the INS peak at 65 meV (assigned as the out-of-plane wagging modes of the N-H group) disappears completely upon inclusion of C_2H_2 molecules in the pore, indicating loss of this mode and confirming unambiguously the direct formation of strong H-bonds between the free amides (N-H) and C_2H_2 molecules, as found in the NPD model. This observation confirms the first example of H-bonding between an amide group (N-H) and C_2H_2 in solid state. Overall, the INS study is in excellent agreement with NPD results and confirms the crucial role of the free amides in the pore for gas uptakes.

6.33 Computational modelling of gas binding sites in MFM-188

To further understand these observations from INS and NPD, DFT calculations were carried out on two fragments of the H_8L linker (Figure 6.27) using the same method as for MFM-160. These two linker fragments are representative of different cage sites within the MOF. Figure 6.27a shows a cavity-like site which is found in cage A and C, without the OMSs that is accessible to guest molecules. Figure 6.27 b shows a site found along cage B and in cage C comprising of the amide groups accessible to guest molecules. A broad search for binding sites between guest molecules and the two linker fragments was performed including the two main gases of interest CO_2 and C_2H_2 and also CH_4.

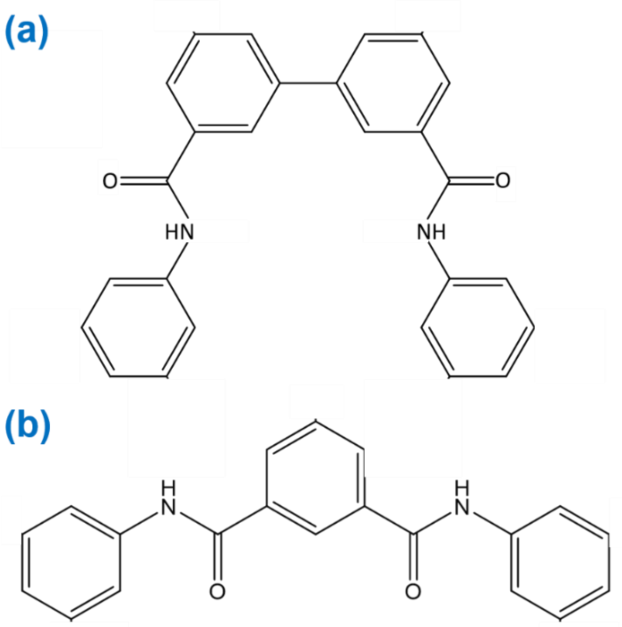

Figure 6.27: Fragments of the MFM-188 H_8L linker used for binding energy calculations. (a) Cavity-like fragment found in cage A and C, without OMSs. (b) Fragment containing amide groups accessible in cage B and C without OMSs.

Binding sites of CO_2 molecules and the two linker fragments are shown in Figure 6.28. The first binding site is the strongest interaction between the CO_2 molecule and the linker found by DFT calculations and shows cooperative binding within the cavity of the fragment. (Figure 6.28 a) with a BE of -27.54 kJ mol^{-1}. The CO_2 molecule lies to the centre of the cavity with electrostatic interactions between the oxygen of the CO_2 molecule and the nitrogen atoms of the two amide groups and interactions between the carbon of the CO_2 molecule and isophthalate –CH groups of the outer phenyl rings. This is similar to sites found by NPD within cage C where the

CO_2 molecule was seen to form H-bonds with both the free amide groups and the adjacent isophthalate groups, second in occupancy to the OMSs in cage C. A range binding sites were found along the length of the linker (Figure 6.28 b) with binding energies of -11.85 to -17.30 kJ mol^{-1}. The top of Figure 6.28 b shows a weak H-bond interaction between an oxygen of the CO_2 molecule and the –CH group of the central phenyl ring. The bottom of the figure shows a reasonable binding between the CO_2 molecule and the linker fragment with cooperative binding between the –CH groups of the phenyl rings and the CO_2 oxygen atoms and electrostatic interaction between the oxygen of the linker and the carbon of CO_2. This site is occupied in cage C with weak interactions according to NPD data. Within cage A and B NPD shows no specific binding at these sites which shows how important the OMSs are at these points within the MOF structure for CO_2 binding.

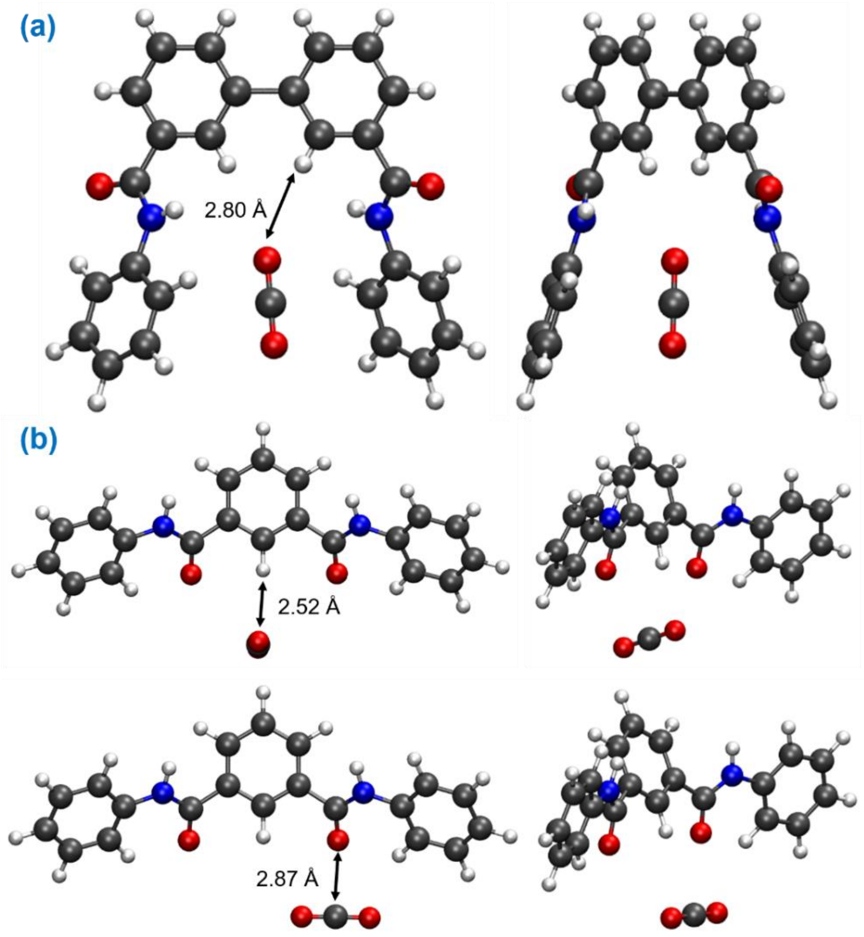

Figure 6.28: Binding sites of CO_2-MFM-188 found at (a) cavity similar to cage A and C (b) alongside of the linker in cage B and C.

The binding of the C_2H_2 molecule with the two linker fragments of MFM-188 was also investigated using DFT calculations, giving a range of interaction sites shown in Figure 6.29. The strongest binding site is found within the cavity and shows cooperative binding effects between both of the N-H groups pointing into the pore and the π electrons of the C_2H_2 molecule (-23.96 kJ mol^{-1}). This agrees with the NPD data where H-bonds *via* its C≡C(δ-) π electrons to the N-H groups pointing into the pore are found in both cage C and A with high occupancy, only being higher near OMSs. Again, a range of binding sites were found across the length of the linker for C_2H_2 (Figure 6.29 b). The first of the sites shown (top of Figure 6.29 b) is the weakest binding of C_2H_2 to the linker fragment found by DFT (-9.34 kJ mol^{-1}) and is made up of weak electrostatic interactions between π electrons of the C_2H_2 molecule and the isophthalate oxygen atom and weak vdW interactions between the hydrogen of the central phenyl ring and the hydrogen of C_2H_2. The bottom of Figure 6.29 shows much stronger binding of C_2H_2 to the length of the linker (-16.56 kJ mol^{-1}) formed from a H-bond interaction between one hydrogen of C_2H_2 and the carboxylate oxygen. These calculations confirm the NPD results with the C_2H_2 showing a role as a H-bond acceptor and donator and significant binding occurring near the free amides. The difference in binding in the cages of the MOF given by the DFT calculations compared to NPD and INS shows the importance of the OMSs and how the combination of the free amides and OMSs in the pores plays a crucial role in gas uptake.

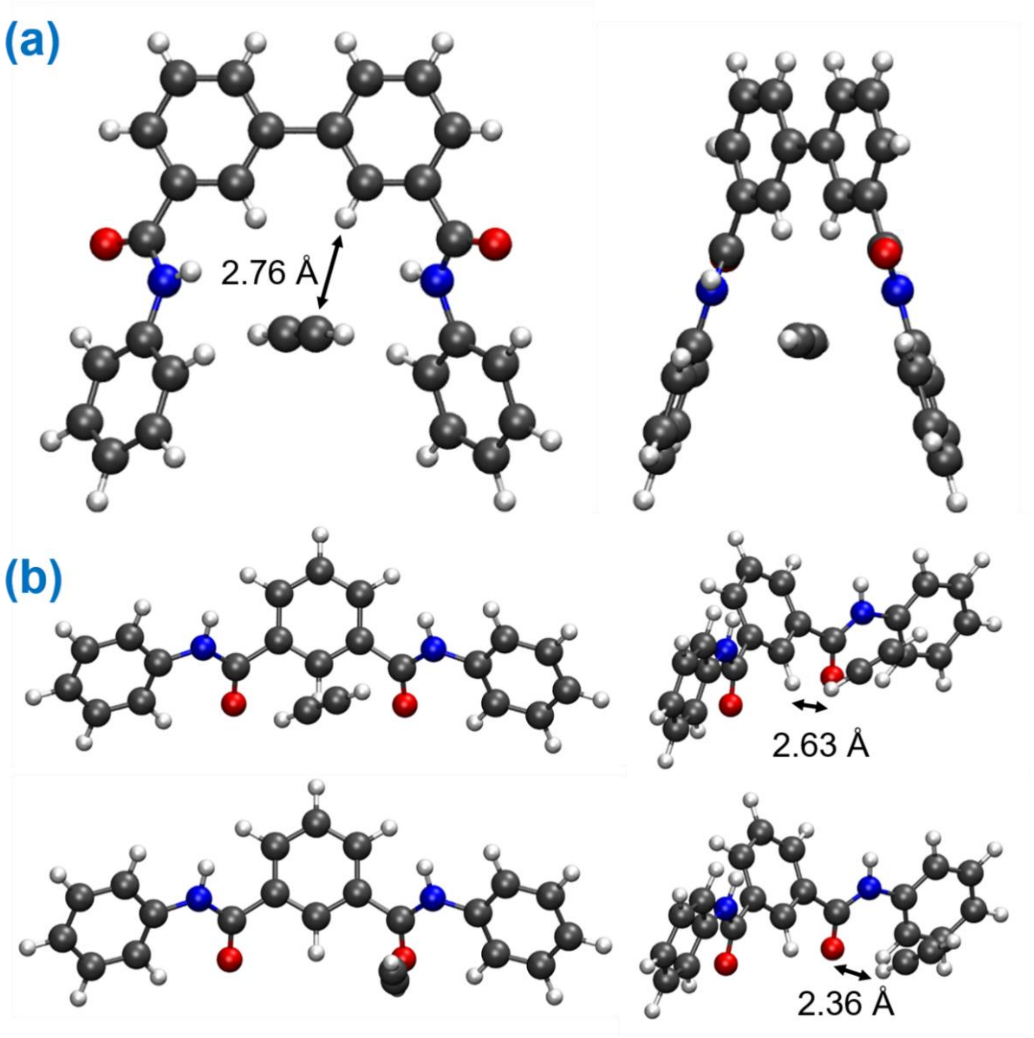

Figure 6.29: The binding sites of C_2H_2-MFM-188 found at (a) cavity found in cage A and C and (b) alongside of the linker in cage B and C.

With such strong uptake of C_2H_2, there is a potential for this MOF to be used for hydrocarbon separation from methane like MFM-160. Therefore, to complete the computational study of MFM-188 the binding of CH_4 was also investigated. The strongest binding site of CH_4 and the linker fragments of MFM-188 is within the cage with a binding of -10.54 kJ mol^{-1} (Figure 6.30 a). This is an interaction between one of the outer phenyl rings and a hydrogen atom of the CH_4 molecule. The range of binding sites found over the arm of the linker and the free amides only produce weak interactions (Figure 6.30 b). The first site shows an interaction between the oxygen on the linker and a hydrogen of CH_4 to give a BE of -5.20 kJ mol^{-1} (top of Figure 6.30 b).

Another binding site shows a weak interaction between the hydrogen of the central phenyl ring to give a BE of -4.00 kJ mol^{-1} (bottom of Figure 6.30). These results suggest the amides will not have a strong effect on binding of CH_4 within MFM-188 either within the cages or as free amides available when compared with binding of C_2H_2.

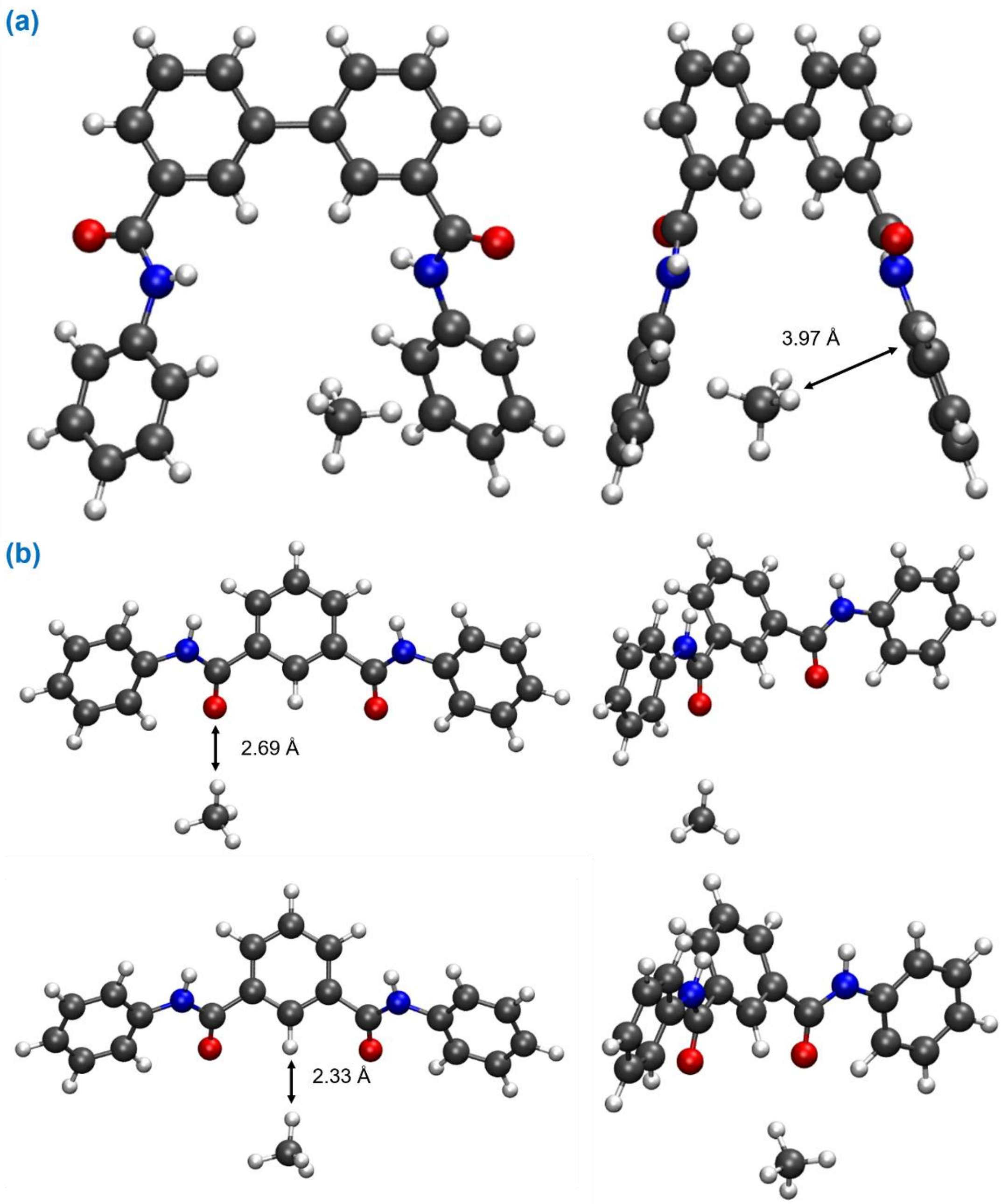

Figure 6.30: The strongest CH_4-MFM-188 sites found at (a) cavity and (b) alongside of the linker.

6.34 Summary

Overall, MFM-188 shows excellent performance for potential applications for C_2H_2 storage (27.0 wt%) and exhibits high adsorption uptake of CO_2 (23.7 wt%) under ambient conditions. It is clear that to achieve high C_2H_2 uptake capacity, integration of high BET surface area (and porosity to a wider extent) and high density of binding sites in the pore structure is required. However, this is often inherently contradictory since high surface area/porosity will naturally dilute the binding sites in the pore, leading to an inevitable trade-off between these two factors. MFM-188 displays a suitably high BET surface area and high density of binding sites owing to its framework topology and pore geometry, and therefore, shows a record high C_2H_2 uptake.

Although it is widely believed that the pendent amide groups in pores will actively participate in gas adsorption *via* H-bonding, no cogent experimental evidence has been reported to date. The present study represents a unique example of a comprehensive investigation of the gas-sorbent binding interaction in a tetra-amide functionalized MOF *via* a combination of neutron diffraction, spectroscopic techniques and computational methods. These experiments offer key insights into the molecular details of this host-guest system from both crystallographic, dynamic and *ab initio* perspectives. A highly cooperative binding mechanism of CO_2 and C_2H_2 was found on the OMSs and free amide groups in the pores of MFM-188, with one site enhancing binding at the other.

6.4 Conclusions

In conclusion, this work not only offers two, new porous materials for purification of natural gas and high capacity CO_2 and C_2H_2 storage, but also, more importantly, facilitates the design and structural optimisation for new porous materials with improved performance in gas adsorption. The combination of experimental and computational techniques gives detailed insight into interactions within these MOFs and reveals the importance of a balance between surface area, pore volume and functionality within MOFs is essential to designing MOFs for targeted applications.

Chapter 7

Conclusions

> You'll know her more by your questions than by her answers. Keep looking at her long enough. One day you might see someone you know.
>
> - *Jerry Spinelli, Stargirl*

Over recent years, MOFs have emerged as possible materials for a range of gas storage and separation applications, offering a potentially more energy-efficient alternative to traditional gas storage and separation techniques. The use of computational tools is essential to find and design new MOF materials adapted for function. A range of computational techniques has been used over the past decade to investigate MOFs and the work presented here shows a number of these methods including *ab initio* methods in the form of DFT calculations and molecular simulations methods using GCMC ensembles. In particular, the investigation of binding between MOF-like structures and small organic molecules using these approaches is focussed on to further understand and aid design of MOFs as adsorbents.

In the case of computational investigations using generic force fields, evaluation through a combination of classical and quantum chemical simulations illustrates that the DREIDING FF provides excellent quantitative agreement with experimental data in agreement with literature as shown in Chapter 3. DREIDING and OPLS-AA are also shown to predict gas-ligand binding location and energy with a high level accuracy when compared to DFT calculations. However, DFT calculations are still necessary when ligands contain a high concentration of oxygen or nitrogen as the accuracy of FF methods decrease greatly for MOFs containing these atoms. Therefore, using these *ab initio* methods to investigate gas-ligand binding is essential for many functionalised MOF structures.

Following this, an *ab initio* investigation into the binding of functional organic molecules with methane was carried out. Selected functional groups and their binding interactions with methane were studied to show various interactions involving weak H bonding. These weak interactions play an important role in low pressure adsorption within porous materials so the functionalised organic molecules were identified to have potential to be incorporated into various structures to potentially increase the interactions between adsorbent and adsorbate.

The computational study was continued in the next chapter which investigated a series of theoretical MOFs containing hexabenzocoronene to further develop the understanding of the potential of functionalised groups to enhance methane binding and uptake. GCMC simulations of CH_4 uptake were carried out on the whole series of MOFs and illustrated the importance of a combination of functionalisation and optimum pore size is essential to reaching gas adsorption targets as some gravimetric and volumetric targets are met by the MOFs, but no MOF simultaneously satisfies both. Overall, this study illustrated that incorporation of a hexabenzocoronene molecule within the central ligand fragment is a viable linker modification method, which could have potential in enhancement of gas uptake for gaseous molecules including methane. Experimental work is currently being carried out in an attempt to synthesise similar MOF structures, showing how the computational study of theoretical MOFs can help to guide experimental investigations.

In the last chapter, a combination of experimental and computational data was presented for the two, new copper MOFs MFM-160 and MFM-188. Both MOFs exhibit a potential for use in natural gas separation applications and high capacity CO_2 and C_2H_2 storage. The experimental part of the study on MFM-160 revealed a slow phenyl rotation resulting from interference of gas binding into intramolecular forces within the MOF. This was confirmed by DFT calculations with the strongest binding between the linker fragment and gaseous molecules studied occurring over that particular hydrogen bond. The studies on MFM-188 show that a combination of high surface area and high density of binding sites are essential to achieve a high capacity of gas uptake, in this case C_2H_2 uptake. The use of both experimental and computational investigations on this MOF revealed how cooperative binding effects of free amide groups and OMSs has an important role in how uptake occurs within MFM-188, leading to a high uptake of both C_2H_2 and CO_2.

In summary, all work undertaken through this thesis has illustrated that computational investigations into the binding between organic molecules and MOFs is essential to further understand and develop MOFs for gas adsorption. The combination of experimental and computational work provides a detailed understanding of the different interactions that occur upon adsorption within MOFs and overall, shows the vital importance of functionalisation of organic linkers when designing MOFs for targeted adsorption and separation applications, along with optimum pore volume and OMSs. Computational work will continue to be used in this regard, supporting and developing understanding and synthesis of porous materials with further insight available as computational techniques advance.

References

(1) Gahleitner, G. Hydrogen from Renewable Electricity: An International Review of Power-to-Gas Pilot Plants for Stationary Applications. *Int. J. Hydrogen Energy* **2013**, *38* (5), 2039–2061.

(2) Winsche, W. E.; Hoffman, K. C.; Salzano, F. J. Hydrogen: Its Future Role in the Nation's Energy Economy. *Science (80-.).* **1973**, *180* (4093), 1325–1332.

(3) Zhou, L. Progress and Problems in Hydrogen Storage Methods. *Renew. Sustain. Energy Rev.* **2005**, *9* (4), 395–408.

(4) Alcañiz-Monge, J.; Román-Martínez, M. C. Upper Limit of Hydrogen Adsorption on Activated Carbons at Room Temperature: A Thermodynamic Approach to Understand the Hydrogen Adsorption on Microporous Carbons. *Microporous Mesoporous Mater.* **2008**, *112* (1–3), 510–520.

(5) Czaja, A. U.; Trukhan, N.; Müller, U. Industrial Applications of Metal–organic Frameworks. *Chem. Soc. Rev.* **2009**, *38* (5), 1284.

(6) Liu, K.; Ma, D.; Li, B.; Li, Y.; Yao, K.; Zhang, Z.; Han, Y.; Shi, Z. High Storage Capacity and Separation Selectivity for C $_2$ Hydrocarbons over Methane in the Metal–organic Framework Cu–TDPAT. *J. Mater. Chem. A* **2014**, *2* (38), 15823–15828.

(7) Menon, V. C.; Komarneni, S. Porous Adsorbents for Vehicular Natural Gas Storage: A Review. *J. Porous Mater.* **1998**, *58*, 43–58.

(8) Liu, K.; Li, B.; Li, Y.; Li, X.; Yang, F.; Zeng, G.; Peng, Y.; Zhang, Z.; Li, G.;

Shi, Z.; et al. An N-Rich Metal–organic Framework with an Rht Topology: High CO2 and C2 Hydrocarbons Uptake and Selective Capture from CH4. *Chem. Commun.* **2014**, *50* (39), 5031.

(9) Lozano-Castello, D.; Alcañiz-Monge, J.; de la Casa-Lillo, M. A.; Cazorla-Amorós, D.; Linares-Solano, A. Advances in the Study of Methane Storage in Porous Carbonaceous Materials. *Fuel* **2002**, *81*, 1777–1803.

(10) Peng, Y.; Krungleviciute, V.; Eryazici, I.; Hupp, J. T.; Farha, O. K.; Yildirim, T. Methane Storage in Metal-Organic Frameworks: Current Records, Surprise Findings, and Challenges. *J. Am. Chem. Soc.* **2013**, *135* (32), 11887–11894.

(11) Mason, J. A.; Veenstra, M.; Long, J. R. Evaluating Metal–organic Frameworks for Natural Gas Storage. *Chem. Sci.* **2014**, *5* (1), 32.

(12) Makal, T. A.; Li, J.-R.; Lu, W.; Zhou, H.-C. Methane Storage in Advanced Porous Materials. *Chem. Soc. Rev.* **2012**, *41* (23), 7761–7779.

(13) He, Y.; Song, C.; Ling, Y.; Wu, C.; Krishna, R.; Chen, B. A New MOF-5 Homologue for Selective Separation of Methane from C2 Hydrocarbons at Room Temperature. *APL Mater.* **2014**, *2* (12), 124102.

(14) Herm, Z. R.; Bloch, E. D.; Long, J. R. Hydrocarbon Separations in Metal−Organic Frameworks. *Chem. Mater.* **2013**, *26*, 323–338.

(15) Trung, T. K.; Trens, P.; Tanchoux, N.; Bourrelly, S.; Llewellyn, P. L.; Loera-Serna, S.; Serre, C.; Loiseau, T.; Fajula, F.; Rard, G.; et al. Hydrocarbon Adsorption in the Flexible Metal Organic Frameworks MIL-53(Al, Cr). *J. Am. Chem. Soc.* **2008**, *130*, 16926–16932.

(16) Xu, H.; He, Y.; Zhang, Z.; Xiang, S.; Cai, J.; Cui, Y.; Yang, Y.; Qian, G.; Chen, B. A Microporous Metal-Organic Framework with Both Open Metal and Lewis Basic Pyridyl Sites for Highly Selective C2H2/CH4 and C2H2/CO2 Gas Separation at Room Temperature. *J. Am. Chem. Soc.* **2013**, *1* (1), 77–81.

(17) Verma, P.; Xu, X.; Truhlar, D. G. Adsorption on Fe-MOF-74 for C1−C3 Hydrocarbon Separation. *J. Phys. Chem. C* **2013**, *117,* 12648–12660.

(18) Chen, Z.; Xiang, S.; Arman, H. D.; Mondal, J. U.; Li, P.; Zhao, D.; Chen, B. Three-Dimensional Pillar-Layered Copper(II) Metal-Organic Framework with Immobilized Functional OH Groups on Pore Surfaces for Highly Selective CO2/CH4 and C2H2/CH4 Gas Sorption at Room Temperature. *Inorg. Chem.* **2011**, *50*, 3442–3446.

(19) Cai, J.; Yu, J.; Xu, H.; He, Y.; Duan, X.; Cui, Y.; Wu, C.; Chen, B.; Qian, G. A Doubly Interpenetrated Metal−Organic Framework with Open Metal Sites and Suitable Pore Sizes for Highly Selective Separation of Small Hydrocarbons at Room Temperature. *Cryst. Growth Des.* **2013**, *13*, 2094–2097.

(20) Sabouni, R.; Kazemian, H.; Rohani, S. Carbon Dioxide Capturing Technologies: A Review Focusing on Metal Organic Framework Materials (MOFs). *Environ. Sci. Pollut. Res. Int.* **2014**, *21* (8), 5427–5449.

(21) D'Alessandro, D. M.; Smit, B.; Long, J. R. Carbon Dioxide Capture: Prospects for New Materials. *Angew. Chem. Int. Ed. Engl.* **2010**, *49* (35), 6058–6082.

(22) Yang, S.; Sun, J.; Ramirez-Cuesta, A. J.; Callear, S. K.; David, W. I. F.; Anderson, D. P.; Newby, R.; Blake, A. J.; Parker, J. E.; Tang, C. C.; et al. Selectivity and Direct Visualization of Carbon Dioxide and Sulfur Dioxide in a Decorated Porous Host. *Nat. Chem.* **2012**, *4*, 887–894.

(23) An, J.; Geib, S. J.; Rosi, N. L. High and Selective CO2 Uptake in a Cobalt Adeninate Metal-Organic Framework Exhibiting Pyrimidine- and Amino-Decorated Pores. *J. Am. Chem. Soc.* **2010**, *132* (1), 38–39.

(24) Millward, A. R.; Yaghi, O. M. Metal-Organic Frameworks with Exceptionally High Capacity for Storage of Carbon Dioxide at Room Temperature. *J. Am. Chem. Soc.* **2005**, *127* (51), 17998–17999.

(25) McDonald, T. M.; Ram Lee, W.; Mason, J. A.; Wiers, B. M.; Seop Hong, C.; Long, J. R. Capture of Carbon Dioxide from Air and Flue Gas in the Alkylamine- Appended Metal−Organic Framework Mmen-Mg2(Dobpdc). *J. Am. Chem. Soc.* **2012**, *134*, 7056–7065.

(26) Arstad, B.; Fjellvåg, H.; Kjell, ·; Kongshaug, O.; Swang, O.; Blom, R.; Arstad, B.; Swang, O.; Blom, · R; Fjellvåg, H.; et al. Amine Functionalised Metal Organic Frameworks (MOFs) as Adsorbents for Carbon Dioxide. *Adsorption* **2008**, *14*, 755–762.

(27) Alsmail, N. H.; Suyetin, M.; Yan, Y.; Cabot, R.; Krap, C. P.; Lü, J.; Easun, T. L.; Bichoutskaia, E.; Lewis, W.; Blake, A. J.; et al. Analysis of High and Selective Uptake of CO2 in an Oxamide-Containing {Cu2 (OOCR)4 }-Based Metal-Organic Framework. *Chem. Eur. J.* **2014**, *20* (24), 7317–7324.

(28) Mulfort, K.; Farha, O.; Malliakas, C.; Kanatzidis, M.; Hupp, J. An

Interpenetrated Framework Material with Hysteretic CO $_2$ Uptake. *Chem. - A Eur. J.* **2010**, *16* (1), 276–281.

(29) Bae, Y.-S.; Snurr, R. Q. Development and Evaluation of Porous Materials for Carbon Dioxide Separation and Capture. *Angew. Chemie Int. Ed.* **2011**, *50* (49), 11586–11596.

(30) Chang, F.; Zhou, J.; Chen, P.; Chen, Y.; Honghua, J.; Saad, S. M. I.; Gao, Y.; Cao, X.; Zheng, T. Microporous and Mesoporous Materials for Gas Storage and Separation: A Review. *Asia-Pacific J. Chem. Eng.* **2013**, *8*, 618–626.

(31) Yaghi, O. M.; Li, H. Hydrothermal Synthesis of a Metal-Organic Framework Containing Large Rectangular Channels. *J. Am. Chem. Soc.* **1995**, *117* (41), 10401–10402.

(32) Férey, G. Hybrid Porous Solids: Past, Present, Future. *Chem. Soc. Rev.* **2008**, *37* (1), 191–214.

(33) Mueller, U.; Schubert, M.; Teich, F.; Puetter, H.; Schierle-Arndt, K.; Pastré, J. Metal–organic Frameworks—prospective Industrial Applications. *J. Mater. Chem.* **2006**, *16* (7), 626.

(34) Ma, L.; Abney, C.; Lin, W. Enantioselective Catalysis with Homochiral Metal-Organic Frameworks. *Chem. Soc. Rev.* **2009**, *38* (5), 1248–1256.

(35) Lee, J.; Farha, O. K.; Roberts, J.; Scheidt, K. A.; Nguyen, S. T.; Hupp, J. T. Metal-Organic Framework Materials as Catalysts. *Chem. Soc. Rev.* **2009**, *38* (5), 1450–1459.

(36) Allendorf, M. D.; Bauer, C. A.; Bhakta, R. K.; Houk, R. J. T. Luminescent

Metal-Organic Frameworks. *Chem. Soc. Rev.* **2009**, *38* (5), 1330–1352.

(37) Min, K. S.; Suh, M. P. Silver (I)-Polynitrile Network Solids for Anion Exchange: Anion-Induced Transformation of Supramolecular Structure in the Crystalline State. *J. Am. Chem. Soc.* **2000**, *122* (I), 6834–6840.

(38) An, J.; Geib, S. J.; Rosi, N. L. Cation-Triggered Drug Release from a Porous Zinc-Adeninate Metal-Organic Framework. *J. Am. Chem. Soc.* **2009**, *131* (24), 8376–8377.

(39) Horcajada, P.; Serre, C.; Vallet-Regí, M.; Sebban, M.; Taulelle, F.; Férey, G. Metal-Organic Frameworks as Efficient Materials for Drug Delivery. *Angew. Chem. Int. Ed. Engl.* **2006**, *45* (36), 5974–5978.

(40) Sava, D. F.; Kravtsov, V. C.; Eckert, J.; Eubank, J. F.; Nouar, F.; Eddaoudi, M. Exceptional Stability and High Hydrogen Uptake in Hydrogen-Bonded Metal-Organic Cubes Possessing ACO and AST Zeolite-like Topologies. *J. Am. Chem. Soc.* **2009**, *131* (30), 10394–10396.

(41) Lin, X.; Telepeni, I.; Blake, A. J.; Dailly, A.; Brown, C. M.; Simmons, J. M.; Zoppi, M.; Walker, G. S.; Thomas, K. M.; Mays, T. J.; et al. High Capacity Hydrogen Adsorption in Cu(II) Tetracarboxylate Framework Materials: The Role of Pore Size, Ligand Functionalization, and Exposed Metal Sites. *J. Am. Chem. Soc.* **2009**, *131* (6), 2159–2171.

(42) Murray, L. J.; Dincă, M.; Long, J. R. Hydrogen Storage in Metal-Organic Frameworks. *Chem. Soc. Rev.* **2009**, *38* (5), 1294–1314.

(43) Kaye, S. S.; Dailly, A.; Yaghi, O. M.; Long, J. R. Impact of Preparation and

Handling on the Hydrogen Storage Properties of Zn4O (1,4benzenedicarboxylate)3 (MOF-5). *J. Am. Chem. Soc.* **2007**, *3*, 14176–14177.

(44) Furukawa, H.; Miller, M. A.; Yaghi, O. M. Independent Verification of the Saturation Hydrogen Uptake in MOF-177 and Establishment of a Benchmark for Hydrogen Adsorption in Metal–organic Frameworks. *J. Mater. Chem.* **2007**, *17* (30), 3197.

(45) Koh, K.; Wong-Foy, A. G.; Matzger, A. J. A Porous Coordination Copolymer with over 5000 M2/g BET Surface Area. *J. Am. Chem. Soc.* **2009**, *131* (12), 4184–4185.

(46) Rosi, N. L.; Eckert, J.; Eddaoudi, M.; Vodak, D. T.; Kim, J.; O'Keeffe, M.; Yaghi, O. M. Hydrogen Storage in Microporous Metal-Organic Frameworks. *Science* **2003**, *300* (5622), 1127–1129.

(47) Eddaoudi, M.; Kim, J.; Rosi, N.; Vodak, D.; Wachter, J.; O'Keeffe, M.; Yaghi, O. M. Systematic Design of Pore Size and Functionality in Isoreticular MOFs and Their Application in Methane Storage. *Science* **2002**, *295* (5554), 469–472.

(48) Li, J.-R.; Kuppler, R. J.; Zhou, H.-C. Selective Gas Adsorption and Separation in Metal-Organic Frameworks. *Chem. Soc. Rev.* **2009**, *38* (5), 1477–1504.

(49) Tranchemontagne, D. J.; Mendoza-Cortés, J. L.; O'Keeffe, M.; Yaghi, O. M. Secondary Building Units, Nets and Bonding in the Chemistry of Metal-Organic Frameworks. *Chem. Soc. Rev.* **2009**, *38* (5), 1257–1283.

(50) Zhang, J.-P.; Zhang, Y.-B.; Lin, J.-B.; Chen, X.-M. Metal Azolate Frameworks: From Crystal Engineering to Functional Materials. *Chem. Rev.* **2012**, *112* (2), 1001–1033.

(51) Li, H.; Eddaoudi, M.; O'Keeffe, M.; Yaghi, O. M. Design and Synthesis of an Exceptionally Stable and Highly Porous Metal-Organic Framework. *Nature* **1999**, *402* (November), 276–279.

(52) Botas, J. A.; Calleja, G.; Sánchez-Sánchez, M.; Orcajo, M. G. Cobalt Doping of the MOF-5 Framework and Its Effect on Gas-Adsorption Properties. *Langmuir* **2010**, *26* (8), 5300–5303.

(53) Sumida, K.; Rogow, D. L.; Mason, J. A.; McDonald, T. M.; Bloch, E. D.; Herm, Z. R.; Bae, T.-H.; Long, J. R. Carbon Dioxide Capture in Metal-Organic Frameworks. *Chem. Rev.* **2012**, *112* (2), 724–781.

(54) Suh, M. P.; Park, H. J.; Prasad, T. K.; Lim, D.-W. Hydrogen Storage in Metal-Organic Frameworks. *Chem. Rev.* **2012**, *112* (2), 782–835.

(55) Ockwig, N. W.; Delgado-Friedrichs, O.; O'Keeffe, M.; Yaghi, O. M. Reticular Chemistry: Occurrence and Taxonomy of Nets and Grammar for the Design of Frameworks. *Acc. Chem. Res.* **2005**, *38* (3), 176–182.

(56) Keeffe, M. O.; Peskov, M. A.; Ramsden, S. J.; Yaghi, O. M. The Reticular Chemistry Structure Resource (RCSR) Database of, and Symbols for, Crystal Nets. *Acc. Chem. Res.* **2008**, *41* (12), 1782–1789.

(57) Chui, S. S. Y.; Lo, S. M. F.; Charmant, J. P. H.; Orpen, a G.; Williams, I. D. A Chemically Functionalizable Nanoporous Material [Cu3(TMA)2(H2O)3]N.

Science (80-.). **1999**, *283* (February), 1148–1150.

(58) Yan, Y.; Lin, X.; Yang, S.; Blake, A. J.; Dailly, A.; Champness, N. R.; Schro, M.; Hubberstey, P.; Schröder, M. Exceptionally High H2 Storage by a Metal-Organic Polyhedral Framework. *Chem. Commun. (Camb).* **2009**, No. 9, 1025–1027.

(59) Wilmer, C. E.; Leaf, M.; Lee, C. Y.; Farha, O. K.; Hauser, B. G.; Hupp, J. T.; Snurr, R. Q. Large-Scale Screening of Hypothetical Metal-Organic Frameworks. *Nat. Chem.* **2012**, *4* (2), 83–89.

(60) Duren, T.; Millange, F.; Férey, G.; Walton, K. S.; Snurr, R. Q. Calculating Geometric Surface Areas as a Characterization Tool for Metal-Organic Frameworks. *J. Phys. Chem. C* **2007**, *111* (2), 15350–15356.

(61) Farha, O. K.; Yazaydın, A. Ö.; Eryazici, I.; Malliakas, C. D.; Hauser, B. G.; Kanatzidis, M. G.; Nguyen, S. T.; Snurr, R. Q.; Hupp, J. T. De Novo Synthesis of a Metal-Organic Framework Material Featuring Ultrahigh Surface Area and Gas Storage Capacities. *Nat. Chem.* **2010**, *2* (11), 944–948.

(62) Yang, S.; Ramirez-Cuesta, A. J.; Newby, R.; Garcia-Sakai, V.; Manuel, P.; Callear, S. K.; Campbell, S. I.; Tang, C. C.; Schröder, M. Supramolecular Binding and Separation of Hydrocarbons within a Functionalized Porous Metal–organic Framework. *Nat. Chem.* **2015**, *7*, 121–129.

(63) Liu, D.; Zhong, C. Understanding Gas Separation in Metal–organic Frameworks Using Computer Modeling. *J. Mater. Chem.* **2010**, *20* (46), 10308.

(64) Yang, Q.; Liu, D.; Zhong, C.; Li, J.-R. Development of Computational Methodologies for Metal-Organic Frameworks and Their Application in Gas Separations. *Chem. Rev.* **2013**, *113* (10), 8261–8323.

(65) Pillai, R. S.; Pinto, M. L.; Pires, J. O.; Jorge, M.; Gomes, J. B. Understanding Gas Adsorption Selectivity in IRMOF-8 Using Molecular Simulation. *ACS Appl. Mater. Interfaces* **2015**, *7*, 624–637.

(66) Yan, Y.; Telepeni, I.; Yang, S.; Lin, X.; Kockelmann, W.; Dailly, A.; Blake, A. J.; Lewis, W.; Walker, G. S.; Allan, D. R.; et al. Metal-Organic Polyhedral Frameworks: High H2 Adsorption Capacities and Neutron Powder Diffraction Studies. *J. Am. Chem. Soc.* **2010**, *132* (12), 4092–4094.

(67) Queen, W. L.; Brown, C. M.; Britt, D. K.; Zajdel, P.; Hudson, M. R.; Yaghi, O. M. Site-Specific CO2 Adsorption and Zero Thermal Expansion in an Anisotropic Pore Network. *J. Phys. Chem. C* **2011**, *115*, 24915–24919.

(68) Pang, J.; Jiang, F.; Wu, M.; Liu, C.; Su, K.; Lu, W.; Yuan, D.; Hong, M. A Porous Metal-Organic Framework with Ultrahigh Acetylene Uptake Capacity under Ambient Conditions. *Nat. Commun.* **2015**, *6*, 7575.

(69) Bloch, E. D.; Queen, W. L.; Krishna, R.; Zadrozny, J. M.; Brown, C. M.; Long, J. R. Hydrocarbon Separations in a Metal-Organic Framework with Open Iron(II) Coordination Sites. *Science (80-.).* **2012**, *335* (6076), 1606–1610.

(70) Wu, H.; Zhou, W.; Yildirim, T. High-Capacity Methane Storage in Metal-Organic Frameworks M2(Dhtp): The Important Role of Open Metal Sites. *J. Am. Chem. Soc.* **2009**, *131* (13), 4995–5000.

(71) Callear, S. K.; Ramirez-Cuesta, A. J.; David, W. I. F.; Millange, F.; Walton, R. I. High-Resolution Inelastic Neutron Scattering and Neutron Powder Diffraction Study of the Adsorption of Dihydrogen by the Cu(II) Metal-Organic Framework Material HKUST-1. *Chem. Phys.* **2013**, *427*, 9–17.

(72) Vaidhyanathan, R.; Iremonger, S. S.; Shimizu, G. K. H.; Boyd, P. G.; Alavi, S.; Woo, T. K. Direct Observation and Quantification of CO2 Binding Within an Amine-Funtionalized Nanoporous Solid. *Science (80-.).* **2010**, *330* (6004), 650–653.

(73) Lin, J.-B.; Xue, W.; Zhang, J.-P.; Chen, X.-M. An Ionic Porous Coordination Framework Exhibiting High CO2 Affinity and CO2/CH4 Selectivity. *Chem. Commun.* **2011**, *47* (3), 926–928.

(74) Liao, P.-Q.; Zhou, D.-D.; Zhu, A.-X.; Jiang, L.; Lin, R.-B.; Zhang, J.-P.; Chen, X.-M. Strong and Dynamic CO2 Sorption in a Flexible Porous Framework Possessing Guest Chelating Claws. *J. Am. Chem. Soc.* **2012**, *134*, 17380–17383.

(75) Krishna, R.; van Baten, J. M. In Silico Screening of Metal-Organic Frameworks in Separation Applications. *Phys. Chem. Chem. Phys.* **2011**, *13* (22), 10593–10616.

(76) Torrisi, A.; Mellot-Draznieks, C.; Bell, R. G. Impact of Ligands on CO2 Adsorption in Metal-Organic Frameworks: First Principles Study of the Interaction of CO2 with Functionalized Benzenes. I. Inductive Effects on the Aromatic Ring. *J. Chem. Phys.* **2009**, *130* (19), 194703.

(77) Torrisi, A.; Mellot-Draznieks, C.; Bell, R. G. Impact of Ligands on CO2

Adsorption in Metal-Organic Frameworks: First Principles Study of the Interaction of CO2 with Functionalized Benzenes. II. Effect of Polar and Acidic Substituents. *J. Chem. Phys.* **2010**, *132* (4), 044705.

(78) Kim, K. C.; Yu, D.; Snurr, R. Q. Computational Screening of Functional Groups for Ammonia Capture in Metal-Organic Frameworks. *Langmuir* **2013**, *29* (5), 1446–1456.

(79) Amrouche, H.; Aguado, S.; Pérez-Pellitero, J.; Chizallet, C.; Siperstein, F.; Farrusseng, D.; Bats, N.; Nieto-Draghi, C. Experimental and Computational Study of Functionality Impact on Sodalite-Zeolitic Imidazolate Frameworks for CO2 Separation. *J. Phys. Chem. C* **2011**, *115* (33), 16425–16432.

(80) Yu, D.; Ghosh, P.; Snurr, R. Q. Hierarchical Modeling of Ammonia Adsorption in Functionalized Metal-Organic Frameworks. *Dalton Trans.* **2012**, *41* (14), 3962–3973.

(81) Torrisi, A.; Bell, R. G.; Mellot-Draznieks, C. Predicting the Impact of Functionalized Ligands on CO2 Adsorption in MOFs: A Combined DFT and Grand Canonical Monte Carlo Study. *Microporous Mesoporous Mater.* **2013**, *168*, 225–238.

(82) Vardhan, H.; Yusubov, M.; Verpoort, F. Self-Assembled Metal-Organic Polyhedra: An Overview of Various Applications. *Coord. Chem. Rev.* **2016**, *306* (P1), 171–194.

(83) Davankov, V. A.; Rogozhin, S. V.; Tsjurupa, M. P. Factors Determining Degree of Swelling of Crosslinked Polymers. *Angew. Makromol. Chemie* **1973**, *32*, 145–151.

(84) Lu, W.; Yuan, D.; Zhao, D.; Schilling, C. I.; Plietzsch, O.; Muller, T.; Bräse, S.; Guenther, J.; Blümel, J.; Krishna, R.; et al. Porous Polymer Networks: Synthesis, Porosity, and Applications in Gas Storage/Separation. *Chem. Mater.* **2010**, *22* (21), 5964–5972.

(85) Mendoza-cortes, J. L.; Goddard, W. a; Furukawa, H.; Yaghi, O. M. A Covalent Organic Framework That Exceeds the DOE 2015 Volumetric Target for H 2 Uptake at 298 K. *J. Phys. Chem. Lett.* **2012**, *3*, 2671–2675.

(86) Cossi, M.; Gatti, G.; Canti, L.; Tei, L.; Errahali, M.; Marchese, L. Theoretical Prediction of High Pressure Methane Adsorption in Porous Aromatic Frameworks (PAFs). *Langmuir* **2012**, *28*, 14405–14414.

(87) Wang, G.; Leus, K.; Zhao, S.; Van Der Voort, P. Newly Designed Covalent Triazine Framework Based on Novel N-Heteroaromatic Building Blocks for Efficient CO2and H2Capture and Storage. *ACS Appl. Mater. Interfaces* **2017**, *10* (1), 1244–1249.

(88) Tian, J.; Thallapally, P. K.; McGrail, B. P. Porous Organic Molecular Materials. *CrystEngComm* **2012**, *14* (6), 1909–1919.

(89) Lennox, M. J.; Bound, M.; Henley, A.; Besley, E. Molecular Simulation The Right Isotherms for the Right Reasons? Validation of Generic Force Fields for Prediction of Methane Adsorption in Metal-Organic Frameworks. *Mol. Simul.* **2017**, *43*, 828–837.

(90) Henley, A.; Bound, M.; Besley, E. Effective Binding of Methane Using a Weak Hydrogen Bond. *J. Phys. Chem. A* **2016**, *120*, 3701–3709.

(91) Bichoutskaia, E.; Suyetin, M.; Bound, M.; Yan, Y.; Schröder, M. Methane Adsorption in Metal−Organic Frameworks Containing Nanographene Linkers: A Computational Study. *J. Phys. Chem. C* **2014**, *118*, 15573–15580.

(92) Trenholme, W. J. F.; Kolokolov, D. I.; Bound, M.; Argent, S. P.; Gould, J. A.; Barnett, S. A.; Blake, A. J.; Stepanov, A. G.; Besley, E.; Easun, T. L.; et al. Highly Selective Gas Uptake and Unique Rotational Dynamics in a (3,24)-Connected Cu(II). **2017**, In Preparation.

(93) Moreau, F.; da Silva, I.; Al Smail, N. H.; Easun, T. L.; Savage, M.; Godfrey, H. G. W.; Parker, S. F.; Manuel, P.; Yang, S.; Schröder, M. Unravelling Exceptional Acetylene and Carbon Dioxide Adsorption within a Tetra-Amide Functionalized Metal-Organic Framework. *Nat. Commun.* **2017**, *8*, 14085.

(94) Hohenberg, P.; Kohn, W. Inhomogeneous Electron Gas. *Phys. Rev.* **1964**, *136*, 864–871.

(95) Kohn, W.; Sham, L. J. Self-Consistent Equations Including Exchange and Correlation Effects. *Phys. Rev.* **1965**, *140*, 1133–1138.

(96) Ceperley, D. M.; Alder, B. J. Ground State of the Electron Gas by a Stochastic Method. *Phys. Rev. Lett.* **1980**, *45* (7), 566–569.

(97) Vosko, S. H.; Wilk, L.; Nusair, D. M. Accurate Spin-Dependent Electron Liquid Correlation Energies for Local Spin Density Calculations: A Critical Analysis. *Can. J. Phys.* **1980**, *58*, 1200–1211.

(98) Perdew, J. P.; Wang, Y. Accurate and Simple Analytic Representation of the Electron-Gas Correlation Energy. *Phys. Rev. B* **1992**, *45* (23), 13244–13249.

(99) Becke, A. D. A Density-Functional Exchange-Energy Approximation with Correct Asymptotic Behavior. *Phys. Rev. A* **1988**, *38* (15), 3098–3100.

(100) Lee, C.; Yang, E.; Parr, R. G. Development of the Colic-Salvetti Correlation-Energy Formula into a Functional of the Electron Density. *Phys. Rev. B* **1988**, *37* (2), 785–789.

(101) Stephens, P. J.; Devlin, F. J.; Chabalowski, C. F.; Frisch, M. J. Ab Initio Calculation of Vibrational Absorption and Circular Dichroism Spectra Using Density Functional Force Fields. *J. Phys. Chem.* **1994**, *98* (10), 11623–11627.

(102) Becke, A. D. Density-Functional Thermochemistry. III. The Role of Exact Exchange. *J. Chem. Phys.* **1993**, *98* (56), 5648–5652.

(103) Grimme, S. Semiempirical GGA-type Density Functional Constructed with a Long-range Dispersion Correction. *J. Comput. Chem.* **2006**, *27* (15), 1787–1799.

(104) Grimme, S.; Antony, J.; Ehrlich, S.; Krieg, H. A Consistent and Accurate Ab Initio Parametrization of Density Functional Dispersion Correction (DFT-D) for the 94 Elements H-Pu. *J. Chem. Phys.* **2010**, *132* (118), 154104.

(105) Grimme, S. Accurate Description of van Der Waals Complexes by Density Functional Theory Including Empirical Corrections. *J. Comput. Chem.* **2004**, *25* (12), 1463–1473.

(106) van Duijneveldt, F. B.; van Duijneveldt-van De Rijdt, J. G. C. M.; van Lenthe, J. H. State of the Art in Counterpoise Theory. *Chem. Rev* **1994**, *94*, 1873–1.

(107) Frenkel, D. and Smit, B. *Understanding Molecular Simulation: From*

Algorithms to Applications, 2nd ed.; San Diego, CA, USA, 2002.

(108) Dill, K. A.; Bromberg, S. Molecular Driving Forces: Statistical Thermodynamics in Chemistry and Biology. *Macromol. Chem. Phys.* **2003**, *204* (14), 1800–1800.

(109) Metropolis, N.; Rosenbluth, A. W.; Rosenbluth, M. N.; Teller, A. H.; Teller, E. Equation of State Calculations by Fast Computing Machines. *J. Chem. Phys.* **1953**, *21*, 1087–5648.

(110) Allen, M. P.; Tildesley, D. J. *Computer Simulation of Liquids*; Clarendon Press: Oxford, UK, 1989.

(111) Peng, D.-Y.; Robinson, D. B. A New Two-Constant Equation of State. *Ind. Eng. Chem. Fundam.* **1976**, *15* (1), 59–64.

(112) Düren, T.; Bae, Y.-S.; Snurr, R. Q. Using Molecular Simulation to Characterise Metal-Organic Frameworks for Adsorption Applications. *Chem. Soc. Rev.* **2009**, *38* (5), 1237–1247.

(113) Fraccarollo, A.; Canti, L.; Marchese, L.; Cossi, M. Monte Carlo Modeling of Carbon Dioxide Adsorption in Porous Aromatic Frameworks. *Langmuir* **2014**, *30* (14), 4147–4156.

(114) Amirjalayer, S.; Schmid, R. Adsorption of Hydrocarbons in Metal−Organic Frameworks: A Force Field Benchmark on the Example of Benzene in Metal−Organic Framework 5. *J. Phys. Chem. C* **2012**, *116*, 15369–15377.

(115) Rana, M. K.; Koh, H. S.; Zuberi, H.; Siegel, D. J. Methane Storage in Metal-Substituted Metal–Organic Frameworks: Thermodynamics, Usable Capacity,

and the Impact of Enhanced Binding Sites. *J. Phys. Chem. C* **2014**, *118* (6), 2929–2942.

(116) Morse, P. M. Diatomic Molecules According to the Wave Mechanics. II. Vibrational Levels. *Phys. Rev.* **1929**, *34*, 57–64.

(117) Rappe, A. K.; Casewit, C. J.; Colwell, K. S.; Goddard III, W. A.; Skiff, W. M.; Rappé, A. K.; Casewit, C. J. UFF, a Full Periodic Table Force Field for Molecular Mechanics and Molecular Dynamics Simulations. *J. Am. Chem. Soc.* **1992**, *2* (114), 10024–10035.

(118) Mayo, S. L.; Olafson, B. D.; Goddard, W. A. DREIDING: A Generic Force Field for Molecular Simulations. *J. Phys. Chem.* **1990**, *101* (Suite 540), 8897–8909.

(119) Martin, M. G.; Siepmann, J. I. Transferable Potentials for Phase Equilibria. 1. United-Atom Description of n-Alkanes. *J. Phys. Chem. B* **1998**, *102* (97), 2569–2577.

(120) Jorgensen, W. L.; Maxwell, D. S.; Tirado-Rives, J. Development and Testing of the OPLS All-Atom Force Field on Conformational Energetics and Properties of Organic Liquids. *J. Am. Chem. Soc.* **1996**, *118* (15), 11225–11236.

(121) Levesque, D.; Gicquel, A.; Darkrim, F. L.; Kayiran, S. B. Monte Carlo Simulations of Hydrogen Storage in Carbon Nanotubes. *J. Physics-Condensed Matter* **2002**, *14* (40), 9285–9293.

(122) Gupta, A.; Chempath, S.; Sanborn, M. J.; Clark, L. A.; Snurr, R. Q. Object-

Oriented Programming Paradigms for Molecular Modeling. *Mol. Simul.* **2003**, *29* (1), 29–46.

(123) Breneman, C. M.; Wiberg, K. B. Determining Atom-Centered Monopoles from Molecular Electrostatic Potentials. The Need for High Sampling Density in Formamide Conformational Analysis. *J. Comput. Chem.* **1990**, *11* (3), 361–373.

(124) Potoff, J. J.; Errington, J. R.; Panagiotopoulos, A. Z. Molecular Simulation of Phase Equilibria for Mixtures of Polar and Non-Polar Components. *Mol. Phys.* **1999**, *97* (10), 1073–1083.

(125) Gomez-Gualdron, D. A.; Gutov, O. V; Krungleviciute, V.; Borah, B.; Mondloch, J. E.; Hupp, J. T.; Yildirim, T.; Farha, O. K.; Snurr, R. Q. Computational Design of Metal−Organic Frameworks Based on Stable Zirconium Building Units for Storage and Delivery of Methane. *Chem. Mater.* **2014**, *26*, 5632–5639.

(126) Ozturk, T. N.; Keskin, S. Computational Screening of Porous Coordination Networks for Adsorption and Membrane-Based Gas Separations. *J. Phys. Chem. C* **2014**, *118*, 13988–13997.

(127) Wang, S. Comparative Molecular Simulation Study of Methane Adsorption in Metal-Organic Frameworks. *Energy & Fuels* **2007**, *21*, 953–956.

(128) Brunauer, S. *Adsorption of Gases and Vapors,* 1st ed.; Princeton University Press, 1943.

(129) Rouquerol, F.; Rouquerol, J.; Sing, K. S. W.; Llewellyn, P.; Maurin, G.

Adsorption by Powders and Porous Solids. Principles, Methodology and Applications, 2nd ed.; Academic Press, 2014.

(130) Rouquerol, F.; Rouquerol, J. (Jean); Sing, K. S. W. *Adsorption by Powders and Porous Solids. Principles, Methodology, and Applications*, 1st ed.; Academic Press, 1999.

(131) Sing, K. S. W.; Everett, D. H.; Haul, R. A. W.; Moscou, L.; Pierotti, R. A.; Rouquerol, J.; Siemieniewska, T. Reporting Physisorption Data for Gas/Solid Systems with Special Reference to the Determination of Surface Area and Porosity. *Pure Appl. Chem.* **1985**, *57* (4), 603–619.

(132) Brunauer, S.; Emmett, P. H.; Teller, E. Adsorption of Gases in Multimolecular Layers. *J. Am. Chem. Soc.* **1938**, *60* (2), 309–319.

(133) Langmuir, I. The Adsorption of Gases on Plane Surfaces of Glass, Mica and Platinum. *J. Am. Chem. Soc.* **1918**, *40* (9), 1361–1403.

(134) Walton, K. S.; Snurr, R. Q. Applicability of the BET Method for Determining Surface Areas of Microporous Metal-Organic Frameworks. *J. Am. Chem. Soc.* **2007**, *129* (27), 8552–8556.

(135) Jensen, F. *Introduction to Computational Chemistry*; Wiley, 1998.

(136) Myers, A. L.; Monson, P. A. Adsorption in Porous Materials at High Pressure: Theory and Experiment. *Langmuir* **2002**, *18* (26), 10261–10273.

(137) Sarkisov, L.; Harrison, A. Computational Structure Characterisation Tools in Application to Ordered and Disordered Porous Materials. *Mol. Simul.* **2011**, *37* (15), 1248–1257.

(138) Gelb, L. D.; Gubbins, K. E. Characterization of Porous Glasses: Simulation Models, Adsorption Isotherms, and the Brunauer−Emmett−Teller Analysis Method. *Langmuir* **1998**, *14* (8), 2097–2111.

(139) Düren, T.; Sarkisov, L.; Yaghi, O. M.; Snurr, R. Q. Design of New Materials for Methane Storage. *Langmuir* **2004**, *20* (7), 2683–2689.

(140) Sarkisov, L.; Düren, T.; Snurr, R. Q. Molecular Modelling of Adsorption in Novel Nanoporous Metal-Organic Materials. *Mol. Phys.* **2004**, *102* (2), 211–221.

(141) Chen, L.; Grajciar, L.; Nachtigall, P.; Düren, T. Accurate Prediction of Methane Adsorption in a Metal-Organic Framework with Unsaturated Metal Sites by Direct Implementation of an Ab Initio Derived Potential Energy Surface in GCMC Simulation. *J. Phys. Chem. C* **2011**, *115*, 23074–23080.

(142) Fernandez, M.; Woo, T. K.; Wilmer, C. E.; Snurr, R. Q. Large-Scale Quantitative Structure−Property Relationship (QSPR) Analysis of Methane Storage in Metal−Organic Frameworks. *J. Phys. Chem. C* **2013**, *117*, 7681–7689.

(143) Garberoglio, G. Computer Simulation of the Adsorption of Light Gases in Covalent Organic Frameworks. *Langmuir* **2007**, *23*, 12154–12158.

(144) Garberoglio, G.; Skoulidas, A. I.; Johnson, J. K. Adsorption of Gases in Metal Organic Materials: Comparison of Simulations and Experiments. *J. Phys. Chem. B* **2005**, *109*, 13094–13103.

(145) Yang, Q.; Wiersum, A. D.; Jobic, H. E.; Guillerm, V.; Serre, C.; Llewellyn, P.

L.; Maurin, G. Understanding the Thermodynamic and Kinetic Behavior of the CO2/CH4 Gas Mixture within the Porous Zirconium Terephthalate UiO-66(Zr): A Joint Experimental and Modeling Approach. *J. Phys. Chem. C* **2011**, *115*, 13768–13774.

(146) Perez-Pellitero, J.; Amrouche, H.; Siperstein, F.; Pirngruber, G.; Nieto-Draghi, C.; Chaplais, G.; Simon-Masseron, A.; Bazer-Bachi, D.; Peralta, D.; Bats, N. Adsorption of CO2 , CH4 , and N2 on Zeolitic Imidazolate Frameworks: Experiments and Simulations. *Chem. - A Eur. J.* **2010**, *16* (5), 1560–1571.

(147) Jorgensen, W. L.; Laird, E. R.; Nguyen, T. B.; Tirado-Rives, J. Monte Carlo Simulations of Pure Liquid Substituted Benzenes with OPLS Potential Functions. *J. Comput. Chem.* **1993**, *14* (2), 206–215.

(148) Coudert, F.-X.; Fuchs, A. H. Computational Characterization and Prediction of Metal–organic Framework Properties. *Coord. Chem. Rev.* **2016**, *307*, 211–236.

(149) Getman, R. B.; Bae, Y.-S.; Wilmer, C. E.; Snurr, R. Q. Review and Analysis of Molecular Simulations of Methane, Hydrogen, and Acetylene Storage in Metal-Organic Frameworks. *Chem. Rev.* **2012**, *112* (2), 703–723.

(150) Orefuwa, S.; Iriowen, E.; Yang, H.; Wakefield, B.; Goudy, A. Effects of Nitro-Functionalization on the Gas Adsorption Properties of Isoreticular Metal-Organic Framework-Eight (IRMOF-8). *Microporous Mesoporous Mater.* **2013**, *177*, 82–90.

(151) Henley, A.; Lennox, M. J.; Easun, T. L.; Moreau, F.; Schröder, M.; Besley, E.

Computational Evaluation of the Impact of Incorporated Nitrogen and Oxygen Heteroatoms on the Affinity of Polyaromatic Ligands for Carbon Dioxide and Methane in Metal−Organic Frameworks. *J. Phys. Chem. C* **2016**, *120*, 27342–27348.

(152) He, Y.; Zhang, Z.; Xiang, S.; Fronczek, F. R.; Krishna, R.; Chen, B. A Microporous Metal-Organic Framework for Highly Selective Separation of Acetylene, Ethylene, and Ethane from Methane at Room Temperature. *Chem. - A Eur. J.* **2012**, *18* (2), 613–619.

(153) Goerigk, L.; Grimme, S. A Thorough Benchmark of Density Functional Methods for General Main Group Thermochemistry, Kinetics, and Noncovalent Interactions. *Phys. Chem. Chem. Phys.* **2011**, *13* (14), 6670.

(154) Shao, Y.; Gan, Z.; Epifanovsky, E.; Gilbert, A. T. B.; Wormit, M.; Kussmann, J.; Lange, A. W.; Behn, A.; Deng, J.; Feng, X.; et al. Advances in Molecular Quantum Chemistry Contained in the Q-Chem 4 Program Package. *Mol. Phys.* **2015**, *113* (2), 184–215.

(155) Vogiatzis, K. D.; Klopper, W.; Friedrich, J. Non-Covalent Interactions of CO2 with Functional Groups of Metal−Organic Frameworks from a CCSD(T) Scheme Applicable to Large Systems. *J. Chem. Theory Comput.* **2015**, *11*, 1574–1584.

(156) Grajciar, L.; Nachtigall, P.; Bludsky, O.; Rubeš, M. Accurate Ab Initio Description of Adsorption on Coordinatively Unsaturated Cu2+ and Fe3+ Sites in MOFs. *J. Chem. Theory Comput.* **2015**, *11*, 230–238.

(157) Supronowicz, B.; Mavrandonakis, A.; Heine, T. Interaction of Small Gases

with the Unsaturated Metal Centers of the HKUST-1 Metal Organic Framework. *J. Phys. Chem. C* **2013**, *117*, 14570–14578.

(158) Boys, S. F.; Bernardi, F. The Calculation of Small Molecular Interactions by the Differences of Separate Total Energies. Some Procedures with Reduced Errors. *Mol. Phys.* **1970**, *19* (4), 553–566.

(159) Haldoupis, E.; Borycz, J.; Shi, H.; Vogiatzis, K. D.; Bai, P.; Queen, W. L.; Gagliardi, L.; Siepmann, J. I. Ab Initio Derived Force Fields for Predicting CO2 Adsorption and Accessibility of Metal Sites in the Metal−Organic Frameworks M-MOF-74 (M = Mn, Co, Ni, Cu). *J. Phys. Chem. C* **2015**, *119*, 16058–16071.

(160) Kulkarni, A. R.; Sholl, D. S. DFT-Derived Force Fields for Modeling Hydrocarbon Adsorption in MIL-47(V). *Langmuir* **2015**, *31*, 8452–8468.

(161) Casewit, C. J.; Colwell, K. S.; Rappe, A. K. Application of a Universal Force Field to Organic Molecules. *J. Am. Chem. Soc.* **1992**, *114* (25), 10035–10046.

(162) Rappe, A. K.; Colwell, K. S.; Casewit, C. J. Application of a Universal Force Field to Metal Complexes. *Inorg. Chem.* **1993**, *32*, 3438–3450.

(163) Sarkisov, L. Toward Rational Design of Metal−Organic Frameworks for Sensing Applications: Efficient Calculation of Adsorption Characteristics in Zero Loading Regime. *J. Phys. Chem. C* **2012**, *116*, 3025–3033.

(164) Yang, Q.; Zhong, C. Molecular Simulation of Carbon Dioxide/Methane/Hydrogen Mixture Adsorption in Metal-Organic Frameworks. *J. Phys. Chem. B* **2006**, *110* (36), 17776–17783.

(165) Fairen-Jimenez, D.; Galvelis, R.; Torrisi, A.; Gellan, A. D.; Wharmby, M. T.; Wright, P. A.; Mellot-Draznieks, C.; D?ren, T. Flexibility and Swing Effect on the Adsorption of Energy-Related Gases on ZIF-8: Combined Experimental and Simulation Study. *Dalt. Trans.* **2012**, *41* (35), 10752.

(166) Alejandre, A. T.; Trokhymchuk, A.; Alejandre, J. Computer Simulations of Liquid/Vapor Interface in Lennard-Jones Fluids: Some Questions and Answers. *J. Chem. Phys.* **1999**, *111*, 8510–8523.

(167) Pàmies, J. C.; McCabe, C.; Cummings, P. T.; Vega, L. F. Coexistence Densities of Methane and Propane by Canonical Molecular Dynamics and Gibbs Ensemble Monte Carlo Simulations. *Mol. Simul.* **2003**, *29* (6–7), 463–470.

(168) Dubbeldam, D.; Frost, H.; Walton, K. S.; Snurr, R. Q. Molecular Simulation of Adsorption Sites of Light Gases in the Metal-Organic Framework IRMOF-1. *Fluid Phase Equilib.* **2007**, *261* (1–2), 152–161.

(169) Fischer, M.; Gomes, J. R. B.; Jorge, M. Computational Approaches to Study Adsorption in MOFs with Unsaturated Metal Sites. *Mol. Simul.* **2014**, *40* (7–9), 537–556.

(170) Koh, H. S.; Rana, M. K.; Wong-Foy, A. G.; Siegel, D. J. Predicting Methane Storage in Open-Metal-Site Metal-Organic Frameworks. *J. Phys. Chem. C* **2015**, *119* (24), 13451–13458.

(171) Desiraju, G. R.; Steiner, T. *The Weak Hydrogen Bond: In Structural Chemistry and Biology*; IUCr monographs on crystallography; Oxford University Press, 1999.

(172) Takahashi, O.; Kohno, Y.; Nishio, M. Relevance of Weak Hydrogen Bonds in the Conformation of Organic Compounds and Bioconjugates: Evidence from Recent Experimental Data and High-Level Ab Initio MO Calculations. *Chem. Rev.* **2010**, *110* (10), 6049–6076.

(173) Nishio, M. CH/Pi Hydrogen Bonds in Crystals. *CrystEngComm* **2004**, *6* (27), 130.

(174) Grande, C. A.; Araujo, J. D. P.; Cavenati, S.; Firpo, N.; Basaldella, E.; Rodrigues, A. E. New π-Complexation Adsorbents for Propane−Propylene Separation. *Langmuir* **2004**, *20* (13), 5291–5297.

(175) Perry, J. J.; Perman, J. A.; Zaworotko, M. J. Design and Synthesis of Metal-Organic Frameworks Using Metal-Organic Polyhedra as Supermolecular Building Blocks. *Chem. Soc. Rev.* **2009**, *38* (5), 1400–1417.

(176) Ribas, J.; Cubero, E.; Luque, F. J.; Orozco, M. Theoretical Study of Alkyl-Pi and Aryl-Pi Interactions. Reconciling Theory and Experiment. *J. Org. Chem.* **2002**, *67* (20), 7057–7065.

(177) Takahashi, O.; Kohno, Y.; Saito, K.; Nishio, M. Prevalence of the Alkyl/Phenyl-Folded Conformation in Benzylic Compounds C6H5CH2-X-R (X = O, CH2, CO, S, SO, SO2): Significance of the CH/Pi Interaction as Evidenced by High-Level Ab Initio MO Calculations. *Chem. Eur. J.* **2003**, *9* (3), 756–762.

(178) Sodupe, M.; Rios, R.; Nicholas, T.; Oliva, A.; Dannenberg, J. J. A Theoretical Study of the Endo / Exo Selectivity of the Diels-Alder Reaction between Cyclopropene and Butadiene. *J. Am. Chem. Soc.* **1997**, *119* (18), 4232–4238.

(179) Ujaque, G.; Lee, P. S.; Houk, K. N.; Hentemann, M. F.; Danishefsky, S. J. The Origin of Endo Stereoselectivity in the Hetero-Diels-Alder Reactions of Aldehydes with Ortho-Xylylenes: CH-π, π-π, and Steric Effects on Stereoselectivity. *Chem. Eur. J.* **2002**, *8* (15), 3423–3430.

(180) Samanta, U. .; Chakrabarti, P. .; Chandrasekhar, J. . Ab Initio Study of Energetics of X-H ... Pi (X) N , O , and C) Interactions Involving a Heteroaromatic Ring. *J. Phys. Chem. A* **1998**, 8964–8969.

(181) Re, S.; Nagase, S. How Is the CH/Pi Interaction Important for Molecular Recognition? *Chem. Commun. (Camb).* **2004**, No. 6, 658–659.

(182) Ringer, A. L.; Figgs, M. S.; Sinnokrot, M. O.; Sherrill, C. D. Aliphatic C-H/π Interactions: Methane-Benzene, MethanePhenol, and Methane-Indole Complexes. *J. Phys. Chem. A* **2006**, *110*, 10822–10828.

(183) Alsmail, N. H.; Suyetin, M.; Yan, Y.; Cabot, R.; Krap, C. P.; Lü, J.; Easun, T. L.; Bichoutskaia, E.; Lewis, W.; Blake, A. J.; et al. Analysis of High and Selective Uptake of CO2 in an Oxamide-Containing {Cu2(OOCR)4}-Based Metal-Organic Framework. *Chemistry* **2014**, *20* (24), 7317–7324.

(184) Shao, Y.; Molnar, L. F.; Jung, Y.; Kussmann, J.; Ochsenfeld, C.; Brown, S. T.; Gilbert, A. T. B.; Slipchenko, L. V; Levchenko, S. V; O'Neill, D. P.; et al. Advances in Methods and Algorithms in a Modern Quantum Chemistry Program Package. *Phys. Chem. Chem. Phys.* **2006**, *8* (27), 3172–3191.

(185) Yu, D.; Matteucci, S.; Stangland, E.; Calverley, E.; Wegener, H.; Anaya, D. Quantum Chemistry Calculation and Experimental Study of CO2/CH4 and Functional Group Interactions for the Design of Solubility Selective

Membrane Materials. *J. Memb. Sci.* **2013**, *441*, 137–147.

(186) Yan, Y.; Yang, S.; Blake, A. J.; Schröder, M. Studies on Metal-Organic Frameworks of Cu(II) with Isophthalate Linkers for Hydrogen Storage. *Acc. Chem. Res.* **2014**, *47* (2), 296–307.

(187) Farha, O. K.; Eryazici, I.; Jeong, N. C.; Hauser, B. G.; Wilmer, C. E.; Sarjeant, A. A.; Snurr, R. Q.; Nguyen, S. T.; Yazaydın, A. Ö.; Hupp, J. T. Metal-Organic Framework Materials with Ultrahigh Surface Areas: Is the Sky the Limit? *J. Am. Chem. Soc.* **2012**, *134* (36), 15016–15021.

(188) Furukawa, H.; Cordova, K. E.; O'Keeffe, M.; Yaghi, O. M. The Chemistry and Applications of Metal-Organic Frameworks. *Science* **2013**, *341* (6149), 1230444.

(189) Bayliss, P. A.; Ibarra, I. A.; Pérez, E.; Yang, S.; Tang, C. C.; Poliakoff, M.; Schröder, M. Synthesis of Metal–organic Frameworks by Continuous Flow. *Green Chem.* **2014**, *16*, 3796–3802.

(190) Farha, O. K.; Wilmer, C. E.; Eryazici, I.; Hauser, B. G.; Parilla, P. A.; O'Neill, K.; Sarjeant, A. A.; Nguyen, S. T.; Snurr, R. Q.; Hupp, J. T. Designing Higher Surface Area Metal-Organic Frameworks: Are Triple Bonds Better than Phenyls? *J. Am. Chem. Soc.* **2012**, *134* (24), 9860–9863.

(191) Mendoza-Cortés, J. L.; Han, S. S.; Furukawa, H.; Yaghi, O. M.; Goddard III, W. A. Adsorption Mechanism and Uptake of Methane in Covalent Organic Frameworks: Theory and Experiment. *J. Phys. Chem. A* **2010**, *114*, 10824–10833.

(192) Materials Studio. *Materials Studio v. 5.0 Accelrys Software Inc. San Diego, CA 92121, USA.* Accelrys Software Inc.: San Diego, CA 92121, USA.

(193) Ewald, P. P. The Calculation of Optical and Electrostatic Grid Potential. *Ann. Phys.* **1921**, *64* (3), 253–287.

(194) Rappé, A. K.; Goddard III, W. A. Charge Equilibration for Molecular Dynamics Simulations. *J. Phys. Chem.* **1991**, *95* (8340), 3358–3363.

(195) Yuan, D.; Zhao, D.; Sun, D.; Zhou, H.-C. An Isoreticular Series of Metal-Organic Frameworks with Dendritic Hexacarboxylate Ligands and Exceptionally High Gas-Uptake Capacity. *Angew. Chem. Int. Ed. Engl.* **2010**, *49* (31), 5357–5361.

(196) Fairen-Jimenez, D.; Colo, Y. J.; Farha, O. K.; Bae, Y.-S.; Hupp, J. T.; Snurr, R. Q. Metal-Organic Frameworks Understanding Excess Uptake Maxima for Hydrogen Adsorption Isotherms in Frameworks with Rht Topology. *Chem. Commun. Chem. Commun* **2012**, *48* (48), 10496–10498.

(197) Yuan, D.; Zhao, D.; Zhou, H.-C. Pressure-Responsive Curvature Change of a “Rigid” Geodesic Ligand in a (3,24)-Connected Mesoporous Metal-Organic Framework. *Inorg. Chem.* **2011**, *50* (21), 10528–10530.

(198) Furukawa, H.; Go, Y. B.; Ko, N.; Park, Y. K.; Uribe-Romo, F. J.; Kim, J.; O’Keeffe, M.; Yaghi, O. M. Isoreticular Expansion of Metal-Organic Frameworks with Triangular and Square Building Units and the Lowest Calculated Density for Porous Crystals. *Inorg. Chem.* **2011**, *50,* 9147–9152.

(199) Lin, X.; Champness, N. R.; Schröder, M. Hydrogen, Methane and Carbon

Dioxide Adsorption in Metal-Organic Framework Materials. *Top. Curr. Chem.* **2010**, *293*, 35–76.

(200) Peng, Y.; Srinivas, G.; Wilmer, C. E.; Eryazici, I.; Snurr, R. Q.; Hupp, J. T.; Yildirim, T.; Farha, O. K. Simultaneously High Gravimetric and Volumetric Methane Uptake Characteristics of the Metal-Organic Framework NU-111. *Chem. Commun. (Camb).* **2013**, *49* (29), 2992–2994.

(201) DOE MOVE program at https://arpa-e-foa.energy.gov/.

(202) Zheng, B.; Bai, J.; Duan, J.; Wojtas, L.; Zaworotko, M. J. Enhanced CO2 Binding Affinity of a High-Uptake Rht-Type Metal-Organic Framework Decorated with Acylamide Groups. *J. Am. Chem. Soc.* **2011**, *133* (4), 748–751.

(203) Furukawa, H.; Ko, N.; Go, Y. B.; Aratani, N.; Choi, S. B.; Choi, E.; Yazaydin, A. O.; Snurr, R. Q.; O'Keeffe, M.; Kim, J.; et al. Ultrahigh Porosity in Metal-Organic Frameworks. *Science* **2010**, *329* (5990), 424–428.

(204) Llewellyn, P. L.; Bourrelly, S.; Serre, C.; Vimont, A.; Daturi, M.; Hamon, L.; De Weireld, G.; Chang, J.-S.; Hong, D.-Y.; Kyu Hwang, Y.; et al. High Uptakes of CO2 and CH4 in Mesoporous Metal-Organic Frameworks MIL-100 and MIL-101. *Langmuir* **2008**, *24* (14), 7245–7250.

(205) Zhang, M.; Li, B.; Li, Y.; Wang, Q.; Zhang, W.; Chen, B.; Li, S.; Pan, Y.; You, X.; Bai, J. Finely Tuning MOFs towards High Performance in C2H2 Storage: Synthesis and Properties of a New MOF-505 Analogue with an Inserted Amide Functional Group. *Chem. Commun.* **2016**, *52* (45), 7241–7244.

(206) Li, B.; Zhang, Z.; Li, Y.; Yao, K.; Zhu, Y.; Deng, Z.; Yang, F.; Zhou, X.; Li, G.; Wu, H.; et al. Enhanced Binding Affinity, Remarkable Selectivity, and High Capacity of CO2 by Dual Functionalization of a Rht-Type Metal-Organic Framework. *Angew. Chemie Int. Ed.* **2012**, *51* (6), 1412–1415.

(207) Luebke, R.; Eubank, J. F.; Cairns, A. J.; Belmabkhout, Y.; Wojtas, L.; Eddaoudi, M. The Unique Rht-MOF Platform, Ideal for Pinpointing the Functionalization and CO2 Adsorption Relationship. *Chem. Commun.* **2012**, *48* (10), 1455–1457.

(208) Spek, A. L. Structure Validation in Chemical Crystallography. *Acta Crystallogr. Sect. D Biol. Crystallogr.* **2009**, *65* (2), 148–155.

(209) Li, J.-R.; Tao, Y.; Yu, Q.; Bu, X.-H.; Sakamoto, H.; Kitagawa, S. Selective Gas Adsorption and Unique Structural Topology of a Highly Stable Guest-Free Zeolite-Type MOF Material with N-Rich Chiral Open Channels. *Chem. - A Eur. J.* **2008**, *14* (9), 2771–2776.

(210) Samsonenko, D. G.; Kim, H.; Sun, Y.; Kim, G.-H.; Lee, H.-S.; Kim, K. Microporous Magnesium and Manganese Formates for Acetylene Storage and Separation. *Chem. – An Asian J.* **2007**, *2* (4), 484–488.

(211) Zhang, Z.; Xiang, S.; Chen, B. Microporous Metal–organic Frameworks for Acetylene Storage and Separation. *CrystEngComm* **2011**, *13* (20), 5983.

(212) Matsuda, R.; Kitaura, R.; Kitagawa, S.; Kubota, Y.; Belosludov, R. V.; Kobayashi, T. C.; Sakamoto, H.; Chiba, T.; Takata, M.; Kawazoe, Y.; et al. Highly Controlled Acetylene Accommodation in a Metal–organic Microporous Material. *Nature* **2005**, *436* (7048), 238–241.

(213) Kolokolov, D. I.; Stepanov, A. G.; Guillerm, V.; Serre, C.; Frick, B.; Jobic, H. Probing the Dynamics of the Porous Zr Terephthalate UiO-66 Framework Using ^{2} H NMR and Neutron Scattering. *J. Phys. Chem. C* **2012**, *116* (22), 12131–12136.

(214) Macho, V.; Brombacher, L.; Spiess, H. W. Applied Magnetic Resonance The NMR-WEBLAB: An Internet Approach to NMR Lineshape Analysis. *Appl. Magn. Reson* **2001**, *20*, 405–432.

(215) Kirstein, O.; Prager, M.; Dimeo, R. M.; Desmedt, A. Rotational Dynamics of Methyl Groups in M-Xylene. *J. Chem. Phys.* **2005**, *122* (1), 014502.

(216) Kolokolov, D. I.; Stepanov, A. G.; Jobic, H. Mobility of the 2-Methylimidazolate Linkers in ZIF-8 Probed by 2 H NMR: Saloon Doors for the Guests. *J. Phys. Chem. C* **2015**, *119* (49), 27512–27520.

(217) Ravikovitch, P. I.; O’Domhnaill, S. C.; Neimark, A. V.; Schiith, F.; Unger, K. K. Capillary Hysteresis in Nanopores: Theoretical and Experimental Studies of Nitrogen Adsorption on MCM-41. *Langmuir* **1995**, *11* (12), 4765–4772.

(218) Caskey, S. R.; Wong-Foy, A. G.; Matzger, A. J. Dramatic Tuning of Carbon Dioxide Uptake via Metal Substitution in a Coordination Polymer with Cylindrical Pores. *J. Am. Chem. Soc.* **2008**, *130* (33), 10870–10871.

(219) Xiang, S.; Zhou, W.; Gallegos, J. M.; Liu, Y.; Chen, B. Exceptionally High Acetylene Uptake in a Microporous Metal−Organic Framework with Open Metal Sites. *J. Am. Chem. Soc.* **2009**, *131* (34), 12415–12419.

(220) Cui, X.; Chen, K.; Xing, H.; Yang, Q.; Krishna, R.; Bao, Z.; Wu, H.; Zhou,

W.; Dong, X.; Han, Y.; et al. Pore Chemistry and Size Control in Hybrid Porous Materials for Acetylene Capture from Ethylene. *Science (80-.).* **2016**, *353* (6295), 141–144.

(221) Hu, T.-L.; Wang, H.; Li, B.; Krishna, R.; Wu, H.; Zhou, W.; Zhao, Y.; Han, Y.; Wang, X.; Zhu, W.; et al. Microporous Metal–organic Framework with Dual Functionalities for Highly Efficient Removal of Acetylene from Ethylene/Acetylene Mixtures. *Nat. Commun.* **2015**, *6*, 7328.

Appendix

Virial Fitting of MFM-160 0-1 Bar Isotherms

To calculate the Henry's law selectivity of one gas over another, the adsorption isotherms from 0-1 bar were fitted to the virial equation shown below in Equation A.1.

$$\ln\left(\frac{n}{P}\right) = A_0 + A_1 n + A_2 n^2 + A_3 n^3 \tag{A.1}$$

In this case P is pressure in Pa, n is the quantity adsorbed in mol g^{-1} and A_0-A_3 are virial coefficients. Each regression coefficient was greater than 0.99, showing that the models used were accurate fits to the data. Having fitted the data, the Henry's law constant was simply calculated as $K_H = e^{A_0}$.

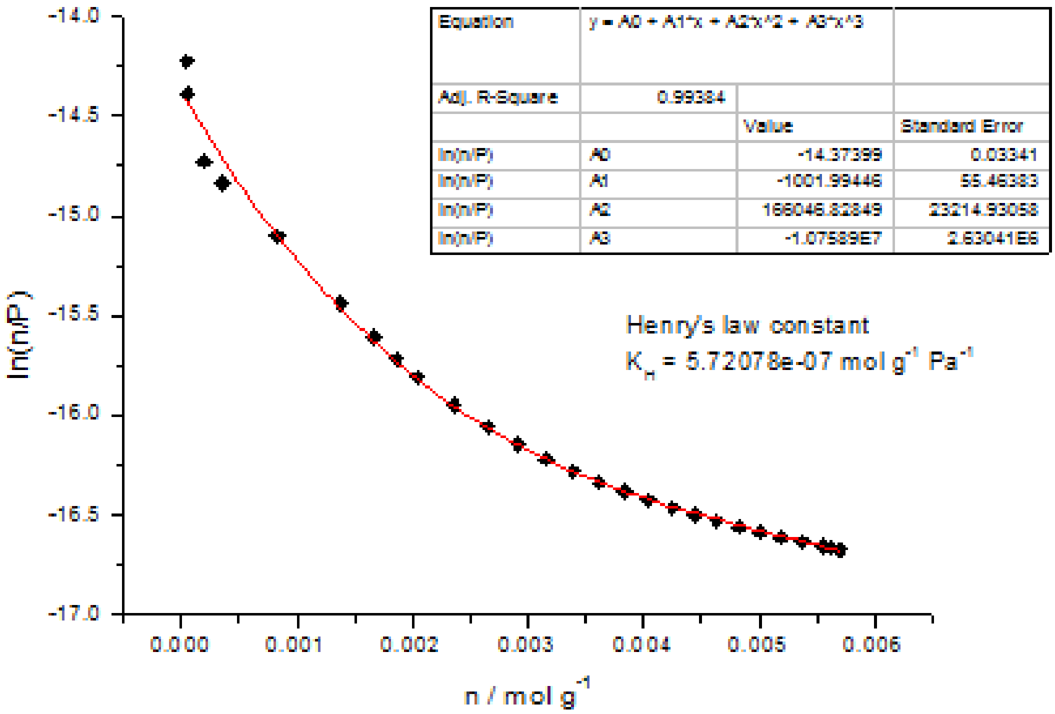

Equation	y = A0 + A1*x + A2*x^2 + A3*x^3		
Adj. R-Square	0.99384		
		Value	Standard Error
ln(n/P)	A0	-14.37399	0.03341
ln(n/P)	A1	-1001.99446	55.46383
ln(n/P)	A2	166046.82849	23214.93058
ln(n/P)	A3	-1.07589E7	2.63041E6

Henry's law constant

K_H = 5.72078e-07 mol g^{-1} Pa^{-1}

Figure A.1: Virial analysis of the C_2H_2 isotherm at 298 K.

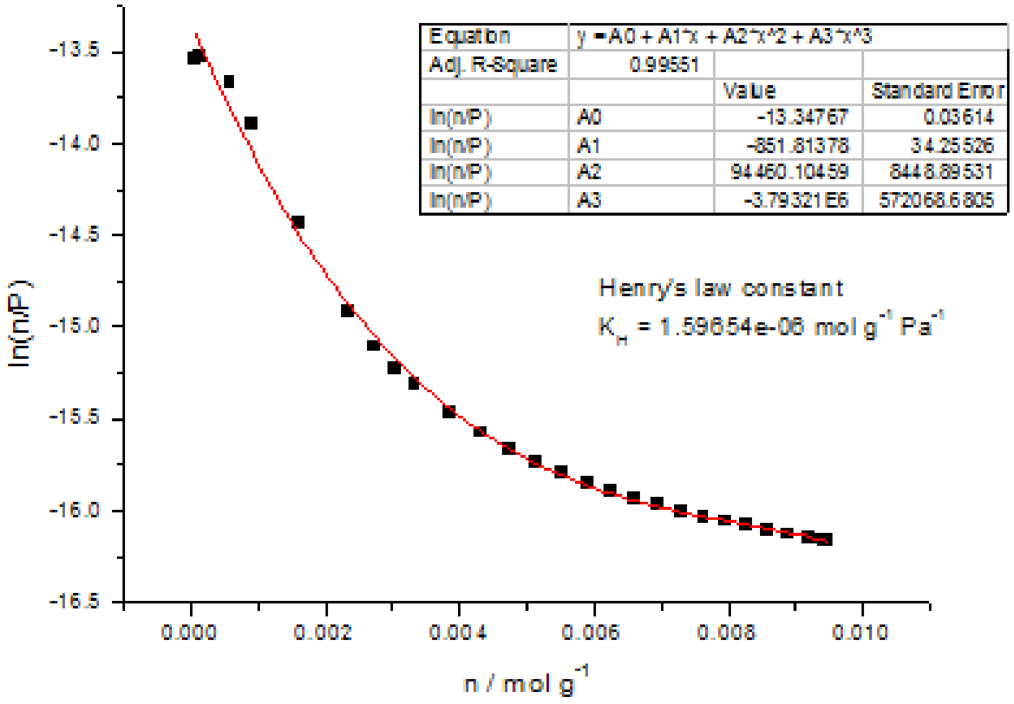

Equation	y = A0 + A1*x + A2*x^2 + A3*x^3		
Adj. R-Square	0.99551		
		Value	Standard Error
ln(n/P)	A0	-13.34767	0.03614
ln(n/P)	A1	-851.81378	34.25526
ln(n/P)	A2	94460.10459	8448.89531
ln(n/P)	A3	-3.79321E6	572068.6805

Henry's law constant

K_H = 1.59654e-06 mol g^{-1} Pa^{-1}

Figure A.2: Virial analysis of the C_2H_2 isotherm at 273 K.

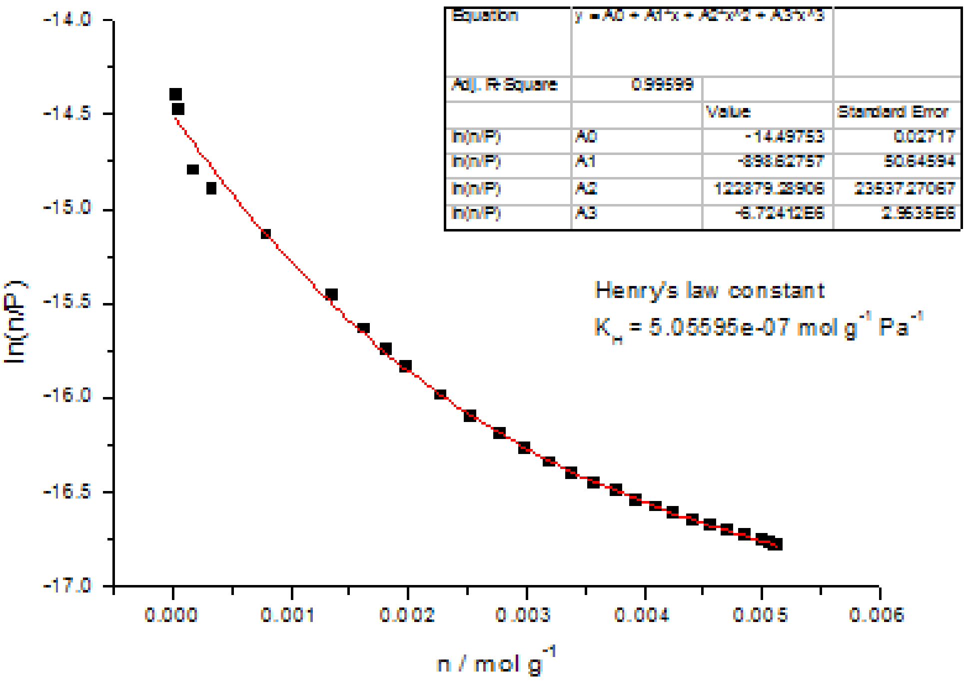

Equation	y = A0 + A1*x + A2*x^2 + A3*x^3		
Adj. R-Square	0.99599		
		Value	Standard Error
ln(n/P)	A0	-14.49753	0.02717
ln(n/P)	A1	-898.82757	50.64594
ln(n/P)	A2	122879.28906	23537.27067
ln(n/P)	A3	-6.72412E6	2.9535E6

Figure A.3: Virial analysis of the C_2H_4 isotherm at 298 K.

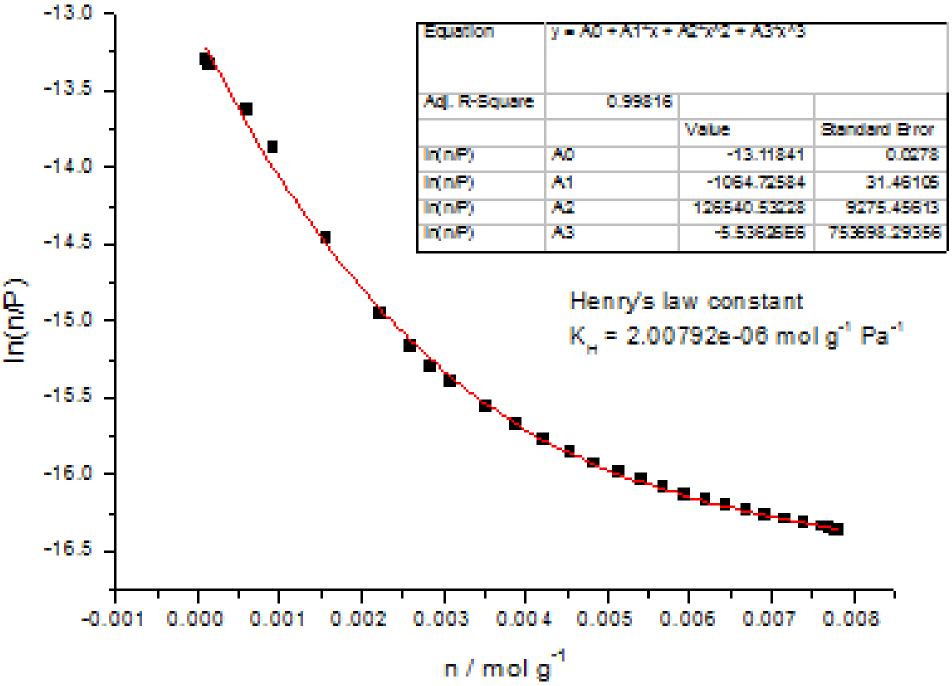

Equation	y = A0 + A1*x + A2*x^2 + A3*x^3		
Adj. R-Square	0.99816		
		Value	Standard Error
ln(n/P)	A0	-13.11841	0.0278
ln(n/P)	A1	-1064.72584	31.46105
ln(n/P)	A2	126540.53228	9275.45613
ln(n/P)	A3	-5.53626E6	753698.29356

Figure A.4: Virial analysis of the C_2H_4 isotherm at 273 K.

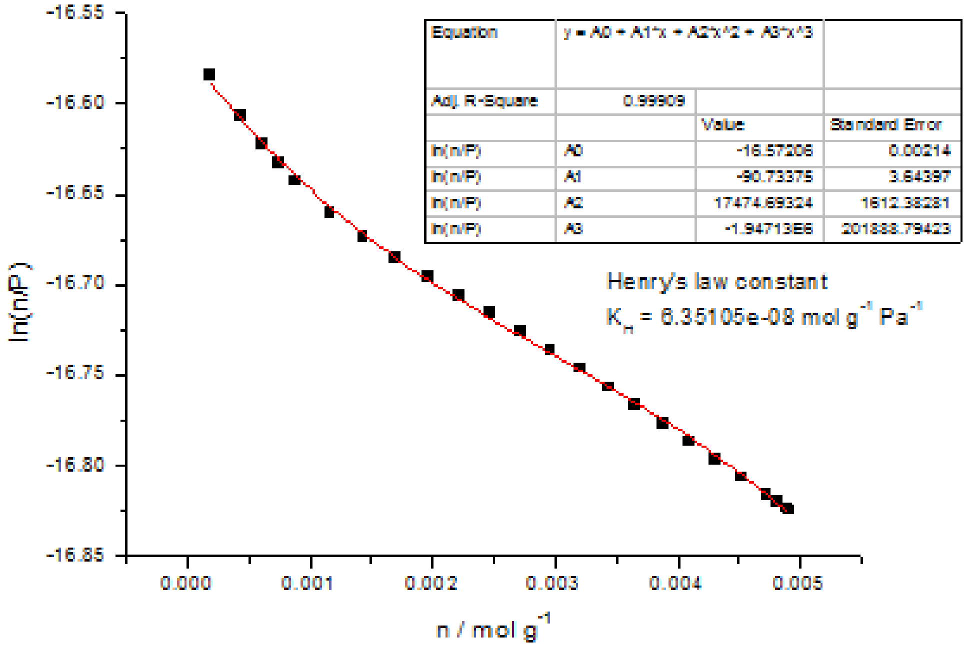

Equation	y = A0 + A1*x + A2*x^2 + A3*x^3		
Adj. R-Square	0.99909		
		Value	Standard Error
ln(n/P)	A0	-16.57206	0.00214
ln(n/P)	A1	-90.73375	3.64397
ln(n/P)	A2	17474.69324	1612.38281
ln(n/P)	A3	-1.94713E6	201888.79423

Figure A.5: Virial analysis of the C_2H_6 isotherm at 298 K.

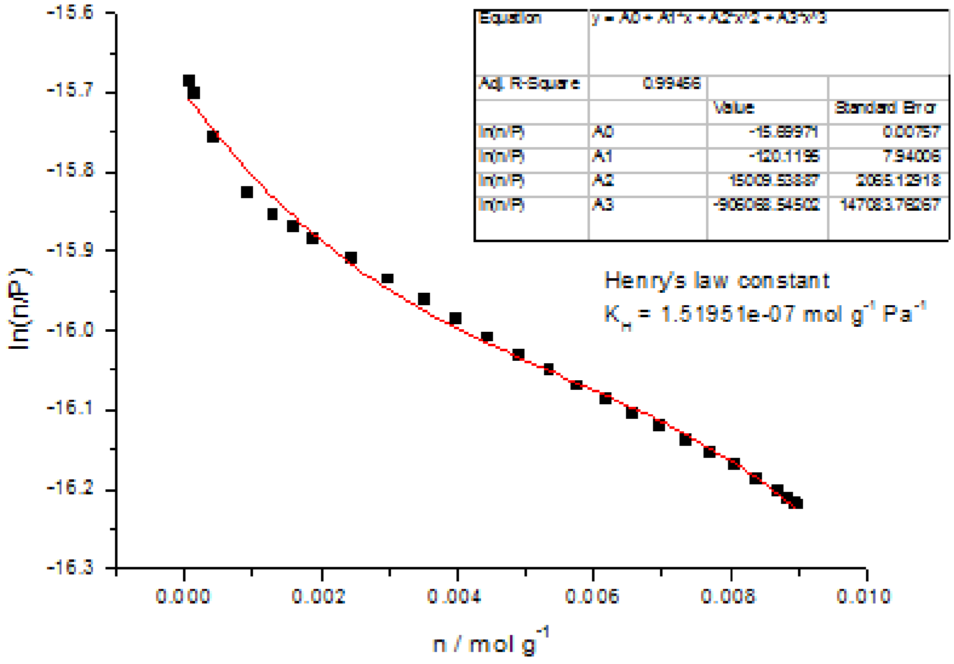

Equation	y = A0 + A1*x + A2*x^2 + A3*x^3		
Adj. R-Square	0.99456		
		Value	Standard Error
ln(n/P)	A0	-15.69971	0.00757
ln(n/P)	A1	-120.1195	7.94006
ln(n/P)	A2	15009.53887	2065.12918
ln(n/P)	A3	-906068.54502	147083.78267

Figure A.6: Virial analysis of the C_2H_6 isotherm at 273 K.

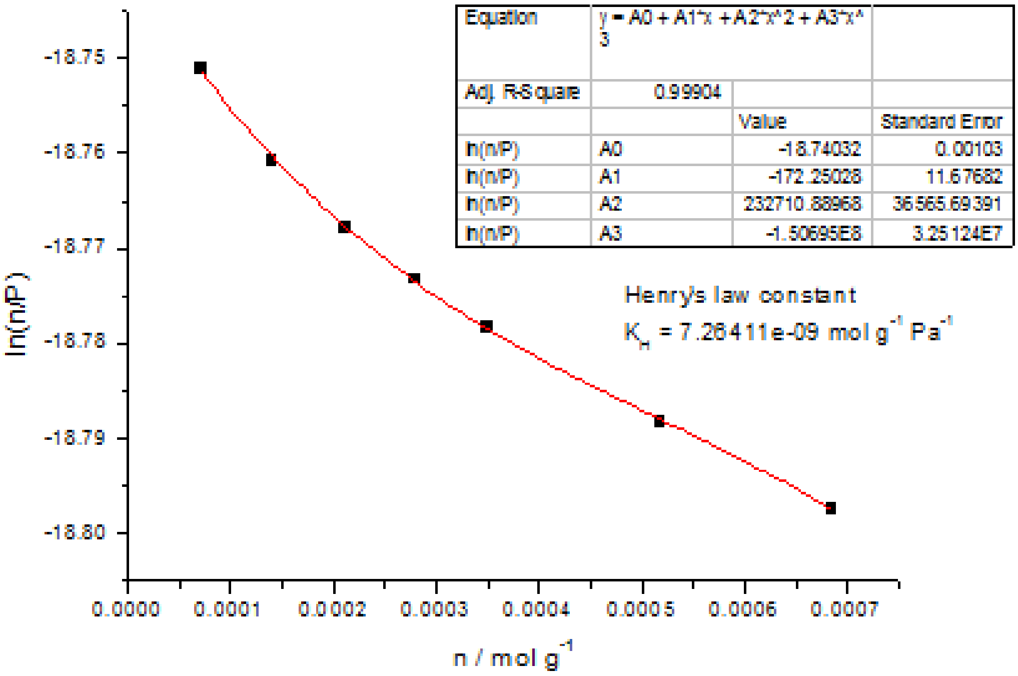

Equation	y = A0 + A1*x +A2*x^2 + A3*x^3		
Adj. R-Square	0.99904		
		Value	Standard Error
ln(n/P)	A0	-18.74032	0.00103
ln(n/P)	A1	-172.25028	11.67682
ln(n/P)	A2	232710.88968	36565.69391
ln(n/P)	A3	-1.50695E8	3.25124E7

Henry's law constant

K_H = 7.26411e-09 mol g^{-1} Pa^{-1}

Figure A.7: Virial analysis of the CH_4 isotherm at 298 K.

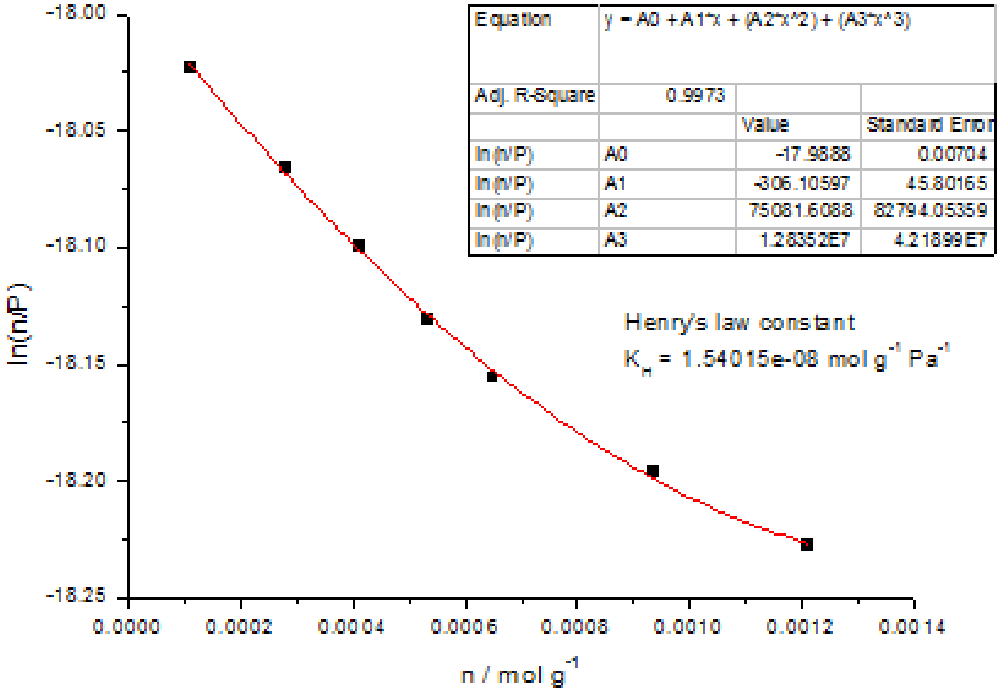

Equation	y = A0 +A1*x + (A2*x^2) + (A3*x^3)		
Adj. R-Square	0.9973		
		Value	Standard Error
ln(n/P)	A0	-17.9888	0.00704
ln(n/P)	A1	-306.10597	45.80165
ln(n/P)	A2	75081.6088	82794.05359
ln(n/P)	A3	1.28352E7	4.21899E7

Henry's law constant

K_H = 1.54015e-08 mol g^{-1} Pa^{-1}

Figure A.8: Virial analysis of the CH_4 isotherm at 273 K.

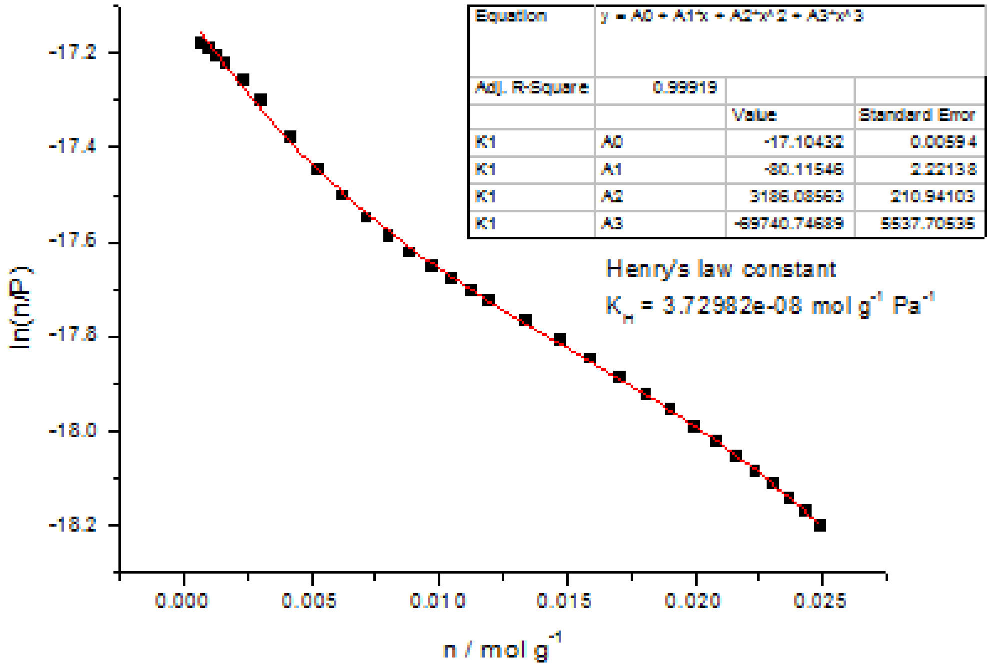

Equation	y = A0 + A1*x + A2*x^2 + A3*x^3		
Adj. R-Square	0.99919		
		Value	Standard Error
K1	A0	-17.10432	0.00594
K1	A1	-80.11546	2.22138
K1	A2	3186.08563	210.94103
K1	A3	-69740.74689	5537.70535

Henry's law constant

K_H = 3.72982e-08 mol g^{-1} Pa^{-1}

Figure A.9: Virial analysis of the CO_2 isotherm at 298 K.

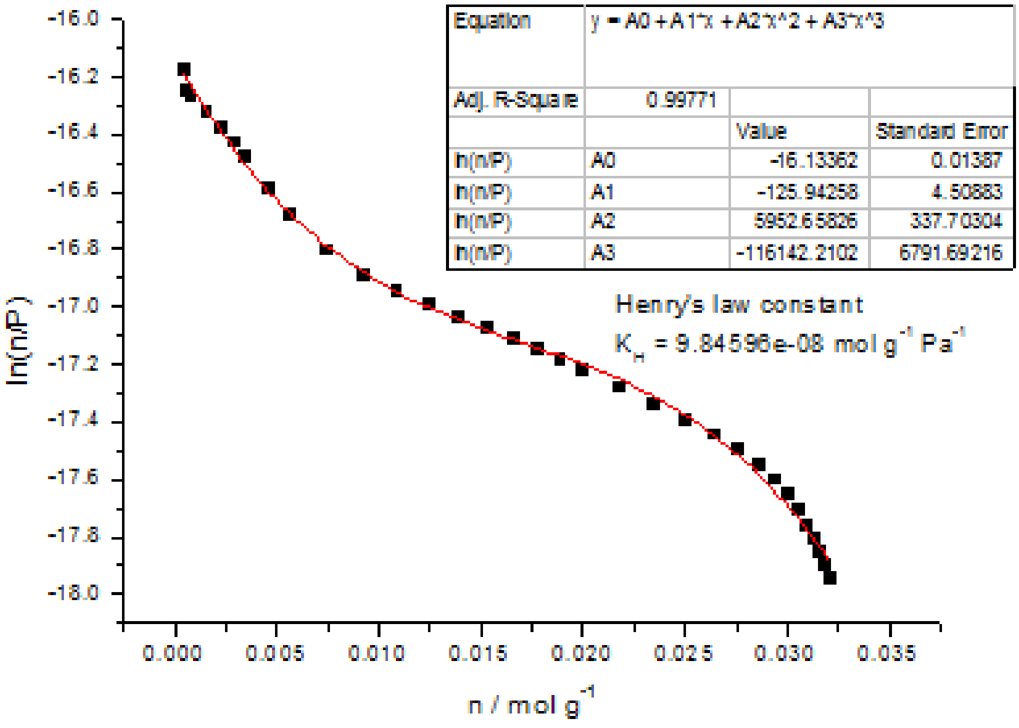

Equation	y = A0 + A1*x + A2*x^2 + A3*x^3		
Adj. R-Square	0.99771		
		Value	Standard Error
ln(n/P)	A0	-16.13362	0.01387
ln(n/P)	A1	-125.94258	4.50883
ln(n/P)	A2	5952.65826	337.70304
ln(n/P)	A3	-116142.2102	6791.69216

Henry's law constant

K_H = 9.84596e-08 mol g^{-1} Pa^{-1}

Figure A.10: Virial analysis of the CO_2 isotherm at 273 K.

Deuterium NMR Study of MFM-160

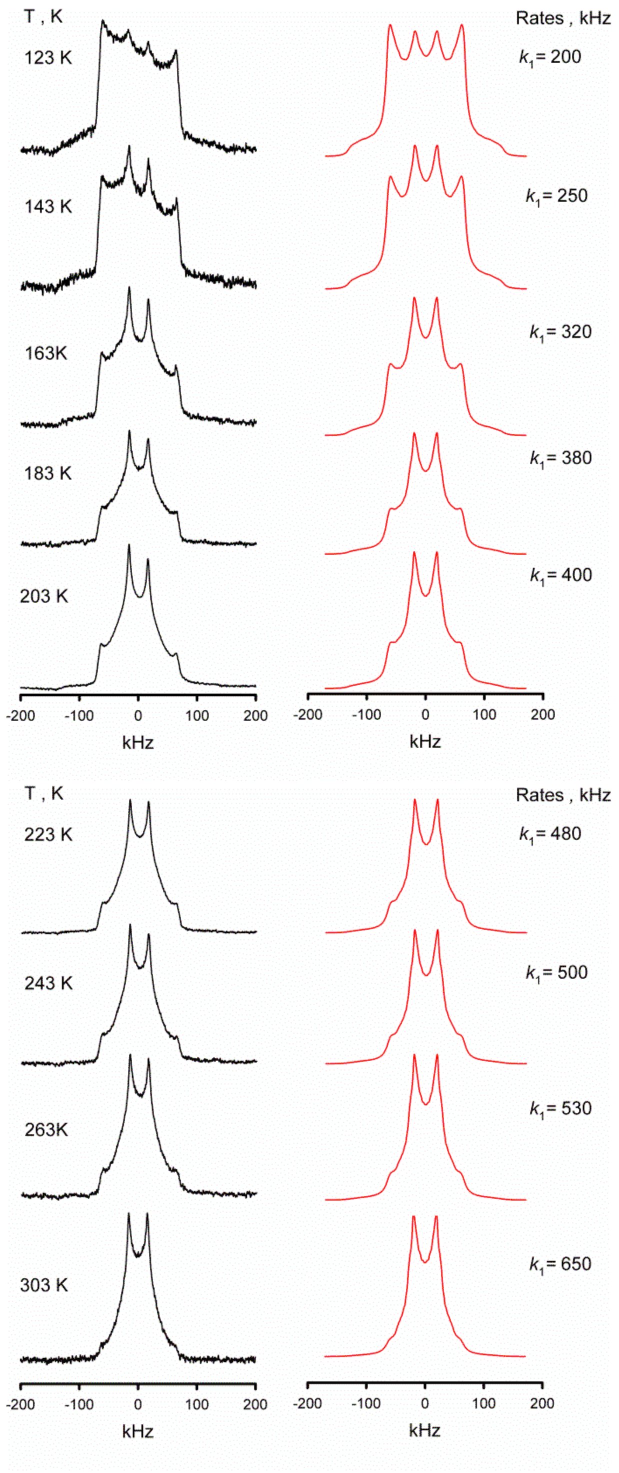

Figure A.11: ^{2}H NMR line shape temperature dependence for guest-free MFM-160 materials phenyl fragments (experimental - left, simulation - right).

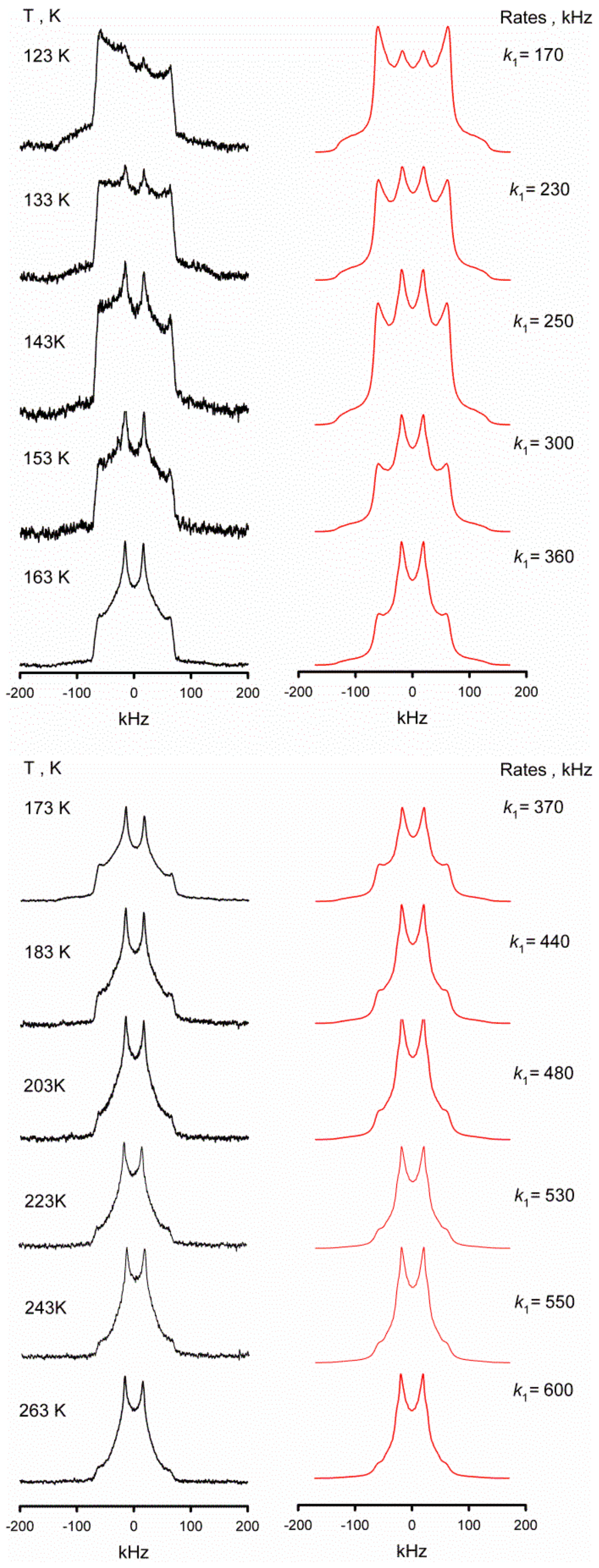

Figure A.12: ^{2}H NMR line shape temperature dependence for CO_2 (1 bar) MFM-160 materials phenyl fragments (experimental - left, simulation - right).

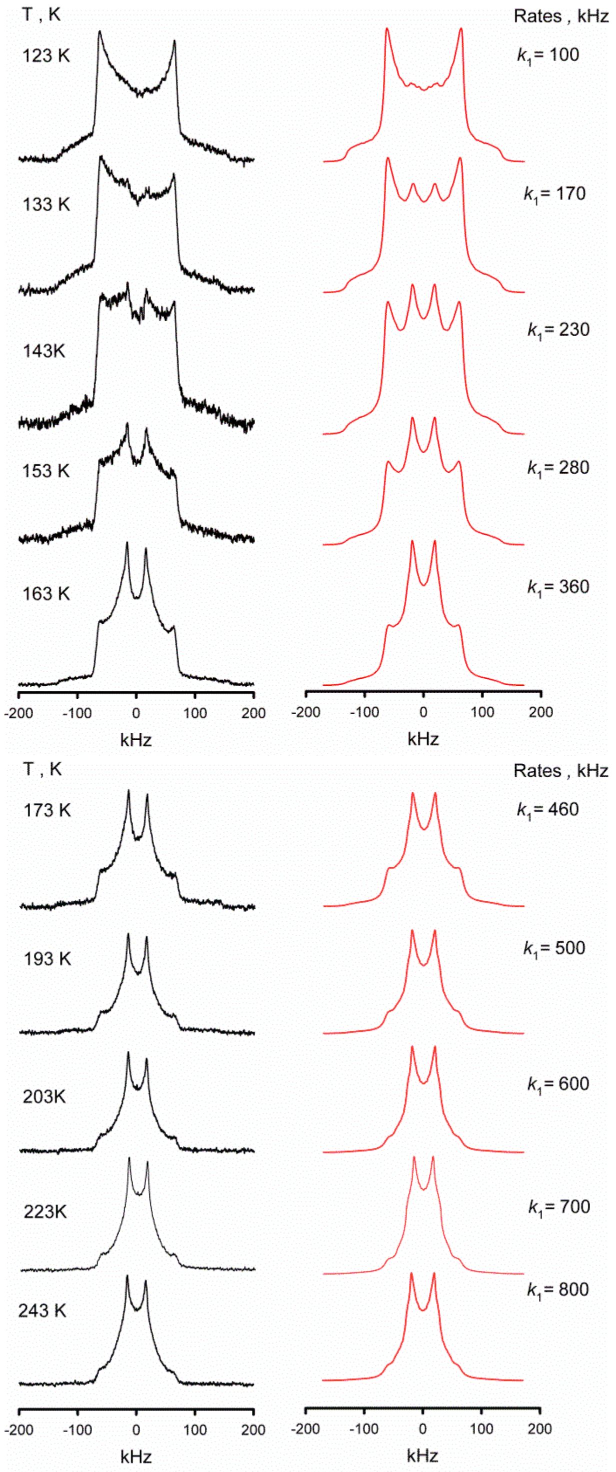

Figure A.13: ^{2}H NMR line shape temperature dependence for CO_2 (5 bar) MFM-160 materials phenyl fragments (experimental - left, simulation - right).

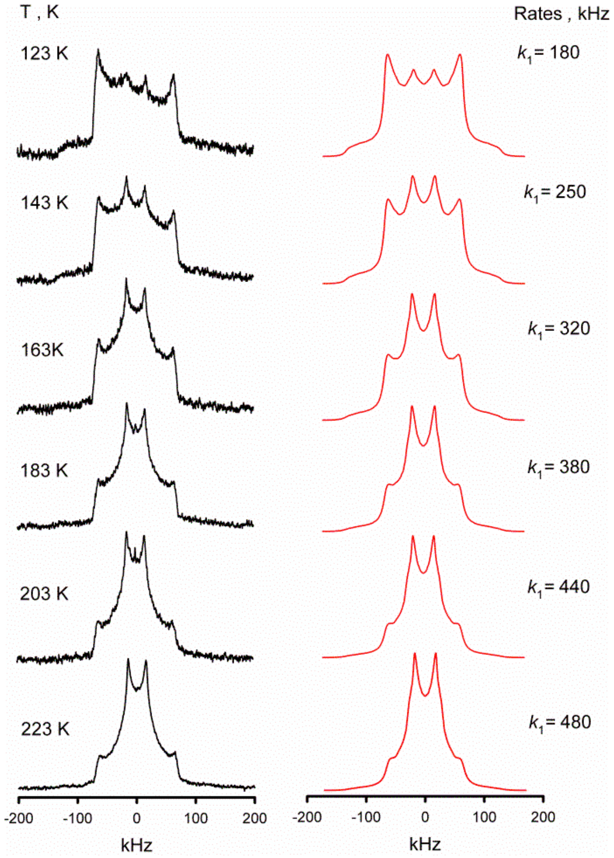

Figure A.14: ^{2}H NMR line shape temperature dependence for C_2H_2 (0.3 bar) MFM-160 materials phenyl fragments (experimental - left, simulation - right).

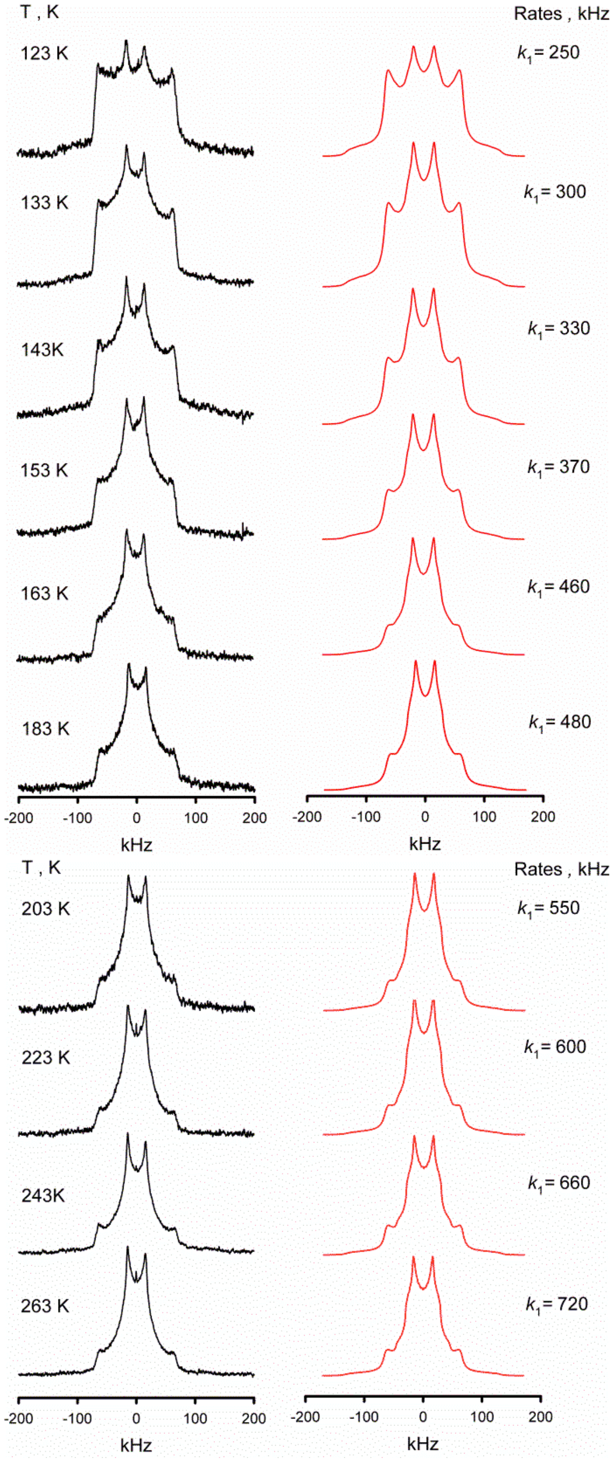

Figure A.15: ^{2}H NMR line shape temperature dependence for C_2H_2 (1 bar) MFM-160 materials phenyl fragments (experimental - left, simulation - right).